

Electronic Thesis and Dissertation Repository

4-9-2024 10:00 AM

Numerical Study of Ozone Decomposition Reaction Behaviours in Gas-Solids Circulating Fluidized Bed Reactors

Zhengyuan Deng, *Western University*

Supervisor: Zhu, Jesse, *The University of Western Ontario*

Joint Supervisor: Zhang, Chao, *The University of Western Ontario*

A thesis submitted in partial fulfillment of the requirements for the Doctor of Philosophy degree in Chemical and Biochemical Engineering

© Zhengyuan Deng 2024

Follow this and additional works at: <https://ir.lib.uwo.ca/etd>

 Part of the [Catalysis and Reaction Engineering Commons](#)

Recommended Citation

Deng, Zhengyuan, "Numerical Study of Ozone Decomposition Reaction Behaviours in Gas-Solids Circulating Fluidized Bed Reactors" (2024). *Electronic Thesis and Dissertation Repository*. 10000. <https://ir.lib.uwo.ca/etd/10000>

This Dissertation/Thesis is brought to you for free and open access by Scholarship@Western. It has been accepted for inclusion in Electronic Thesis and Dissertation Repository by an authorized administrator of Scholarship@Western. For more information, please contact wlsadmin@uwo.ca.

Abstract

This study numerically investigated the reaction behaviours of catalytic ozone decomposition reaction in a 10.2-meter-tall gas-solids circulating fluidized bed (CFB) reactor.

A pseudo-homogeneous reactive transport model for ozone decomposition, integrated with the two-fluid model, was developed and validated using experimental data. Based on the model, the impacts of turbulence models, specular coefficients, and simulation methods on reaction behaviours in the CFB riser reactor were explored. These three factors were found to significantly affect the hydrodynamic characteristics and the reaction behaviours in the riser.

A comparative study of CFB riser and downer reactors was conducted. Operations in the direction of and against gravity resulted in drastically different flow fields and particle clustering in the two reactors. More uniform flow and reaction fields make the downer have better gas-solids contact efficiency than the riser. Flow structure and residence time distributions of gas and solids in the riser and downer were characterized by tracing the gas and particles. The results showed that flow in the downer reactor resembles plug flow, while significant axial backmixing occurs in the riser. An internal circulation mechanism is proposed to explain the backmixing.

A sub-grid reactive transport model was developed using a filtering method and an artificial neural network (ANN) to explore the impact of particle clustering on reaction behaviours. In the development of the filtered model, employing gradient features as inputs enhanced regression accuracy. Additionally, ANN demonstrated superior performance over traditional fitting methods. Consequently, the filtered reactive transport model showed improvements in predicting the reaction behaviours in a CFB riser.

In summary, the hydrodynamic characteristics within CFB predominantly influence reaction behaviours. High-resolution simulations combined with machine learning techniques effectively aid in understanding mechanisms in fluidization system and developing new models, which are crucial for designing and optimizing large-scale reactors.

Keywords: Circulating fluidized bed, ozone decomposition reaction, residence time distribution, particle cluster, meso-scale structure, sub-grid model, machine learning, artificial neural network

Summary for Lay Audience

In this work, the reaction behaviours in a gas-solids circulating fluidized bed (GSCFB) reactor were investigated using the computational fluid dynamics (CFD) approach. GSCFB is a widely used reactor in process industries, capable of continuously processing granular materials. By introducing gas, particles are suspended and behave like a fluid. Due to the significant density difference between gas and particles, particle clustering occurs. Particle clustering, a type of meso-scale structure and heterogeneous flow structure, is a typical characteristic of flow in GSCFB, significantly affecting the flow field in the reactor.

In the GSCFB, heterogeneous reactions typically occur, with these reactions taking place when reactants in the gas phase come into contact with solid catalysts. Consequently, the hydrodynamic characteristics significantly impact reaction behaviours in the GSCFB. Within the scope of this thesis, these hydrodynamic characteristics are defined by both time-averaged and instantaneous flow fields, and are characterized by gas-solids segregation and clustering. The reaction behaviours, in turn, represent the reaction field, such as the reactant concentration and the reaction rate.

The CFD approach, which solves a series of governing equations, has the ability to capture the flow field and reaction field at each moment. This approach has proven effective for both reactor design and theoretical research. In this study, a CFD model for GSCFB reactors was developed. The impact of various factors, including reactor type, turbulence model, and operating conditions, on the hydrodynamic characteristics and reaction behaviours were explored. Additionally, a sub-grid reactive transport model was established to introduce the effects of particle clustering on the reaction behaviours. This model notably improves the accuracy of reaction field predictions by correcting deviations caused by particle clustering.

The development of GSCFB relies on both experimental and numerical works. Experiments provide fundamental understanding and reliable data for reactors. Numerical work offers an abundance of reactor data under various types and conditions, aiding in exploring new applications for reactors and shortening development cycles. Additionally, the ample micro- and meso-scale information provided by numerical work helps researchers better understand and investigate complex phenomena in reactors.

Co-Authorship Statement

Zhengyuan Deng drafted all chapters, and revisions were made under the guidance of Dr. Jesse Zhu and Dr. Chao Zhang. In Chapters 3 to 6, Zhengyuan Deng conducted model development, CFD simulations, and data analysis under the supervision of Dr. Jesse Zhu and Dr. Chao Zhang. Individual papers based on these chapters will be submitted for publication.

Acknowledgements

First and foremost, I would like to express my deepest gratitude to my main supervisor, Dr. Jesse Zhu, for the invaluable guidance and encouragement provided in both academic and personal aspects of my life. I am profoundly grateful for the opportunity to pursue my graduate studies and academic research in Canada, which has been an extraordinary and unforgettable experience. It has been an honour and a privilege to have such an experienced, dedicated, and passionate supervisor. In every research discussion, he consistently led me to deeper thinking and always believed in me, even during times when my performance was not at its best. Not only has he taught me to consider engineering problems from a broader and more long-term perspective, but he has also instilled in me the social responsibilities of an engineer through his words and actions. I am deeply appreciative of the effort he has put into my personal and professional growth and offer my utmost respect for his relentless encouragement and educational investment in a young student like me.

I am equally thankful to my co-supervisor, Dr. Chao Zhang, for her kindness, patience, and support. Her wise teaching rapidly introduced me to the essential techniques needed for my research, transforming me from a complete novice to a competent researcher. Her unwavering support ensured I never had to worry about the expenditure of research resources. Her patient revisions greatly facilitated the smooth completion of my thesis draft. I am deeply thankful for her continuous guidance and advice, which were instrumental in the successful completion of my research. Her wisdom and elegance have always left a profound impression on me.

Deep appreciation is extended to my colleagues in the research group, with special mention of Dr. Zeneng Sun and Dr. Yue Yuan. Their engaging and extensive discussions have consistently enriched my understanding and perspective. Their advice, particularly during challenging times, has been both precise and thought-provoking. My gratitude also goes out to collaborative colleagues, Dr. Rongji Cui from Taiyuan University of Technology, Dr. Junnan Zhao from Harbin Institute of Technology, whose interactions have significantly expanded my knowledge. Additionally, heartfelt thanks are extended to my friend Siyuan Chen from Ghent University for providing invaluable insights for my research.

Heartfelt thanks are due to Dr. Zheng-Hong Luo and Dr. Li-Tao Zhu from Shanghai Jiao Tong University for their generous sharing of knowledge, guidance, and assistance in

everyday life during my visit to their research group. Their openness and willingness to share academic insights have earned my utmost appreciation and respect.

I would like to express my deep appreciation to my friends Siyuan Deng, Fengfan Xiang, Xi Jin, as well as Dr. Yujie Zhang and Dr. Wei Liu. Their companionship, support in everyday life, and the wonderful memories we've created together have been irreplaceable.

My heartfelt gratitude goes to my family: my parents, in-laws, grandparents, and especially my wife, for their unwavering support and companionship during my doctoral studies. Their encouragement and presence gave me the confidence to persevere and complete my research and thesis, ensuring that I had no worries to distract me from my goals. Their contributions to my journey have been incomparable, and I am deeply grateful for their love and support.

Finally, I would like to extend my heartfelt gratitude to everyone who has been a part of my doctoral journey. Their assistance and support have been invaluable, and I am deeply appreciative of their appearances to my doctoral journey.

Table of Contents

Abstract	ii
Summary for Lay Audience	iii
Co-Authorship Statement	iv
Acknowledgements	v
Table of Contents	vii
List of Figures	xi
List of Tables	xvi
List of Abbreviations, Symbols, and Nomenclature	xvii
Chapter 1	
Introduction	1
1.1 Background	1
1.2 Research objectives	4
1.3 Thesis structure	6
References	8
Chapter 2	
Literature review	11
2.1 Gas-solids fluidization systems	11
2.1.1 Hydrodynamic characteristics in CFB reactors	15
2.1.2 Ozone decomposition reaction in CFB reactors	20
2.2 Numerical works on gas-solids CFB reactors	25
2.2.1 Two-fluid models	30
2.2.2 Interphase interactions and sub-grid models	34

2.2.3	Machine learning-based models	40
2.3	Conclusions	43
	References	45

Chapter 3

A pseudo-homogeneous reactive transport model for catalytic ozone decomposition in fluidization systems: Development and parametric study		53
3.1	Introduction	53
3.2	Numerical models	54
3.2.1	Development of the reactive transport model	54
3.2.2	Two-fluid model	57
3.3	Setups for micro fixed-bed reactor simulations	61
3.4	Setups for CFB riser simulations	64
3.5	Results and discussion	68
3.5.1	Validation of the reactive transport model	68
3.5.2	Time-averaged flow fields and reaction fields in the riser	70
3.5.3	Effects of instantaneous flow structures on reaction behaviours	78
3.6	Conclusions	84
	References	86

Chapter 4

Comparative study of hydrodynamic characteristics and reaction behaviours in CFB riser and downer via numerical method		88
4.1	Introduction	88
4.2	Numerical models	88
4.2.1	Two-fluid model	88
4.2.2	Reactive transport model for the ozone decomposition reaction	92
4.3	CFD simulation setups	93
4.3.1	Computational domain, mesh and solver	95
4.3.2	Boundary conditions	95
4.3.3	Setups for the tracers of the gas and solids phases	98
4.3.4	Operating conditions and case information	99
4.4	Results and discussion	100
4.4.1	Time averaged flow and reaction profiles under different operating conditions	100
4.4.2	Instantaneous flow fields and reaction fields	108

4.4.3	Residence time distributions (RTD) in the riser and downer	114
4.5	Conclusion	125
	References	127

Chapter 5

A machine-learning aided filtered reactive transport model for a wide-range of flow field conditions in gas-solids fluidization systems		129
5.1	Introduction	129
5.2	Numerical models	130
5.2.1	Two-fluid model	130
5.2.2	Reactive transport model for ozone the decomposition reaction . .	133
5.3	CFD setups for high-resolution simulations	134
5.4	Development of the filtered correction model	136
5.4.1	Data collection	136
5.4.2	Filtration process	138
5.4.3	Selection and calculation of the features	140
5.4.4	Development and regression of the neural network model	142
5.4.5	Summary of the development of the reaction correction model . . .	144
5.5	Results and discussions	145
5.5.1	Comparison of flow structures at different operating conditions . .	145
5.5.2	Range checking of the features	147
5.5.3	The structure and loss function of the neural network model	149
5.5.4	Analysis of the feature importance	152
5.6	Conclusions	158
	References	159

Chapter 6

Investigating the impact of particle clustering phenomenon on reaction behaviours in a CFB riser reactor		162
6.1	Introduction	162
6.2	Numerical models	163
6.2.1	Two-fluid model	163
6.2.2	Reactive transport model for the ozone decomposition reaction . .	166
6.3	CFB riser simulation	168
6.3.1	Configuration of the CFB riser system	168
6.3.2	Computational domain, mesh, and solver	168

6.3.3	Boundary conditions and operating conditions	169
6.4	Results and discussions	172
6.4.1	Time-averaged flow fields and reaction fields	172
6.4.2	Effects of the reaction correction coefficients in the riser	180
6.5	Conclusions	187
	References	188
Chapter 7		
Conclusions and Recommendations		190
7.1	Thesis summary and conclusions	190
7.2	Limitations and recommendations	193
	References	198
Appendix A		
Codes used in the thesis		199
	References	205
Curriculum Vitae		206

List of Figures

2.1	Sketches of the six flow regimes in upward gas-solids fluidization (Sun & Zhu, 2019)	12
2.2	Typical schematic of a gas-solids circulating fluidized bed system (Li, 2010; Liu, 2016; Wang, 2013)	13
2.3	Schematic diagram of the gas inlet and solids inlet: (a) gas distributor of the riser (Sun, 2019), (b) gas and solids distributor of the downer (top view) (Johnston et al., 1999; Wang, 2013), (c) gas and solids distributor of the downer (side view) (Wang, 2013)	14
2.4	Typical solids holdup profile (Gupta & Berruti, 2000) and illustration of the influence factors on averaged voidage distribution (Bai et al., 1992). The directions of the arrows: A. decreasing gas velocity, B. increasing solid circulation rate, C. decreasing particle diameter, D. decreasing particle density, E. decreasing bed diameter, F. decreasing exit restriction, G. the influence of bed height with different exit restrictions, H. decreasing inlet restriction, I. increasing solid inventory with strong inlet restriction, J. increasing solid inventory with weak inlet restriction.	16
2.5	Typical profiles of solids holdup in the CFB riser reactor (Wang et al., 2014c)	17
2.6	Typical radial flow structure in the CFB riser reactor (Sun, 2019)	18
2.7	Typical profiles of solids holdup in the CFB downer reactor (Wang et al., 2015a, 2016)	19
2.8	Axial profiles of cross-sectional averaged ozone concentration and solids holdup in the riser in the CFB riser reactor (Li et al., 2013a)	23
2.9	Typical profiles of ozone concentration and solids holdup in the CFB riser reactor (Wang et al., 2014b); (a) and (b): cross-sectional averaged profiles, (c) and (d): axial profiles at various radial positions, (e) and (f): radial profiles at various axial positions	24

2.10	Typical profiles of ozone concentration and solids holdup in the CFB downer reactor (Wang et al., 2014a); (a) & (b): cross-sectional averaged profiles, (c) and (d): radial profiles near the inlet and outlet	26
2.11	Simulation methods from micro-scale to macro-scale and their corresponding applications (Zhu, 2021)	27
2.12	Inlet structure: (a) uniform inlet, (b) jet inlet, (c) contour of solids holdup at the inlet using a jet gas inlet and side solids inlet (Sun, 2019)	32
2.13	Effects of specular coefficient on the radial flow structures in a CFB riser (Cloete et al., 2011): (a) solids holdup, (b) solids velocity	33
2.14	Effects of particle-particle restitution coefficient on the radial flow structures in a CFB riser (Cloete et al., 2011): (a) solids holdup, (b) solids velocity	33
2.15	Schematic filtering process of two-dimensional high-resolution TFM simulations ($\Delta_{\text{mesh}} = 3 d_p$, $d_p = 70 \mu\text{m}$)	37
2.16	Categories of machine learning algorithms (Brunton et al., 2020)	41
2.17	Schematic of a single node (neural) in the ANN	42
2.18	Schematic of a one layer ANN structure	42
3.1	Configuration of the micro fixed-bed reactor (Li, 2010)	55
3.2	Computational domain and mesh of the micro fixed-bed reactor	62
3.3	Schematic and mesh of the circulating fluidized bed system	65
3.4	Comparison of Method 1 and Method 2	67
3.5	Comparison of numerical results and experimental data for cross-sectionally averaged time-averaged profiles along the axial direction	71
3.6	Comparison of the time-averaged radial profiles at different axial positions in the riser between the numerical and experimental data	72
3.7	Comparison of numerical results and experimental data for the time-averaged axial profiles at different radial positions of the riser	73
3.8	Instantaneous flow fields and reaction fields of Case 1 (laminar model) and Case 2 ($k-\epsilon$ turbulence model): (1) solids holdup, (2) ozone concentration, and (3) reaction rate	78
3.9	Comparison of the cross-sectional averaged reaction rates along the axial direction of the riser for different cases	81
3.10	Comparison of the contact efficiencies along the axial direction of the riser for different cases	81

3.11	Comparison of the proportions of the reacted ozone in the different height intervals of the riser for different cases	81
4.1	Configuration and meshes of the circulating fluidized bed system	94
4.2	Schematic diagram of the gas inlet and solids inlet: (a) gas distributor of the riser (Sun, 2019), (b) gas and solids distributor of the downer (top view) (Johnston et al., 1999; Wang, 2013), (c) gas and solids distributor of the downer (side view) (Wang, 2013)	97
4.3	Comparison of numerical and experimental results for cross-sectionally averaged time-averaged profiles along the axial direction in the riser for the cases of R5100 and R5300	102
4.4	Comparison of numerical and experimental results for cross-sectionally averaged time-averaged profiles along the axial direction in the downer for the cases of D5100, D5200, D5300, and D5400	102
4.5	Time-averaged radial profiles of the riser and downer cases at the flow developing region and flow developed region	104
4.6	Time-averaged axial profiles of the riser and downer cases at the central region and wall region	107
4.7	Contours of the instantaneous flow fields and reaction fields of the riser and downer	109
4.8	Probability and cumulative distribution functions of gas and solids tracer concentrations in the riser	115
4.9	Probability and cumulative distribution functions of gas and solids tracer concentrations in the downer	116
4.10	Contours of the gas and solids tracer in the (a) riser and (b) downer	118
4.11	Particle flow path in the (a) riser and (b) downer	123
5.1	Periodic domain configuration	135
5.2	Time series of the mean gas, solids, and slip velocity in the periodic domain ($\varepsilon_{s,0} = 0.05$)	137
5.3	Example of the filtration process for solids holdups	138
5.4	Neural network structure	143
5.5	Contours of the solids holdup and the ozone concentration in the cases using the high-resolution mesh	146

5.6	Comparison of the probability density distributions of the features in the cases of using the high-resolution mesh (results from this study) and the case of the riser simulation (results from Chapter 3 and 4)	148
5.7	Effects of the number of layers of the neural network model on the training loss	149
5.8	Effects of the number of nodes of the neural network model on the training loss	149
5.9	Comparison of the actual and predicted reaction correction coefficients for the regression results using the different loss functions	151
5.10	Probability density distributions of the MAE	151
5.11	Probability density distributions of the MAPE	151
5.12	Shapley values of one data entry	154
5.13	Shapley values of 1000 data entries	154
6.1	Schematic and mesh of the circulating fluidized bed system	169
6.2	Comparison of numerical results and experimental data for cross-sectionally averaged time-averaged profiles along the axial direction for Case 1 (PHRTM) and Case 2 (FRTM)	174
6.3	Comparison of numerical results and experimental data for cross-sectionally averaged time-averaged profiles along the axial direction for Case 3 (PHRTM) and Case 4 (FRTM)	174
6.4	Comparison of the time-averaged radial profiles at flow developing and developed regions between numerical results and experimental data	175
6.5	Comparison of the time-averaged axial profiles at central and wall regions between numerical results and experimental data	176
6.6	Comparison of reaction rates in the cases using the PHRTM and FRTM: (a) time-averaged cross-sectional profiles of the reaction rate and (b) reaction correction coefficient along the axial direction of the riser	181
6.7	Comparison of reaction rate in the simulations using the PHRTM and FRTM: (a) the amount of ozone reacted in different height sections of the riser in 1 s and (b) the distributions of the reaction correction coefficient in each height section for Case 2	182
6.8	Time-averaged results of the reaction correction coefficient of Case 2: (a) contour of the whole computational domain, (b) axial profiles at different radial locations, and (c) radial profiles at different axial locations	182

6.9	Instantaneous flow fields and reaction fields of Case 2	183
7.1	Steps of the ozone decomposition reaction occurring in a gas-solids fluidization system	190
A.1	Order of code usage in the filtering process	201

List of Tables

3.1	CFD Model for the micro fixed-bed reactor simulation	63
3.2	Parameters used for micro fixed-bed reactor simulations	63
3.3	Information on CFD model for the CFB riser simulation	66
3.4	CFB riser case information	68
3.5	Parameters used for CFB riser simulations	68
3.6	Comparison of numerical results with experimental data	69
4.1	Parameters used for the CFB riser and downer simulations	93
4.2	Information on CFD model for the CFB riser and downer simulations . . .	96
4.3	Case information	100
4.4	Statistical results for the flow developing and developed regions in the instantaneous contours	110
4.5	Summary of time points and durations [s] of tracers behaviour	117
5.1	Parameters used in the simulations using a periodic domain	134
5.2	CFD model for simulations in a periodic domain	136
5.3	Importance and contribution of features	157
6.1	Parameters used for the CFB riser simulation	167
6.2	Information on CFD model for the CFB riser simulation	170
6.3	CFB riser case information	172

List of Abbreviations, Symbols, and Nomenclature

Abbreviations

AI	Artificial intelligence	GSCFB	Gas-solids circulating fluidized bed
ANN	Artificial neural network	HDCFB	High-density circulating fluidized bed
APE	Absolute percentage error	HPC	High-performance computing
BFB	Bubbling fluidized bed	KTGF	Kinetic theory of granular flow
CDF	Cumulative distribution function	LBM	Lattice-Boltzmann method
CFB	Circulating fluidized bed	LDCFB	Low-density circulating fluidized bed
CFD	Computational fluid dynamics	MAE	Mean absolute error
CSTR	Continuous stirred-tank reactor	MAPE	Mean absolute percentage error
CTFB	Circulating turbulent fluidized bed	ML	Machine learning
DEM	Discrete element method	MP-PIC	Multiphase particle-in-cell
DNS	Direct numerical simulation	MSE	Mean squared error
FCC	Fluid catalytic cracking	PDF	Probability distribution function
FRTM	Filtered reactive transport model	PFR	Plug flow reactor
fTFM	Filtered two-fluid model	PHRTM	Pseudo-homogeneous reactive transport model

PR-DNS	Particle-resolved direct numerical simulation	ε_s	Solids holdup, the volume fraction of solids
PSD	Particle size distribution	ϵ	Turbulence dissipation rate
RANS	Reynolds-averaged Navier-Stokes	η	Proportion of reacted ozone in different height intervals
RTD	Residence time distribution	Γ	Mass diffusivity, kg/m/s
SD	Standard deviation	γ_g	Opening area ratio of gas distributors
SHAP	Shapley additive explanations	∇	Gradient operator
TFB	Turbulence fluidized bed	λ_s	Bulk viscosity of the solids phase
TFM	Two-fluid model	μ	Viscosity, kg/m/s
UDF	User-defined function	μ_s	Shear viscosity of the solids phase
UDM	User-defined memory	ϕ	Specularity coefficient
UDS	User-defined scalar	ρ	Density, kg/m ³
Subscripts		$\bar{\bar{\tau}}$	Stress-strain tensor
0	Initial condition	Θ_s	Granular temperature
g	Gas phase	Symbols	
p	Particle	\dot{V}	Volumetric flow rate, m ³ /s
s	Solids phase	Re_s	Particle Reynolds number
Symbols (greek letters and others)		\mathcal{D}	Mass diffusion coefficient, m ² /s
α	Contact efficiency	$\bar{\bar{\mathbf{I}}}$	Unit tensor
Δ_{filter}	Length of a filter box, m	\vec{g}	Gravitational acceleration vector, m/s ²
Δ_{mesh}	Mesh size, m	\vec{u}	Velocity vector, m/s
$\nabla \cdot$	Divergence operator	A	Area, m ²
ε_g	Voidage, the volume fraction of gas	a_v	Specific surface area, m ² /m ³

C	Concentration, kg/m ³ or mol/m ³	M	Molar mass, kg/mol
C_D	Drag coefficient	m	Mass, kg
D	Diameter, m	p	Pressure, Pa
d_p	Particle diameter, m	R	Radius, m
e_{ss}	Restitution coefficient for particle collisions	R	Reaction rate, g/s or g/m ³ /s
e_{sw}	Restitution coefficient for particle-wall collisions	r	Radial position, m
F_g	Gas flow rate, kg/s	r	Reaction rate, g/s or g/m ³ /s
F_s	Solids flux, kg/m ² /s	Sc	Schmidt number
G_s	Solids circulation rate, kg/m ² /s	t	Time, s
H	Height, m	U_g	Superficial gas velocity, m/s
h	Axial/vertical position, m	V	Volume, m ³
H_r	Reaction correction coefficient	v	Local velocity, m/s
k	Turbulence kinetic energy	x	Radial/lateral position, m
k_r	Apparent reaction constant based on the volume of the catalys, s ⁻¹	$Y_g^{O_3}$	Ozone mass fraction in the gas phase
K_{sg}	Interphase momentum exchange coefficient between the gas phase and solids phase	Y_g^{tr}	Tracer mass fraction in the gas phase
		Y_s^{tr}	Tracer mass fraction in the solids phase

Chapter 1

Introduction

Reaction behaviours of the ozone decomposition reaction within gas-solids circulating fluidized bed reactors are investigated in this work via the computational fluid dynamic (CFD) approach. The research background, objectives, and thesis structure are presented in this chapter.

1.1 Background

Fluidization is a process of stationary solid granular materials brought in to a dynamic fluid-like state by introducing a fluid (gas or liquid) (Fan & Zhu, 1999). The fluidized bed reactor was first operated commercially in 1923 as a coal gasifier by Winkler (1928). The technique of fluidization is now widely employed in process industries, such as fluid catalytic cracking (FCC) (Jahnig et al., 1980), Fischer-Tropsch synthesis (Schulz, 1999), coal combustion and gasification (Basu, 1999; Gómez-Barea & Leckner, 2010), and gas-phase olefin polymerization (Xie et al., 1994). Additionally, fluidization is gaining prominence in emerging applications such as methanol to olefins (Tian et al., 2015), wastewater treatment (Nelson et al., 2017), particle coating (Cui et al., 2019), and pharmaceutical processes (Ye et al., 2022).

In the upward gas-solids fluidization system, as the superficial gas velocity increases,

the fluidization transitions through six regimes: bubbling fluidized bed, turbulent fluidized bed, circulating turbulent fluidized bed, high-density circulating fluidized bed (CFB), low-density CFB, and pneumatic transport (Sun & Zhu, 2019). The bubbling and turbulent bed regimes are classified as conventional fluidization, characterized by particles that are not entrained out of the reactor by the gas flow. In contrast, in CFB riser reactors, particles are carried out of the reactor by the high-velocity upward gas stream. Consequently, to maintain the solids inventory, fresh particles are continually introduced into the reactor.

Compared to conventional fluidized bed reactors, CFB riser reactors offer numerous advantages: operational flexibility, effective gas-solids contact at short residence times, excellent heat and mass transfer capabilities, and a high capacity for handling granular materials (Berruti et al., 1995; Zhu et al., 1995). In 1942, the first commercial FCC unit, the ESSO Model I, was established as a CFB system (Avidan, 1997). The cracking reaction primarily occurs in the riser of the CFB reactors. As of 2020, there were active refineries with FCC units in 59 countries, with a total capacity of approximately 14,259,000 barrels per day. (Offshore Technology, 2021). The FCC unit has already become one of the most widely used CFB systems in the world. However, CFB riser reactors also present challenges: significant solids backmixing, macro-segregation of gas and solids in the radial direction, and micro-segregation due to particle clustering (Wang et al., 2014a, 2014b). These issues substantially reduce the contact efficiency between the gas and solid phases. Therefore, understanding the hydrodynamic characteristics and their impact on reaction behaviours in CFB reactors is crucial for optimizing these reactors and advancing the global energy sector.

Over the past decades, numerous experimental studies have focused on investigating the hydrodynamic characteristics and reaction behaviours in CFB riser reactors. Advanced measurement techniques, alongside the catalytic ozone decomposition reaction conducted

in the fluidization systems, have enabled the acquisition of extensive time series data of flow fields and reaction fields at various locations within these reactors (Li, 2010; Liu, 2016; Wang, 2013). However, the presence of macro-segregation and micro-segregation flow structures makes it challenging to accurately correlate flow fields with reaction fields using time-averaged profiles alone. The difficulties of simultaneously measuring solids holdup, particle velocity, and reactant concentration further complicates the analysis of impact of hydrodynamic characteristics on reaction behaviours based on time series data. Consequently, CFD techniques, which have matured significantly in recent years, offer a more effective approach for studying reactions within CFB reactors. In terms of scaling up, substituting a testing facility with CFD modelling can save at least three years and millions of dollars during the development and design process of a reactor unit (Chew et al., 2022). Therefore, developing a reliable CFD model to investigate the hydrodynamic characteristics and reaction behaviours in CFB reactors holds considerable importance.

With the rapid development of high-performance computing, the CFD technique have become one of the key research methods for studying gas-solids multiphase flows. Researchers have found that accurately describing the impact of meso-scale flow structures (particle clustering) on the performances of the fluidized bed reactors is a core issue for precise and efficient prediction of flow fields and reaction fields within the reactor (Agrawal et al., 2001; Li & Huang, 2018; Sundaresan et al., 2018). Currently, the methods commonly used to simulate the gas-solids fluidization systems include direct numerical simulation (DNS), discrete element method (DEM), multiphase particle-in-cell (MP-PIC), and the two-fluid model (TFM). Typically, an industry-scale reactor contains more than 10^{12} particles. However, DNS is generally used for simulations at the particle size scale, and tracking such a large number of particles simultaneously poses a challenge for the DEM. Therefore, the TFM based on the Eulerian-Eulerian approach is more suitable for simulations of industry-scale reactors at present. However, the closure models or

parameters used in the TFM (drag model, reaction rate, etc.) often overlook the influence of the meso-scale flow structures when simulations are conducted using a coarse mesh, leading to distortions in the model's predictive results. Currently, numerous sub-grid models have been proposed to address these issues. From the hydrodynamic perspective, methods such as semi-empirical method (Gao et al., 2009; Sun et al., 2022), the filtration method (Igci & Sundaresan, 2011; Zhu et al., 2016), and the energy minimization multi-scale (EMMS) model (Lu et al., 2009; Yang et al., 2003) have been introduced to correct the interaction between gas and solids phases. These methods have subsequently been extended to adjust parameters such as interphase heat transfer and chemical reactions.

In recent years, artificial intelligence (AI) technologies, represented by machine learning (ML), have gradually been applied in various fields of chemical engineering. ML possesses strong capabilities in handling large amounts of data and complex nonlinear relationships. Currently, ML has been applied and developed in areas such as solid heterogeneous catalyst design (Guan et al., 2022), intelligent control and optimization of chemical processes (Kramer & Morgado-Dias, 2018; Nascimento et al., 2000), flow regime analysis for gas-liquid multiphase reactors (Manjrekar & Dudukovic, 2019), drag force correction for gas-solids fluidized bed reactors (Tausendschön et al., 2023; Zhu et al., 2020), and etc. The capabilities of the ML enable it to play a significant role in understanding complex heterogeneous flow structures and transport phenomena within the fluidized bed reactors. It is believed that ML can also contribute to the understanding of reaction behaviour and the correction of reaction rates in fluidized bed reactors.

1.2 Research objectives

The overall objective is to comprehensively investigate the ozone decomposition reaction that took place in the gas-solids circulating fluidized bed reactors, in order to reveal the

effects of the hydrodynamic characteristics on the reaction behaviours. In the process of achieving this objective, the impact of micro-segregation flow structure and macro-segregation flow structure within CFB reactors on reaction behaviours will be revealed. Consequently, this aims to shorten the scaling-up and design period of reactors as well as provide guidance for the optimization of reactors. The detailed objectives are as follows:

1. To develop a pseudo-homogeneous reactive transport model and then to explore the effects of hydrodynamic characteristics on the reaction behaviours in CFB reactors. (Chapter 3 and Chapter 4)
 - (a) To develop a pseudo-homogeneous reactive transport model for the catalytic ozone decomposition reaction based on experimental data. This model can integrate with the two-fluid model and can describe the ozone behaviours in reactors.
 - (b) To validate the pseudo-homogeneous model by comparing the simulation results with the experimental data of a micro fixed-bed reactor.
 - (c) To investigate the impacts of turbulence models, specular coefficients, and simulation methods on the flow fields and reaction fields in a CFB riser reactor.
 - (d) To explore the influence of instantaneous flow structures on reaction behaviours in the CFB riser reactor, focusing specifically on the effects of the turbulence models.
 - (e) To compare the time-averaged profiles of the solids holdup, particle velocity, and ozone concentration between CFB riser and downer reactors from dilute to dense flow conditions.
 - (f) To compare instantaneous flow fields and their effects on the reaction behaviours between the CFB riser and downer reactors.
 - (g) To investigate the flow structures in the CFB riser and downer reactors via

residence time distribution analysis for both gas and solids phases.

2. To develop a filtered reactive transport model that adjusts the reaction rate by employing the influence of particle clustering phenomenon and then to explore the effects of the phenomenon on the reaction behaviours in the CFB riser reactor. (Chapter 5 and Chapter 6)
 - (a) To conduct high-resolution gas-solids fluidization simulations to obtain the data of flow field and reaction field under a wide-range of operating conditions.
 - (b) To obtain a dataset of reaction correction coefficients and filtered features by a filtering algorithm.
 - (c) To develop a filtered correction model by training a neural network model with the dataset.
 - (d) To evaluate the influence of the features on the reaction correction coefficients by Shapley value analysis.
 - (e) To validate the filtered reactive transport model by integrating with the TFM model and comparing the simulation results with the experimental data.
 - (f) To study the effects of the filtered reactive transport model on the time-averaged profiles in the CFB riser reactor.
 - (g) To study the effects of the particle clustering phenomena on the reaction behaviours in the CFB riser reactor.

1.3 Thesis structure

This thesis follows the integrated-article format as outlined in the thesis guide of Western University. The thesis is organized as follows:

1. Chapter 1 gives the general introduction of the research work.

2. Chapter 2 provides a detailed literature review of the research background, include experimental and numerical works on gas-solids circulating fluidized bed reactors, the ozone decomposition reaction for gas-solids catalytic systems, the sub-grid models, and the machine learning application for fluidization systems.
3. Chapter 3 presents the development of a pseudo-homogeneous reactive transport model for the catalytic ozone decomposition reaction and the investigation of the impacts of turbulence models, specularly coefficients, and simulation methods on the hydrodynamic characteristics and reaction behaviours in a CFB riser reactor.
4. Chapter 4 compares the hydrodynamic characteristics and reaction behaviours between CFB riser and downer reactors under various operating conditions. The instantaneous flow structures of the two reactors are also compare via residence time distribution analysis.
5. Chapter 5 presents the development of a filtered correction model and the investigation of the effects of particle clustering phenomena on the local reaction rate in general gas-solids fluidization systems.
6. Chapter 6 applies the filtered reactive transport model to the CFB riser reactor and investigates the effects of the particle clustering phenomena on the reaction behaviours in a CFB riser reactor.
7. Chapter 7 provides the conclusions of this research work and recommendations for future works.

References

- Agrawal, K., Loezos, P. N., Syamlal, M., & Sundaresan, S. (2001). The role of meso-scale structures in rapid gas–solid flows. *Journal of Fluid Mechanics*, 445, 151–185.
- Avidan, A. A. (1997). Fluid catalytic cracking. In *Circulating fluidized beds* (pp. 466–488). Springer.
- Basu, P. (1999). Combustion of coal in circulating fluidized-bed boilers: A review. *Chemical Engineering Science*, 54(22), 5547–5557.
- Berruti, F., Pugsley, T., Godfroy, L., Chaouki, J., & Patience, G. S. (1995). Hydrodynamics of circulating fluidized bed risers: A review. *The Canadian Journal of Chemical Engineering*, 73(5), 579–602.
- Chew, J. W., LaMarche, W. C. Q., & Cocco, R. A. (2022). 100 years of scaling up fluidized bed and circulating fluidized bed reactors. *Powder Technology*, 409, 117813.
- Cui, J., Yeasmin, R., Shao, Y., Zhang, H., Zhang, H., & Zhu, J. (2019). Fabrication of Ag^+ , Cu^{2+} , and Zn^{2+} ternary ion-exchanged zeolite as an antimicrobial agent in powder coating. *Industrial & Engineering Chemistry Research*, 59(2), 751–762.
- Fan, L.-S., & Zhu, C. (1999). Principles of gas-solid flows.
- Gao, J., Lan, X., Fan, Y., Chang, J., Wang, G., Lu, C., & Xu, C. (2009). Cfd modeling and validation of the turbulent fluidized bed of fcc particles. *AIChE journal*, 55(7), 1680–1694.
- Gómez-Barea, A., & Leckner, B. (2010). Modeling of biomass gasification in fluidized bed. *Progress in Energy and Combustion Science*, 36(4), 444–509.
- Guan, Y., Chaffart, D., Liu, G., Tan, Z., Zhang, D., Wang, Y., Li, J., & Ricardez-Sandoval, L. (2022). Machine learning in solid heterogeneous catalysis: Recent developments, challenges and perspectives. *Chemical Engineering Science*, 248, 117224.
- Igci, Y., & Sundaresan, S. (2011). Constitutive models for filtered two-fluid models of fluidized gas–particle flows. *Industrial & Engineering Chemistry Research*, 50(23), 13190–13201.
- Jahnig, C., Campbell, D., & Martin, H. (1980). History of fluidized solids development at Exxon. In *Fluidization* (pp. 3–24). Springer.
- Kramer, A., & Morgado-Dias, F. (2018). Applications of artificial neural networks in process control applications: A review. *2018 International Conference on Biomedical Engineering and Applications (ICBEA)*, 1–6.

- Li, D. (2010). *Investigation of circulating fluidized bed riser and downer reactor performance for catalytic ozone decomposition* [Doctoral dissertation, The University of Western Ontario].
- Li, J., & Huang, W. (2018). From multiscale to mesoscience: Addressing mesoscales in mesoregimes of different levels. *Annual review of chemical and biomolecular engineering*, 9, 41–60.
- Liu, J. (2016). *Reactor performances and hydrodynamics of various gas-solids fluidized beds* [Doctoral dissertation, The University of Western Ontario]. <https://ir.lib.uwo.ca/etd/3967/>
- Lu, B., Wang, W., & Li, J. (2009). Searching for a mesh-independent sub-grid model for cfd simulation of gas–solid riser flows. *Chemical Engineering Science*, 64(15), 3437–3447.
- Manjrekar, O. N., & Dudukovic, M. P. (2019). Identification of flow regime in a bubble column reactor with a combination of optical probe data and machine learning technique. *Chemical Engineering Science: X*, 2, 100023.
- Nascimento, C. A. O., Giudici, R., & Guardani, R. (2000). Neural network based approach for optimization of industrial chemical processes. *Computers & Chemical Engineering*, 24(9-10), 2303–2314.
- Nelson, M. J., Nakhla, G., & Zhu, J. (2017). Fluidized-bed bioreactor applications for biological wastewater treatment: A review of research and developments. *Engineering*, 3(3), 330–342.
- Offshore Technology. (2021). *US leads globally with highest operational refinery FCCU capacity*. Retrieved October 14, 2023, from <https://www.offshore-technology.com/comment/us-leads-global-fccu-capacity/>
- Schulz, H. (1999). Short history and present trends of fischer–tropsch synthesis. *Applied Catalysis A: General*, 186(1), 3–12.
- Sun, Z., Zhang, C., & Zhu, J. (2022). Numerical investigations on gas–solid flow in circulating fluidized bed risers using a new cluster-based drag model. *Particuology*, 63, 9–23.
- Sun, Z., & Zhu, J. (2019). A consolidated flow regime map of upward gas fluidization. *AIChE Journal*, 65(9), e16672.
- Sundaresan, S., Ozel, A., & Kolehmainen, J. (2018). Toward constitutive models for momentum, species, and energy transport in gas–particle flows. *Annual review of chemical and biomolecular engineering*, 9, 61–81.

- Tausendschön, J., Sundaresan, S., Salehi, M., & Radl, S. (2023). Machine learning-based filtered drag model for cohesive gas-particle flows. *Chemical Engineering & Technology*.
- Tian, P., Wei, Y., Ye, M., & Liu, Z. (2015). Methanol to olefins (MTO): From fundamentals to commercialization. *Acs Catalysis*, 5(3), 1922–1938.
- Wang, C. (2013). *High density gas-solids circulating fluidized bed riser and downer reactors* [Doctoral dissertation, The University of Western Ontario]. <https://ir.lib.uwo.ca/etd/1572/>
- Wang, C., Zhu, J., Barghi, S., & Li, C. (2014a). Axial and radial development of solids holdup in a high flux/density gas–solids circulating fluidized bed. *Chemical Engineering Science*, 108, 233–243.
- Wang, C., Zhu, J., Li, C., & Barghi, S. (2014b). Detailed measurements of particle velocity and solids flux in a high density circulating fluidized bed riser. *Chemical Engineering Science*, 114, 9–20.
- Winkler, F. (1928). Manufacturing fuel gas [US Patent 1,687,118].
- Xie, T., McAuley, K. B., Hsu, J. C., & Bacon, D. W. (1994). Gas phase ethylene polymerization: Production processes, polymer properties, and reactor modeling. *Industrial & Engineering Chemistry Research*, 33(3), 449–479.
- Yang, N., Wang, W., Ge, W., & Li, J. (2003). Cfd simulation of concurrent-up gas–solid flow in circulating fluidized beds with structure-dependent drag coefficient. *Chemical Engineering Journal*, 96(1-3), 71–80.
- Ye, Y., Ma, Y., & Zhu, J. (2022). The future of dry powder inhaled therapy: Promising or discouraging for systemic disorders? *International journal of pharmaceuticals*, 614, 121457.
- Zhu, J.-X., Yu, Z.-Q., Jin, Y., Grace, J., & Issangya, A. (1995). Cocurrent downflow circulating fluidized bed (downer) reactors—a state of the art review. *The Canadian Journal of chemical engineering*, 73(5), 662–677.
- Zhu, L.-T., Tang, J.-X., & Luo, Z.-H. (2020). Machine learning to assist filtered two-fluid model development for dense gas–particle flows. *AIChE Journal*, 66(6), e16973.
- Zhu, L.-T., Xie, L., Xiao, J., & Luo, Z.-H. (2016). Filtered model for the cold-model gas–solid flow in a large-scale mto fluidized bed reactor. *Chemical Engineering Science*, 143, 369–383.

Chapter 2

Literature review

This chapter reviews the literature related to the topics outlined in Chapter 1 and presents information that will be used in the following works. It focuses on the hydrodynamic characteristics and the ozone decomposition reaction behaviours in gas-solids circulating fluidized bed reactors. Additionally, it covers multiphase models, sub-grid models, and machine learning-based models specific to gas-solids fluidization systems.

2.1 Gas-solids fluidization systems

By introducing fluid media into a vessel containing solid granular materials, the particles can be suspended. Subsequently, the distances between particles can be increased, and their interactions can be reduced. As a result, the particles can flow freely and exhibit fluid-like properties (Fan & Zhu, 1999; Liu, 2016). This phenomenon is known as fluidization, and the unit operations that utilize this physical principle to handle particles are referred to as fluidized beds. By changing the superficial gas velocity in the gas-solids fluidization system, the fluidized bed can be categorized into low-velocity conventional fluidized beds and high-velocity continuous fluidized beds (Yerushalmi et al., 1976). Under low-velocity operations, particles are suspended by the relatively low superficial gas velocity (usually less than 1 to 2 m/s), resulting in minimal particle entrainment. The flow regimes in the conventional fluidized bed include bubbling fluidization and turbulent fluidization,

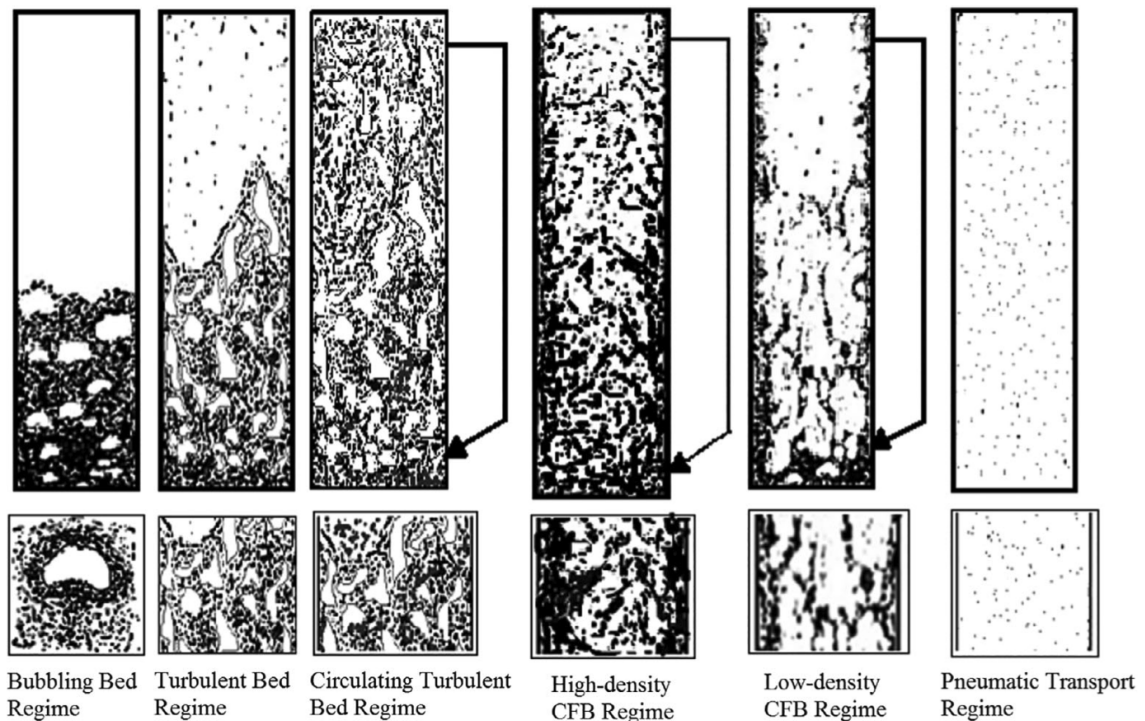


Figure 2.1: Sketches of the six flow regimes in upward gas-solids fluidization (Sun & Zhu, 2019)

as illustrated in Figure 2.1. With an increase in the superficial gas velocity beyond a critical value (usually more than 3 to 5 m/s), solids entrainment significantly increases and can quickly empty the particulate bed if no particles are fed back into it (Sun & Zhu, 2019). Continuous operations can be achieved by separating the solids from the discharged streams and reintroducing them into the bed. Thus, reactors that operate with continuous operations are called circulating fluidized beds (CFB). The flow regimes in CFB include circulating turbulent fluidization, high-density (HD) fluidization, and low-density (LD) fluidization. As mentioned in Chapter 1, gas-solids CFB reactors have been widely used in the process industry, especially in fluid catalytic cracking (FCC) units in refineries.

Figure 2.2 shows a typical schematic of a gas-solids CFB system (Li, 2010; Liu, 2016; Wang, 2013). The system consists of a riser, a downer, a downcomer, a returning pipe, and separators. In the riser, gas and solids are introduced into the reactor from the

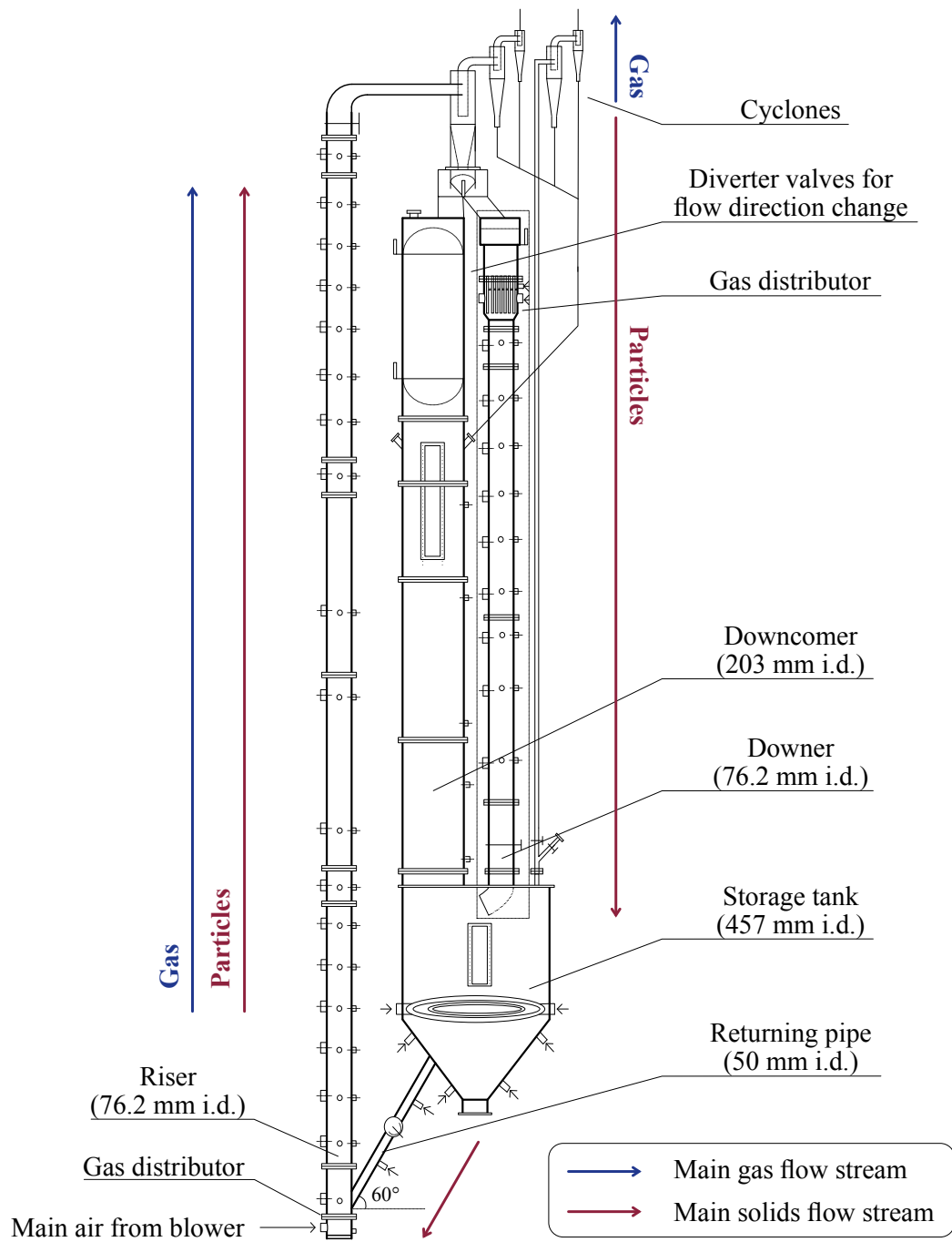


Figure 2.2: Typical schematic of a gas-solids circulating fluidized bed system (Li, 2010; Liu, 2016; Wang, 2013)

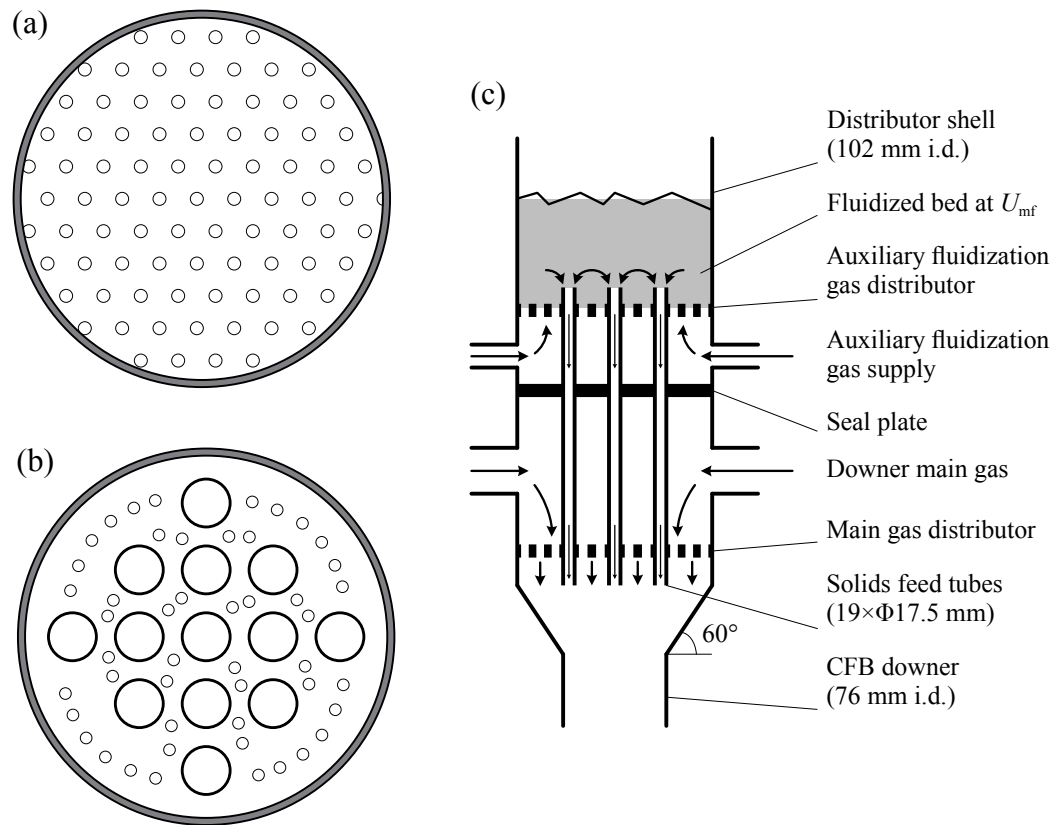


Figure 2.3: Schematic diagram of the gas inlet and solids inlet: (a) gas distributor of the riser (Sun, 2019), (b) gas and solids distributor of the downer (top view) (Johnston et al., 1999; Wang, 2013), (c) gas and solids distributor of the downer (side view) (Wang, 2013)

gas distributor and the return pipe at the bottom of the riser, respectively. The solids are then entrained upward by the high-velocity upflow gas and separated from it in separators. These separators typically consist of several cyclones and bag filters, located at the top of the system. The separated solids flow downward along the downcomer and are stored in the storage tank, prepared to be fed into the riser again. Finally, the particles are reintroduced into the riser through the return pipe, completing the circulation. Normally, chemical reactions take place in the riser. However, in some cases, the downer is also utilized as the reaction zone for quick chemical reactions. In the CFB system, diverter valves can alter the direction of solids flow. When the solids flow through the downer rather than the downcomer, the riser in the system serves simply as a lifting pipe for cycling

the particles. The path of solids circulation remains the same as in the riser-downcomer system.

This CFB system was constructed in the laboratory of Particle Technology Research Centre at Western University by Dr. Jesse Zhu's group. The detailed dimensions of the system are provided, as shown in Figure 2.2 and Figure 2.3. Plenty of experimental data, including the hydrodynamic and reaction data, have been collected and reported (Li et al., 2011, 2012, 2013a, 2013b; Liu, 2016; Wang et al., 2014c, 2014b, 2014d, 2014a, 2015a, 2015b, 2015c, 2016). Therefore, it is a good choice to use this CFB system as the research target of this work.

2.1.1 Hydrodynamic characteristics in CFB reactors

Hydrodynamic characteristics typically refer to the flow fields of gas and solids in the CFB reactors, specifically the distributions of solids holdup, gas velocity, and solids velocity. The mass transfer, heat transfer, and reaction behaviours in CFB reactors are largely influenced by the hydrodynamic characteristics. Therefore, understanding the hydrodynamic characteristics in CFB reactors is essential for the design and operation of these reactors (Grace, 1990).

Riser In a CFB riser reactor, the gas and solids flow upward concurrently and against the gravity. In the axial direction, the solids holdup profiles in the riser are typically exhibited as an exponential shape or an S-shape (Li et al., 2012; Li & Kwauk, 1980; Pärssinen & Zhu, 2001; Schnitzlein & Weinstein, 1988; Wang et al., 2014b). The exponential shape profiles are usually observed in the LDCFB riser reactors, while the S-shape profiles are observed in the HDCFB riser reactors. The overall bed solids holdup, $\varepsilon_s = 0.10$, is considered as a criteria for distinguishing the LDCFB and HDCFB flow regimes (Bai et al., 1997; Sun & Zhu, 2019; Wang et al., 2014c). Typical axial profiles of solids holdup for the LDCFB and

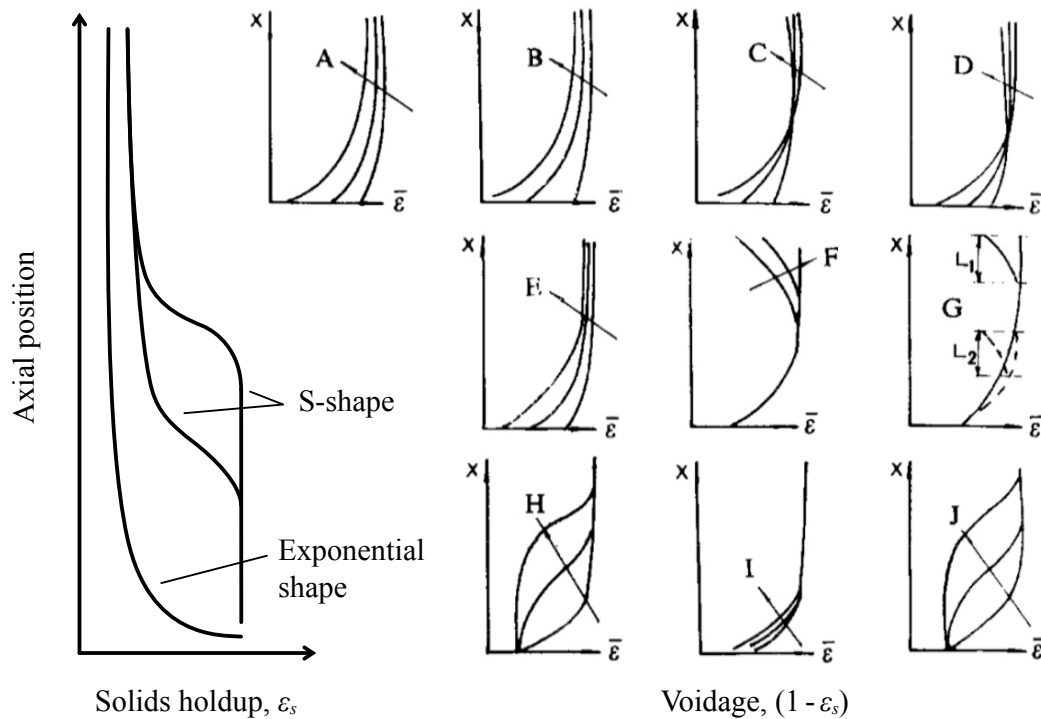


Figure 2.4: Typical solids holdup profile (Gupta & Berruti, 2000) and illustration of the influence factors on averaged voidage distribution (Bai et al., 1992). The directions of the arrows: A. decreasing gas velocity, B. increasing solid circulation rate, C. decreasing particle diameter, D. decreasing particle density, E. decreasing bed diameter, F. decreasing exit restriction, G. the influence of bed height with different exit restrictions, H. decreasing inlet restriction, I. increasing solid inventory with strong inlet restriction, J. increasing solid inventory with weak inlet restriction.

HDCFB riser reactors are shown in Figure 2.5 (a). According to the profiles, the riser can be divided into three regions: the bottom dense region, the middle transition region, and the upper dilute region. Normally, the length of the bottom dense region in the HDCFB risers is much longer than that in the LDCFB risers. The accumulation of particles in the bottom region is caused by the solids inventory in the storage tanks and the downcomer of the CFB system (Bai et al., 1997; Bi & Zhu, 1993). To increase the solids circulation rate in a CFB system, particles require more driving force to enter the riser. This demand for additional force necessitates a larger inventory of particles. In a CFB system, which essentially acts like a U-tube, the increased pressure from a higher number of particles in

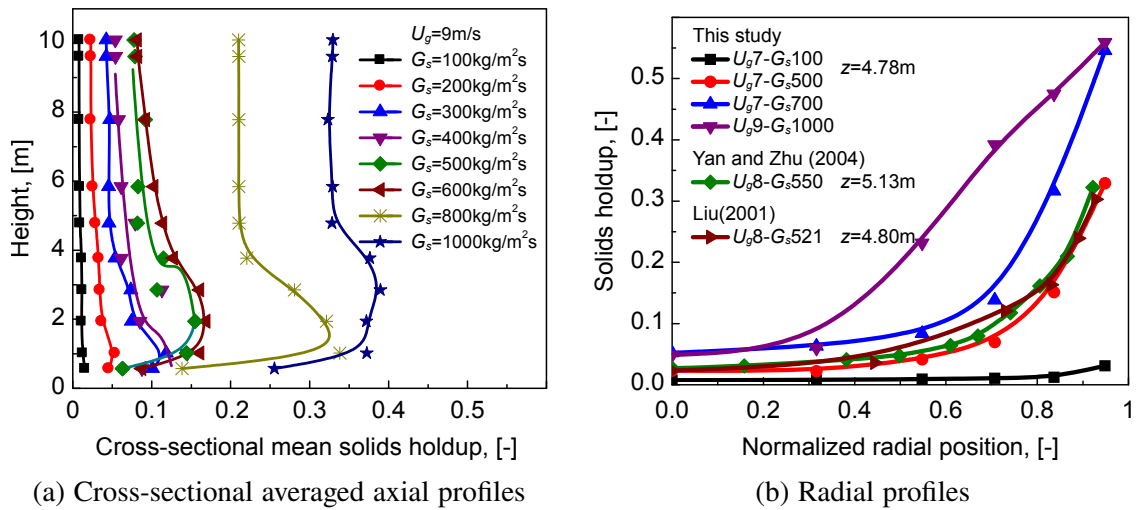


Figure 2.5: Typical profiles of solids holdup in the CFB riser reactor (Wang et al., 2014c)

the downflow columns must be balanced by a corresponding increase in the number of particles in the riser. Furthermore, due to the phenomenon of particle clustering, these additional particles are more likely to accumulate at the bottom of the riser (Horio & Clift, 1992). As a result, a dense region formed at the bottom. The solids holdup in the upper dilute region is related to the saturation carrying capacity of the gas flow, which is determined by the superficial gas velocity and the gas properties (Bai & Kato, 1995). Except for the superficial gas velocity and the solids circulation rate, the axial profiles of solids holdup are also influenced by other factors, such as the particle properties, bed sizes, restriction of inlet and exit, etc. Bai et al. (1992) gives a comprehensive summary of the influence factors on the axial profiles of solids holdup, as shown in Figure 2.4.

The radial profiles of solids holdup in LDCFB riser reactors exhibit a core-annulus structure (Ishii & Horio, 1991), as illustrated in Figure 2.6. Compared to conventional fluidized beds, the gas phase dominates the flow field in CFB riser reactors, forming a wide and dilute core region at the center of the riser. In this core region, the solids holdup is relatively low, and the velocities of gas and solids are relatively high. Due to wall effects and particle clustering, a dense annulus region with high solids holdup and low

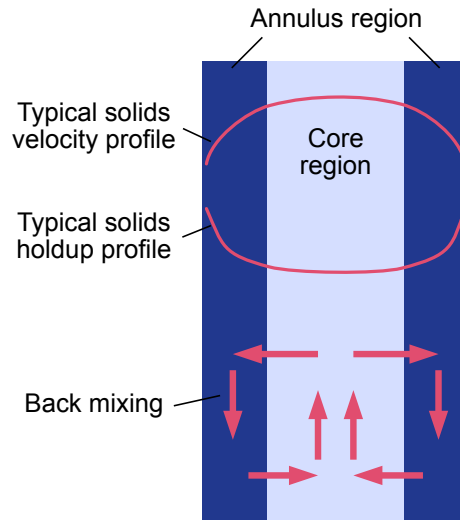


Figure 2.6: Typical radial flow structure in the CFB riser reactor (Sun, 2019)

gas/solids velocity is formed near the wall. Compared to the flow regime in LDCFB, the annulus region in HDCFB risers becomes wider and thicker (Wang et al., 2014c). The boundary between the core and annulus regions can shift from $r/R > 0.8$ to $r/R < 0.5$ when transitioning from LDCFB to HDCFB, as depicted in Figure 2.5 (b). The shrunken core region and less uniform radial profiles of solids holdup and solids velocity in the HDCFB risers result in a much higher overall bed solids holdup than that in the LDCFB risers (Wang et al., 2014c). Thereby, the higher solids holdup provides a larger area for the gas-solids contact, which is beneficial for the mass transfer and reaction in the CFB riser reactors (Wang et al., 2014b).

Downer Different from CFB riser reactors, in CFB downer reactors, gas and solids concurrently flow downward from the top to the bottom of the column. After gas and solids are introduced into the downer through separate inlets, as shown in Figure 2.3 (b) and (c), the particles undergo three flow stages: the initial acceleration stage, the secondary acceleration stage, and the constant velocity stage (Wang et al., 2015a; Zhang et al., 1999). When gas and solids first enter the downer, the gas velocity is at the superficial gas velocity, while the particle velocity is close to 0. Since the gas velocity is greater than the particle

velocity, at this point, the particles are accelerated downwards by the combined effects of gravitational and drag forces. This is the initial acceleration stage for the particles. Once the particle velocity exceeds the gas velocity, the direction of the drag force reverses, acting upwards, and the acceleration of the particles begins to decrease, leading the particles into the second acceleration stage. When the slip velocity is sufficiently large so that the upward drag force can offset the effect of gravity, the particle velocity remains constant, no longer accelerating, and then enters the third stage.

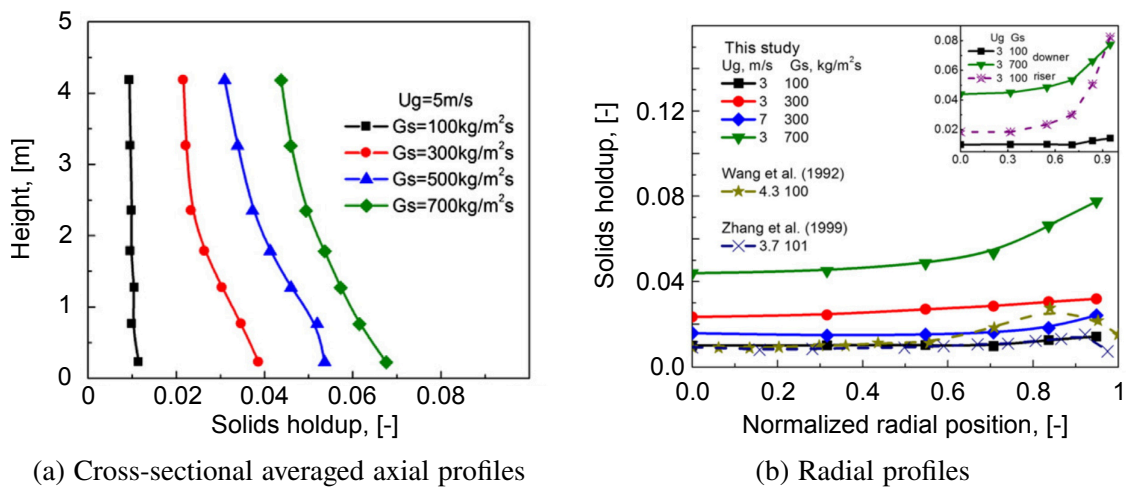


Figure 2.7: Typical profiles of solids holdup in the CFB downer reactor (Wang et al., 2015a, 2016)

Although the downer features three distinct flow stages, the differences between them are not significant, and the transitions among these stages are mild. Axially, the solids holdup profiles in the downer are relatively uniform, as illustrated in Figure 2.7 (a). The dense region is shorter than that in the riser because the quick acceleration of particles in the first stage (Sun, 2019; Wang et al., 2015a). Radially, the slip velocity between gas and solids results in less extensive particle back-mixing compared to the riser. Consequently, the radial profiles of solids holdup in the downer are much more uniform than those in the riser, as demonstrated in Figure 2.7 (b). Therefore, the downers create a broader and more uniform dilute region in the central area of the column, with a marginally higher solids

holdup near the wall. Owing to these hydrodynamic characteristics, the residence time of particles in the downer is reduced. However, this results in a more uniform distribution of residence time for both gas and solid phases, leading to a more consistent contact time between the reactants and catalysts (Bai et al., 1995; Luo et al., 2007).

Inlet structure As shown in Figure 2.4 (H), (I), and (J), the inlet structure of the riser significantly influences the axial profiles of solids holdup. The riser's inlet structure also affects the radial profiles of solids holdup and velocity, particularly in the bottom region (Yan et al., 2008). In the CFB downer reactor, the inlet structures for gas and solids not only impact the flow development length but also influence the radial dispersion and mixing of solids (Johnston et al., 1999). Furthermore, in CFD simulations of CFB riser reactors, the inlet distributor structure greatly influences the entire flow structure. Numerical results using jet inlet profiles provide a more accurate prediction of the core-annulus structure than those using uniform inlet profiles (Peng et al., 2010, 2012). Therefore, it is crucial to thoroughly understand the inlet structure of both the riser and downer before undertaking CFD simulation work, in order to achieve the desired hydrodynamic characteristics.

2.1.2 Ozone decomposition reaction in CFB reactors

Studying hydrodynamic characteristics is indeed very important for the understanding and design of fluidized bed reactors. However, conducting chemical reactions in the CFB reactors and measuring the concentrations of reactants or products can provide direct data to investigate the reaction performance in the reactors. Various chemical reactions have been employed in gas-solids fluidized bed reactors, such as the catalytic decomposition of nitrous oxide (Johnsson et al., 1996; Shen & Johnstone, 1955) and the catalyzed oxidation of carbon monoxide (Venderbosch et al., 1998). However, since the temperatures required for these reactions are often too high, implementing them in

large-scale laboratory equipment is costly. Moreover, the kinetics of these reactions are quite complex, and the reactions involve issues of heat transfer and catalyst deactivation, which are not conducive to studying the impact of hydrodynamic characteristics in CFB reactors on reaction behaviours. Therefore, these reactions have not been widely adopted in the study of CFB reactors.

In 1958, Frye et al. (1958) first introduced the ozone decomposition reaction to analyse the reaction behaviour in a fluidized bed. Sun and Grace (1990) impregnated FCC particles with ferric nitrate solution to prepared catalysts for the ozone decomposition reaction. Jiang et al. (1991) introduced the contact efficiency coefficient in the plug-flow reactor (PFR) and continuous stirred-tank reactor (CSTR) model to simulate the ozone decomposition reaction in a baffled CFB reactor. Ouyang et al. (1993, 1995) conducted the ozone decomposition reaction in a 10 m riser and obtain the radial and axial profiles of ozone concentration. The catalytic ozone decomposition reaction,



has been widely utilized as a template reaction in the study of CFB reactors due to its advantages, although it holds no commercial value in the industry. According to the experimental results of Li (2010), the ozone decomposition reaction can be considered a first-order reaction. This reaction occurs at very low ozone concentrations (about 10 to 100 ppmv), ensuring that the heat transfer and volume change of the reaction are negligible. Additionally, the detection of ozone is rapid, accurate, and inexpensive using the ultraviolet (UV) photometric method (Li et al., 2013a; Wang et al., 2014b). Furthermore, this reaction takes place at ambient temperature and pressure (Frye et al., 1958), making it easy to operate. Importantly, ozone only decomposes in contact with catalysts, allowing for the isolation of gas-solids contacting, which simplifies the quantification of

gas-solids interactions (Syamlal & O'Brien, 2003). These advantages not only make the experimental measurement data more accurate but also simplify the development of reactive transport models used in CFD simulations.

In addition, the ozone decomposition reaction has already been conducted in the CFB system that mentioned above, and the plenty of experimental data on ozone concentration have been collected and reported (Li et al., 2011, 2013a, 2013b; Liu, 2016; Wang et al., 2014b, 2014a, 2015c). Therefore, it is a good choice to use the ozone decomposition reaction as the research target of this work.

Li et al. (2013a) reports the axial and radial profiles of ozone concentration in a CFB riser reactor under different operating conditions as well as the corresponding solids holdup profiles. The results show that most of the ozone is converted in the flow developing region of the riser reactor, as shown in Figure 2.8. Above this region, the ozone concentration remains almost constant along the axial direction. Additionally, Li et al. suggests that there is a strong correlation between the solids holdup and the ozone concentration in both radial and axial directions. However, all the experiments conducted by Li et al. were at low reaction rates and the operating conditions belonged to the low-density flow regime.

Riser Wang et al. (2014b) investigated the performance of ozone decomposition reactions in the same CFB riser reactor under a wider range of operating conditions. The operating conditions reported in the study cover superficial gas velocities ranging from 0 to 5 m/s and solids circulation rates from 100 to 800 kg/m²/s. These operating conditions span fluidization regimes from LDCFB to HDCFB. Moreover, the reaction constant and inlet ozone concentration in Wang et al.'s experiments were approximately 10 times higher than those in Li et al. (2013a)'s experiments. Wang et al.'s results (Figure 2.9 (a)) indicated that 30 to 60 % of ozone conversion occurred within the 0 to 1 m of the riser under different operating conditions. Beyond this region, a significant reduction in the

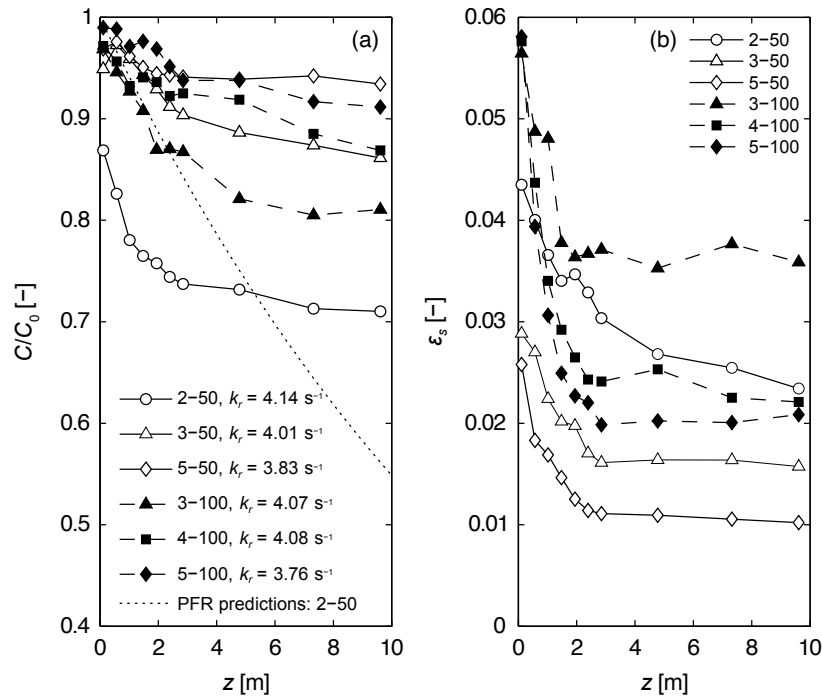


Figure 2.8: Axial profiles of cross-sectional averaged ozone concentration and solids holdup in the riser in the CFB riser reactor (Li et al., 2013a)

conversion rate is observed. This finding is consistent with Li et al.'s, but with a notable difference: when a large amount of catalysts is retained in the riser, the ozone concentration continues to decrease in the region above the flow developing region. Axially, as shown in Figure 2.9 (c), the region near the wall has a lower and constant ozone concentration, while the profile of the central region shows a continuous and significant decline, suggesting severe lateral gas/solids segregation in the reactor. Radially, as shown in Figure 2.9 (e) and (f), a strong correlation between ozone concentration and solids holdup is evident, further indicating that the reaction in the CFB riser reactor is controlled by the gas-solids flow structure. Additionally, Wang et al. found that although solids holdup is an important factor affecting reaction performance, its impact is more pronounced under conditions of high superficial gas velocity and low solids circulation rate.

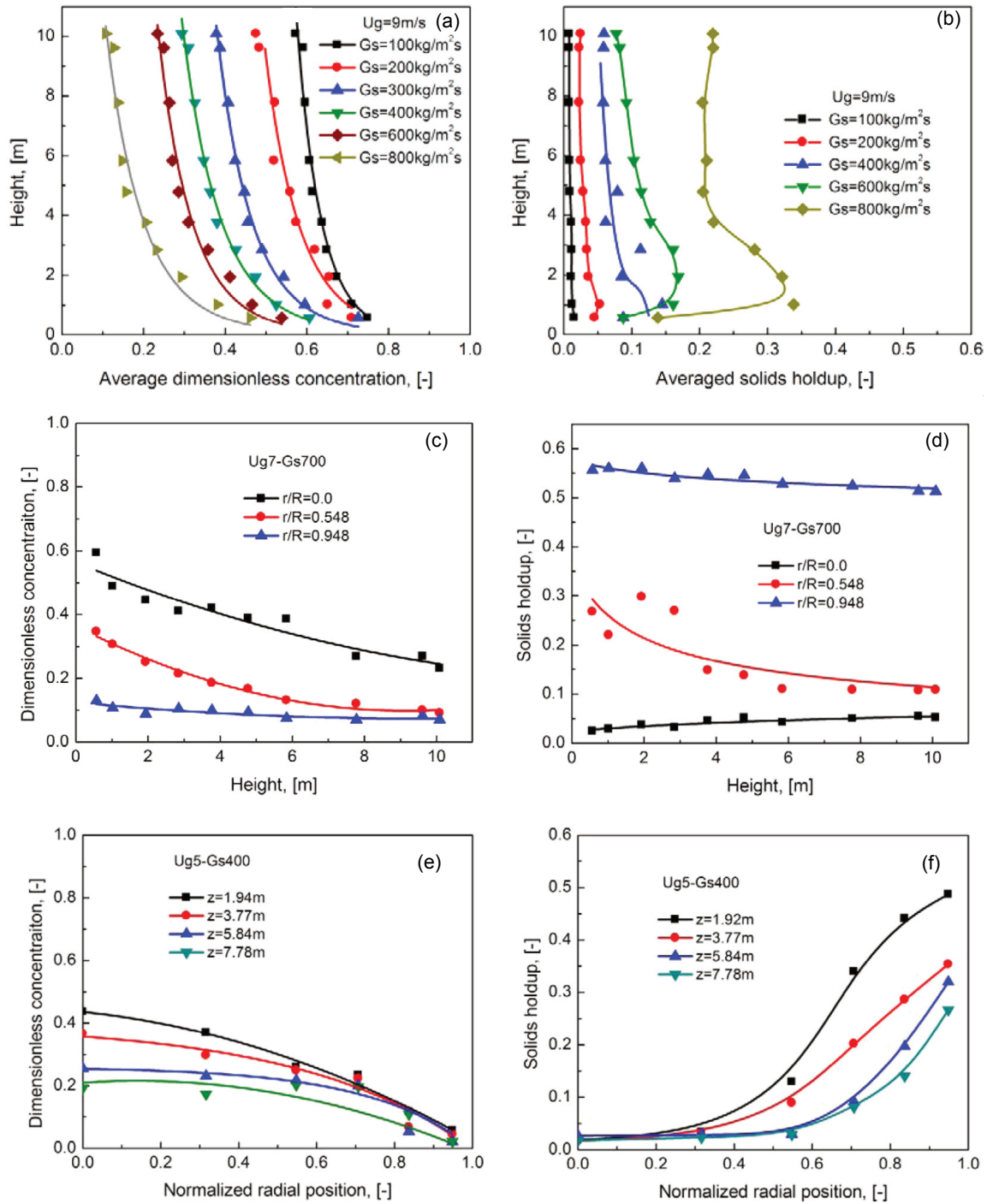


Figure 2.9: Typical profiles of ozone concentration and solids holdup in the CFB riser reactor (Wang et al., 2014b); (a) and (b): cross-sectional averaged profiles, (c) and (d): axial profiles at various radial positions, (e) and (f): radial profiles at various axial positions

Downer The Downer, as a newly proposed reactor, has attracted widespread attention, with hopes of understanding its reaction performance through observations of reactions within it. However, experimental data are rarely reported. In 2008, Fan et al. published data on ozone decomposition observed in a CFB downer reactor under low solids circulation rate operating conditions (about 10 to 30 kg/m²/s). Fan et al. found that the ozone concentration was rapidly reduced in the first acceleration region, while in the subsequent fully developed region, the decrease was much slower. These phenomena were also observed in Wang et al. (2014a)'s experiments under higher solids circulation rate operating conditions (100 to 300 kg/m²/s). This is believed to be caused by the combined effects of high solids holdup and high ozone concentration. Similar to the riser, ozone concentration profiles in the axial and radial directions are strongly correlated with profiles of solids holdup. However, in the radial direction, the distributions of ozone and particles are quite uniform, without the presence of a core-annulus structure or parabolic profiles, as shown in Figure 2.10 (c). Axially, as shown in Figure 2.10 (d), ozone profiles at different radial positions have the same axial trends, unlike in the riser, where profiles differ significantly between the central and wall regions. This is related to the simpler flow structure in the downer. Therefore, Wang considers the reaction performance of the CFB downer to be very close to that of an ideal PFR.

2.2 Numerical works on gas-solids CFB reactors

With the advancement of high-performance computation technology and numerical algorithms, the simulation of large-scale CFB reactors using computational fluid dynamics (CFD) techniques has become possible. Consequently, various multiphase models have been developed to address the diverse flow structures in gas-solids fluidization systems. With the aid of CFD, at least one intermediate scale-up unit can be eliminated in the entire

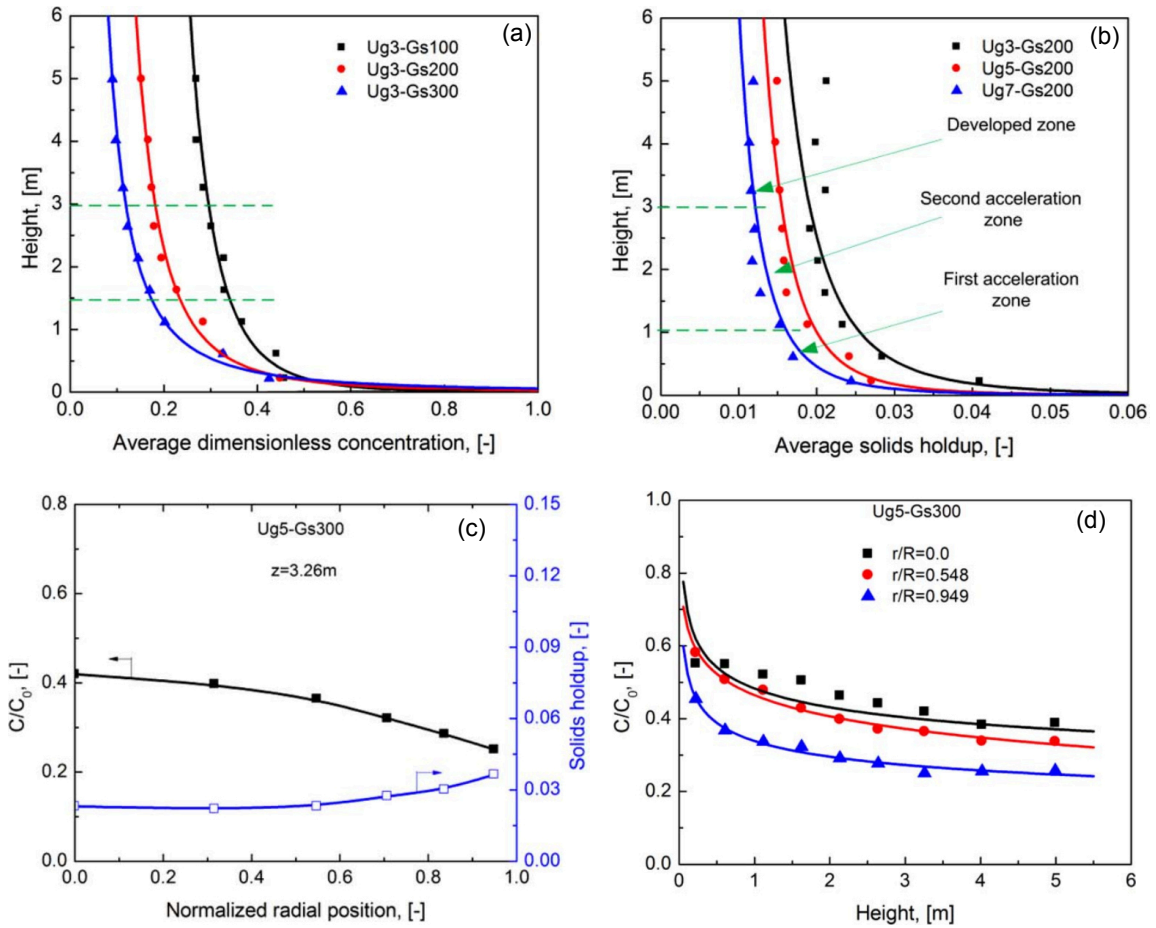


Figure 2.10: Typical profiles of ozone concentration and solids holdup in the CFB downer reactor (Wang et al., 2014a); (a) & (b): cross-sectional averaged profiles, (c) and (d): radial profiles near the inlet and outlet

reactor scale-up process, potentially saving years of time and millions of dollars in costs (Chew et al., 2022). Therefore, both industry and academia are increasingly emphasizing the application of CFD and the development of related models.

Currently, there are many widely used numerical simulation methods. If categorized based on the spatial scale of the objects being simulated, they can be roughly divided into three types from smallest to largest: micro-scale simulation (about 10^{-2} m), meso-scale simulation (10^{-1} to 10^0 m), and macro-scale simulation (10^0 to 10^1 m). Here is the brief introduction of these simulation methods:

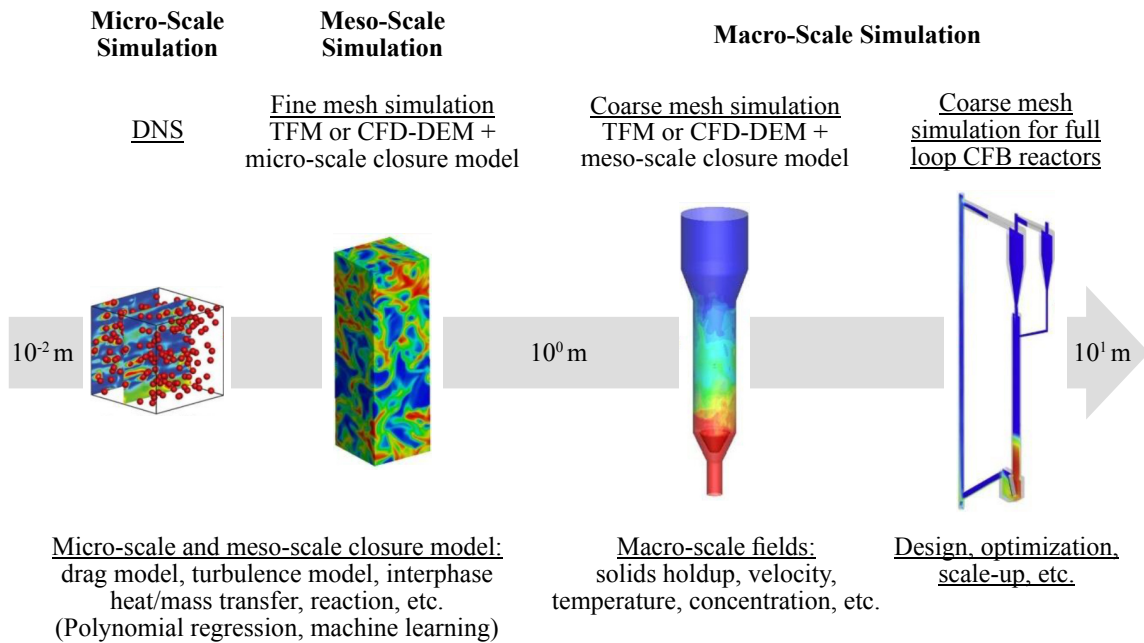


Figure 2.11: Simulation methods from micro-scale to macro-scale and their corresponding applications (Zhu, 2021)

1. In micro-scale simulation, a representative method is particle-resolved direct numerical simulation (PR-DNS) (Deen et al., 2012; Liu et al., 2017; Tenneti & Subramaniam, 2014). In this method, the gas phase is solved directly on a grid at the Kolmogorov scale using the DNS method, eliminating the need for introducing a turbulence model. The particle phase is either fixed in space or simulated using the discrete element method (DEM) for particle motion. However, this method requires extremely high grid resolution and small time steps, making it challenging to even simulate small-scale laboratory fluidized beds. Therefore, the PR-DNS method is currently more suitable for studying the fundamental flow and transfer mechanisms in gas-solids fluidization systems and for further developing more accurate inter-phase transfer models.
2. Meso-scale simulation is currently the most focused research scale for researchers. This is because the heterogeneous flow structures in gas-solids fluidization systems, such as bubbles and clusters, can be considered as meso-scale flow structures (Li &

Huang, 2018). They are related to the interactions between gas-solids as well as the interactions among particles. These meso-scale structures are the core factors that differentiate fluidized bed reactors from other reactors and are central to our study of fluidization. Currently, CFD-DEM and two-fluid model (TFM) are the two most commonly used methods.

- (a) In CFD-DEM, gas is treated as a continuous medium and the gas flow field is solved under the Eulerian frame using Reynolds-averaged Navier-Stokes (RANS) equations (Alfonsi, 2009), while particles are considered as discrete entities and their motion trajectories are tracked under the Lagrangian frame (Guo & Curtis, 2015; Zhu et al., 2008). Particle collisions are described using hard-sphere or soft-sphere models, and models such as the drag model are required to describe the interactions between gas and particles. As DEM can track the motion of each particle, it allows for the easier introduction of other particle-related forces, such as van der Waals forces, magnetic forces, etc., and can handle systems with particles of low sphericity or a wide particle size distribution (Zhong et al., 2016). However, because DEM tracks each particle individually, it becomes challenging for systems with a huge number of small particles, such as pilot or industrial-scale fluidized bed reactors, making DEM less feasible for such large-scale systems.
- (b) TFM (two-fluid model), another important simulation method, treats both gas and solids as continuous media. The treatment of the gas phase is the same as in CFD-DEM, while the solids phase is treated as a pseudo-fluid using the kinetic theory of granular flow (KTGF) (Gidaspow, 1994; Gidaspow & Bacelos, 2018; Huilin & Gidaspow, 2003; Syamlal et al., 1993). Therefore, the solver does not need to track the motion of each particle, significantly reducing computational costs. KTGF, analogous to the kinetic theory of gases,

closes the collisional stresses in the solids phase through statistic analysis on the motion of local particle groups. Previous research suggested that a grid size of 10 to 50 d_p was proper to accurately reflect the particle collisions. However, recent studies have shown that a grid size as small as 3 d_p is required to fully capture meso-scale structures in gas-solids systems (Fullmer & Hrenya, 2016; Wang et al., 2009; Zhu et al., 2020). Such a small grid size makes simulating three-dimensional industry-scale reactors very difficult. However, when using relative coarse grids, the heterogeneous flow structures in the flow field are ignored, leading to model predictions deviating from experimental data (Agrawal et al., 2001; Sundaresan et al., 2018).

3. To address the current computational cost limitations that hinder accurate simulation of industry-scale reactors, two methods, multiphase particle-in-cell (MP-PIC) and TFM+subgrid model, have been proposed. To reduce the number of particles tracked in DEM, MP-PIC groups particles into parcels, with multiple particles in each parcel sharing the same velocity, position, and forces (Andrews & O'Rourke, 1996). Particle collisions are treated by KTGF. This approach allows for tracking particle motion trajectories while significantly reducing computational costs, making accurate macro-scale simulation feasible. In the TFM+subgrid model, the subgrid model quantifies the impact of heterogeneous flow structures and modifies models for drag force, heat/mass interphase transport, and reaction rates. Common methods include semi-empirical models (O'Brien & Syamlal, 1993; Sun et al., 2022), filtration methods (Agrawal et al., 2001; Igci et al., 2008), and the energy minimization multi-scale (EMMS) model (Li, 1994; Li et al., 1988).

2.2.1 Two-fluid models

To treat the particles as the pseudo-fluid when using TFM, the fluid properties of particle fluids, such as pressure and viscosity, need to be defined. Granular temperature was first introduced by Sinclair and Jackson (1989) and is proportional to the kinetic energy of particle random motion (Ding & Gidaspow, 1990), as shown below:

$$\Theta_s = \frac{1}{3} v'_{s\tau} v'_{s\tau}, \quad (2.2)$$

where $v'_{s\tau}$ represents the fluctuating velocity of particles in the τ direction. According to KTGF, the granular temperature can be described by the transport equation of granular temperature (Gidaspow, 1994):

$$\begin{aligned} \frac{3}{2} \left[\frac{\partial}{\partial t} (\varepsilon_s \rho_s \Theta_s) + \nabla \cdot (\varepsilon_s \rho_s \vec{u}_s \Theta_s) \right] = & \left(-p_s \bar{\bar{\mathbf{I}}} + \bar{\bar{\tau}}_s \right) : \nabla \vec{v}_s + \\ & + \nabla \cdot (k_{\Theta_s} \nabla \Theta_s) - \gamma_{\Theta_s} + \phi_{gs}, \end{aligned} \quad (2.3)$$

where $\left(-p_s \bar{\bar{\mathbf{I}}} + \bar{\bar{\tau}}_s \right) : \nabla \vec{v}_s$ is the generation of energy by the solids stress tensor, $(k_{\Theta_s} \nabla \Theta_s)$ is the diffusion energy, (γ_{Θ_s}) is the collisional dissipation of energy, and (ϕ_{gs}) is the energy exchange between the gas and solids phases. After the granular temperature is obtained, the pressure and viscosity of the particle phase can be calculated (Gidaspow, 1994; Lun et al., 1984; Schaeffer, 1987).

Turbulence models In TFM, either a laminar flow model or a turbulence model is required to calculate the viscous stress tensor. The Reynolds-Averaged Navier-Stokes (RANS) equations are often used to simplify the treatment of turbulence phenomena in fluid flow. Two-equation turbulence models based on Boussinesq eddy viscosity assumption are widely used in most fields of engineering to close the time evolution equation of

Reynolds stress. k - ϵ model (Hanjalić & Launder, 1972) and k - ω model (Wilcox, 2008) are two of the most used two-equation turbulence models. However, there is still significant argument regarding whether to use a turbulence model and, if so, which turbulence model to use.

Almuttahir and Taghipour (2008) found that using the k - ϵ turbulence model tends to overestimate the solids flux compared to using the laminar flow model when simulating a two-dimensional riser. Gao et al. (2009) discovered that in the simulation of a 2D TFB (turbulent fluidized bed), employing the k - ϵ turbulence model results in more stable and less variable radial profiles of solids holdup than when using the laminar flow model. Li et al. (2021) conducted a comprehensive study of the performance of the laminar flow model and various turbulence models in full loop CFB, BFB, and TFB systems. The laminar flow model, RNG k - ϵ model, and SST k - ω model predictions agree more closely with experimental results across different flow regimes, while the standard k - ϵ model and standard k - ω model fail to accurately predict the solids holdup distributions.

It is noteworthy that the fluidization regimes studied in these researches either belong to conventional fluidized beds or to riser reactors with extremely low solids circulation rates ($G_s < 20 \text{ kg/m}^2/\text{s}$). The hydrodynamic characteristics investigated in these studies are quite different from the objectives of the present study, so it cannot be conclusively said that any one of these studies' conclusions is correct. Additionally, researchers in the aforementioned studies typically compare time-averaged profiles from numerical results with experimental outcomes, while overlooking the more important instantaneous flow structures in fluidization systems. Therefore, in the simulations of this study, whether to use a turbulence model and which turbulence model to use still need to be further validated according to our own system, and the validation method should not be limited to comparing time-averaged results.

Inlet structures The uniform inlet structure is the most commonly used inlet structure in CFB riser reactor simulations, as shown in Figure 2.12 (a). However, Peng et al. (2010) and Peng et al. (2012) found that using a jet inlet profile instead of a uniform inlet profile can improve the prediction accuracy of the core-annulus structure in the CFB riser reactor. Sun (2019) separated the gas inlet and solids inlet of the riser, allowing particles to enter from the side at the bottom of the riser and then meet with the gas, which is closer to the experimental operation, as shown in Figure 2.12 (b). The results showed that the solids holdup distribution and the velocity distributions of gas and solids were more consistent with the experimental data.

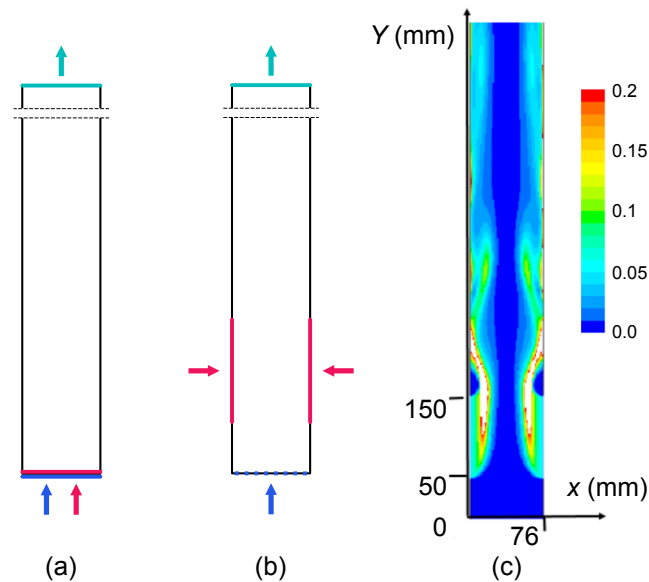


Figure 2.12: Inlet structure: (a) uniform inlet, (b) jet inlet, (c) contour of solids holdup at the inlet using a jet gas inlet and side solids inlet (Sun, 2019)

Important parameters In TFM, there are three parameters related to the material of the used fluidized bed and the particles that need to be determined through trial for the final selection. These are the particle-particle restitution coefficient (e_{ss}), the particle-wall restitution coefficient (e_{sw}), and the specular coefficient (ϕ). The restitution coefficient characterizes the degree of kinetic energy retention after two objects collide. When $e = 1$, the collision is perfectly elastic, with no loss of mechanical energy, while when $e = 0$, the

two objects stick together after the collision, with kinetic energy completely transformed into other forms of energy (ANSYS, Inc., 2022). The specularity coefficient, on the other hand, characterizes the direction of a particle's rebound after colliding with a wall. When $\phi = 1$, specular reflection occurs, while when $\phi = 0$, the direction of the particle's reflection is unrelated to the direction of incidence (ANSYS, Inc., 2022). Therefore, these two parameters respectively determine the speed and direction of the particles' motion after collision, having a significant impact on the flow structure in CFB.

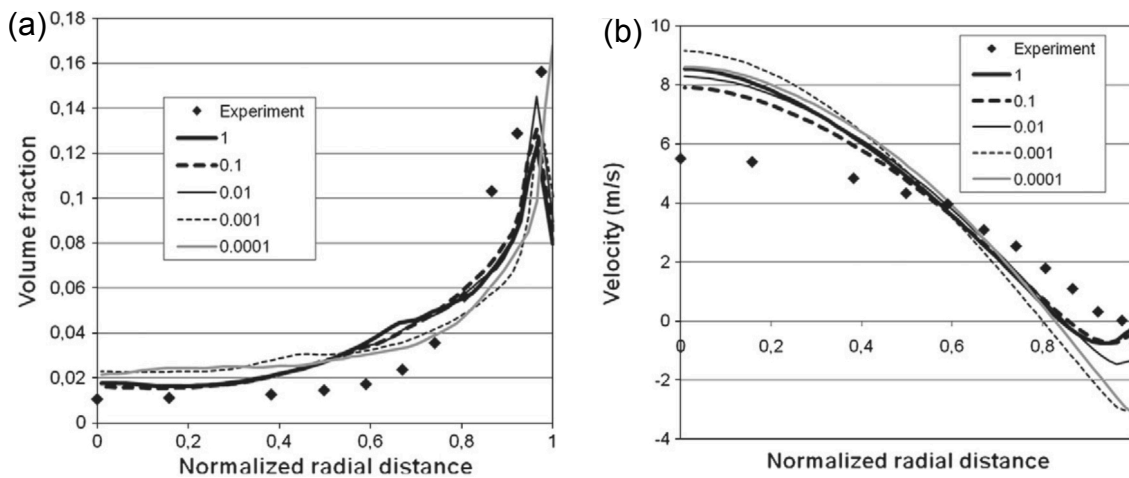


Figure 2.13: Effects of specularity coefficient on the radial flow structures in a CFB riser (Cloete et al., 2011): (a) solids holdup, (b) solids velocity

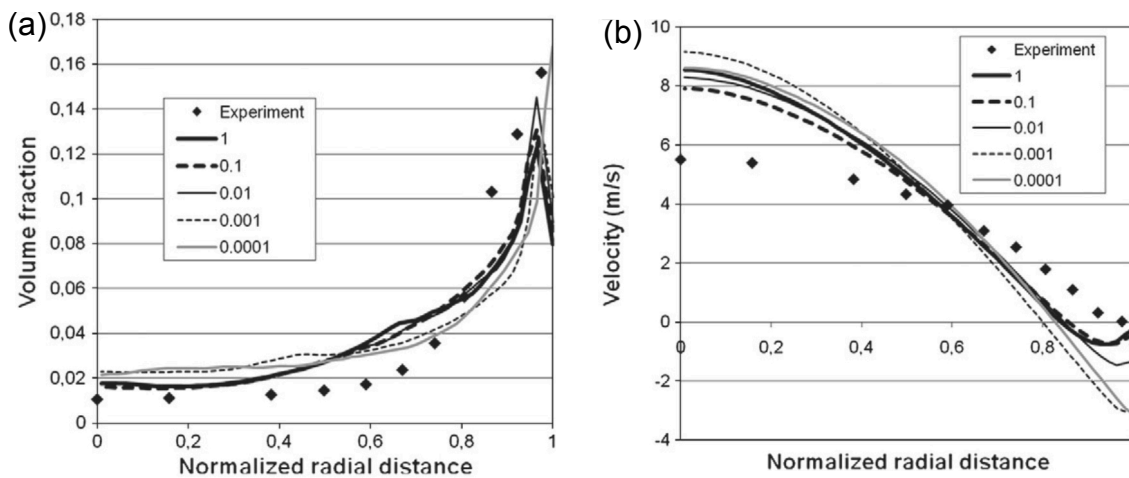


Figure 2.14: Effects of particle-particle restitution coefficient on the radial flow structures in a CFB riser (Cloete et al., 2011): (a) solids holdup, (b) solids velocity

Cloete et al. (2011) conducted a parametric study on the effects of e_{ss} , e_{sw} and ϕ on the flow structure in a CFB riser reactor. The results found that e_{sw} changes the granular temperature near the wall, but it does not have a significant impact on the final flow field. However, e_{ss} and the ϕ together affect the particle velocity and solids holdup near the wall region. With a decrease in e_{ss} , the solids holdup near the wall region increases, and correspondingly, the sliding velocity of particles in this area also increases. Cloete et al. believes that a value of 0.9 is the best choice for the CFB system from Dr. Zhu's group (Yan & Zhu, 2004). The impact of ϕ is more pronounced on the velocity of particles near the wall. The smaller the ϕ , the more severe the downward sliding tendency of particles near the wall. Benyahia et al. (2007) believes that a ϕ value of 0.0001 can predict a better core-annulus structure in the simulation of a CFB riser, but according to Cloete et al.'s research, this could lead to particle sliding velocities as high as 3 m/s. Therefore, Cloete et al. considers 0.01 to be a more appropriate value.

2.2.2 Interphase interactions and sub-grid models

Subgrid models for interphase momentum transfer Interphase momentum exchange refers to the interaction forces between the gas phase and the solid phase. In gas-solids fluidization systems, the density of particles is often thousands of times greater than that of the gas; therefore, the drag force dominates the interphase force for momentum exchange. In previous studies, the drag force has always been considered the most critical factor affecting the flow structure in fluidized beds.

Currently, the drag coefficient of gas-particles is generally provided by two types of models: empirical correlations established from experimental data, and correlations established from particle-resolved simulation data. Gidaspow model and the Syamlal-O'Brien model are the most widely used drag models that developed from experimental

data. Syamlal-O'Brien model (Syamlal et al., 1993) was developed by converting the correlations of terminal velocity of fluidized beds and settled beds. The model performs better when predicting the flow in conventional fluidized beds. Gidaspow model (Gidaspow et al., 1991) integrates the Ergun equation for $\varepsilon_s \geq 0.2$ and the Wen-Yu model for $\varepsilon_s < 0.2$. The Ergun equation (Ergun, 1952) was developed using packed-bed pressure drop data, while the Wen-Yu model (Wen & Yu, 1966) was derived from experimental data on liquid-solids fluidized beds. This model is more suitable for use in the CFB systems. Hill et al. (2001) and Beetstra et al. (2007) fixed various particle arrays in space and used lattice-Boltzmann methods (LBM) to simulate airflow through these arrays. Subsequently, they collected drag force data under various operating conditions, thereby establishing correlations for drag force respective to voidages and Reynolds numbers. Their simulations are more akin to measuring pressure drop in a "customizable" packed bed, similar to the experiment conducted by Ergun. The results show that their correlations underestimate the drag force at low Reynolds numbers, while overestimating it at high Reynolds numbers. This is likely due to the difference between the fixed particle setting and the actual flow in a fluidized bed, as well as the influence of sphericity.

Section 2.2 mentions that current HPC systems struggle to support simulations of industrial-scale CFB reactors with the necessary grid size requirements of TFM. Blindly enlarging the grid size can overlook the gas-solids heterogeneous flow structures, leading to distorted predictions. However, subgrid models can correct the calculation of interphase interactions in coarse grids. The commonly used subgrid models include:

1. Semi-empirical models: This method usually involves correcting the drag force using experimental data combined with semi-theoretical approaches. For example, Sun et al. (2022) categorized the solids phase in a cell into discrete particles and clusters based on cluster information collected from image processing and wavelet

analysis from Wei and Zhu (2019). The adjusted drag force is the summary of the drag force on the two classes.

2. Filtered methods: This approach obtains high-resolution gas-solids flow field data through TFM simulations in fine grids. Then, a uniform drag force correction model is established through the statistical analysis of the high-resolution data.
3. EMMS methods: This approach considered the particle clustering phenomenon as a dynamic equilibrium state formed by the mutual competition between gas and solids phases in flow. Therefore, it establishes a correction model based on the condition of minimizing energy consumption when entraining a unit mass of particles in a gas-solid system (Li et al., 1988; Lu et al., 2009; Wang & Li, 2007).

Filtered method for drag models Current studies indicates that the TFM needs to be implemented in a mesh of about $3 d_p$ size to capture detailed gas-solids heterogeneous flow structures, which roughly corresponds to 10^{-4} to 10^{-3} m (Fullmer & Hrenya, 2016; Wang et al., 2009; Zhu, 2021). This mesh size is impractical for industrial CFB reactors (10^1 m). Dr. Sundaresan's group at Princeton University, inspired by the filtering method LES, proposed a filtered statistical analysis for models related to KTGF and interphase interaction forces (Agrawal et al., 2001; Igci & Sundaresan, 2011; Igci et al., 2008; Milioli et al., 2013). Taking the filtered drag model as an example, the development generally involves 5 steps, as shown in Figure 2.15:

1. Implement high-resolution simulations for gas-solids fluidization systems in a periodic computational domain. The boundaries surrounding the computational domain are transition boundaries. Therefore, a large computational domain is not necessary to obtain a flow field containing various heterogeneous flow structures.
2. Record flow field data. Once the flow field in the periodic domain reaches a steady state, record the required flow field data, such as solids holdup, gas velocity, particle

velocity, etc.

3. Select a region smaller than the domain, referred to as a filter box, within the domain. Calculate the average flow field parameters in the filter box based on the recorded flow field data, such as average solids holdup, average gas-solid velocity, average slip velocity, etc., as well as the total drag force in the filter box.
4. Move the filter box and change its size to create a database containing the filter box size, average flow field parameters, and total drag force.
5. Establish a correlation of drag force with respect to the filter box size and average flow field parameters.

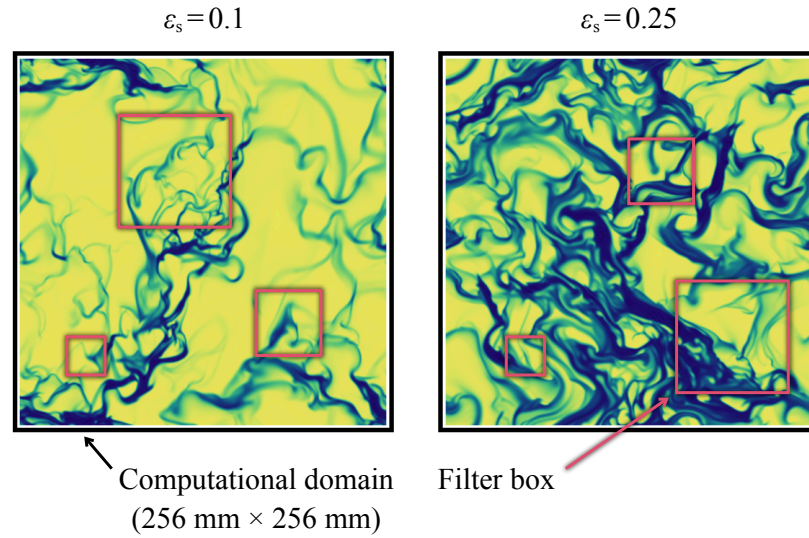


Figure 2.15: Schematic filtering process of two-dimensional high-resolution TFM simulations ($\Delta_{\text{mesh}} = 3 d_p$, $d_p = 70 \mu\text{m}$)

The subgrid filtered drag coefficient, β_{filter} , is defined as (Milioli et al., 2013):

$$\tilde{v}_{\text{slip}} = \frac{\overline{\beta_{\text{micro}} v_{\text{slip}} - \varepsilon'_g \nabla \cdot \sigma'_g}}}{\beta_{\text{filter}}}, \quad (2.4)$$

where

$$\beta_{\text{micro}} = \frac{18 \mu_g \varepsilon_g \varepsilon_s}{d_p^2} f_{d,\text{micro}}(Re_s, \varepsilon_s) \quad (2.5)$$

is the drag coefficient in cells of high-resolution simulations. $f_{d,\text{micro}}$ is the dimensionless drag coefficient, which is defined differently for different drag models, such as the Gidaspow model and the Syamlal-O'Brien model. \tilde{v}_{slip} is the average slip velocity in the filter box. Zhu (2021) then presented a subgrid filtered drag force correction coefficient in the axial direction:

$$H_d = \frac{F_{d,\text{filter},y}}{F_{d,\text{homo},y}} = \frac{\overline{\beta_{\text{micro}}(\varepsilon_s, |v_{\text{slip},y}|) v_{\text{slip},y}}}{\beta_{\text{micro}}(\bar{\varepsilon}_s, |\tilde{v}_{\text{slip},y}|) \tilde{v}_{\text{slip},y}}, \quad (2.6)$$

where $F_{d,\text{filter},y}$ is the filtered drag force in the y -direction within the filter box, $F_{d,\text{homo},y}$ is the homogeneous drag force in the y -direction within the filter box. Thus, H_d represents the differences that arise due to the effects of heterogeneous flow structures.

The above content is just a brief introduction to the ideas and implementations of the filtered method. This research mainly revolves around reactions in CFB reactors and will not delve much into interphase drag force. However, most advanced concepts first introduce hydrodynamic modelling works, and heterogeneous flow structures play a crucial role in reaction behaviours. Therefore, understanding hydrodynamic modelling works is beneficial for the study of reaction behaviours in CFB reactors.

Filtered method for chemical reactions With the thriving development of subgrid drag models, an increasing number of scholars have also begun to explore the subgrid reactive transport models. Liu et al. (2015), based on the EMMS theory, proposed a structure-dependent multi-fluid model, which introduces the influence of heterogeneous flow structures on mass transfer and reaction to modify the reactive transport model. The model was validated through comparison with Ouyang et al. (1995)'s experimental data on ozone decomposition in a riser. Hou et al. (2017) believes that reactions in fluidized beds are controlled by the mass transfer rate between gas and clusters. By introducing gas-cluster mass transfer to modify the reaction rate in coarse mesh simulations, it effectively

reduces the overestimated reaction rate of the original reactive transport model in CFB riser reactors.

Based on the concept of filtering methods, researchers have also attempted to perform filtering analysis on reactive transport models. Holloway and Sundaresan (2012) developed a filtered reactive transport model to simulate a first-order, isothermal reaction with no volume change. They defined a cluster-scale effectiveness factor to quantify the effects of the cluster on the reaction in gas-solids fluidization systems and argued that if this factor is not considered, coarse-grid TFM simulations would overestimate the reaction rate. Huang et al. (2021) studied the impact of different orders of chemical reactions on the effectiveness factor through filtering methods and found that the factor depends on solids holdup, filter box size, and the Damköhler number. Zhu et al. (2021) applied filtering to the models of momentum transfer, heat transfer, and reaction, and introduced new marks such as gas pressure gradient and temperature to correlate flow field parameters with the effectiveness factor. The new model resulted in better consistency with experimental results.

The filtered reactive transport model is expressed as (Holloway & Sundaresan, 2012):

$$\frac{\partial}{\partial t} \left(\overline{\varepsilon_g} \rho_g \widetilde{Y_g} \right) + \nabla \cdot \left(\rho_g \overline{\varepsilon_g \vec{v}_g Y_g} - \Gamma_g \overline{\varepsilon_g \nabla Y_g} \right) = -k_r \rho_g \overline{\varepsilon_s Y_g}. \quad (2.7)$$

Cloete (2018) found that the diffusion term has little influence on the overall conversion of reactants. Thus, the correction coefficient of the filtered reaction rate can be expressed as:

$$H_r = \frac{\overline{\varepsilon_s Y_g}}{\overline{\varepsilon_s \widetilde{Y_g}}}. \quad (2.8)$$

Compared to the research of filtered drag models, there is still very little research and analysis on filtered reactive transport models. Moreover, most of the research focuses

on the development of the model, without gaining a deeper understanding and analysis of the reactions occurring in CFB reactors through the developed model.

2.2.3 Machine learning-based models

With the advancement and development of measurement techniques and numerical methods, researchers can obtain much more data than before, such as time series data of solids holdup from optical fibres (Zhang et al., 1998), high-frame-rate image data (Yang & Zhu, 2014), and data of flow field and reaction field from high-resolution CFD simulations (Zhu et al., 2020). However, researchers often analyze the obtained data by averaging them over space or time (Wang, 2013; Wei & Zhu, 2019). This process causes the loss of a large amount of detail and instantaneous characteristics. Without such averaged processing, the sheer volume of data also overwhelms the researchers.

Since the development of the back-propagation algorithm in the 1980s (Rumelhart et al., 1986), there has been renewed interest in neural networks, followed by the development of more algorithms and their applications in the field of machine learning (ML). Figure 2.16 lists the different uses of ML and corresponding algorithms. With the increase in computing power, the powerful capabilities of artificial intelligence (AI) have led researchers and industries to use and consider how to use AI in their fields. AI is playing an irreplaceable role in more and more fields.

Artificial neural networks In the previously mentioned filtering method, the high-resolution flow field data processed through the filtering process can amount to millions to tens of millions of data entries (Zhu et al., 2020). Traditional filtering modelling developments generally start by bucketing the collected data based on solids holdup, then averaging the data within each bucket, and finally obtaining individual correlations regarding solids holdup within each bucket. The averaging of data within the buckets

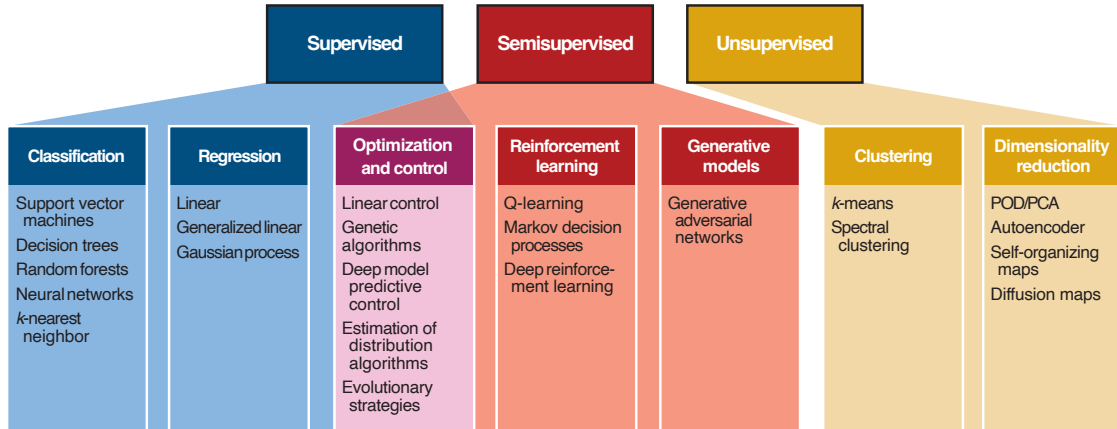


Figure 2.16: Categories of machine learning algorithms (Brunton et al., 2020)

causes the model to overlook the impact of other key flow field parameters, such as slip velocity, which results in the filtered model not fully representing the information of the flow field being filtered, leading to biased corrections. Machine learning, especially the artificial neural network (ANN) method, is highly suitable for processing such large volumes of data.

ANN was proposed by McCulloch and Pitts (1943) and experienced a revival after the introduction of the back-propagation algorithm (Rumelhart et al., 1986). ANN is a mathematical model that mimics the structure and function of biological neural networks, and it serves as a nonlinear statistical data modelling tool. ANN perform computations through a large number of interconnected artificial neurons. A schematic of a single node in the ANN is shown in Figure 2.17. In the figure, a is the input, w is the weight, b is the bias, f is the transfer function, and t is the output. The function of a neuron is to compute a scalar result by obtaining the inner product of the input vector ($\vec{A} = [a_1, a_2, \dots, a_n]$) and the weight vector ($\vec{W} = [w_1, w_2, \dots, w_n]$), and then processing it through a nonlinear transfer function. The mathematical expression of the neuron function is:

$$t = f(\vec{W}^T \vec{A} + b). \quad (2.9)$$

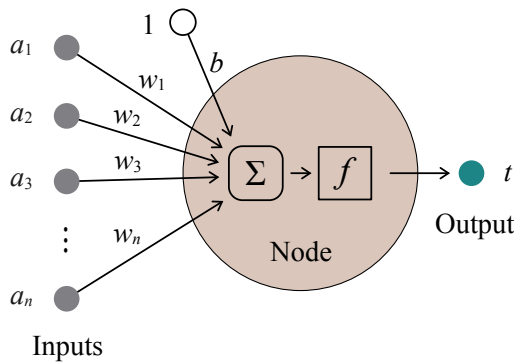


Figure 2.17: Schematic of a single node (neural) in the ANN

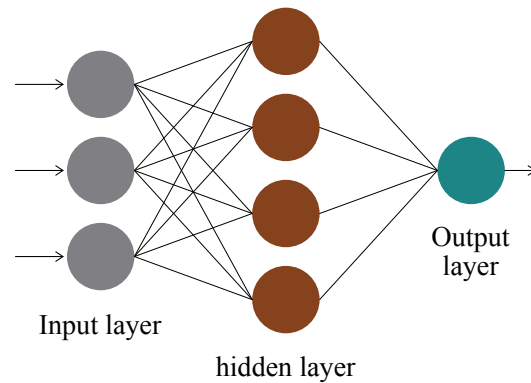


Figure 2.18: Schematic of a one layer ANN structure

By combining multiple neurons, we can form the simplest single-layer ANN structure, as shown in Figure 2.18. The “synapses” between neurons, represented by weight vectors, are the parameters of the model, which are obtained through various iterative algorithms. This fitting process is known as training, and the effectiveness of the training is indicated by the loss, which is derived from loss functions. As more hidden layers are added between the input layer and the output layer, making the ANN structure more “deep”, this evolves into deep learning. These additional hidden layers enable the model to extract higher-level features from the raw input, thereby enhancing its ability to model complex nonlinear systems (LeCun et al., 2015).

In the filtering method, ANN serves as a surrogate modelling method, replacing traditional approaches such as polynomial regression. With the assistance of ANN, Jiang et al. (2019) used filtered solids holdup, filtered slip velocity, and filtered gradient of gas pressure as input features to model the filtered drag force. The predictive capability of the ANN model far surpasses that of the traditional filtered models. Zhang et al. (2020)’s research found that information from adjacent coarse grids could enhance the predictive accuracy of the filtered drag model. Zhu et al. (2020) also experimented with using ANN and Xgboost methods to model filtered drag force, and ANN demonstrated superior

capabilities in modelling complex systems. However, currently, the application of ANN in filtered reactive transport models is still rarely reported.

2.3 Conclusions

Experiments have provided an initial understanding of the flow structure inside CFB reactors. Hydrodynamic characteristics are characterized by solids holdup and particle velocity.

The profile of solids holdup exhibits an exponential shape in the axial direction of LDCFB riser reactors, while in HDCFB, it shows an S-shape profile with a dense bottom region. Radially, a typical core-annulus structure appears in LDCFB, whereas in HDCFB, the thickness of the annulus significantly increases, and there is a phenomenon of particles slipping in the wall region. According to the direction of slip velocity between gas and particles, a downer can be divided into three regions in the axial direction. However, the distribution of solids holdup and particle velocity are uniform in the axial and radial direction.

Catalytic ozone decomposition reaction is used as a template reaction to investigate the reaction performance in CFB reactors. According to the profiles of ozone concentration, most of the ozone is converted in the region from the inlet to 1 m. Subsequently, the ozone concentration decreases slightly with height. Risers and downers share the same characteristic in the axial direction. Radially, there is a significant gradient in the riser, while in the downer, ozone concentration is distributed uniformly.

Numerical methods are then used to simulate CFB reactors for more detailed information and cost savings. TFM is the most appropriate method for simulations of industrial-scale CFB reactors. Inlet structure, turbulence model, and KTGF parameters

significantly influence the numerical results. For different sizes of CFB reactors and operating conditions, it is essential to make appropriate choices and adjustments regarding these three aspects.

To address the issue of excessive computational demand due to a high number of grids when using a fine mesh, and the distortion of drag models, reactive transport models, etc., when using a coarse mesh, the sub-grid model has been introduced into the TFM. The filtering method is one of the most commonly used methods. It collects data through a filtering process and creates model, which can correct bias caused by heterogeneous flow structures (e.g., clusters) in models using coarse mesh.

To cope with the large amount of data generated by the filtering method, ANN is adopted and replaces traditional fitting methods. However, currently, the use of the filtering method for reactive transport modelling and comprehensive investigation of reaction behaviours in CFB reactors is still not widespread.

References

- Agrawal, K., Loezos, P. N., Syamlal, M., & Sundaresan, S. (2001). The role of meso-scale structures in rapid gas–solid flows. *Journal of Fluid Mechanics*, 445, 151–185.
- Alfonsi, G. (2009). Reynolds-averaged navier–stokes equations for turbulence modeling.
- Almutterah, A., & Taghipour, F. (2008). Computational fluid dynamics of high density circulating fluidized bed riser: Study of modeling parameters. *Powder Technology*, 185(1), 11–23.
- Andrews, M. J., & O’Rourke, P. J. (1996). The multiphase particle-in-cell (mp-pic) method for dense particulate flows. *International Journal of Multiphase Flow*, 22(2), 379–402.
- ANSYS, Inc. (2022). *Ansys Fluent, Release 2022R1, Help System, Ansys Fluent Theory Guide, Section 14.5 Eulerian Model Theory*. ANSYS, Inc.
- Bai, D., Issangya, A., Zhu, J.-X., & Grace, J. (1997). Analysis of the overall pressure balance around a high-density circulating fluidized bed. *Industrial & engineering chemistry research*, 36(9), 3898–3903.
- Bai, D., Shibuya, E., Masuda, Y., Nishio, K., Nakagawa, N., & Kato, K. (1995). Distinction between upward and downward flows in circulating fluidized beds. *Powder Technology*, 84(1), 75–81.
- Bai, D., & Kato, K. (1995). Saturation carrying capacity of gas and flow regimes in cfb. *Journal of chemical engineering of Japan*, 28(2), 179–185.
- Bai, D.-R., Jin, Y., Yu, Z.-Q., & Zhu, J.-X. (1992). The axial distribution of the cross-sectionally averaged voidage in fast fluidized beds. *Powder Technology*, 71(1), 51–58.
- Beetstra, R., van der Hoef, M. A., & Kuipers, J. (2007). Drag force of intermediate reynolds number flow past mono-and bidisperse arrays of spheres. *AIChE journal*, 53(2), 489–501.
- Benyahia, S., Syamlal, M., & O’Brien, T. J. (2007). Study of the ability of multiphase continuum models to predict core-annulus flow. *AIChE Journal*, 53(10), 2549–2568.
- Bi, H., & Zhu, J. (1993). Static instability analysis of circulating fluidized beds and concept of high-density risers. *AIChE Journal*, 39(8), 1272–1280.
- Brunton, S. L., Noack, B. R., & Koumoutsakos, P. (2020). Machine learning for fluid mechanics. *Annual review of fluid mechanics*, 52, 477–508.
- Chew, J. W., LaMarche, W. C. Q., & Cocco, R. A. (2022). 100 years of scaling up fluidized bed and circulating fluidized bed reactors. *Powder Technology*, 409, 117813.
- Cloete, J. H. (2018). *Development of anisotropic filtered two fluid model closures* [Doctoral dissertation, Norwegian University of Science and Technology].

- Cloete, S., Amini, S., & Johansen, S. T. (2011). A fine resolution parametric study on the numerical simulation of gas–solid flows in a periodic riser section. *Powder Technology*, 205(1-3), 103–111.
- Deen, N. G., Kriebitzsch, S. H., van der Hoef, M. A., & Kuipers, J. (2012). Direct numerical simulation of flow and heat transfer in dense fluid–particle systems. *Chemical engineering science*, 81, 329–344.
- Ding, J., & Gidaspow, D. (1990). A bubbling fluidization model using kinetic theory of granular flow. *AIChE journal*, 36(4), 523–538.
- Ergun, S. (1952). Fluid flow through packed columns. *Chemical engineering progress*, 48(2), 89.
- Fan, C., Zhang, Y., Bi, X., Song, W., Lin, W., et al. (2008). Evaluation of downer reactor performance by catalytic ozone decomposition. *Chemical Engineering Journal*, 140(1-3), 539–554.
- Fan, L.-S., & Zhu, C. (1999). Principles of gas-solid flows.
- Frye, C., Lake, W., & Eckstrom, H. (1958). Gas-solid contacting with ozone decomposition reaction. *AIChE Journal*, 4(4), 403–408.
- Fullmer, W. D., & Hrenya, C. M. (2016). Quantitative assessment of fine-grid kinetic-theory-based predictions of mean-slip in unbounded fluidization. *AIChE Journal*, 62(1), 11–17.
- Gao, J., Lan, X., Fan, Y., Chang, J., Wang, G., Lu, C., & Xu, C. (2009). Cfd modeling and validation of the turbulent fluidized bed of fcc particles. *AIChE journal*, 55(7), 1680–1694.
- Gidaspow, D. (1994). *Multiphase flow and fluidization: Continuum and kinetic theory descriptions*. Academic Press.
- Gidaspow, D., & Bacelos, M. S. (2018). Kinetic theory based multiphase flow with experimental verification. *Reviews in Chemical Engineering*, 34(3), 299–318.
- Gidaspow, D., Bezburuah, R., & Ding, J. (1991). Hydrodynamics of circulating fluidized beds: Kinetic theory approach. *Proceedings of the 7th International Conference on Fluidization, Gold Coast, Australia, 3-8 May 1992*.
- Grace, J. (1990). High-velocity fluidized bed reactors. *Chemical Engineering Science*, 45(8), 1953–1966.
- Guo, Y., & Curtis, J. S. (2015). Discrete element method simulations for complex granular flows. *Annual Review of Fluid Mechanics*, 47, 21–46.
- Gupta, S. K., & Berruti, F. (2000). Evaluation of the gas–solid suspension density in cfb risers with exit effects. *Powder Technology*, 108(1), 21–31.
- Hanjalić, K., & Launder, B. E. (1972). A reynolds stress model of turbulence and its application to thin shear flows. *Journal of fluid Mechanics*, 52(4), 609–638.

- Hill, R. J., Koch, D. L., & Ladd, A. J. (2001). Moderate-reynolds-number flows in ordered and random arrays of spheres. *Journal of Fluid Mechanics*, 448, 243–278.
- Holloway, W., & Sundaresan, S. (2012). Filtered models for reacting gas–particle flows. *Chemical engineering science*, 82, 132–143.
- Horio, M., & Clift, R. (1992). A note on terminology-clusters and agglomerates. *Powder Technology*, 70(3), 196–196.
- Hou, B., Wang, X., Zhang, T., & Li, H. (2017). A model for improving the euler–euler two-phase flow theory to predict chemical reactions in circulating fluidized beds. *Powder Technology*, 321, 13–30.
- Huang, Z., Wang, L., & Zhou, Q. (2021). Development of a filtered reaction rate model for reactive gas–solid flows based on fine-grid simulations. *AIChE Journal*, 67(5), e17185.
- Huilin, L., & Gidaspow, D. (2003). Hydrodynamics of binary fluidization in a riser: Cfd simulation using two granular temperatures. *Chemical engineering science*, 58(16), 3777–3792.
- Igci, Y., Andrews IV, A. T., Sundaresan, S., Pannala, S., & O’Brien, T. (2008). Filtered two-fluid models for fluidized gas-particle suspensions. *AIChE Journal*, 54(6), 1431–1448.
- Igci, Y., & Sundaresan, S. (2011). Constitutive models for filtered two-fluid models of fluidized gas–particle flows. *Industrial & Engineering Chemistry Research*, 50(23), 13190–13201.
- Ishii, H., & Horio, M. (1991). The flow structures of a circulating fluidized bed. *Advanced Powder Technology*, 2(1), 25–36.
- Jiang, P., Bi, H., Jean, R.-H., & Fan, L.-S. (1991). Baffle effects on performance of catalytic circulating fluidized bed reactor. *AIChE journal*, 37(9), 1392–1400.
- Jiang, Y., Kolehmainen, J., Gu, Y., Kevrekidis, Y. G., Ozel, A., & Sundaresan, S. (2019). Neural-network-based filtered drag model for gas-particle flows. *Powder Technology*, 346, 403–413.
- Johnsson, J. E., Åmand, L.-E., Dam-Johansen, K., & Leckner, B. (1996). Modeling n₂o reduction and decomposition in a circulating fluidized bed boiler. *Energy & fuels*, 10(4), 970–979.
- Johnston, P. M., Zhu, J.-X., de Lasa, H. I., & Zhang, H. (1999). Effect of distributor designs on the flow development in downer reactor. *AIChE journal*, 45(7), 1587–1592.
- LeCun, Y., Bengio, Y., & Hinton, G. (2015). Deep learning. *nature*, 521(7553), 436–444.
- Li, D. (2010). *Investigation of circulating fluidized bed riser and downer reactor performance for catalytic ozone decomposition* [Doctoral dissertation, The University of Western Ontario].

- Li, D., Ray, A. K., Ray, M. B., & Zhu, J. (2012). Rotational asymmetry of reactant concentration and its evolution in a circulating fluidized bed riser. *Particuology*, *10*(5), 573–581.
- Li, D., Ray, A. K., Ray, M. B., & Zhu, J. (2013a). Catalytic reaction in a circulating fluidized bed riser: Ozone decomposition. *Powder technology*, *242*, 65–73.
- Li, D., Ray, M. B., Ray, A. K., & Zhu, J. (2013b). A comparative study on hydrodynamics of circulating fluidized bed riser and downer. *Powder technology*, *247*, 235–259.
- Li, D., Zhu, J., Ray, M. B., & Ray, A. K. (2011). Catalytic reaction in a circulating fluidized bed downer: Ozone decomposition. *Chemical engineering science*, *66*(20), 4615–4623.
- Li, J. (1994). *Particle-fluid two-phase flow: The energy-minimization multi-scale method*. Metallurgical Industry Press.
- Li, J., & Huang, W. (2018). From multiscale to mesoscience: Addressing mesoscales in mesoregimes of different levels. *Annual review of chemical and biomolecular engineering*, *9*, 41–60.
- Li, J., Tung, Y., & Kwauk, M. (1988). Method of energy minimization in multi-scale modeling of particle-fluid two-phase flow. In *Circulating fluidized bed technology* (pp. 89–103). Elsevier.
- Li, J.-S., Zhu, L.-T., Yan, W.-C., Rashid, T. A. B., Xu, Q.-J., & Luo, Z.-H. (2021). Coarse-grid simulations of full-loop gas-solid flows using a hybrid drag model: Investigations on turbulence models. *Powder Technology*, *379*, 108–126.
- Li, Y., & Kwauk, M. (1980). The dynamics of fast fluidization. In *Fluidization* (pp. 537–544). Springer.
- Liu, C., Wang, W., Zhang, N., & Li, J. (2015). Structure-dependent multi-fluid model for mass transfer and reactions in gas–solid fluidized beds. *Chemical Engineering Science*, *122*, 114–129.
- Liu, J. (2016). *Reactor performances and hydrodynamics of various gas-solids fluidized beds* [Doctoral dissertation, The University of Western Ontario]. <https://ir.lib.uwo.ca/etd/3967/>
- Liu, X., Wang, L., & Ge, W. (2017). Meso-scale statistical properties of gas–solid flow—a direct numerical simulation (dns) study. *AIChE Journal*, *63*(1), 3–14.
- Lu, B., Wang, W., & Li, J. (2009). Searching for a mesh-independent sub-grid model for cfd simulation of gas–solid riser flows. *Chemical Engineering Science*, *64*(15), 3437–3447.
- Lun, C. K. K., Savage, S. B., Jeffrey, D. J., & Chepurniy, N. (1984). Kinetic theories for granular flow: Inelastic particles in couette flow and slightly inelastic particles in a general flowfield. *Journal of fluid mechanics*, *140*, 223–256.

- Luo, B., Yan, D., Ma, Y. L., Barghi, S., & Zhu, J. (2007). Characteristics of gas–solid mass transfer in a cocurrent downflow circulating fluidized bed reactor. *Chemical Engineering Journal*, 132(1-3), 9–15.
- McCulloch, W., & Pitts, W. A. (1943). A logical calculus of the ideas immanent in nervous activity. *Bulletin of Mathematical Biophysics*, 5, 115–133.
- Milioli, C. C., Milioli, F. E., Holloway, W., Agrawal, K., & Sundaresan, S. (2013). Filtered two-fluid models of fluidized gas-particle flows: New constitutive relations. *AIChE Journal*, 59(9), 3265–3275.
- O’Brien, T. J., & Syamlal, M. (1993). Particle cluster effects in the numerical simulation of a circulating fluidized bed. *Circulating fluidized bed technology IV*, 367–372.
- Ouyang, S., Li, X.-G., & Potter, O. (1995). Circulating fluidized bed as a catalytic reactor: Experimental study. *AIChE Journal*, 41(6), 1534–1542.
- Ouyang, S., Lin, J., & Potter, O. (1993). Ozone decomposition in a 0.254 m diameter circulating fluidized bed reactor. *Powder Technology*, 74(1), 73–78.
- Pärssinen, J., & Zhu, J.-X. (2001). Axial and radial solids distribution in a long and high-flux cfb riser. *AIChE Journal*, 47(10), 2197–2205.
- Peng, B., Zhang, C., & Zhu, J. (2012). Improvement of the uniformity of radial solids concentration profiles in circulating fluidized-bed risers. *Chemical engineering & technology*, 35(4), 627–634.
- Peng, B., Zhu, J., & Zhang, C. (2010). Numerical study on the effect of the air jets at the inlet distributor in the gas- solids circulating fluidized-bed risers. *Industrial & Engineering Chemistry Research*, 49(11), 5310–5322.
- Rumelhart, D. E., Hinton, G. E., & Williams, R. J. (1986). Learning representations by back-propagating errors. *nature*, 323(6088), 533–536.
- Schaeffer, D. G. (1987). Instability in the evolution equations describing incompressible granular flow. *Journal of differential equations*, 66(1), 19–50.
- Schnitzlein, M. G., & Weinstein, H. (1988). Flow characterization in high-velocity fluidized beds using pressure fluctuations. *Chemical engineering science*, 43(10), 2605–2614.
- Shen, C., & Johnstone, H. (1955). Gas-solid contact in fluidized beds. *AIChE Journal*, 1(3), 349–354.
- Sinclair, J. L., & Jackson, R. (1989). Gas-particle flow in a vertical pipe with particle-particle interactions. *AIChE Journal*, 35, 1473–1486. <https://doi.org/10.1002/aic.690350908>
- Sun, G., & Grace, J. R. (1990). The effect of particle size distribution on the performance of a catalytic fluidized bed reactor. *Chemical Engineering Science*, 45(8), 2187–2194.

- Sun, Z. (2019). *Numerical studies on hydrodynamics in various circulating fluidization systems* [Doctoral dissertation, The University of Western Ontario]. <https://ir.lib.uwo.ca/etd/6423/>
- Sun, Z., Zhang, C., & Zhu, J. (2022). Numerical investigations on gas–solid flow in circulating fluidized bed risers using a new cluster-based drag model. *Particuology*, *63*, 9–23.
- Sun, Z., & Zhu, J. (2019). A consolidated flow regime map of upward gas fluidization. *AIChE Journal*, *65*(9), e16672.
- Sundaresan, S., Ozel, A., & Kolehmainen, J. (2018). Toward constitutive models for momentum, species, and energy transport in gas–particle flows. *Annual review of chemical and biomolecular engineering*, *9*, 61–81.
- Syamlal, M., Rogers, W., & O'Brien, T. (1993, December). *Mfix documentation theory guide* (1). Office of Scientific and Technical Information. <https://doi.org/10.2172/10145548>
- Syamlal, M., & O'Brien, T. J. (2003). Fluid dynamic simulation of O₃ decomposition in a bubbling fluidized bed. *AIChE journal*, *49*(11), 2793–2801.
- Tenneti, S., & Subramaniam, S. (2014). Particle-resolved direct numerical simulation for gas-solid flow model development. *Annual review of fluid mechanics*, *46*, 199–230.
- Venderbosch, R., Prins, W., & van Swaij, W. P. M. (1998). Platinum catalyzed oxidation of carbon monoxide as a model reaction in mass transfer measurements. *Chemical Engineering Science*, *53*(19), 3355–3366.
- Wang, C. (2013). *High density gas-solids circulating fluidized bed riser and downer reactors* [Doctoral dissertation, The University of Western Ontario]. <https://ir.lib.uwo.ca/etd/1572/>
- Wang, C., Barghi, S., & Zhu, J. (2014a). Hydrodynamics and reactor performance evaluation of a high flux gas-solids circulating fluidized bed downer: Experimental study. *AIChE Journal*, *60*(10), 3412–3423.
- Wang, C., Li, C., & Zhu, J. (2015a). Axial solids flow structure in a high density gas–solids circulating fluidized bed downer. *Powder Technology*, *272*, 153–164.
- Wang, C., Li, C., Zhu, J., Wang, C., Barghi, S., & Zhu, J. (2015b). A comparison of flow development in high density gas-solids circulating fluidized bed downer and riser reactors. *AIChE Journal*, *61*(4), 1172–1183.
- Wang, C., Wang, G., Li, C., Barghi, S., & Zhu, J. (2014b). Catalytic ozone decomposition in a high density circulating fluidized bed riser. *Industrial & Engineering Chemistry Research*, *53*(16), 6613–6623.
- Wang, C., Zhu, J., & Barghi, S. (2015c). Performance evaluation of high density riser and downer: Experimental study using ozone decomposition. *Chemical Engineering Journal*, *262*, 478–489.

- Wang, C., Zhu, J., Barghi, S., & Li, C. (2014c). Axial and radial development of solids holdup in a high flux/density gas–solids circulating fluidized bed. *Chemical Engineering Science*, *108*, 233–243.
- Wang, C., Zhu, J., Lan, X., Gao, J., & Barghi, S. (2016). Radial solids flow structure in high flux gas-solids circulating fluidized bed downers. *Powder Technology*, *301*, 848–857.
- Wang, C., Zhu, J., Li, C., & Barghi, S. (2014d). Detailed measurements of particle velocity and solids flux in a high density circulating fluidized bed riser. *Chemical Engineering Science*, *114*, 9–20.
- Wang, J., van der Hoef, M. A., & Kuipers, J. (2009). Why the two-fluid model fails to predict the bed expansion characteristics of geldart a particles in gas-fluidized beds: A tentative answer. *Chemical Engineering Science*, *64*(3), 622–625.
- Wang, W., & Li, J. (2007). Simulation of gas–solid two-phase flow by a multi-scale cfd approach—of the emms model to the sub-grid level. *Chemical Engineering Science*, *62*(1-2), 208–231.
- Wei, X., & Zhu, J. (2019). Capturing the instantaneous flow structure in gas-solid circulating fluidized bed using high-speed imaging and fiber optic sensing. *Chemical Engineering Science*, *207*, 713–724.
- Wen & Yu. (1966). Mechanics of fluidization. *Fluid Particle Technology, Chem. Eng. Progress. Symposium Series*, *62*, 100–111.
- Wilcox, D. C. (2008). Formulation of the kw turbulence model revisited. *AIAA journal*, *46*(11), 2823–2838.
- Yan, A., Huang, W., & Zhu, J. (2008). The influence of distributor structure on the solids distribution and flow development in circulating fluidized beds. *The Canadian Journal of Chemical Engineering*, *86*(6), 1023–1031.
- Yan, A., & Zhu, J. (2004). Scale-up effect of riser reactors (1): Axial and radial solids concentration distribution and flow development. *Industrial & engineering chemistry research*, *43*(18), 5810–5819.
- Yang, J., & Zhu, J. (2014). A novel method based on image processing to visualize clusters in a rectangular circulating fluidized bed riser. *Powder technology*, *254*, 407–415.
- Yerushalmi, J., Turner, D. H., & Squires, A. M. (1976). The fast fluidized bed. *Industrial & Engineering Chemistry Process Design and Development*, *15*(1), 47–53.
- Zhang, H., Johnston, P., Zhu, J.-X., De Lasa, H., & Bergounou, M. (1998). A novel calibration procedure for a fiber optic solids concentration probe. *Powder Technology*, *100*(2-3), 260–272.
- Zhang, H., Zhu, J.-X., & Bergounou, M. A. (1999). Flow development in a gas-solids downer fluidized bed. *The Canadian Journal of Chemical Engineering*, *77*(2), 194–198.

- Zhang, Y., Jiang, M., Chen, X., Yu, Y., & Zhou, Q. (2020). Modeling of the filtered drag force in gas–solid flows via a deep learning approach. *Chemical Engineering Science*, 225, 115835.
- Zhong, W., Yu, A., Liu, X., Tong, Z., & Zhang, H. (2016). Dem/cfd-dem modelling of non-spherical particulate systems: Theoretical developments and applications. *Powder technology*, 302, 108–152.
- Zhu, H., Zhou, Z., Yang, R., & Yu, A. (2008). Discrete particle simulation of particulate systems: A review of major applications and findings. *Chemical Engineering Science*, 63(23), 5728–5770.
- Zhu, L.-T. (2021). *Development of mesoscale models for gas-solid fluidization reactors and data-driven modeling* [Doctoral dissertation, Shanghai Jiao Tong University].
- Zhu, L.-T., Ouyang, B., Lei, H., & Luo, Z.-H. (2021). Conventional and data-driven modeling of filtered drag, heat transfer, and reaction rate in gas–particle flows. *AIChE Journal*, 67(8), e17299.
- Zhu, L.-T., Tang, J.-X., & Luo, Z.-H. (2020). Machine learning to assist filtered two-fluid model development for dense gas–particle flows. *AIChE Journal*, 66(6), e16973.

Chapter 3

A pseudo-homogeneous reactive transport model for catalytic ozone decomposition in fluidization systems: Development and parametric study

3.1 Introduction

The present investigation aims to establish a pseudo-homogeneous reactive transport model for the ozone decomposition reaction for CFD simulations. The model will be developed using the data obtained from an experiment in a micro fixed-bed reactor. The validation of the reactive transport model will be carried out by comparing the numerical results with the experimental data of the reaction in the fixed bed reactor. Subsequently, the reactive transport model will be employed for simulating the CFB riser reactor, with the aim of investigating the impact of the change of turbulence models, specularly coefficients, and simulation methods on the flow fields and reaction behaviours of the riser. At the end, a discussion of the influence of instantaneous flow structures on reaction behaviours will be presented.

This chapter comprises four parts. Section 3.2 presents the development process of the reactive transport model and introduces the two-fluid model. The simulation details of the fixed bed reactor and the CFB riser reactor are presented in Section 3.3 and 3.4,

respectively. The results of the simulations are analyzed in Section 3.5.

3.2 Numerical models

3.2.1 Development of the reactive transport model

The ozone mass transport equation in the gas phase can be described as follows:

$$\frac{\partial}{\partial t} \left(\varepsilon_g \rho_g Y_g^{O_3} \right) + \nabla \cdot \left(\varepsilon_g \rho_g \vec{u}_g Y_g^{O_3} - \varepsilon_g \Gamma_g^{O_3} \nabla Y_g^{O_3} \right) = \text{reaction term.} \quad (3.1)$$

The unit of Equation (3.1) is $\left[\frac{\text{kg}(\text{O}_3)}{\text{m}^3 \text{s}} \right]$. This equation consists of four terms: accumulation, convection, diffusion, and reaction. The accumulation term is the change of the amount of ozone mass with time. The convection describes the change in the amount of ozone due to fluid-phase flow. The diffusion term is the mass transfer due to the molecular diffusion. The $\Gamma_g^{O_3}$ is the diffusivity of ozone in the gas phase. For laminar and turbulence flows, $\Gamma_g^{O_3}$ are given by the following two equations, respectively.

$$\Gamma_{g,l}^{O_3} = \rho_g \mathcal{D}_{O_3,m},$$

$$\Gamma_{g,t}^{O_3} = \rho_g \mathcal{D}_{O_3,m} + \frac{\mu_{g,t}}{Sc_{g,t}},$$

where $\mu_{g,t}$ is the dynamic turbulence viscosity of the gas, $Sc_{g,t}$ is the turbulent Schmidt number of the gas, and $\mathcal{D}_{O_3,m}$ is the effective mass diffusion coefficient of ozone in the gas phase (Zehner & Schlünder, 1970):

$$\mathcal{D}_{O_3,m} = \frac{\mathcal{D}_{O_3\text{-air}} (1 - \varepsilon_s^{0.5})}{\varepsilon_g},$$

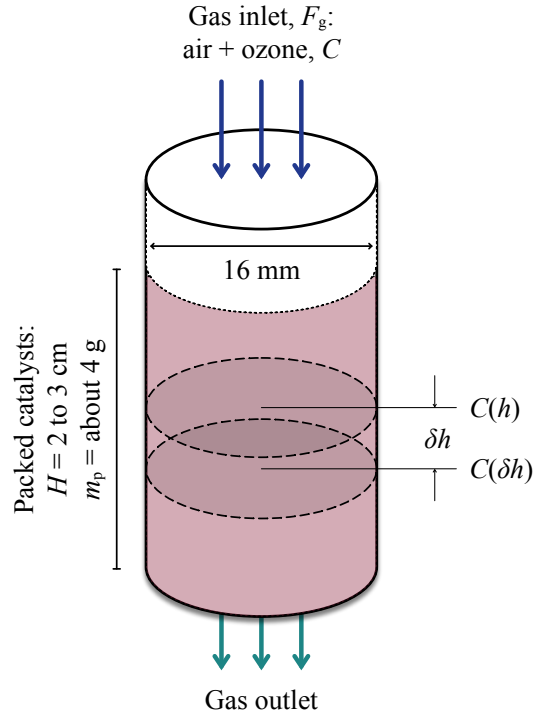


Figure 3.1: Configuration of the micro fixed-bed reactor (Li, 2010)

where $\mathcal{D}_{O_3\text{-air}} = 1.48535 \times 10^{-5} \text{ m}^2/\text{s}$ is the mass diffusion coefficient of ozone in the air (Bird et al., 2015).

The reaction term accounts for the amount of ozone consumed as a result of ozone decomposition. In the works by Li (2010), Liu (2016), and Wang (2013), the kinetic parameters of the ozone decomposition reaction are measured in a copper micro-reactor. The reactor is a fixed bed type, with an inner diameter of 16 mm, as illustrated in Figure 3.1 (Wang et al., 2014). The reactor is vertically oriented and contains 4 g of catalyst. The inflow gas, a mixture of air and ozone, is fed into the reactor from the top. The reaction products are collected from the bottom of the reactor. If the velocity of the inlet gas is high enough, the reactor can be considered as a plug flow reactor (PFR) (Jiang et al., 1991; Li, 2010). Then, the reaction process can be described by the following equation:

$$F_g C_g^{O_3}(h) - F_g C_g^{O_3}(h + \delta h) = - \left(\frac{\delta h}{H} \right) \left(\frac{m_s}{\rho_s} \right) k_r C_g^{O_3}, \quad (3.2)$$

where F_g [m^3/s] is the volumetric flow rate of the gas phase, $C_g^{\text{O}_3}$ [mol/m^3] is the concentration of the gas phase species, h [m] is the axial location, H [m] is the height of the reactor, m_s [kg] is the mass of the catalyst particle, ρ_s [kg/m^3] is the density of the catalyst particle, and δh [m] is the infinitesimal height of the reactor. k_r [s^{-1}] is the apparent reaction constant based on the volume of the catalyst, which includes the reaction kinetics and the internal mass transfer of the catalyst particle. From Equation (3.2), the reaction constant can be obtained:

$$\frac{C_g^{\text{O}_3}(h + \delta h) - C_g^{\text{O}_3}(h)}{\delta h} = -\frac{1}{H} \frac{1}{F_g} \frac{m_s}{\rho_s} k_r C_g^{\text{O}_3},$$

$$\frac{dC_g^{\text{O}_3}}{dh} = -\frac{1}{H} \frac{1}{F_g} \frac{m_s}{\rho_s} k_r C_g^{\text{O}_3}, \quad (3.3)$$

$$C_g^{\text{O}_3}(h) = C_{g,\text{in}}^{\text{O}_3} \exp\left(-\frac{k_r h m_s}{F_g H \rho_s}\right),$$

$$\implies k_r = \frac{F_g \rho_s}{m_s} \ln \frac{C_{g,\text{in}}^{\text{O}_3}}{C_{g,\text{out}}^{\text{O}_3}}. \quad (3.4)$$

According to Equation (3.3), the following equation can be derived for the mass transport of the gas phase species:

$$\frac{dC_g^{\text{O}_3}}{dh} = -\frac{\varepsilon_s}{U_g} k_r C_g^{\text{O}_3},$$

$$\frac{M_{\text{O}_3}}{\rho_g} \frac{dC_g^{\text{O}_3}}{dh} = -\frac{\varepsilon_s}{U_g} k_r \left(\frac{M_{\text{O}_3}}{\rho_g} C_g^{\text{O}_3} \right),$$

$$U_g \frac{dY_g^{\text{O}_3}}{dh} = -(\varepsilon_s k_r) Y_g^{\text{O}_3},$$

$$\Rightarrow \frac{d}{dh} \left(\varepsilon_g v_g \rho_g Y_g^{O_3} \right) = -(\varepsilon_s k_r) \rho_g Y_g^{O_3}. \quad (3.5)$$

Extending Equation (3.5) to the multi-dimensional space:

$$\nabla \cdot \left(\varepsilon_g \vec{u}_g \rho_g Y_g^{O_3} \right) = -(\varepsilon_s k_r) \rho_g Y_g^{O_3}, \quad (3.6)$$

where \vec{u}_g is the velocity vector of the gas phase, and $\nabla \cdot \vec{u}_g$ can be expressed by $(\partial u_g / \partial x + \partial v_g / \partial y + \partial w_g / \partial z)$ in the Cartesian coordinate system. The left-side term in Equation (3.6) is the general form of the convection term of ozone mass fraction in the gas phase of a multiphase flow. According to Equation (3.1), the pseudo-homogeneous reactive transport equation for the ozone decomposition reaction in the gas phase can be expressed as:

$$\frac{\partial}{\partial t} \left(\varepsilon_g \rho_g Y_g^{O_3} \right) + \nabla \cdot \left(\varepsilon_g \rho_g \vec{u}_g Y_g^{O_3} - \varepsilon_g \Gamma_g^{O_3} \nabla Y_g^{O_3} \right) = -(\varepsilon_s k_r) \rho_g Y_g^{O_3}. \quad (3.7)$$

This equation describes the ozone mass transportation and consumption per unit time and volume.

3.2.2 Two-fluid model

The Eulerian-Eulerian two-fluid model coupling with the kinetic theory for granular flow (KTGF) is used in this study to simulate the flows in gas-solids fluidization systems.

Governing equations The mass conservation equations of gas and solids phases are given as:

$$\partial_t (\varepsilon_g \rho_g) + \nabla \cdot (\varepsilon_g \rho_g \vec{u}_g) = 0, \quad (3.8)$$

$$\partial_t (\varepsilon_s \rho_s) + \nabla \cdot (\varepsilon_s \rho_s \vec{u}_s) = 0, \quad (3.9)$$

$$\varepsilon_g + \varepsilon_s = 1, \quad (3.10)$$

where ε is the volume fraction, ρ is the density, and \vec{u} is the velocity of certain phase.

The momentum conservation equations of gas and solids phases are given as:

$$\frac{\partial}{\partial t} (\varepsilon_g \rho_g \vec{u}_g) + \nabla \cdot (\varepsilon_g \rho_g \vec{u}_g \otimes \vec{u}_g) = -\varepsilon_g \nabla P + \bar{\bar{\tau}}_g + \varepsilon_g \rho_g \vec{g} + K_{sg} (\vec{u}_s - \vec{u}_g), \quad (3.11)$$

$$\bar{\bar{\tau}}_g = \varepsilon_g \mu_g \left(\nabla \vec{u}_g + \nabla \vec{u}_g^T \right) + \varepsilon_g \left(\lambda_g - \frac{2}{3} \mu_g \right) \nabla \cdot \vec{u}_g \bar{\bar{I}},$$

$$\frac{\partial}{\partial t} (\varepsilon_s \rho_s \vec{u}_s) + \nabla \cdot (\varepsilon_s \rho_s \vec{u}_s \otimes \vec{u}_s) = -\varepsilon_s \nabla P + \bar{\bar{\tau}}_s + \varepsilon_s \rho_s \vec{g} + K_{sg} (\vec{u}_g - \vec{u}_s), \quad (3.12)$$

$$\bar{\bar{\tau}}_s = \varepsilon_s \mu_s \left(\nabla \vec{u}_s + \nabla \vec{u}_s^T \right) + \varepsilon_s \left(\lambda_s - \frac{2}{3} \mu_s \right) \nabla \cdot \vec{u}_s \bar{\bar{I}},$$

where $\bar{\bar{\tau}}$ is the stress-strain tensor, μ and λ are the shear and bulk viscosity, $\bar{\bar{I}}$ is the unit tensor. K_{sg} is the interphase momentum exchange coefficient between the gas phase and solids phase. As for the solids phase, the solids pressure, p_s , solids shear viscosity, μ_s , and solids bulk viscosity, λ_s , are related to the granular temperature, which is obtained from the kinetic theory of granular flow (Gidaspow, 1994).

Kinetic theory of granular flow The granular temperature of the particles, Θ_s , is related to the kinetic energy of the random motion of the particles (Sinclair & Jackson, 1989) and calculated by

$$\Theta_s = \frac{1}{3} v'_{s\tau} v'_{s\tau}, \quad (3.13)$$

where $v'_{s\tau}$ is the fluctuating solids velocity, which related to the collisions among particles.

The equation for the granular temperature derived from the kinetic theory (Gidaspow,

1994) is shown as

$$\begin{aligned} \frac{3}{2} \left[\frac{\partial}{\partial t} (\varepsilon_s \rho_s \Theta_s) + \nabla \cdot (\varepsilon_s \rho_s \vec{u}_s \Theta_s) \right] = & \left(-p_s \bar{\bar{\mathbf{I}}} + \bar{\bar{\boldsymbol{\tau}}}_s \right) : \nabla \vec{v}_s + \\ & + \nabla \cdot (k_{\Theta_s} \nabla \Theta_s) - \gamma_{\Theta_s} + \phi_{gs}, \end{aligned} \quad (3.14)$$

where $\left(-p_s \bar{\bar{\mathbf{I}}} + \bar{\bar{\boldsymbol{\tau}}}_s \right) : \nabla \vec{v}_s$ is the energy generation by the solids stress tensor, $(k_{\Theta_s} \nabla \Theta_s)$ is the diffusion energy, (γ_{Θ_s}) is the collisional dissipation of energy, and (ϕ_{gs}) is the energy exchange between the gas and solids phases. The collisional dissipation of energy is given by Lun et al. (1984), which can be calculated by:

$$\gamma_{\Theta_s} = \frac{12 (1 - e_{ss}^2) g_{0,ss}}{d_p \sqrt{\pi}} \rho_s \varepsilon_s \Theta_s^{1.5}, \quad (3.15)$$

where the e_{ss} is the particle-particle restitution coefficient and $g_{0,ss}$ is the radial distribution function of particles. The diffusion coefficient for granular energy, k_{Θ_s} , is given by Gidaspow (1994):

$$\begin{aligned} k_{\Theta_s} = & \frac{150 \rho_s d_p \sqrt{\Theta_s} \pi}{384 (1 + e_{ss}) g_{0,ss}} \left(1 + \frac{6}{5} \varepsilon_s g_{0,ss} (1 + e_{ss}) \right)^2 + \\ & + 2 \rho_s \varepsilon_s^2 d_p (1 + e_{ss}) g_{0,ss} \sqrt{\Theta_s / \pi}. \end{aligned} \quad (3.16)$$

The solids pressure in the solids-phase momentum equation composes of a kinetic term and a particle collision term:

$$p_s = \varepsilon_s \rho_s \Theta_s + 2 \rho_s (1 + e_{ss}) \varepsilon_s^2 g_{0,ss} \Theta_s, \quad (3.17)$$

where e_{ss} is the restitution coefficient for particle collisions and $g_{0,ss}$ is the radial distribution function.

The solids shear stresses in the solids-phase momentum equation are related to the shear and bulk viscosities. The bulk viscosity (Lun et al., 1984) is calculated by:

$$\lambda_s = \frac{4}{3} \varepsilon_s^2 \rho_s d_p g_{0,ss} (1 + e_{ss}) \left(\frac{\Theta_s}{\pi} \right)^{0.5}. \quad (3.18)$$

The shear viscosity contains collisional, kinetic (Gidaspow, 1994), and fractional viscosity (Schaeffer, 1987) are calculated by:

$$\mu_{s,col} = \frac{4}{5} \varepsilon_s \rho_s d_p g_{0,ss} (1 + e_{ss}) (\Theta_s/\pi)^{0.5}, \quad (3.19)$$

$$\mu_{s,kin} = \frac{10 \rho_s d_p \sqrt{\Theta_s \pi}}{96 \varepsilon_s (1 + e_{ss}) g_{0,ss}} \left(1 + \frac{4}{5} g_{0,ss} \varepsilon_s (1 + e_{ss}) \right)^2, \quad (3.20)$$

$$\mu_{s,fr} = \frac{p_{fr} \sin \phi}{2\sqrt{I_{2D}}}. \quad (3.21)$$

Gidaspow drag model Combining the Wen and Yu model (Wen & Yu, 1966) and the Ergun equation (Ergun, 1952) results in the Gidaspow drag model (Gidaspow et al., 1991).

$$K_{sg} = \begin{cases} \frac{3}{4} C_D \frac{\varepsilon_s \varepsilon_g \rho_g |\vec{v}_s - \vec{v}_g|}{d_p} \varepsilon_g^{-2.65}, & \varepsilon_g > 0.8 \\ 150 \frac{\varepsilon_s^2 \mu_g}{\varepsilon_g d_p^2} + 1.75 \frac{\rho_g \varepsilon_s |\vec{v}_s - \vec{v}_g|}{d_p}, & \varepsilon_g \leq 0.8 \end{cases}, \quad (3.22)$$

where

$$C_D = \frac{24}{\varepsilon_g Re_s} \left(1 + 0.15 (\varepsilon_g Re_s)^{0.687} \right). \quad (3.23)$$

Turbulence model In this study, the k - ε turbulence model for TFM with enhanced wall treatment (Launder, Spalding, et al., 1972) is used for the gas phase of the micro-reactor simulation. Regarding the gas phase of the CFB riser simulations, the same turbulence

model and the laminar model are used. In the k - ϵ turbulence model, the turbulence kinetic energy, k , and the energy dissipation rate, ϵ , of the gas phase are described by the following equations:

$$\frac{\partial}{\partial t}(\epsilon_g \rho_g k_g) + \nabla \cdot (\epsilon_g \rho_g k_g \vec{u}_g) = \nabla \cdot \left(\epsilon_g \left(\mu_g + \frac{\mu_{t,g}}{\sigma_k} \right) \nabla k_g \right) + \quad (3.24)$$

$$+ \epsilon_g G_{k,g} - \epsilon_g \rho_g \epsilon_g + \epsilon_g \rho_g \Pi_{k_g},$$

$$\frac{\partial}{\partial t}(\epsilon_g \rho_g \epsilon_g) + \nabla \cdot (\epsilon_g \rho_g \epsilon_g \vec{u}_g) = \nabla \cdot \left(\epsilon_g \left(\mu_g + \frac{\mu_{t,g}}{\sigma_\epsilon} \right) \nabla \epsilon_g \right) + \quad (3.25)$$

$$+ \epsilon_g \frac{\epsilon_g}{k_g} (C_{1\epsilon} G_{k,g} - C_{2\epsilon} \rho_g \epsilon_g) +$$

$$+ \epsilon_g \rho_g \Pi_{\epsilon_g},$$

where Π_{k_g} and Π_{ϵ_g} are source terms that due to the interphase turbulent momentum transfer from the solids phase to the gas phase (ANSYS, Inc., 2022b).

3.3 Setups for micro fixed-bed reactor simulations

Figure 3.2 shows (a) the computational domain, (b) the mesh of the cross section, and (c) the mesh of the part of the longitudinal section. The computational domain is established based on the configuration of the reactor (Figure 3.1). The length of the reactor is 32.35 mm, with 4 g of catalyst packed in the middle region, while a 5 mm empty space is left above and below the packed catalysts. The computational domain is discretized into 1,170,944 polyhedral cells. The max size of the cells is set as three times of the particle diameter. The cells next to the wall are refined in a trilayered structure, whereby the growth rate of adjacent cells did not surpass 1.05. The geometry and mesh shown in Figure 3.1 are generated using the ANSYS SpaceClaim (ANSYS, Inc., 2022c) and

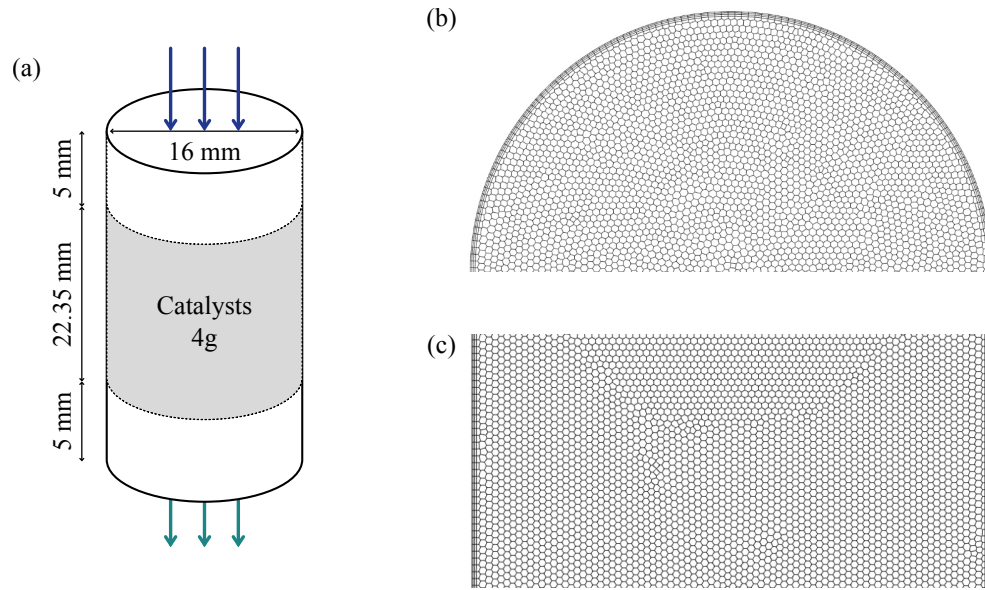


Figure 3.2: Computational domain and mesh of the micro fixed-bed reactor

ANSYS Fluent Meshing (ANSYS, Inc., 2022a).

The three-dimensional steady solver is used for calculating this flow field, as the particles remain fixed in their packed positions, since the particles are fixed in the bed, models for the solids phase are not required. However, the volume fraction of the solids phase is required in the gas phase equations. The $k-\epsilon$ turbulence model with enhanced wall treatment is utilized in order to obtain a more precise representation of the gas flow field. Other detailed information on the simulation is listed in Table 3.1.

The ozone is mixed with the air introduced from the top of the tube. The gas velocity and the ozone concentration at the inlet is specified based on the experimental operating conditions (Table 3.6). The outlet at the bottom is set as the outflow. The boundary condition for the wall is set as no-slip for the gas phase. The particles are pre-packed in the middle region of the tube, and the solids holdup is set as 0.5. The particle velocity is set as zero at the whole cell zone since they do not move. Table 3.2 provides a comprehensive list of the physical parameters related to this simulation.

Table 3.1: CFD Model for the micro fixed-bed reactor simulation

Software & Solver	
Software	ANSYS fluent 2022R1
Solver	Three-dimensional, steady-state
Models	
Multiphase model	Eulerian-Eulerian
Drag coefficient	Huilin and Gidaspow (2003)
Viscous model	$k-\epsilon$ model (Lauder, Spalding, et al., 1972)
Solvers	
Scheme	Phase coupled SIMPLE
Gradient discretization	Least squares cell based
Pressure discretization	PRESTO!
Momentum discretization	Second order upwind
Volume fraction discretization	Second order upwind
UDS discretization	Second order upwind
Residual	1×10^{-10}

Table 3.2: Parameters used for micro fixed-bed reactor simulations

Physical parameters		
Gas		Air
Inlet ozone mass fraction	1.6653×10^{-4}	
Diffusion coefficient of ozone	1.48535×10^{-5}	m^2/s
Particle		FCC
Particle density	1780	kg/m^3
Particle diameter	70	μm
Particle packing fraction	0.5	
Particle velocity	0	m/s
Mesh information		
Domain size	$\Phi 16 \times 32.35$	mm
Max cell length	0.21	mm
Cell number	1,170,944	

3.4 Setups for CFB riser simulations

The CFB system depicted in Figure 3.3 (a) is employed by Wang et al. (2014) to carry out the ozone decomposition reaction. It contains a riser, a downer/downcomer, a returning pipe, separations, and other accessories. In the operation of the CFB riser, the air mixed with ozone entered from the gas distributor at the bottom of the riser in a high velocity. The particles that are discharged from the returning pipe into the riser are pushed upwards by the gas flow. The mixture of the gas and particles exits the riser from its top and is separated subsequently. The particles flow in a downward direction along the downcomer and enter the riser through the returning pipe. Then, the particles start a new circulation in the system.

Mesh and solver Based on the grid independence test by Sun et al. (2022), an unstructured quadrilateral mesh with the max cell size of $27 d_p$ and a total of around 270,000 cells is used, as shown in Figure 3.3 (b). Near the wall, a five-layer mesh with the initial layer having a thickness of $3 d_p$ is implemented. In the comparison to a finer mesh (total cell number of around 480,000), the deviations of key hydrodynamic characteristics are below 2%. The ANSYS Fluent (ANSYS, Inc., 2022a) is used to run the simulation of this gas-solids system. Table 3.3 provides a summary of the CFD models.

Boundary conditions and operating conditions In this study, two simulation methods are used to simulate the CFB riser system. The first method (referred to as Method 1 hereafter) is a more accurate approach to implementing experimental operating conditions, as shown in Figure 3.4 (a). This method uses the velocity profiles based on the superficial gas velocity (U_g) and the solids circulation rate (G_s), which are the riser's operating conditions. As illustrated in Figure 3.3 (b), the gas inlet boundary condition is defined as a jet velocity profile to consider the effects of the gas distributor on the gas velocity

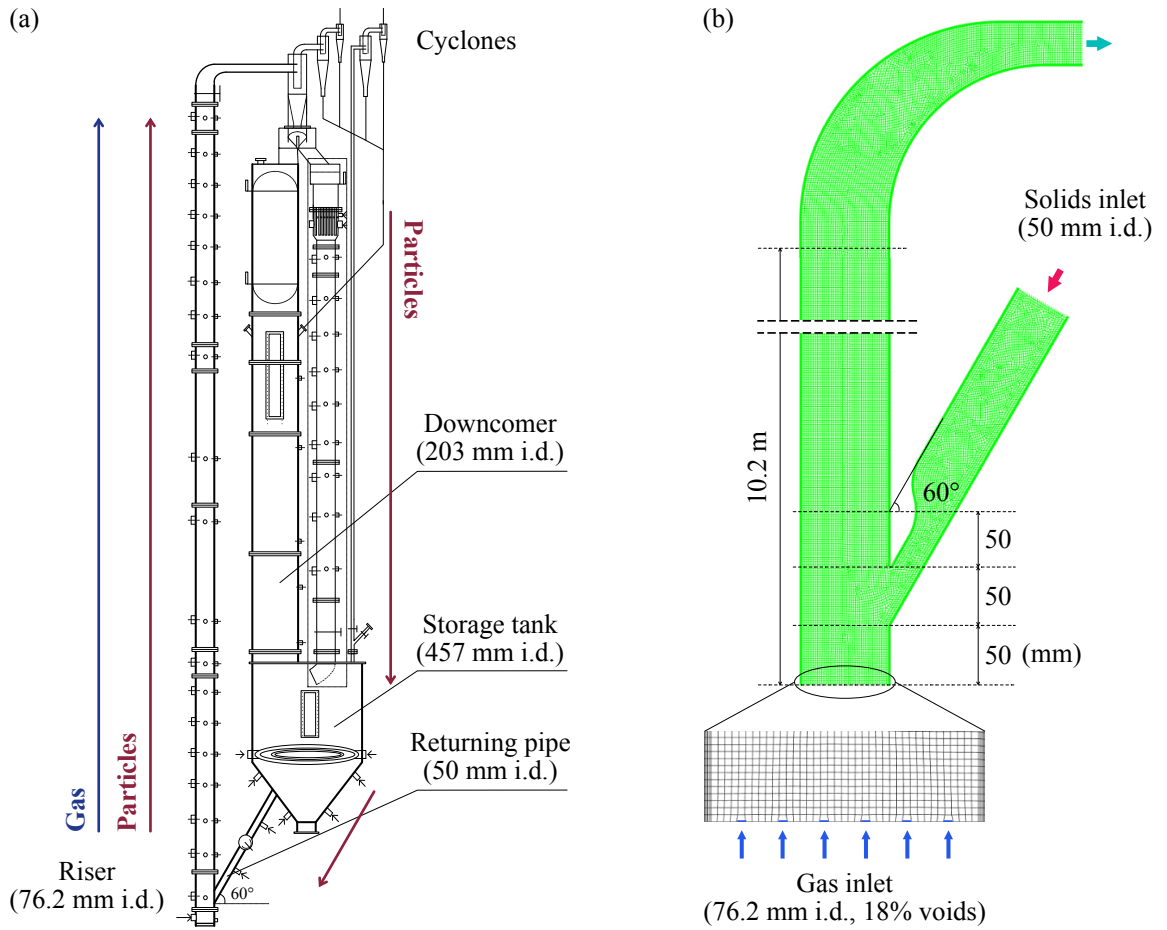


Figure 3.3: Schematic and mesh of the circulating fluidized bed system

distribution at the inlet (Peng et al., 2010). The gas velocity at the gas inlet is determined as:

$$v_g = \frac{U_g}{\gamma_g}, \quad (3.26)$$

where $\gamma_g = 0.18$ is the opening area ratio of the gas distributor. Solids enter the riser via the returning pipe. The solids velocity at the solids inlet is derived from the following equation:

$$v_s = \frac{G_s A_r}{\rho_p \varepsilon_{s,0} A_{rp}}, \quad (3.27)$$

where $\varepsilon_{s,0} = 0.5$ is the inlet solids holdup, A_r and A_{rp} are the cross-sectional areas of the riser and returning pipe, respectively. The gas velocity at the solids inlet is set to be equal

Table 3.3: Information on CFD model for the CFB riser simulation

Software & Solver	
Software	ANSYS fluent 2022R1
Solver	Two-dimensional, transient
Models	
Multiphase model	Eulerian-Eulerian
Granular temperature model	Ding and Gidaspow (1990)
Granular viscosity & Granular conductivity	Gidaspow (1994)
Granular bulk viscosity & Solids pressure	Lun et al. (1984)
Frictional viscosity	Schaeffer (1987)
Frictional pressure	KTGF
Radial distribution	Lun et al. (1984)
Drag coefficient	Huilin and Gidaspow (2003)
Solvers	
Scheme	Phase coupled SIMPLE
Gradient discretization	Least squares cell based
Pressure discretization	PRESTO!
Momentum discretization	Second order upwind
Volume fraction discretization	Second order upwind
Granular temperature discretization	Second order upwind
Turbulent kinetic energy	Second order upwind
Specific dissipation rate	Second order upwind
UDS discretization	Second order upwind
Residual	5×10^{-5}
Time step [s]	5×10^{-5}

to the solids inlet velocity to ensure the particles flow into the riser column smoothly. The outlet on the top is set as the outflow.

The second method (referred to as Method 2 hereafter) aims to simulate the solids circulating operation in the riser reactor, as shown in Figure 3.4 (b). It uses the same gas inlet boundary conditions as Method 1. However, the solids flux at the solids inlet is set to be equal to the solids flux at the riser outlet. Therefore, the solids flux at the outlet should be monitored in real-time to adjust the solids inlet velocity. The solids velocity at

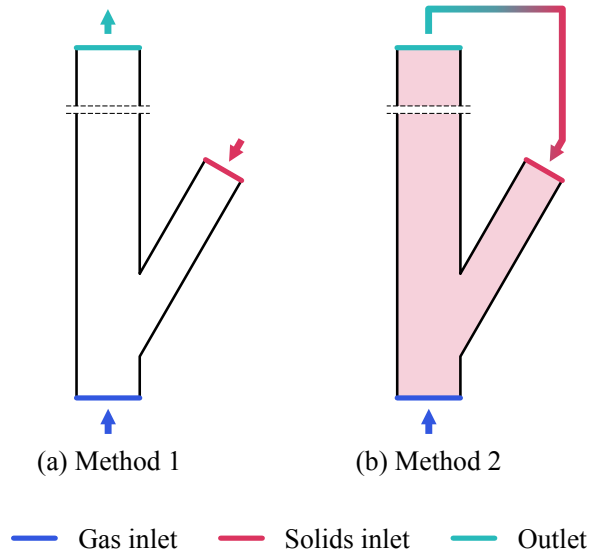


Figure 3.4: Comparison of Method 1 and Method 2

the solids inlet is:

$$v_s(t) = \frac{\dot{V}_{s,\text{outlet}}(t)}{A_{rp}}, \quad (3.28)$$

where $\dot{V}_{s,\text{outlet}}(t)$ is the solids volume flow rate at the outlet of the riser. Due to the absence of external particles entering the system, the solids that circulate in the riser will be pre-packed. According to Wang (2013), the average solids holdup for case of $U_g = 5$ m/s and $G_s = 300$ kg/m²/s is 0.105.

In order to investigate the effects of different turbulence models, specularly coefficients, and methods that mentioned above on the hydrodynamic characteristics and reaction behaviours in the CFB riser reactor, studies of a total of four cases are carried out (as shown in Table 3.4). Other CFD information of the riser simulation is listed in Table 3.5.

Table 3.4: CFB riser case information

Case	U_g [m/s]	G_s [kg/m ² /s]	Turbulence model	Specularity coefficient	Method
Case 1	5	300	Laminar	0.01	1
Case 2	5	300	k - ϵ model	0.01	1
Case 3	5	300	Laminar	0.0001	1
Case 4	5	300	Laminar	0.0001	2

Table 3.5: Parameters used for CFB riser simulations

Physical parameters*		
Friction packing limit		0.54
Packing limit		0.56
Particle-particle restitution coefficient		0.9
Catalytic reaction constant	5.74×10^{-4}	m/s
Mesh information		
Domain size	$76.2 \times 10,200$	mm
Cell length	1.89	mm
Cell number	271,884	

* Other physical parameters are the same as those in Table 3.2.

3.5 Results and discussion

3.5.1 Validation of the reactive transport model

The factors that influence the reaction behaviours in the CFB riser reactor are reaction rate, internal mass transfer, external mass transfer, meso-scale flow structures, and reactor geometry. The apparent reaction constant, measured in the micro fixed-bed reactor, characterizes the effects of reaction rate and internal mass transfer rate. So, the source term in the ozone decomposition reactive transport model that is developed based on the apparent reaction constant can account for the effect of these two factors on the reaction in the CFD simulation.

The flow field in the micro fixed-bed reactor minimizes the effects of factors other than the reaction rate and internal mass transfer rate on the reaction behaviours. Therefore, before simulating the CFB riser reactor, the reaction behaviours in the micro fixed-bed are simulated, and then the numerical results are compared with the experimental data to validate the accuracy of the source term in the developed reactive transport model.

Table 3.6 shows the comparison of numerical results with experimental data under different operating conditions (Liu, 2016; Wang et al., 2014). The absolute percentage errors (APE) of $C_{g,out}^{O_3}/C_{g,in}^{O_3}$ for the numerical results are below 1 % under different operating conditions. Therefore, the reactive transport model using the source term developed based on the apparent reaction constant that obtained through the experiments can accurately predict the reaction of the ozone decomposition in the gas-solids system.

Table 3.6: Comparison of numerical results with experimental data

Case	$C_{g,in}^{O_3}$	Packed ε_s	U_g	k_r	$C_{g,out}^{O_3}$	$C_{g,out}^{O_3}/C_{g,in}^{O_3}$	APE
Unit	ppmv	-	m/s	s^{-1}	ppmv	-	%
Exp. 1*	115.1	0.5	0.1124	4.12	50.70	0.44000	-
Num. 1	115.1	0.5	0.1124	4.12	50.84	0.44170	0.39
Exp. 2**	100.0	0.5	0.57	49.12	9.054	0.09054	-
Num. 2	100.0	0.5	0.57	49.12	9.049	0.09049	0.06

* Data from the work of Liu (2016).

** Data from the work of Wang et al. (2014).

It is noteworthy that only the source term within the reactive transport model has been validated in these simulations. There are complicated interactions between gas and particles in the fluidized bed systems. The external mass transfer, meso-scale flow structures, etc., which affect the reaction behaviours in the reactor are not within the scope of this section.

3.5.2 Time-averaged flow fields and reaction fields in the riser

Figure 3.5 shows the time-averaged profiles of the cross-sectional averaged solids holdup, solids flux, and relative ozone concentration along the axial direction of the CFB riser reactor from both numerical and experimental results. The open-markers represents experimental data from Wang et al. (2014), and the solid lines represent the numerical results in this work. The time-averaged numerical results are calculated by following equations:

$$\bar{\varepsilon}_{s,h}(h) = \frac{1}{t_1 - t_0} \int_{t_0}^{t_1} \left(\frac{1}{d_{rs}} \int_0^{d_{rs}} \varepsilon_s(t, x, h) dx \right) dt, \quad (3.29)$$

$$\bar{F}_{s,h}(h) = \frac{\rho_s}{t_1 - t_0} \int_{t_0}^{t_1} \left(\frac{1}{d_{rs}} \int_0^{d_{rs}} (\varepsilon_s(t, x, h) v_s(t, x, h)) dx \right) dt, \quad (3.30)$$

$$\bar{Y}_{g,h}^*(h) = \frac{1}{t_1 - t_0} \int_{t_0}^{t_1} \left(\frac{1}{d_{rs}} \frac{1}{\bar{\varepsilon}_{g,h_i}(t, h)} \int_0^{d_{rs}} (\varepsilon_g(t, x, h) Y_g^*(t, x, h)) dx \right) dt, \quad (3.31)$$

where d_{rs} donates the diameter/width of the riser, x donates the radial/horizontal direction position, and h donates the axial/vertical direction position. Figure 3.6 and Figure 3.7 depict the radial and axial profiles of the time-averaged solids holdup, particle velocity, and relative ozone concentration at four axial and three radial positions, respectively. The relative ozone concentration is a dimensionless concentration:

$$Y_g^* = \frac{Y_g}{Y_{g,0}}, \quad (3.32)$$

where the $Y_{g,0}$ is the ozone concentration at the inlet. In this study, except for the ozone concentrations in the transport model, all ozone concentrations refer to this dimensionless concentration.

The experimental data indicate that a higher concentration of particles is present within the 0 to 2 m range of the CFB riser, resulting in a dense region at the bottom of the

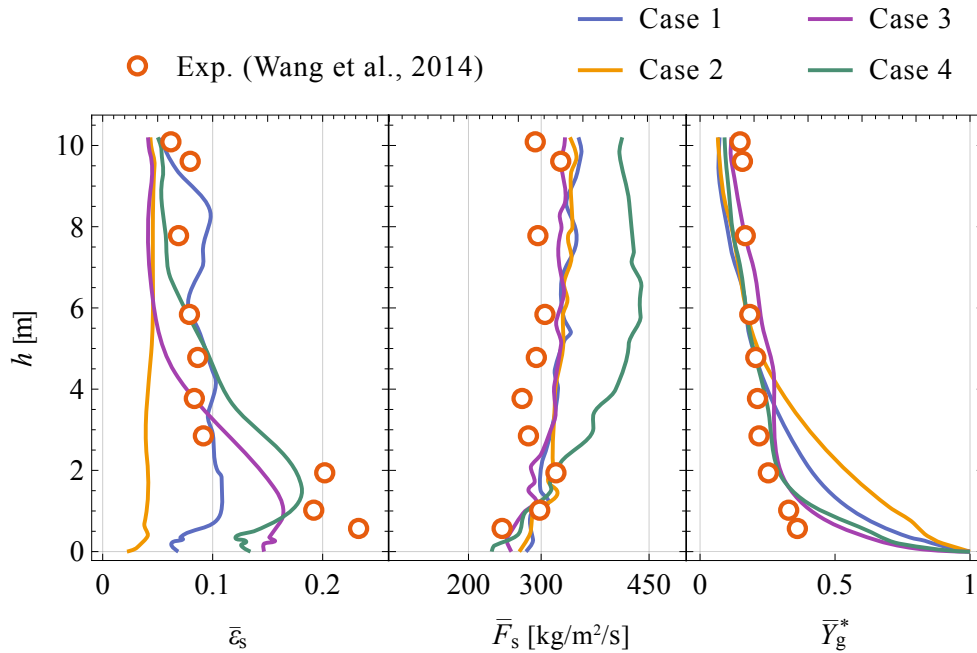


Figure 3.5: Comparison of numerical results and experimental data for cross-sectionally averaged time-averaged profiles along the axial direction

riser. The mean solids holdup within this region is approximately 0.2. These particles are mainly concentrated in the area close to the wall, thus forming the typical core-annulus structure (Ishii & Horio, 1991). The range of the solids holdup in the region above 2 m is observed to be between 0.05 to 0.1, with a slight decrease along the axial direction of the riser. The flux of solids is almost constant (equal to the G_s) along the axial direction of the riser. Approximately 60% of the ozone undergo reaction within 1 m from the inlet, followed by a slight decrease in ozone concentration along the axial direction of the riser from 2 to 10 m.

At the centre of the riser, the velocity of particles can be three times higher than the superficial gas velocity, which is 15 m/s. The solids velocity is close to zero near the wall due to the wall effect. The concentration of ozone decreases along the axial direction at the core region, while remaining a low value close to the wall.

Taking Case 1 as the benchmark, the time-averaged results exhibit a general con-

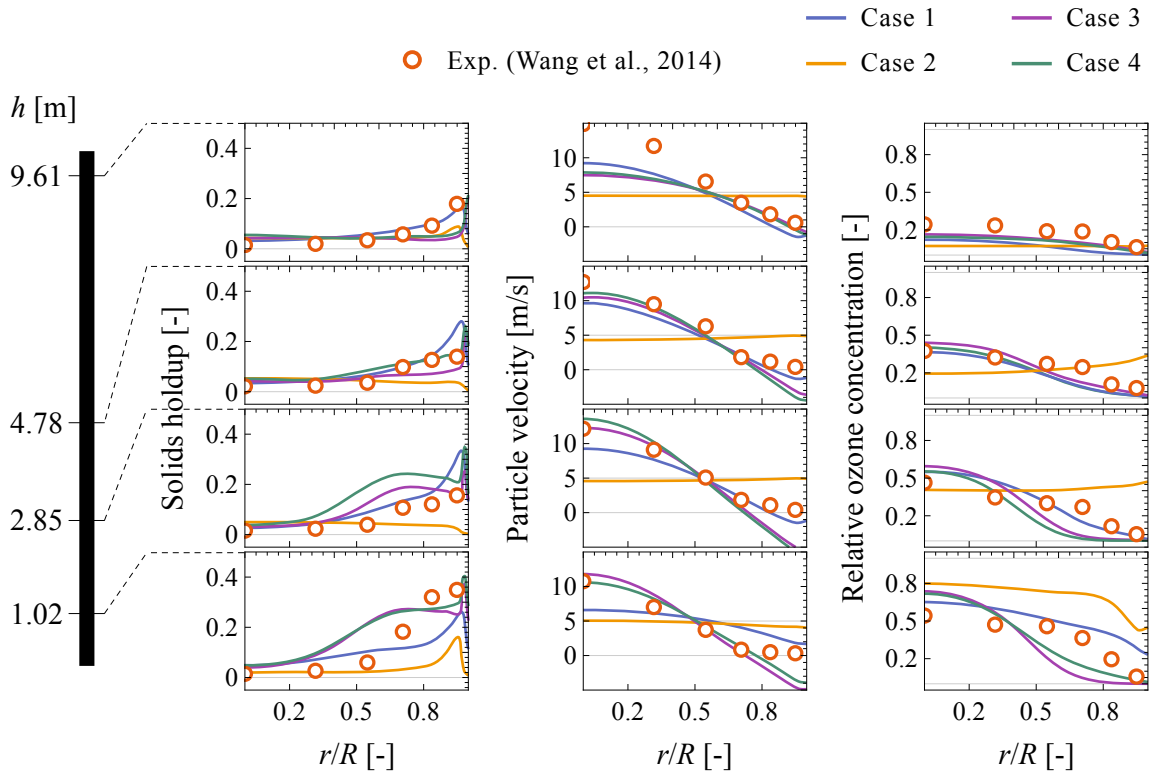


Figure 3.6: Comparison of the time-averaged radial profiles at different axial positions in the riser between the numerical and experimental data

formity with the experimental data. However, there are three differences between the numerical results and the experimental data. First, it is observed that there is no dense region at the riser's bottom from the numerical result. Second, the velocity of particles can only reach twice of the superficial gas velocity in the core region. Third, it is found that the amount of ozone that reacts in the 0 to 2 m region is higher than in the experiments. The third difference can be attributed to fewer particles that appear and participate in the reaction in the bottom region, as indicated by the numerical results.

Effects of the turbulence model The cross-sectional averaged profiles depicted in Figure 3.5 indicate notable differences between results from Case 1 and Case 2, which employ laminar and $k-\epsilon$ turbulence models, respectively. In Case 2, the quantity of particles remaining within the reactor using a turbulence model is merely half of that in the case of using laminar model (Case 1), despite being under the same operating

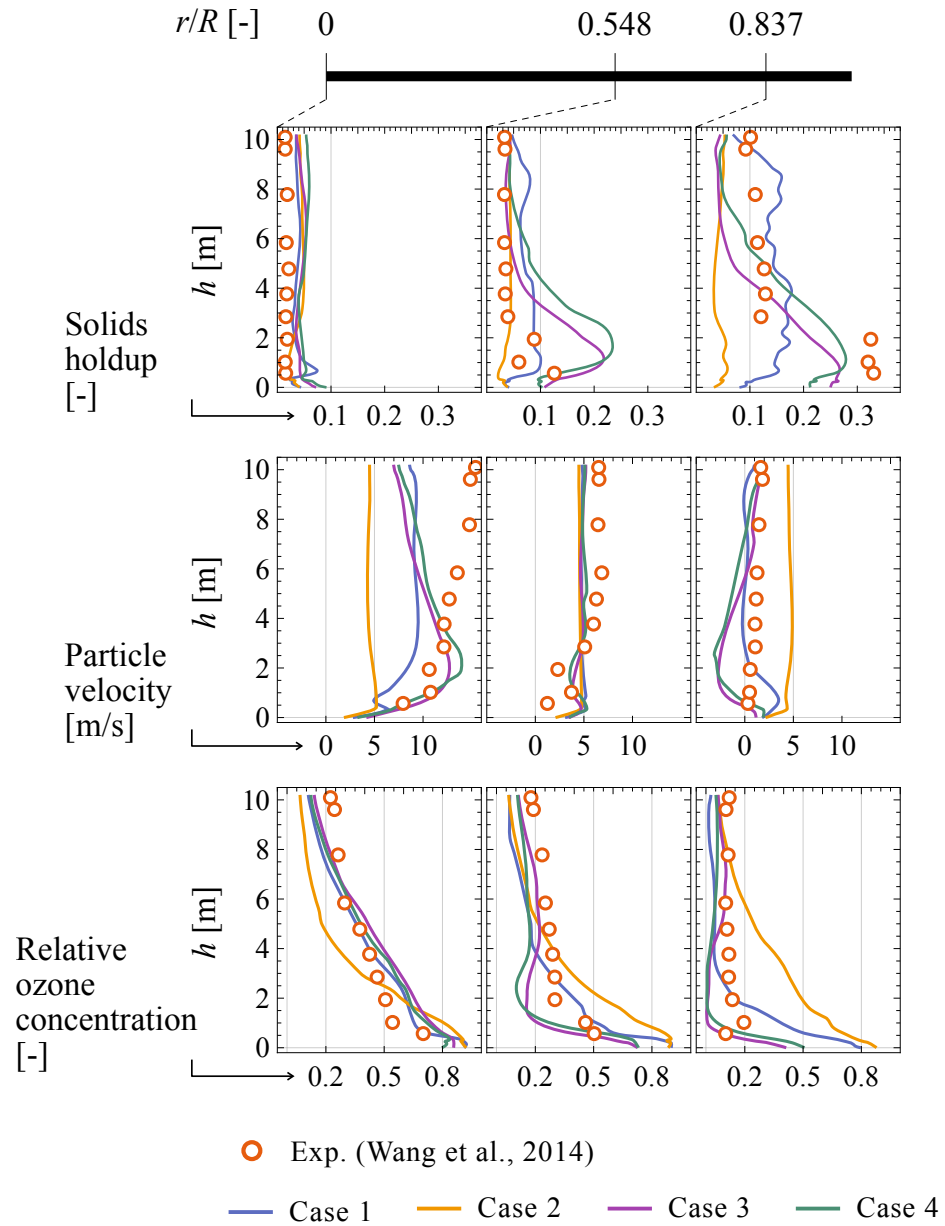


Figure 3.7: Comparison of numerical results and experimental data for the time-averaged axial profiles at different radial positions of the riser

condition. Regarding the reaction behaviours, in the region from 0 to 4 m of the riser, the reaction rate in Case 1 is significantly higher than that in Case 2. However, in the region above 4 m, the ozone concentration profiles exhibit good agreement between both cases, and the residuals of unreacted ozone at the reactor outlet are identical for both cases.

Regarding the detailed flow fields, the radial profiles of Case 2 have uniform distributions of solids and particle velocity, particularly in the region from 2 to 10 m of the riser, as shown in Figure 3.6. The axial profiles depicted in Figure 3.7 can also support the above characteristics in Case 2 — the solids holdup and particle velocity remain constant along the axial direction at different radial positions. These numerical results from the case using the k - ϵ turbulence model do not agree with the experimental data.

Hwang and Eaton (2006) and Vreman (2007) demonstrated that even with a small number of particles in a gas flow (up to 0.015 of solids holdup), the air turbulence intensities strongly reduced in comparison to a no-particle flow in a vertical pipe. In their experiments, the turbulent kinetic energy and dissipation rate for the gas phase are reduced by 35 to 40 % and 40 to 50 %, respectively. However, the numerical results of Case 2 indicates that the turbulence model significantly overestimated the turbulence intensities for the gas phase, resulting in a higher degree of homogeneity in the flow fields throughout the riser. Even though the k - ϵ dispersed model has been modified to account for continuous-dispersed phase, it is still unable to accurately describe the turbulence in the gas phase within the fluidized bed. Therefore, it is not suitable to apply the modified turbulence model for the gas phase in multiphase flows based on the turbulence model for single-phase flows. Not only is the modified k - ϵ model not suitable, but other models developed based on single-phase flows are also not appropriate. After comparing the results of Case 1 and Case 2 with the experiments, it can be concluded that, until there are more accurate modifications of single-phase turbulence models for continuous-dispersed

phase systems or turbulence models specially developed for dense gas-particle systems, the laminar model is a better choice.

Effects of the specular coefficient In this section, the numerical results of Case 1 and Case 3 are compared, where specular coefficients of 0.01 and 0.0001 are used, respectively. The cross-sectional mean profiles in Case 3 are obviously different compared to Case 1. The distribution of the solids holdup along the axial direction is of an S-shape instead of a uniform distribution in Case 1, as shown in Figure 3.5. The solids holdup is up to 0.15 at the region from 0 to 2 m of the riser. The particle concentration decreases gradually from 2 to 6 m, while the solids holdup above 6 m remains constant at 0.05. Such trend of the distribution along the axial direction of the riser is similar to that of the experimental data. However, despite the S-shaped profile of solids holdup observed in Case 3, the total amount of particles in the riser remains the same as in Case 1. Therefore, using a smaller specular coefficient does not lead to a better agreement between the numerical results and experimental data for particle distribution. Instead, it introduces errors to the particle distribution in the previously well-agreed region between 2 to 10 m. Regarding the ozone concentration profiles depicted in the figure, the results from the Case 3 have a better agreement with the experimental data. This can be attributed to the increased number of particles involved in the reaction in the bottom region, resulting in more ozone being reacted at the bottom.

Based on the radial and axial profiles of the solids holdup depicted in Figure 3.6 and Figure 3.7, it can be suggested that the addition of particles in the lower region (0 to 2 m) did not result in a corresponding increase in the solids holdup at the core region. However, it leads to a significant increase in the thickness of the annulus region. The thickness of the annulus is increased from 0.1 to 0.5 times the radius of the riser along the radial direction. In the meantime, the decrease in particles in the upper region (6

to 10 m) results in the disappearance of the core-annulus structure in this region, which is inconsistent from the experimental data. With respect to the particle velocity, it can be observed that particles close to the wall did not remain in a dynamic equilibrium but slide downward along the wall. This is a result of a reduced specular coefficient, which means a smoother wall surface. The particles' downward flow further led to an S-shaped solids holdup profile.

Accordingly, the trends of cross-sectional average profile of the solids holdup and ozone concentration in the numerical results from the case with a lower specular coefficient are observed to be closer to the experimental data. However, the low specular coefficient leads to a worse agreement with the experimental data in the radial distribution of the solids holdup, particle velocity, and ozone concentration.

Effects of Method 1 and 2 According to the effects of the specular coefficient, the trends of the cross-sectional averaged profiles for Case 3 have a better agreement with the experimental data. However, the number of particles in the riser is lower than what appears in the experiment. Thus, Case 4 using the Method 2 is carried out based on Case 3. This is also a strategy widely adopted in many studies to address the issue of a lower number of particles in the riser from numerical results.

In Case 4, according to the experimental data, there is a 25% increase in the pre-packing of particles in the riser compared to the result of Case 3. The solids flux at the solids inlet is adjusted to match the solids flux at the riser's outlet. Therefore, the total solids amount within the riser remains consistent, but the solids circulation rate is uncontrolled.

Case 3 and 4 have the same S-shaped profile of solids holdup along the axial direction of the riser, but the solids holdup is higher in Case 4 than Case 3. As shown in Figure 3.5,

among the results of the four cases, the cross-sectional averaged profile of solids holdup in Case 4 has the best agreement with the experimental data. As for the particle velocity, the profiles are almost the same between Cases 3 and 4. However, due to the increased number of particles presented in the riser in Case 4, the solids flux is higher. According to the results presented in Figure 3.5, the solids flux in Case 4 is 1.5 times that of Case 3.

In general, the operating conditions of a CFB riser are classified based on the superficial gas velocity and the solids flux. From the perspective of this, the case using Method 2 has already placed the riser to a different operating condition because the circulating boundary condition for the solids inlet changes the solids flux in the riser. Therefore, the rationality of employing Method 2 for CFB riser simulations by some researchers is debatable. If for a special research purpose, the study requires a solids holdup distribution from the simulation that is agreed with the experimental data, this method is also acceptable. Additionally, it should be stated that the dense region at the bottom of the riser is formed, in large part, to balance the pressure caused by the particles in the downcomer (Bi & Zhu, 1993). The CFB system is like a U-shaped tube. The pressure from the solids inventory in the downcomer leads to more particles staying in the riser to balance the pressure. However, the total amount of particles in the riser exceeds the carrying capacity of the gas flow, causing more particles to stay at the bottom region of the riser. The solids inventory is intended to achieve a higher solids circulation rate and put the CFB system in a high-density operating regime. The amount of solids inventory depends on the dimensions of the CFB system and the valve opening. This, in turn, can affect the height of the dense region at the bottom of the riser. Therefore, the height of the dense region can change due to different combinations of solids inventory and valve opening or different CFB systems, even under the same operating conditions. Accordingly, the dense region observed in the numerical results from the case using Method 2 may be attributed to the wrong reason, making the rationality of using Method 2 debatable once again.

3.5.3 Effects of instantaneous flow structures on reaction behaviours

The instantaneous contours of Case 1 and Case 2 are depicted in Figure 3.8 (a) and (b), respectively. Each of the depicted figures consists of three contour plots that illustrate the solids holdup, ozone concentration, and reaction rate from 2.8 to 3.3 m in the axial direction of the riser. The results of Case 1 indicate that a higher concentration of particles aggregate in the region near the walls, as shown in Figure 3.8 (a). The particles in the central region of the riser aggregate into streamers and flow upward, reaching velocities up to three times that of the superficial gas velocity. The ozone tends to distribute in the spaces within the riser that are not occupied by particles or are only sparsely occupied by particles. Therefore, it is found to be concentrated in the central region and has a lower concentration near the wall.

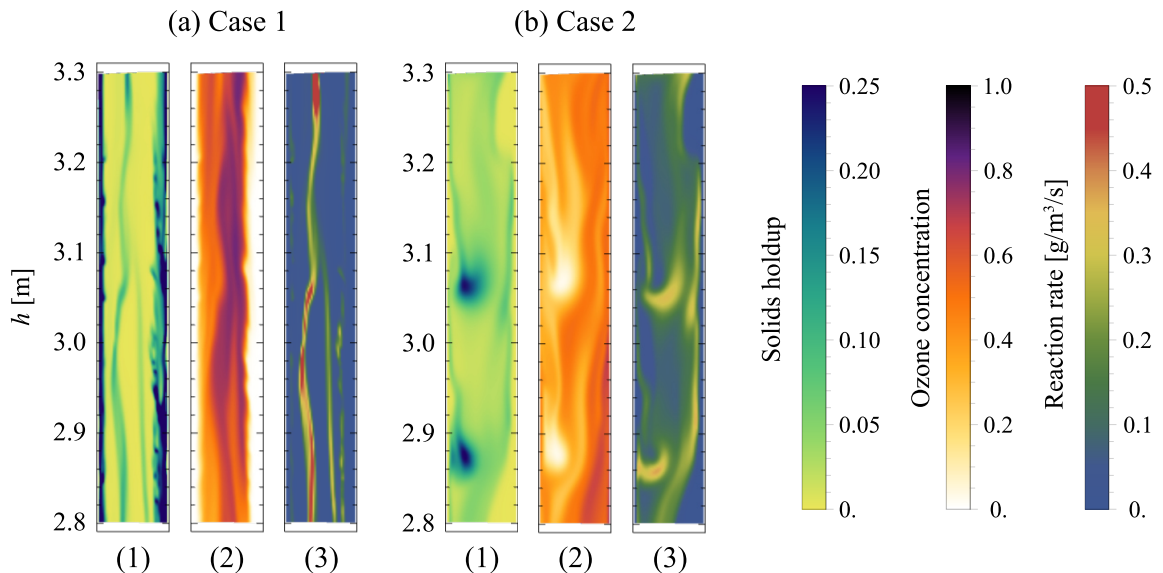


Figure 3.8: Instantaneous flow fields and reaction fields of Case 1 (laminar model) and Case 2 ($k-\epsilon$ turbulence model): (1) solids holdup, (2) ozone concentration, and (3) reaction rate

In the case using the turbulent model depicted in Figure 3.8 (b), the flow structures are different from those in the case using the laminar model. The particles aggregate,

forming spherical clusters with an aspect ratio close to 1. Other spaces in the riser are dilute solids regions. The distribution of ozone in the case using the turbulence model is observed to be more uniform compared to the case using the laminar model. Therefore, in the case using the laminar model, the chemical reaction predominantly occurs in the edge region of the solid streamers and takes place at high rates. This higher rate is attributed to the higher concentration of particles, higher ozone concentration, and higher slip velocity. In the case using the turbulence model, the chemical reaction occurs almost throughout the entire riser at a lower rate.

The spatially averaged solids holdup, ozone concentration, and reaction rate in the region shown in Figure 3.8 (a) and (b) are 0.083, 0.34, and 0.061 for Case 1 and 0.031, 0.40, and 0.098 for Case 2, so, the solids holdup for Case 2 is 38 % lower than Case 1. Despite the lower particle concentration in Case 2, the reaction rate is observed to be 60 % higher than that of Case 1.

The reaction rate (r), contact efficiency (α), and proportions of the reacted ozone (η) are introduced to conduct a more thorough analysis of the reaction behaviours and further explain the differences between the numerical results of the cases using the laminar model and turbulence model. The time-averaged cross-sectional reaction rates are calculated using the following equation:

$$r_h(h) = \frac{1}{t_1 - t_0} \int_{t_0}^{t_1} \left(\frac{1}{d_{rs}} \int_0^{d_{rs}} (k_s a_v \rho_g \varepsilon_s(t, x, h) Y_g(t, x, h)) dx \right) dt. \quad (3.33)$$

The time-averaged cross-sectional reaction rates along the axial direction of the riser for the four cases are plotted in Figure 3.9. The profiles for the four cases shown in the figure are similar—they decrease from 0.23 to 0.02 as the ozone moves from the inlet to the outlet. In the 1 to 4 m region, the reaction rates for the four cases gradually decrease, but the rate of decrease are different, ranging from slowest to fastest in the order of Case 2,

1, 3, and 4. At the height of 4 m, the reaction rates of the four cases are almost the same and remain the almost the same among the cases until the outlet.

The efficiency of gas-solids contact is determined with reference to the ideal plug flow reactor (PFR) and can be expressed as follows:

$$\alpha = -\frac{dY_g}{dh} \frac{U_g}{k_r \varepsilon_s Y_g}. \quad (3.34)$$

The contact efficiency indicates the proportion of the catalyst's external surface area that is accessible to the diffused reactant from the gas phase (Li et al., 2013). Alternatively, this could also be understood as the catalyst utilization efficiency in the CFB riser reactor, assuming that the efficiency in a PFR is 1.0. A decrease in contact efficiency indicates a decline in reactor performance. The gas-solids contact efficiencies along the axial direction of the riser for the four cases are plotted in Figure 3.10. The figure shows the contact efficiency of the four simulation cases at different axial locations in the riser. The coloured horizontal lines indicate the mean contact efficiency for each case. The contact efficiency trends along the riser are similar in the three cases using the laminar model (Cases 1, 3, and 4). However, the contact efficiency for the case using a turbulence model is much higher due to the more uniform flow field.

The variable η represents the proportion of the ozone reacted in each vertical intervals to the total amount of ozone reacted in the riser, which is calculated by the time-averaged ozone concentration:

$$\eta(h) = \frac{\bar{Y}_{g,h}^*(h+1) - \bar{Y}_{g,h}^*(h)}{\bar{Y}_{g,h}^*(10) - \bar{Y}_{g,h}^*(0)}, \quad (3.35)$$

where h is the axial position of the riser. The riser is divided into ten equidistant intervals of one meter each and η for each intervals represents in a rainbow spectrum. Figure 3.11

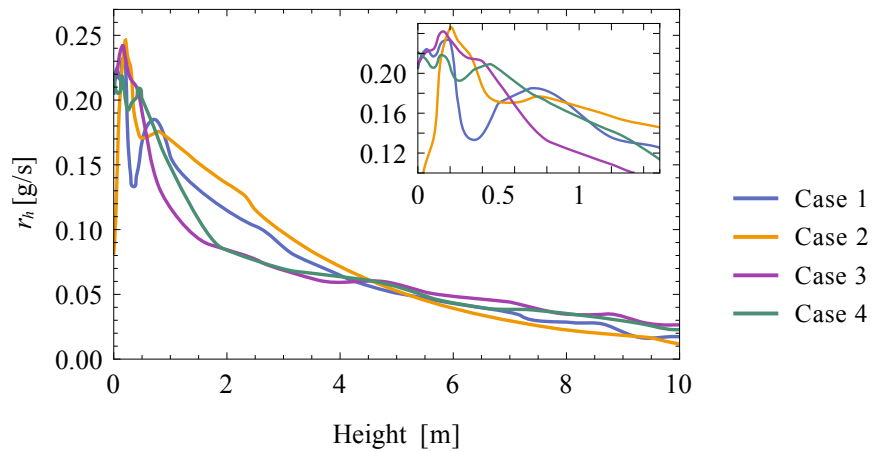


Figure 3.9: Comparison of the cross-sectional averaged reaction rates along the axial direction of the riser for different cases

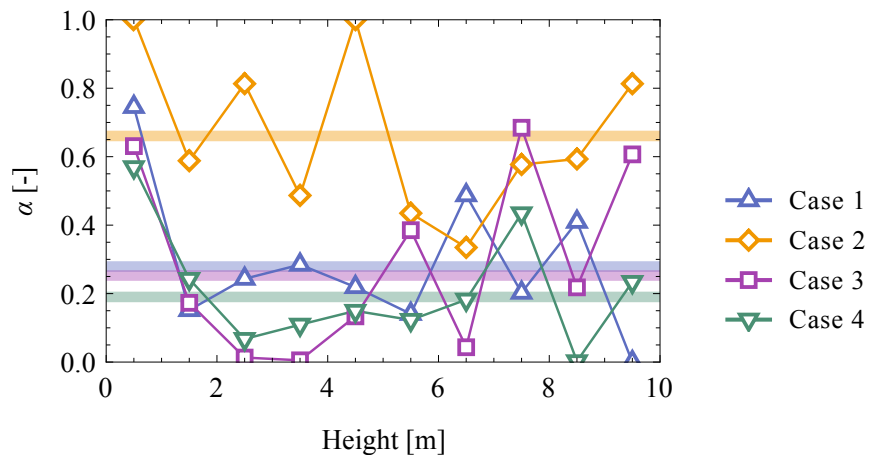


Figure 3.10: Comparison of the contact efficiencies along the axial direction of the riser for different cases

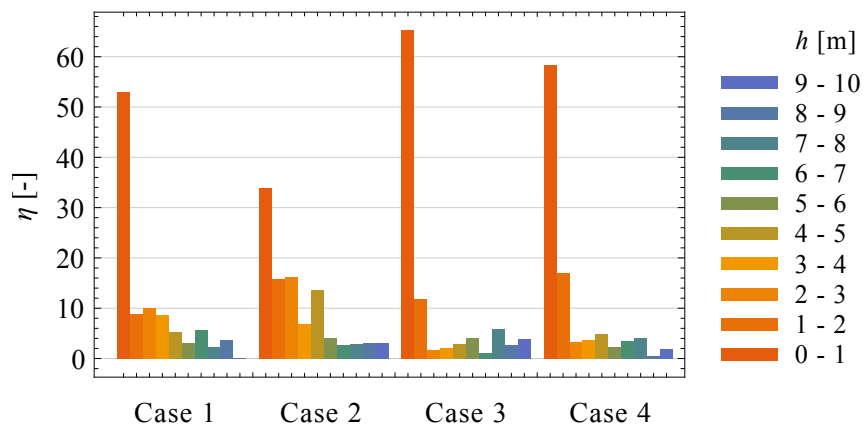


Figure 3.11: Comparison of the proportions of the reacted ozone in the different height intervals of the riser for different cases

shows the proportions of the reacted ozone in the different height intervals of the riser for the four cases.

The highest contact efficiency for Case 1 is approximately 0.8 (see Figure 3.10), which is in the inlet region of the riser. This implies that the catalyst utilization efficiency at the inlet region is very close to that of a PFR. At this location where the concentration of ozone is the highest, the reaction rate is also the highest, as shown in Figure 3.9. According to the results of η presented in Figure 3.11, 53 % of the ozone is reacted in the region from 0 to 1 m of the riser. The higher reaction rate, higher contact efficiency, and higher proportion of the reacted ozone in the inlet region can be attributed to the structure of the gas and solids inlets. As illustrated in Figure 3.3, the particles are introduced into the riser through the returning pipe at a 60° angle relative to the main pipe. When the particles enter the riser, their flow directions are the same as gravity and opposite to the main gas flow direction. Then, the previously introduced particles undergo deceleration due to the gas flow and collide with the particles that entered later. Therefore, in this region, the particles are prone to forming large clusters and are difficult to be quickly carried upward by the upflowing gas. Subsequently, the airflow obstructed by the large cluster disperses the cluster into several smaller clusters and flows away at high speed through the gaps but is shortly obstructed by other clusters. Throughout this process, there is a continuous occurrence of particle clusters being broken and coalesced. The gas flow in this process easily contacts with the particles. This increases the momentum transfer and mixing of the gas and particles in the inlet region, which enhances the gas-particle contact in addition to the high ozone concentration in the inlet region. Therefore, the majority of ozone reactions occur in this region.

The mixing of the gas and solids after the inlet region becomes less, and the segregation between the two phases becomes more distinct. In the region from 1 to 10 m, the

CHAPTER 3. A PSEUDO-HOMOGENEOUS REACTIVE TRANSPORT ...

contact efficiency of Case 1 remains almost constant at about 0.27, and the reaction rate decreases slowly, which is caused by the decrease in the ozone concentration. 33 % of the total reacted ozone is reacted in the region from 1 to 4 m, and 14 % is reacted in the region from 4 to 10 m.

In short, for Case 1, more than half of the ozone is reacted in the region from 0 to 1 m, and the reaction rate and contact efficiency are the highest in this region. This phenomenon is caused by intense gas-solid mixing at the inlet and a higher ozone concentration. In the remaining section of the riser, the reaction rate and contact efficiency are lower, and the amount of reacted ozone is also lower. This is a result of gentler mixing and a lower ozone concentration from 1 to 10 m of the riser.

In contrast to Case 1, a greater proportion of particles is observed to be distributed in the inlet region of the riser in Cases 3 and 4. However, the majority of the additional solids in the region from 0 to 4 m of the riser predominantly contribute to the thickness of the annulus region close to the wall, rather than increasing the probability of contact with the reactant. Therefore, an increase in the amount of solids results in a greater proportion (approximately 80 %) of ozone being reacted in the inlet region of the riser, but the contact efficiency is lower than in Case 1.

The results using the turbulence model (Case 2) exhibit different reaction behaviours. In contrast to the cases using the laminar model, the contact efficiency of Case 2 typically ranges from 0.5 to 0.8, with a mean contact efficiency of 0.66, which is much higher than those in the laminar model cases. Therefore, in Case 2, only one-third of the particles are present in the region from 0 to 4 m of the riser, yet an equivalent amount of reactants (80 %) is reacted. However, while there are differences in the amount of ozone reacted in each interval from 0 to 4 m in Case 2, these differences are not as significant as those observed in cases using the laminar model.

In the region from 6 to 10 m of the riser, although the hydrodynamic characteristics and the contact efficiency differ among the four cases, the profiles of the reaction rate and the proportions of the reacted ozone are almost the same. This is because the ozone concentration is low enough in this region, and the differences in hydrodynamic characteristics and contact efficiency do not have a significant effect on the reaction behaviours.

3.6 Conclusions

The present study involved the development of a pseudo-homogeneous reactive transport equation for the ozone decomposition based on experimental data. The experimental data for a micro fixed-bed reactor were used to validate the reactive transport model. The numerical results and experimental data demonstrated agreement.

Subsequently, the reactive transport model was used for simulations of a 10.2-meter CFB riser reactor. Compared to the cases using the laminar flow, applying a turbulence model to the gas phase resulted in the gas carrying a reduced number of particles in the reactor. The particles have less aggregation, and the distributions of solids holdup and particle velocity in both the axial and radial directions were more uniform than the case of using the laminar model. These homogeneous flow patterns led to a high contact efficiency. The wall boundary condition with a smaller specular coefficient led to a greater tendency for particles to flow downwards along the walls. This resulted in a particle distribution that had a dilute upper region and a dense lower region. Nevertheless, the extra particles led to the thickening of the annulus region rather than direct contact with the reactant, thereby reducing the contact efficiency.

Approximately 50 to 60 % of the ozone underwent its decomposition within the inlet

CHAPTER 3. A PSEUDO-HOMOGENEOUS REACTIVE TRANSPORT ...

region of 0 to 1 m. This can be attributed to the intense mixing of the two phases and the higher ozone concentration at the inlet region. The condition of intense gas-solid mixing can result in a substantial enhancement of contact efficiency, achieving levels up to four times higher than those observed in the upper region where mixing is less pronounced.

References

- ANSYS, Inc. (2022a). Ansys Fluent, Release 2022R1. ANSYS, Inc.
- ANSYS, Inc. (2022b). *Ansys Fluent, Release 2022R1, Help System, Ansys Fluent Theory Guide, Section 14.5.18.1 k- ϵ Turbulence Models*. ANSYS, Inc.
- ANSYS, Inc. (2022c). Ansys SpaceClaim, Release 2022R1. ANSYS, Inc.
- Bi, H., & Zhu, J. (1993). Static instability analysis of circulating fluidized beds and concept of high-density risers. *AIChE Journal*, 39(8), 1272–1280.
- Bird, R. B., Stewart, W. E., Lightfoot, E. N., & Klingenberg, D. J. (2015). *Introductory transport phenomena*. Wiley Global Education.
- Ding, J., & Gidaspow, D. (1990). A bubbling fluidization model using kinetic theory of granular flow. *AIChE journal*, 36(4), 523–538.
- Ergun, S. (1952). Fluid flow through packed columns. *Chemical engineering progress*, 48(2), 89.
- Gidaspow, D. (1994). *Multiphase flow and fluidization: Continuum and kinetic theory descriptions*. Academic Press.
- Gidaspow, D., Bezburuah, R., & Ding, J. (1991). Hydrodynamics of circulating fluidized beds: Kinetic theory approach. *Proceedings of the 7th International Conference on Fluidization, Gold Coast, Australia, 3-8 May 1992*.
- Huilin, L., & Gidaspow, D. (2003). Hydrodynamics of binary fluidization in a riser: Cfd simulation using two granular temperatures. *Chemical engineering science*, 58(16), 3777–3792.
- Hwang, W., & Eaton, J. K. (2006). Homogeneous and isotropic turbulence modulation by small heavy ($St \sim 50$) particles. *Journal of Fluid Mechanics*, 564, 361–393.
- Ishii, H., & Horio, M. (1991). The flow structures of a circulating fluidized bed. *Advanced Powder Technology*, 2(1), 25–36.
- Jiang, P., Bi, H., Jean, R.-H., & Fan, L.-S. (1991). Baffle effects on performance of catalytic circulating fluidized bed reactor. *AIChE journal*, 37(9), 1392–1400.
- Lauder, B. E., Spalding, D. B., et al. (1972). *Lectures in mathematical models of turbulence*.
- Li, D. (2010). *Investigation of circulating fluidized bed riser and downer reactor performance for catalytic ozone decomposition* [Doctoral dissertation, The University of Western Ontario].
- Li, D., Ray, A. K., Ray, M. B., & Zhu, J. (2013). Catalytic reaction in a circulating fluidized bed riser: Ozone decomposition. *Powder technology*, 242, 65–73.

CHAPTER 3. A PSEUDO-HOMOGENEOUS REACTIVE TRANSPORT ...

- Liu, J. (2016). *Reactor performances and hydrodynamics of various gas-solids fluidized beds* [Doctoral dissertation, The University of Western Ontario]. <https://ir.lib.uwo.ca/etd/3967/>
- Lun, C. K. K., Savage, S. B., Jeffrey, D. J., & Chepurniy, N. (1984). Kinetic theories for granular flow: Inelastic particles in couette flow and slightly inelastic particles in a general flowfield. *Journal of fluid mechanics*, *140*, 223–256.
- Peng, B., Zhu, J., & Zhang, C. (2010). Numerical study on the effect of the air jets at the inlet distributor in the gas- solids circulating fluidized-bed risers. *Industrial & Engineering Chemistry Research*, *49*(11), 5310–5322.
- Schaeffer, D. G. (1987). Instability in the evolution equations describing incompressible granular flow. *Journal of differential equations*, *66*(1), 19–50.
- Sinclair, J. L., & Jackson, R. (1989). Gas-particle flow in a vertical pipe with particle-particle interactions. *AIChE Journal*, *35*, 1473–1486. <https://doi.org/10.1002/aic.690350908>
- Sun, Z., Zhang, C., & Zhu, J. (2022). Numerical investigations on gas–solid flow in circulating fluidized bed risers using a new cluster-based drag model. *Particuology*, *63*, 9–23.
- Vreman, A. (2007). Turbulence characteristics of particle-laden pipe flow. *Journal of fluid mechanics*, *584*, 235–279.
- Wang, C. (2013). *High density gas-solids circulating fluidized bed riser and downer reactors* [Doctoral dissertation, The University of Western Ontario]. <https://ir.lib.uwo.ca/etd/1572/>
- Wang, C., Wang, G., Li, C., Barghi, S., & Zhu, J. (2014). Catalytic ozone decomposition in a high density circulating fluidized bed riser. *Industrial & Engineering Chemistry Research*, *53*(16), 6613–6623.
- Wen & Yu. (1966). Mechanics of fluidization. *Fluid Particle Technology, Chem. Eng. Progress. Symposium Series*, *62*, 100–111.
- Zehner, P., & Schlünder, E. (1970). Wärmeleitfähigkeit von schüttungen bei mäßigen temperaturen. *Chemie Ingenieur Technik*, *42*(14), 933–941.

Chapter 4

Comparative study of hydrodynamic characteristics and reaction behaviours in CFB riser and downer via numerical method

4.1 Introduction

Based on Chapter 3, the proper CFD model for a CFB reactor has been developed. In this chapter, the flow and reaction in the CFB riser and downer will be simulated using this CFD model. The numerical results will be compared with the experimental data. The time-averaged hydrodynamic and reaction profiles of the CFB riser and downer will be compared under different operating conditions. The flow structure and reaction behaviours will be compared using instantaneous flow fields and reaction fields. Finally, the residence time distributions of the gas and solids phases will be compared and discussed.

4.2 Numerical models

4.2.1 Two-fluid model

The Eulerian-Eulerian two-fluid model coupling with the kinetic theory for granular flow (KTGF) is used in this study to simulate the gas-solids two-phase flow in fluidization

systems.

Governing equations The mass conservation equations of gas and solids phases are given as:

$$\partial_t (\varepsilon_g \rho_g) + \nabla \cdot (\varepsilon_g \rho_g \vec{u}_g) = 0, \quad (4.1)$$

$$\partial_t (\varepsilon_s \rho_s) + \nabla \cdot (\varepsilon_s \rho_s \vec{u}_s) = 0, \quad (4.2)$$

$$\varepsilon_g + \varepsilon_s = 1, \quad (4.3)$$

where ε is the volume fraction, ρ is the density, and \vec{u} is the velocity of certain phase.

The momentum conservation equations of gas and solids phases are given as:

$$\frac{\partial}{\partial t} (\varepsilon_g \rho_g \vec{u}_g) + \nabla \cdot (\varepsilon_g \rho_g \vec{u}_g \otimes \vec{u}_g) = -\varepsilon_g \nabla P + \bar{\bar{\tau}}_g + \varepsilon_g \rho_g \vec{g} + K_{sg} (\vec{u}_s - \vec{u}_g), \quad (4.4)$$

$$\bar{\bar{\tau}}_g = \varepsilon_g \mu_g \left(\nabla \vec{u}_g + \nabla \vec{u}_g^T \right) + \varepsilon_g \left(\lambda_g - \frac{2}{3} \mu_g \right) \nabla \cdot \vec{u}_g \bar{\bar{I}},$$

$$\frac{\partial}{\partial t} (\varepsilon_s \rho_s \vec{u}_s) + \nabla \cdot (\varepsilon_s \rho_s \vec{u}_s \otimes \vec{u}_s) = -\varepsilon_s \nabla P + \bar{\bar{\tau}}_s + \varepsilon_s \rho_s \vec{g} + K_{sg} (\vec{u}_g - \vec{u}_s), \quad (4.5)$$

$$\bar{\bar{\tau}}_s = \varepsilon_s \mu_s \left(\nabla \vec{u}_s + \nabla \vec{u}_s^T \right) + \varepsilon_s \left(\lambda_s - \frac{2}{3} \mu_s \right) \nabla \cdot \vec{u}_s \bar{\bar{I}},$$

where $\bar{\bar{\tau}}$ is the stress-strain tensor, μ and λ are the shear and bulk viscosity, $\bar{\bar{I}}$ is the unit tensor. K_{sg} is the interphase momentum exchange coefficient between the gas phase and solids phase. As for the solids phase, the solids pressure, p_s , solids shear viscosity, μ_s , and solids bulk viscosity, λ_s , are related to the granular temperature, which is obtained from the kinetic theory of granular flow (Gidaspow, 1994).

Kinetic theory of granular flow The granular temperature of the particles, Θ_s , is related to the kinetic energy of the random motion of the particles (Sinclair & Jackson, 1989) and calculated by

$$\Theta_s = \frac{1}{3} v'_{s\tau} v'_{s\tau}, \quad (4.6)$$

where $v'_{s\tau}$ is the fluctuating solids velocity, which related to the collisions among particles. The equation for the granular temperature derived from the kinetic theory (Gidaspow, 1994) is shown as

$$\begin{aligned} \frac{3}{2} \left[\frac{\partial}{\partial t} (\varepsilon_s \rho_s \Theta_s) + \nabla \cdot (\varepsilon_s \rho_s \vec{u}_s \Theta_s) \right] = & \left(-p_s \bar{\bar{\mathbf{I}}} + \bar{\bar{\tau}}_s \right) : \nabla \vec{v}_s + \\ & + \nabla \cdot (k_{\Theta_s} \nabla \Theta_s) - \gamma_{\Theta_s} + \phi_{gs}, \end{aligned} \quad (4.7)$$

where $\left(-p_s \bar{\bar{\mathbf{I}}} + \bar{\bar{\tau}}_s \right) : \nabla \vec{v}_s$ is the energy generation by the solids stress tensor, $(k_{\Theta_s} \nabla \Theta_s)$ is the diffusion energy, (γ_{Θ_s}) is the collisional dissipation of energy, and (ϕ_{gs}) is the energy exchange between the gas and solids phases. The collisional dissipation of energy is given by Lun et al. (1984), as shown as

$$\gamma_{\Theta_s} = \frac{12 (1 - e_{ss}^2) g_{0,ss}}{d_p \sqrt{\pi}} \rho_s \varepsilon_s \Theta_s^{1.5}, \quad (4.8)$$

where the e_{ss} is the particle-particle restitution coefficient and $g_{0,ss}$ is the radial distribution function of particles. The diffusion coefficient for granular energy, k_{Θ_s} , is given by Gidaspow (1994):

$$\begin{aligned} k_{\Theta_s} = & \frac{150 \rho_s d_p \sqrt{\Theta_s \pi}}{384 (1 + e_{ss}) g_{0,ss}} \left(1 + \frac{6}{5} \varepsilon_s g_{0,ss} (1 + e_{ss}) \right)^2 + \\ & + 2 \rho_s \varepsilon_s^2 d_p (1 + e_{ss}) g_{0,ss} \sqrt{\Theta_s / \pi}. \end{aligned} \quad (4.9)$$

The solids pressure in the solids-phase momentum equation composes of a kinetic term and a particle collision term:

$$p_s = \varepsilon_s \rho_s \Theta_s + 2 \rho_s (1 + e_{ss}) \varepsilon_s^2 g_{0,ss} \Theta_s, \quad (4.10)$$

where e_{ss} is the restitution coefficient for particle collisions and $g_{0,ss}$ is the radial distribution function.

The solids shear stresses in the solids-phase momentum equation are related to the shear and bulk viscosities. The bulk viscosity (Lun et al., 1984) is calculated by:

$$\lambda_s = \frac{4}{3} \varepsilon_s^2 \rho_s d_p g_{0,ss} (1 + e_{ss}) \left(\frac{\Theta_s}{\pi} \right)^{0.5}. \quad (4.11)$$

The shear viscosity contains collisional, kinetic (Gidaspow, 1994), and fractional viscosity (Schaeffer, 1987) are calculated by:

$$\mu_{s,col} = \frac{4}{5} \varepsilon_s \rho_s d_p g_{0,ss} (1 + e_{ss}) (\Theta_s/\pi)^{0.5}, \quad (4.12)$$

$$\mu_{s,kin} = \frac{10 \rho_s d_p \sqrt{\Theta_s \pi}}{96 \varepsilon_s (1 + e_{ss}) g_{0,ss}} \left(1 + \frac{4}{5} g_{0,ss} \varepsilon_s (1 + e_{ss}) \right)^2, \quad (4.13)$$

$$\mu_{s,fr} = \frac{p_{fr} \sin \phi}{2\sqrt{I_{2D}}}. \quad (4.14)$$

Gidaspow drag model Combining the Wen and Yu model (Wen & Yu, 1966) and the Ergun equation (Ergun, 1952) results in the Gidaspow drag model (Gidaspow et al., 1991).

$$K_{sg} = \begin{cases} \frac{3}{4} C_D \frac{\varepsilon_s \varepsilon_g \rho_g |\vec{v}_s - \vec{v}_g|}{d_p} \varepsilon_g^{-2.65}, & \varepsilon_g > 0.8 \\ 150 \frac{\varepsilon_s^2 \mu_g}{\varepsilon_g d_p^2} + 1.75 \frac{\rho_g \varepsilon_s |\vec{v}_s - \vec{v}_g|}{d_p}, & \varepsilon_g \leq 0.8 \end{cases} \quad (4.15)$$

where

$$C_D = \frac{24}{\varepsilon_g Re_s} \left(1 + 0.15 (\varepsilon_g Re_s)^{0.687} \right). \quad (4.16)$$

4.2.2 Reactive transport model for the ozone decomposition reaction

The pseudo-homogeneous reactive transport model for the ozone decomposition reaction that developed in Chapter 3 is used in this study, which is described as:

$$\frac{\partial}{\partial t} (\varepsilon_g \rho_g Y_g^{O_3}) + \nabla \cdot (\varepsilon_g \rho_g \vec{u}_g Y_g^{O_3} - \varepsilon_g \Gamma_g^{O_3} \nabla Y_g^{O_3}) = -k_r \rho_g \varepsilon_s Y_g^{O_3}. \quad (4.17)$$

where $Y_g^{O_3}$ is the mass fraction of ozone in the gas phase.

$$\Gamma_g^{O_3} = \rho_g \mathcal{D}_{O_3,m} \quad (4.18)$$

is the diffusivity of ozone in the air. $\mathcal{D}_{O_3,m}$ is the effective mass diffusion coefficient of ozone in the air (Zehner & Schlünder, 1970),

$$\mathcal{D}_{O_3,m} = \mathcal{D}_{O_3-air} \frac{1 - \varepsilon_s^{1/2}}{\varepsilon_g}, \quad (4.19)$$

where \mathcal{D}_{O_3-air} represents the mass diffusion coefficient of ozone in air. The apparent reaction constant, k_r , is based on the volume of catalysts and measured by Wang (2013).

The above parameters are listed in Table 4.1.

Table 4.1: Parameters used for the CFB riser and downer simulations

Physical parameters		
Gas		Air
Inlet ozone mass fraction	1.6653×10^{-4}	
Diffusion coefficient of ozone*	1.48535×10^{-5}	m ² /s
Particle		FCC
Particle density	1780	kg/m ³
Particle diameter	70	μm
Friction packing limit	0.54	
Packing limit	0.56	
Particle-particle restitution coefficient	0.9	
Apparent reaction constant	49.2	s ⁻¹
Gravitational acceleration	-9.81	m/s ²
Information of domain and mesh		
Riser		
Domain size	$76.2 \times 10,200$	mm
Max cell length	1.89	mm
Cell number	271,884	
Downer		
Domain size	76.2×6000	mm
Max cell length	1.89	mm
Cell number	229,922	
Wall boundary conditions		
Gas		no-slip
Solids		
Specularity coefficient	0.01	
Particle-wall restitution coefficient	0.9	

* The values are calculated based on the method by Bird et al. (2015).

4.3 CFD simulation setups

Figure 4.1 (a) shows the configuration of the CFB system utilized in the works by Wang et al. (2014a, 2015c). This system comprises a 10.2-meter-high riser and a 6-meter-high

downer, both with a diameter of 7.62 cm. In the riser, the solids are introduced into the riser from the returning pipe at the bottom of the riser. The gas is introduced from the bottom of the riser, which conveys the solids to the top of the riser. The solids are subsequently separated from the gas in the cyclone and returned to the riser through the downcomer, storage tank, and returning pipe. In the downer, solids are introduced into the downer from the top and are discharged into the storage tank at the bottom. Gas is introduced from the top of the downer, flowing downward along with the solids. These solids are then channelled into the riser through the returning pipe and lifted to the top of the riser to feed the downer.

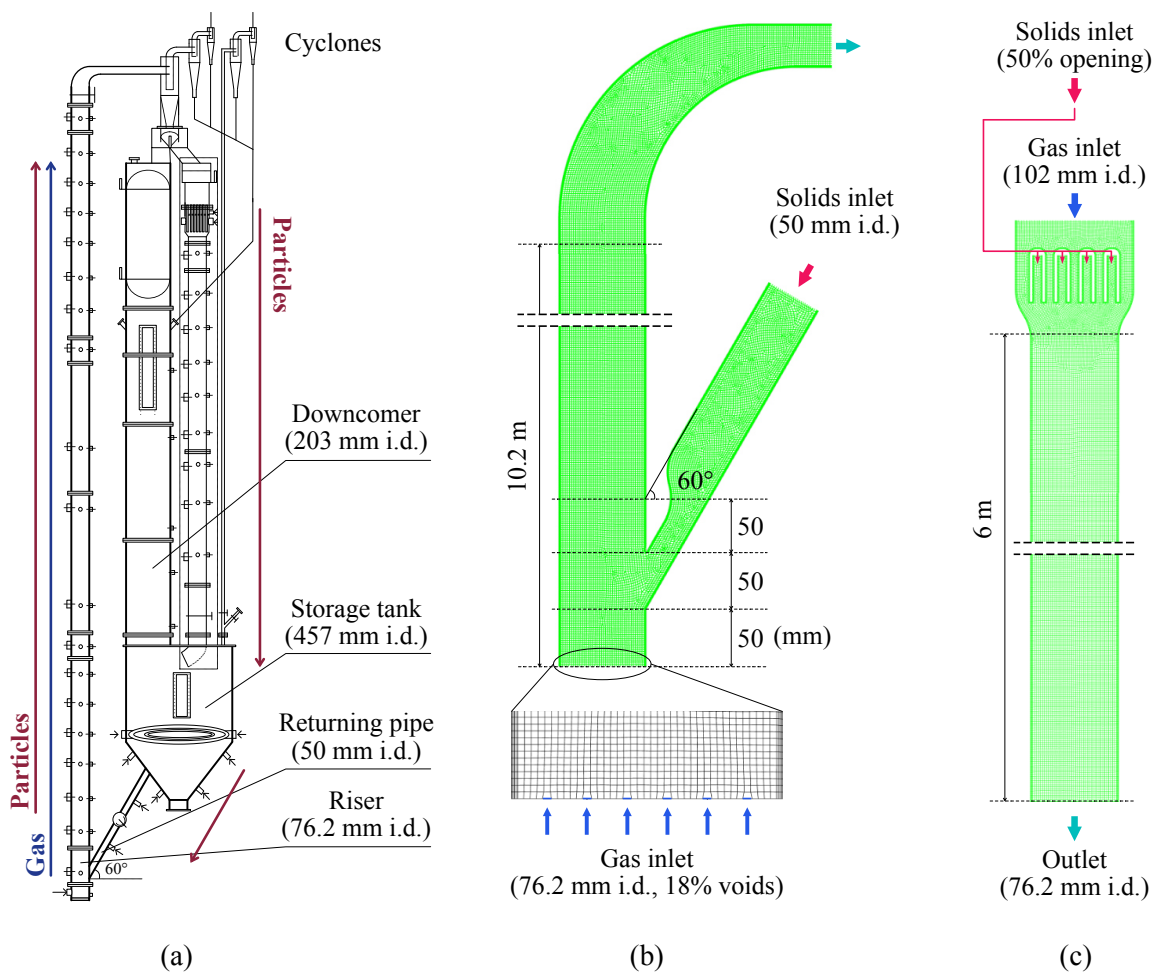


Figure 4.1: Configuration and meshes of the circulating fluidized bed system

4.3.1 Computational domain, mesh and solver

The riser and downer of the CFB system are simplified as two two-dimensional computational domains, as shown in Figure 4.1 (b) and (c), and the domain size for the riser and downer are given in Table 4.1. Unstructured quadrilateral meshes with the max cell size of $27 d_p$ are used for the riser and downer domains. Five-layer refined meshes are used near the wall to capture the boundary layer. The first layer thickness is set to $3 d_p$. The critical parameters of these meshes are consistent with the mesh used in Chapter 3. The meshes are generated by ANSYS Mesh and imported into ANSYS Fluent for the simulations (ANSYS, Inc., 2022). Table 4.2 lists the model and solver information of the simulations.

4.3.2 Boundary conditions

Wall boundary conditions are listed in Table 4.1 for the gas and solids phases. The velocity profiles are used as the inlet boundary condition for both riser and downer, which are based on the superficial gas velocity (U_g) and the solids circulation rate (G_s) from the operating conditions in the experiments.

Riser In the riser, as shown in Figure 4.1 (b), the gas inlet boundary condition is set as a jet velocity profile to consider the influences of the gas distributor in the riser (Peng et al., 2010). In each jet, the gas velocity is uniform, and it is calculated by

$$v_g = \frac{U_g}{\gamma_g}, \quad (4.20)$$

Table 4.2: Information on CFD model for the CFB riser and downer simulations

Software & Solver	
Software	ANSYS fluent 2022R1
Solver	Two-dimensional, transient
Models	
Multiphase model	Eulerian-Eulerian
Granular temperature model	Ding and Gidaspow (1990)
Granular viscosity & Granular conductivity	Gidaspow (1994)
Granular bulk viscosity & Solids pressure	Lun et al. (1984)
Frictional viscosity	Schaeffer (1987)
Frictional pressure	KTGF
Radial distribution	Lun et al. (1984)
Drag coefficient	Huilin and Gidaspow (2003)
Viscous model	Laminar
Solvers	
Scheme	Phase coupled SIMPLE
Gradient discretization	Least squares cell based
Pressure discretization	PRESTO!
Momentum discretization	Second order upwind
Volume fraction discretization	Second order upwind
Granular temperature discretization	Second order upwind
Turbulent kinetic energy	Second order upwind
Specific dissipation rate	Second order upwind
UDS discretization	Second order upwind
Residual	5×10^{-5}
Time step [s]	5×10^{-5}

where γ_g is the opening area ratio of the gas distributor, which is 0.18 for the riser. The inlet velocity for the solids is calculated by

$$v_s = \frac{G_s A_r}{\rho_s \varepsilon_{s,0} A_{rp}}, \quad (4.21)$$

where A_r is the cross-sectional area of the riser, A_{rp} is the cross-sectional area of the returning pipe, and $\varepsilon_{s,0} = 0.5$ is the inlet solids holdup in the riser. The gas velocity at the solids inlet is set to be equal to the solids inlet velocity to ensure that no vortex is formed

in the returning pipe. The outlet at the top is configured as an outflow.

Downer As shown in Figure 4.1 (c), the downer is divided into two parts: the distributor section and the downer section. Four solids inlets are set in the distributor section to consider the effects of the solids feed tubes in the experiments, as shown in Figure 4.2 (b) and (c). The inlet velocity for the solids is calculated by

$$v_s = \frac{G_s}{\rho_s \varepsilon_{s,0} \gamma_s}, \quad (4.22)$$

where $\varepsilon_{s,0} = 0.5$ is the inlet solids holdup in the downer, and γ_s is the opening area ratio for the solids inlet, which is 0.5. The gas inlet boundary condition is set as a uniform

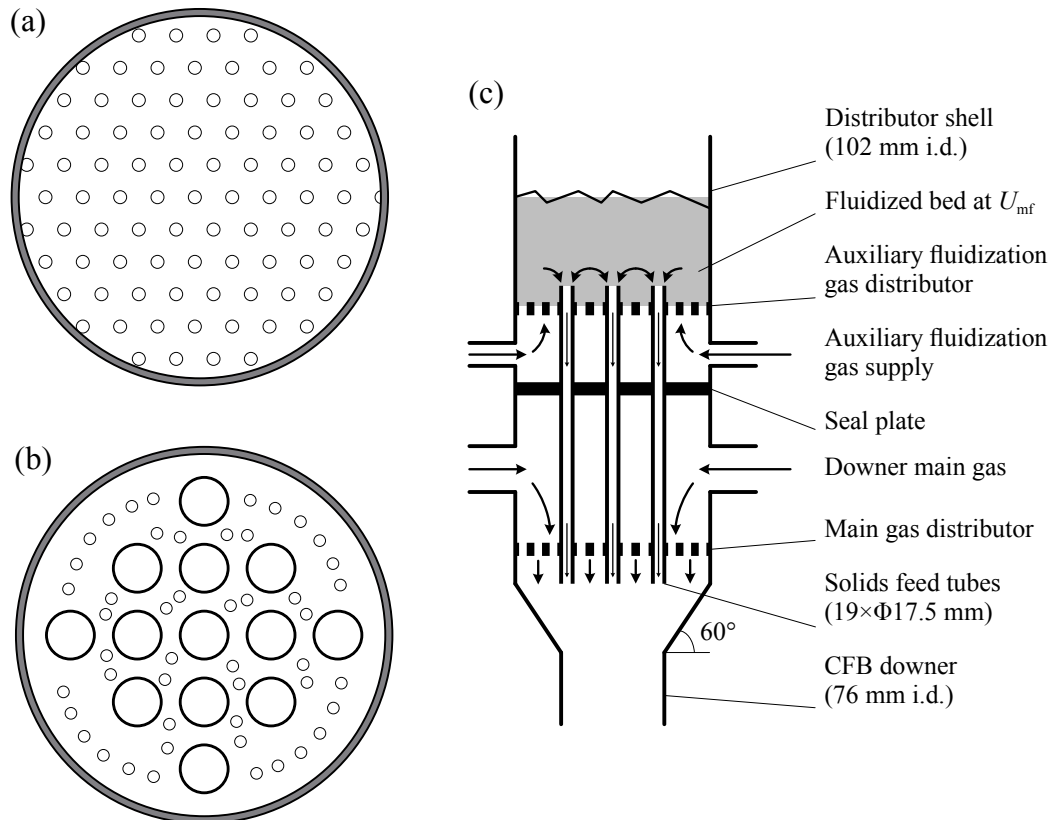


Figure 4.2: Schematic diagram of the gas inlet and solids inlet: (a) gas distributor of the riser (Sun, 2019), (b) gas and solids distributor of the downer (top view) (Johnston et al., 1999; Wang, 2013), (c) gas and solids distributor of the downer (side view) (Wang, 2013)

velocity profile at the top of the distributor section. The gas velocity for the profile is calculated by

$$v_g = \frac{U_g A_r}{A_d}, \quad (4.23)$$

where A_r is the cross-sectional area of the downer, and A_d is the cross-sectional area of the distributor section. After entering the distributor section, the gas flow is divided into five parts by the four solids inlets. The gas flow channels on the left and right sides of the solids inlets are designed to prevent the accumulation of solids in the wall region. To prevent particles from the two solids feed pipes from blocking the gas channel between them, which causes computational divergence, all the gas channels in the distributor sector are consolidated into a single, large passage at the top. This allows the gas to flow downward all the time, rather than getting blocked at the entrance. The outlet at the bottom is set as an outflow.

4.3.3 Setups for the tracers of the gas and solids phases

Residence time distributions, in this study, for both the reactant and catalyst are measured, which requires the development of tracer models in the simulations.

As for the gas phase, a new transport equation for the gas tracer is incorporated into the CFD model. This equation is established based on Equation (4.17) and can be expressed as follows:

$$\frac{\partial}{\partial t} (\varepsilon_g \rho_g Y_g^{\text{tr}}) + \nabla \cdot (\varepsilon_g \rho_g \vec{u}_g Y_g^{\text{tr}} - \varepsilon_g \Gamma_g^{\text{tr}} \nabla Y_g^{\text{tr}}) = 0, \quad (4.24)$$

where Y_g^{tr} represents the mass fraction of the gas tracer within the gas phase. It is important to note that the tracer will not undergo any reaction, hence the reaction term is set to 0 in this equation. Additionally, the physical properties of the gas tracer mirror those of ozone,

and they share the same initial inlet concentration.

For the solids phase, a new transport equation is introduced to trace the particles, and it is given as follows:

$$\frac{\partial}{\partial t} (\varepsilon_s \rho_s Y_s^{\text{tr}}) + \nabla \cdot (\varepsilon_s \rho_s \vec{u}_s Y_s^{\text{tr}}) = 0. \quad (4.25)$$

The reaction term and the diffusion term are both set to 0 in the equation, since the markers on the particles will not undergo any reaction or diffusion. The initial inlet concentration of the solids tracer is set as 1.

Once the flow in the reactor reaches a steady state, the tracers will be introduced into the reactor alongside the gas and solids phases. This injection will be of very short duration, typically lasting for a brief period, e.g., 2×10^{-4} s, in order to achieve a pulse injection. Following the injection, the information about the tracers, including their coordinates, tracer concentrations, solids holdup, as well as gas and solids velocities, will be recorded in each cell. Two heights, 2 m and 5 m from the inlet, are selected as the record locations for the tracers.

4.3.4 Operating conditions and case information

In this study, simulations for four downer cases and two riser cases are carried out, as listed in Table 4.3. They all have the same superficial gas velocity, which is 5 m/s. The solids circulation rates range from 100 to 400 kg/m²/s for the downer cases and from 100 to 300 kg/m²/s for the riser cases. The residence times of the tracers are measured in Case R5300 and D5300, which are the cases with the same U_g and G_s .

Table 4.3: Case information

No.	Case	Type	U_g [m/s]	G_s [kg/m ² /s]	Tracer	Exp. data (flow)	Exp. data (reaction)
1	D5100	downer	5	100	N	Ref. 1	-
2	D5200	downer	5	200	N	Ref. 1	Ref. 2
3	D5300	downer	5	300	Y	Ref. 1	Ref. 2
4	D5400	downer	5	400	N	Ref. 1	-
5	R5100	riser	5	100	N	Ref. 3	Ref. 4
6	R5300	riser	5	300	Y	Ref. 3	Ref. 4

Ref. 1: (Wang et al., 2014a), (Wang et al., 2015a), and (Wang et al., 2015b)

Ref. 2: (Wang et al., 2014a) and (Wang et al., 2015c)

Ref. 3: (Wang et al., 2014c), (Wang et al., 2014d), and (Wang et al., 2015b)

Ref. 4: (Wang et al., 2014b) and (Wang et al., 2015c)

4.4 Results and discussion

4.4.1 Time averaged flow and reaction profiles under different operating conditions

Cross-sectional profiles Figure 4.3 and Figure 4.4 shows the time averaged cross-sectional axial profiles for the solids holdup, solids flux, and ozone concentration in the riser and downer, respectively. The points in the figures are the experimental results and the lines are the numerical results. The time averaged values are calculated by

$$\bar{\varepsilon}_{s,h}(h) = \frac{1}{t_1 - t_0} \int_{t_0}^{t_1} \left(\frac{1}{d_{rs}} \int_0^{d_{rs}} \varepsilon_s(t, x, h) dx \right) dt, \quad (4.26)$$

$$\bar{F}_{s,h}(h) = \frac{\rho_s}{t_1 - t_0} \int_{t_0}^{t_1} \left(\frac{1}{d_{rs}} \int_0^{d_{rs}} (\varepsilon_s(t, x, h) v_s(t, x, h)) dx \right) dt, \quad (4.27)$$

$$\bar{Y}_{g,h}^*(h) = \frac{1}{t_1 - t_0} \int_{t_0}^{t_1} \left(\frac{1}{d_{rs}} \frac{1}{\bar{\varepsilon}_{g,h_i}(t, h)} \int_0^{d_{rs}} (\varepsilon_g(t, x, h) Y_g^*(t, x, h)) dx \right) dt, \quad (4.28)$$

where d is the diameter/width of the riser or downer, x is the position in the radial/horizontal direction, and h is the position in the axial/vertical direction. The ozone concentration shown in Equation (4.28) is the relative ozone concentration, which is given by

$$Y_g^* = \frac{Y_g}{Y_{g,0}}, \quad (4.29)$$

where $Y_{g,0}$ is the inlet ozone concentration.

In the riser reactor, the operation at $U_g = 5$ m/s and $G_s = 100$ kg/m²/s is categorized as being in the low-density flow regime, while the operation at $U_g = 5$ m/s and $G_s = 300$ kg/m²/s is categorized as being in the high-density flow regime (Sun & Zhu, 2019). As shown in Figure 4.3 (a), the predicted solids holdup profile of a low-density flow case, R5100, has a good agreement with the experimental data in the riser. However, in the results of a high-density flow case, R5300, the solids holdup is approximately 50 % lower than the experimental data in the flow developing region (0 to 2 m). These differences are attributed to the pressure exerted by the solids inventory in the storage tank and downcomer during experimental operations. In the experiments, achieving a high-density operation requires a larger quantity of solids inventory, which is not considered in the simulation. With U_g held constant, as G_s increases in the riser, additional particles tend to accumulate more in the flow developing region. This leads to an increase in difference of the solids holdup in the flow developing region compared to the flow developed region when G_s is increased.

In the downer, the region from the inlet to 2 m can be considered as the flow developing region, where particles are accelerated to the same velocity as the gas flow. Hence, the solids holdup in this region is higher than in the flow developed region (2 to 5 m). In the flow developed region, the solids holdup remains relatively constant, as shown in Figure 4.4 (a). In the downer, the increase in G_s while U_g remains the same

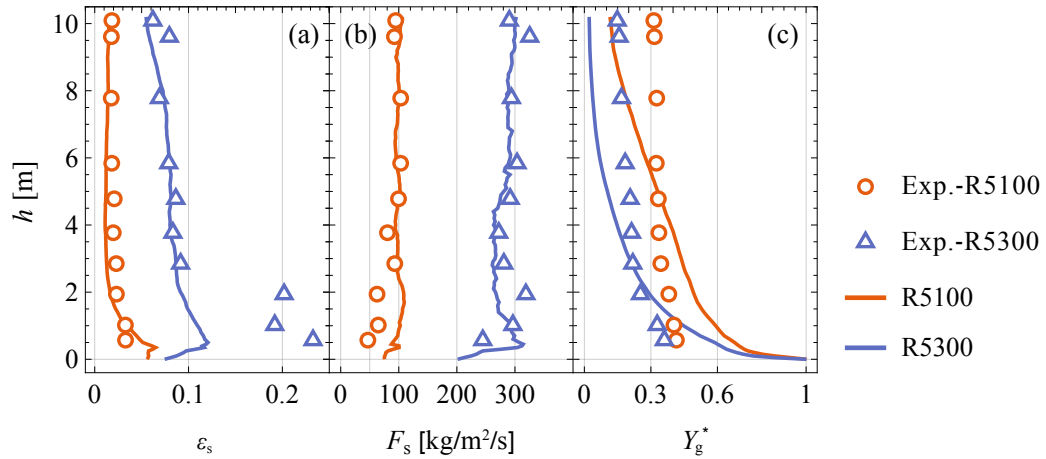


Figure 4.3: Comparison of numerical and experimental results for cross-sectionally averaged time-averaged profiles along the axial direction in the riser for the cases of R5100 and R5300

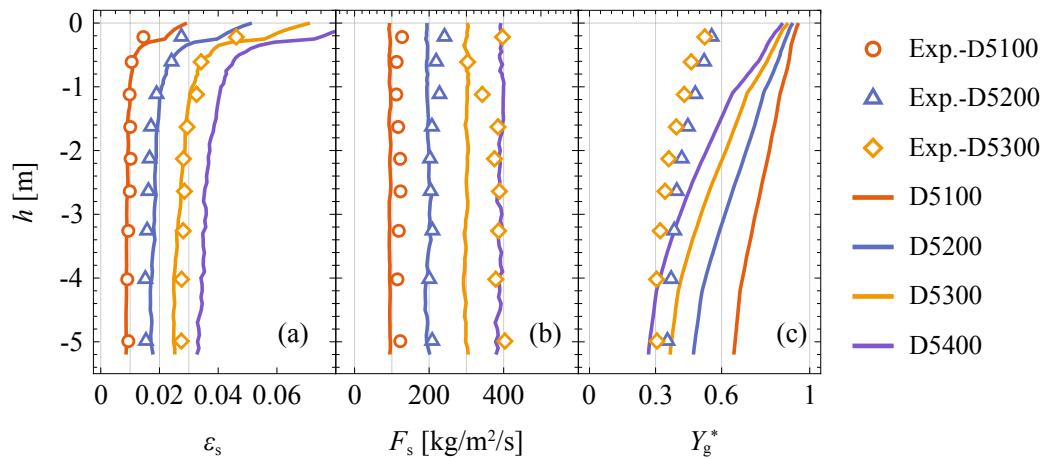


Figure 4.4: Comparison of numerical and experimental results for cross-sectionally averaged time-averaged profiles along the axial direction in the downer for the cases of D5100, D5200, D5300, and D5400

results in an even increase in solids holdup at each height. Therefore, increasing G_s does not significantly alter the shape of solids holdup profiles in the downer, but it increases the values of solids holdup.

As shown in Figure 4.3 (b) and Figure 4.4 (b), whether in the riser or downer, the solids flux is basically equal to G_s at various locations along the axial direction and is also in good agreement with the experimental data. The difference is that the fluctuation of the solids flux profile in the riser is slightly larger than in the downer.

As illustrated in Figure 4.3 (c), the time-averaged cross-sectional profiles of ozone concentration for the riser cases exhibit an exponential shape. In the axial direction, the ozone concentration decreases dramatically in the flow developing region and gradually slows down in the flow developed region. Compared to the riser, the decrease in ozone concentration at the inlet region of the downer is less pronounced, as shown in Figure 4.4 (c). However, the rate of decrease in the region after the inlet in the downer is approximately the same as in the riser. Overall, the ozone concentrations decrease in the reactor with increasing G_s in both the riser and downer, but the shape of the ozone profiles remains almost the same. When compared to the experimental data, the simulation results exhibit greater reductions in ozone along the axial direction of the reactors.

Radial profiles Figure 4.5 shows the time-averaged radial profiles for the riser and downer cases at the flow developing region ($h = 1$ m from the inlet) and flow developed region ($h = 5$ m from the inlet). The results plotted are from Cases R5100 and R5300 with dotted lines, and Cases D5100 and D5300 with solid lines. x/R is the normalized radial position from the centre to the wall.

Figure 4.5 (a) shows the radial profiles of the solids holdup of the four cases at $h = 1$ m and $h = 5$ m. In the flow developing region ($h = 1$ m), the radial distributions for

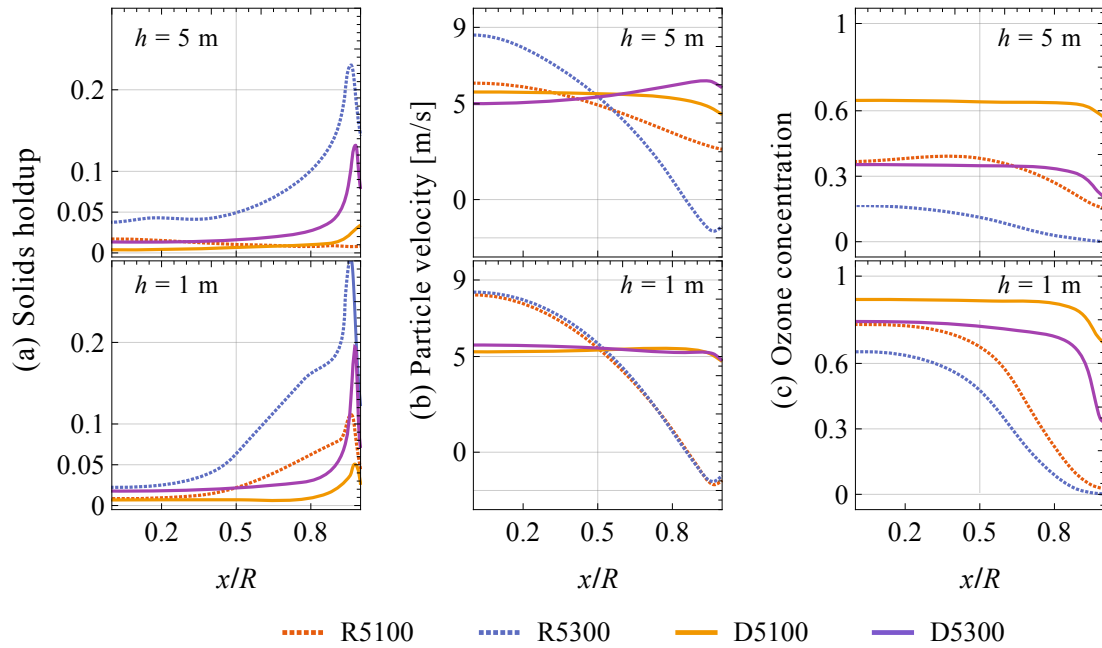


Figure 4.5: Time-averaged radial profiles of the riser and downer cases at the flow developing region and flow developed region

both riser and downer have a lower particle concentration in the central region and a higher concentration near the wall, which is a typical core-annulus structure. In the downer, the boundary between the core and annulus region is located at approximately $x/R = 0.8$. As G_s increases, the solids holdup increases, but the location of the core-annulus boundary does not change. In the riser, however, with the increase in G_s , the thickness of the annulus region increases, and the location of the core-annulus boundary move to around $x/R = 0.5$.

In the flow developed region ($h = 5$ m), the particle distribution in the radial direction becomes more uniform compared to the flow developing region, as shown in Figure 4.5 (a). The core-annulus structure in both the riser and downer significantly weakens at $G_s = 100 \text{ kg/m}^2/\text{s}$. Compared to the results of the cases with a low G_s , the difference in solids holdup between the core and annulus regions in both the riser and downer narrows at $G_s = 300 \text{ kg/m}^2/\text{s}$, but a noticeable core-annulus structure still exists. Furthermore, as G_s

increases, the riser demonstrates a stronger particle containment capacity than the downer in the flow developed region, which leads to a higher solids holdup in the riser than in the downer at the same operating conditions.

There are significant differences in the radial profiles of the particle velocity between the riser and downer, as shown in Figure 4.5 (b). In the flow developing region, changes in G_s do not affect the distribution of particle velocity in the radial direction. The dominant factors here are the gas inlet profile and the direction of particle flow. In the riser, particles near the wall flow downward, causing the gas in this region to flow downward as well. To maintain a constant gas volume flow rate, the gas velocity in the central region increases, resulting in an increase in the particle velocity in the central region. For these reasons, the particle velocity in the riser can differ by over 10 m/s between the central and wall regions, roughly about twice of U_g . In the downer, the situation is much simpler: particles flow downward together with gas due to gravity. More particles are accumulated in the wall region, which are more affected by gravity, counteracting the deceleration caused by wall friction. Consequently, the average particle velocity in the radial direction is the same and equals U_g .

In the flow developed region, the radial profile of the particle velocity in the high-density riser remains the same as in the flow developing region. Conversely, in the low-density riser, the profile becomes flatter due to a decrease in solids holdup near the wall, and the particles near the wall no longer flow downward. This difference in the particle movement is also a contributing factor to the accumulation of more particles in the flow developing region of the high-density riser. As for the downer, in comparison to the profiles in the flow developing region, there are no significant variations in the distribution of particle velocity in the radial direction.

The radial distribution of ozone concentration is largely dependent on the distribution

of the solids holdup, as shown in Figure 4.5 (c). In the flow developing region, there are more particles present in the annulus of the riser. As a result, the ozone concentration remains constant in the core region and then sharply decreases to 0 in the near wall region. In the downer, the ozone concentration can remain constant in the core region, but the core region is much bigger than that in the riser.

In the flow developed region, the ozone profiles for the four cases are similar. However, the ozone distributions in the downer are more uniform than those in the risers, as the solids holdups in the downer are more uniform compared to the risers.

Axial profiles Figure 4.6 shows the time-averaged axial profiles for the riser and downer cases at the central region ($x/R = 0$) and wall region ($x/R = 0.9$). The results plotted are from Cases R5100 and R5300 with dotted lines, and Cases D5100 and D5300 with solid lines. The vertical coordinate in each subfigure represents the axial position from inlet to 5 m. For the purpose of comparing the differences between the riser and downer, the numerical results for the riser have been limited to the region of 0 to 5 m, and the results for the region of 5 to 10.2 m have not been included in the figure.

In the central region, the solids holdups for both the riser and downer are very uniform along the axial direction, and the solids holdup values for the four different cases are also quite close. In the region near the wall, the solids holdup for the downer does not vary significantly along the axial direction. However, in the riser, the solids holdup in the bottom region is noticeably higher than in the upper region. In terms of particle amount, more particles are accumulated near the wall in the riser than the downer.

As for the particle velocity, in the downer, whether in the region near the centre or the wall, the particle velocity is approximately equal to U_g along the axial direction, except for close to the inlet. However, in the riser, there is a significant difference in particle velocity

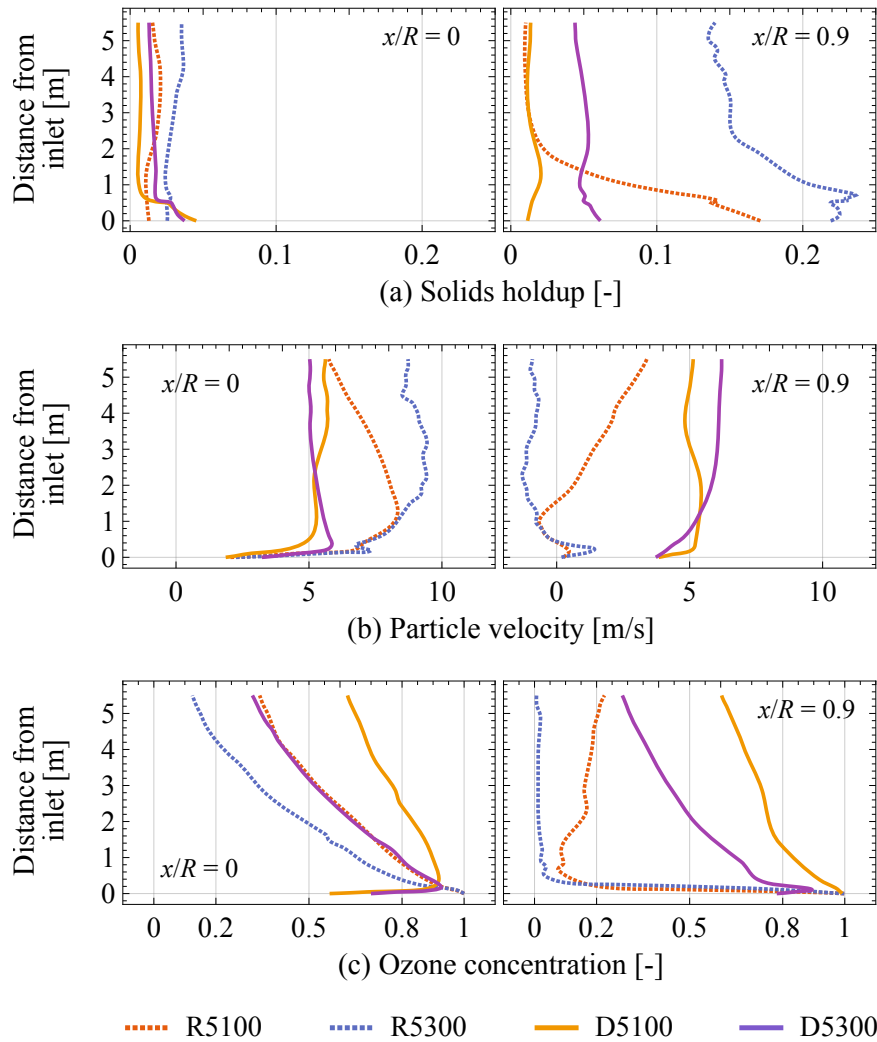


Figure 4.6: Time-averaged axial profiles of the riser and downer cases at the central region and wall region

between the central region and the wall region. In the high-density riser, particles near the wall have negative velocities. In the central region, particles undergo acceleration in the 0 to 2 m range, and their final velocity remains close to $2U_g$. In the low-density riser, the particle velocity profiles in the 0 to 2 m range is similar to those in the high-density riser, but in the region above 2 m, the particle velocity gradually approaches U_g . These characteristics are also reflected in Figure 4.5 (b).

The distribution of the ozone concentration along the axial direction in the central

region and the wall region is greatly influenced by the distribution of the solids holdup. In the downer, the profiles in both the wall and central regions are similar: ozone concentration decreases steadily along the axial direction. In the riser, in the central region, the profile is similar to that in the downer, but in the region near the wall, ozone concentration rapidly decreases within the 0 to 1 m range, and then it does not change much.

4.4.2 Instantaneous flow fields and reaction fields

Figure 4.7 displays the instantaneous contours of solids holdup, slip velocity, ozone concentration, and reaction rate in both the riser and downer. The plotted numerical results are obtained from the cases of riser (R5300) and downer (D5300), with the same operating conditions. The contours are divided into two parts: one for the flow developing region (0.5 to 1.5 m from the inlet) and another for the flow developed region (4 to 5 m from the inlet). To compare the differences in the flow field and reaction field between the riser and downer, the same scales are used for both the riser and downer.

Table 4.4 lists the mean value, standard deviation (S.D.), maximum value, and minimum value of the four variables in the flow developing region and flow developed region for the riser and downer, respectively.

Solids holdup distributions Although the operating conditions for the riser and downer are the same at $U_g = 5$ m/s and $G_s = 300$ kg/m²/s, the particles in the riser move against the direction of gravity, while in the downer, they move in the direction of gravity. Therefore, there are significant differences in the particle distribution between the riser and the downer. In the flow developing region, the amount of particles in the riser is approximately three times that of the downer, and in the flow developed region, it is about twice as much. This phenomenon is also reflected in Figure 4.5 (a). Additionally, there is a noticeable accumulation of particles in the flow developing region of the riser compared

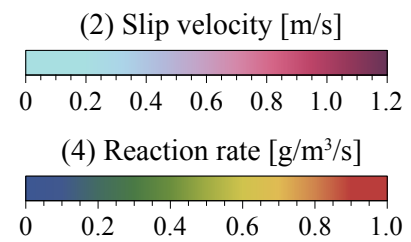
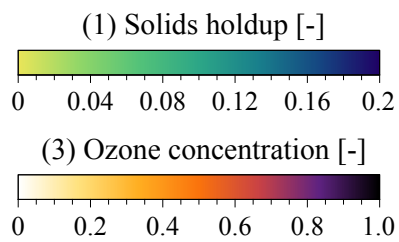
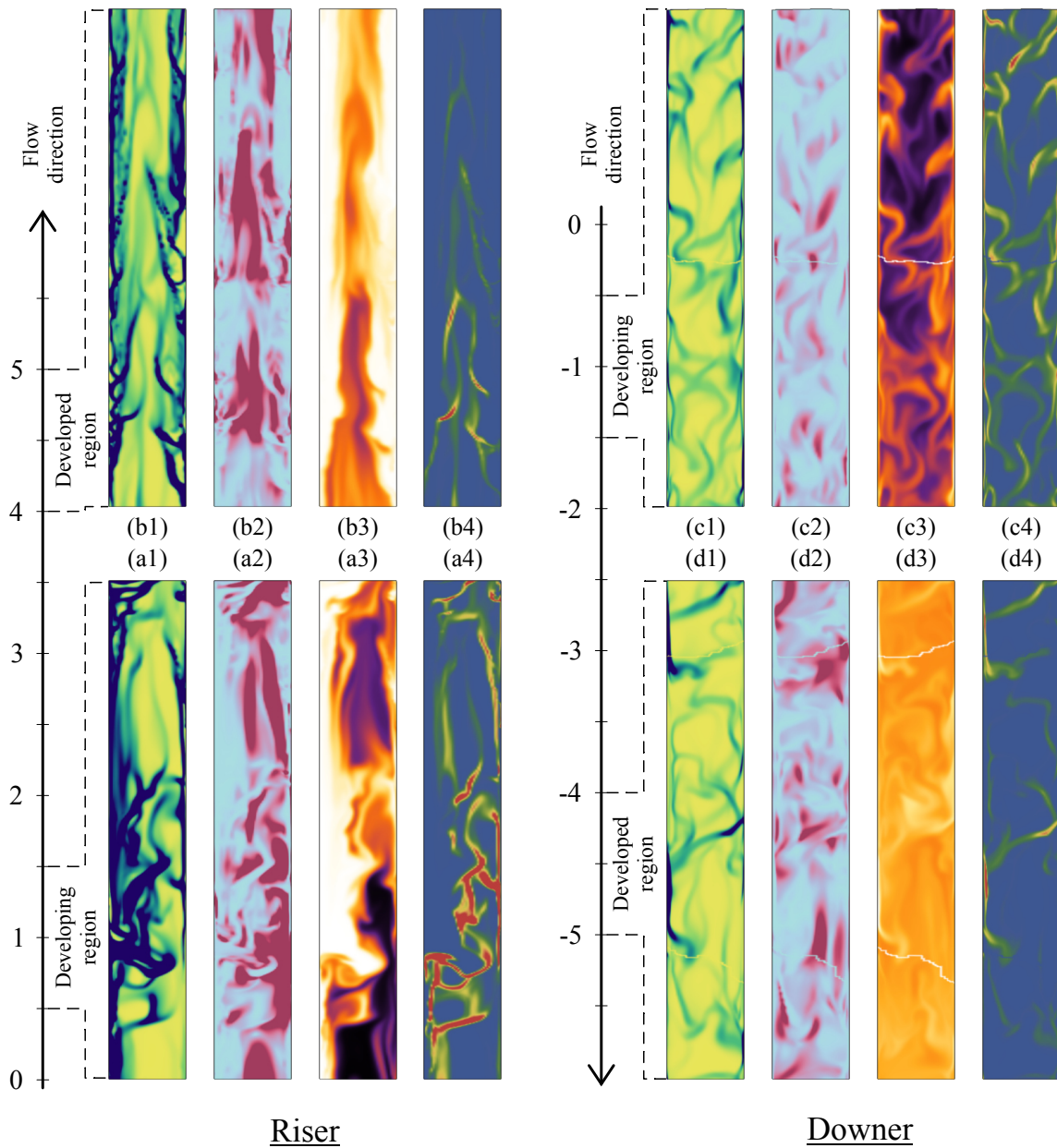


Figure 4.7: Contours of the instantaneous flow fields and reaction fields of the riser and downer

Table 4.4: Statistical results for the flow developing and developed regions in the instantaneous contours

Feature	Reactor type	Mean	S.D.	Max	Min
Developing region (0.5 to 1.5 m from the inlet)					
Solids holdup	Riser	0.159	0.171	0.56	0.0
	Downer	0.0479	0.0699	0.539	0.0
Slip velocity [m/s]	Riser	0.844	1.66	24.86	0.00077
	Downer	0.235	0.227	1.63	0.0
Ozone concentration	Riser	0.405	0.348	0.996	0.0
	Downer	0.658	0.206	0.982	0.0
Reaction rate $\left[\frac{\text{g}}{\text{m}^3\text{s}} \right]$	Riser	0.229	0.312	2.16	0.0
	Downer	0.208	0.197	1.27	0.0
Developed region (4.0 to 5.0 m from the inlet)					
Solids holdup	Riser	0.112	0.132	0.56	0.0
	Downer	0.0445	0.0915	0.558	0.0
Slip velocity [m/s]	Riser	0.648	0.92	9.07	0.00076
	Downer	0.392	0.353	2.37	0.0
Ozone concentration	Riser	0.185	0.217	0.744	0.0
	Downer	0.324	0.0818	0.470	0.0
Reaction rate $\left[\frac{\text{g}}{\text{m}^3\text{s}} \right]$	Riser	0.0745	0.111	1.29	0.0
	Downer	0.100	0.138	1.21	0.0

to the flow developed region, while this phenomenon is not observed in the downer. This phenomenon is also reflected in Figure 4.3 (a) and Figure 4.4 (a).

In both the riser and the downer, particles tend to aggregate and cluster but in different characteristics. In the riser, the clusters have a higher solids holdup and tend to be upright, as shown in Figure 4.7 (a1) and (b1). In the downer, the clusters are not as compact as those in the riser and tend to orient in various directions rather than maintaining an upright state, as shown in Figure 4.7 (c1) and (d1). Therefore, in the riser, the maximum solids holdup can often reach the packing limit of the particle, while this is not observed in the downer. Additionally, the standard deviation indicates that the solids holdups in the downer are distributed more closely around their mean solids holdup, whereas in the

riser, they are distributed much further from the mean value. The difference between the standard deviation of the solids holdup in the riser and downer indicates the downer has a more uniform particle distribution than the riser. Further more, in the radial distribution, dense clusters in the riser tend to accumulate in the wall region, while in the downer, the clusters are distributed more evenly, which leads to a more severe gas-solids segregation in the riser than in the downer.

Slip velocity distributions In the riser, the slip velocity between gas and particles is higher than that in the downer. To counteract the effect of gravity, particles in the riser tend to form dense and upright clusters that gas flow struggles to penetrate. As a result, gas tends to rapidly pass through the spaces between these clusters, leading to large slip velocities in the regions near the boundary of the bulk gas phase and clusters, as shown in Figure 4.7 (a2) and (b2). In the downer, the slip velocity is much lower compared to the riser. Gas also tends to pass between clusters but can also penetrate them, which results in clusters being more sparsely distributed. Moreover, since the particle motion direction aligns with gravity, clusters are more inclined to flow along with the gas, as shown in Figure 4.7 (c2) and (d2). Consequently, gas in the downer tends to flow along with the particles, unlike in the riser where it avoids them, resulting in lower slip velocities in the downer.

In the flow developing region, the maximum slip velocity in the riser is about five times of U_g , while in the downer, it is only about $1/3$ of U_g , as shown in Table 4.4. In the flow developed region, most particles in the riser have been sufficiently accelerated, leading to a decrease in slip velocity. In contrast, in the downer, particle velocity have already surpassed the gas velocity, causing an increase in slip velocity. However, slip velocities in the riser remain significantly higher than those in the downer. It is worth noting that there are no instances of a slip velocity of 0 in the riser, which is related to

the fact that particles must overcome gravity.

Ozone concentration distributions The distribution of ozone concentration in the riser and downer exhibits distinct differences. In the flow developing region, a clear reactant-catalyst segregation is observed in the riser, as shown in Figure 4.7 (a3). High-concentration regions are primarily located in regions with fewer particles, while regions with more particles often result in complete ozone reaction. The downer also experiences segregation in the flow developing region, but it is not severe. Due to the lower solids holdup of the clusters, the ozone in these regions is not entirely consumed, as shown in as shown in Figure 4.7 (c3). Consequently, in the flow developing region, the standard deviations of the ozone concentration for the downer are lower than those of the riser, as shown in Table 4.4.

However, in the flow developed region, the differences between the two reactors become obvious. In the riser, the severe reactant-catalyst segregation still exists in the flow developing region, due to the presence of a core-annulus structure. Ozone in the core region of the riser is not reacted, while the ozone in the annulus region is entirely consumed, as shown in as shown in Figure 4.7 (b3). In contrast, in the flow developed region of the downer, ozone is distributed uniformly in both the axial and radial directions, as shown in as shown in Figure 4.7 (d3). As shown in Table 4.4, although the total remaining ozone in the riser is roughly 40% less than in the downer, the maximum ozone concentration in the riser is approximately 37% higher than in the downer. Moreover, the standard deviation in the riser is approximately 2.6 times that of the downer. These results all indicate that the more severe reactant-catalyst segregation in the riser.

Reaction rate distributions The different distributions of catalysts and reactants in the riser and downer lead to different reaction behaviours. In the flow developing region, due to the reactant-catalyst segregation in the riser, regions with high reaction rates are

typically located at the interfaces of high catalyst and high reactant regions, i.e., the edges of clusters, as shown in Figure 4.7 (a4). Because of the relatively high slip velocity at these interfaces, fresh reactants are continuously supplied, resulting in high reaction rates, reaching up to $2.16 \text{ g/m}^3/\text{s}$. In the downer, reactions occur in any region that has particles, as shown in Figure 4.7 (c4), due to the homogeneous ozone distribution. Consequently, the maximum reaction rate in the flow developing region of the downer is $1.27 \text{ g/m}^3/\text{s}$.

According to Table 4.4, the average reaction rates in the flow developing region of the riser and downer are nearly the same. In a situation with only $1/3$ of the catalyst, the downer achieves reaction rates comparable to the riser, indicating the higher utilization efficiency of catalysts in the downer.

The circumstance in the flow developed region, however, is different. In the riser, the reduction in ozone concentration results in a noticeable decrease in reaction rates, from 0.229 to $0.0745 \text{ g/m}^3/\text{s}$, as shown in Table 4.4. The maximum reaction rate in the riser is higher than in the downer, but the average reaction rate is lower than in the downer. In the downer, the maximum reaction rate do not change, but the average reaction rate decreases from 0.208 to $0.1 \text{ g/m}^3/\text{s}$ due to the reduction of the ozone concentration.

In summary, because the flow direction of the gas and solid phases in the downer aligns with the direction of gravity, this results in particle clustering with fewer constraints from gas flow and a more uniform particle distribution. In the riser, on the other hand, particles form denser and more upright clusters to resist the gravitational constraints, leading to a significantly higher degree of heterogeneity in the particle distribution. The influence of gravity also makes the interaction between the gas phase and solid phase more intense in the riser, whereas in the downer, their interaction is relatively less intense. The ozone distribution in the flow developing region is heterogeneous in both the riser and downer. However, in the flow developed region, the heterogeneity in the riser remains

almost the same as that in the flow developing region, while the ozone distribution in the downer becomes highly homogeneous. The distributions mentioned above result in the average reaction rates in the riser and downer being close, despite there being more catalysts present in the riser. In the riser, regions where reactions occur tend to be concentrated, with some areas having very high reaction rates while others have very low rates. In the downer, the distribution of reaction regions is more uniform, which might enable the downer to perform better in certain reactions limited by heat and mass transfer.

4.4.3 Residence time distributions (RTD) in the riser and downer

Figure 4.8 and 4.9 shows the probability (solids lines) and cumulative (colour blocks) distributions of the gas and solids tracer concentrations in the riser and downer. Figure 4.8 (a) shows the results during the 0 to 10 s period in the riser. Figure 4.8 (b) and 4.9 show the results during the 0 to 1.4 s period in the riser and downer, respectively. In accordance with Section 4.3.3, the tracer concentrations at 2 m and 5 m are monitored, with the former represented in orange and the latter in blue in the figure. The probability distribution functions (PDF) of the gas and solids tracers are the time series of cross-sectional tracer concentrations at the two observation lines, which are calculated by

$$\bar{Y}_g^{tc}(t, h) = \frac{1}{d} \frac{1}{\bar{\varepsilon}_g(t, h) \bar{v}_g(t, h)} \int_0^d \left(\varepsilon_g(t, h, x) v_g(t, h, x) Y_g^{tc}(t, h, x) \right) dx, \quad (4.30)$$

$$\bar{Y}_s^{tc}(t, h) = \frac{1}{d} \frac{1}{\bar{\varepsilon}_s(t, h) \bar{v}_s(t, h)} \int_0^d \left(\varepsilon_s(t, h, x) v_s(t, h, x) Y_s^{tc}(t, h, x) \right) dx, \quad (4.31)$$

where

$$\bar{\varepsilon}_s(t, h) = \frac{1}{d} \int_0^d \varepsilon_s(t, h, x) dx, \quad (4.32)$$

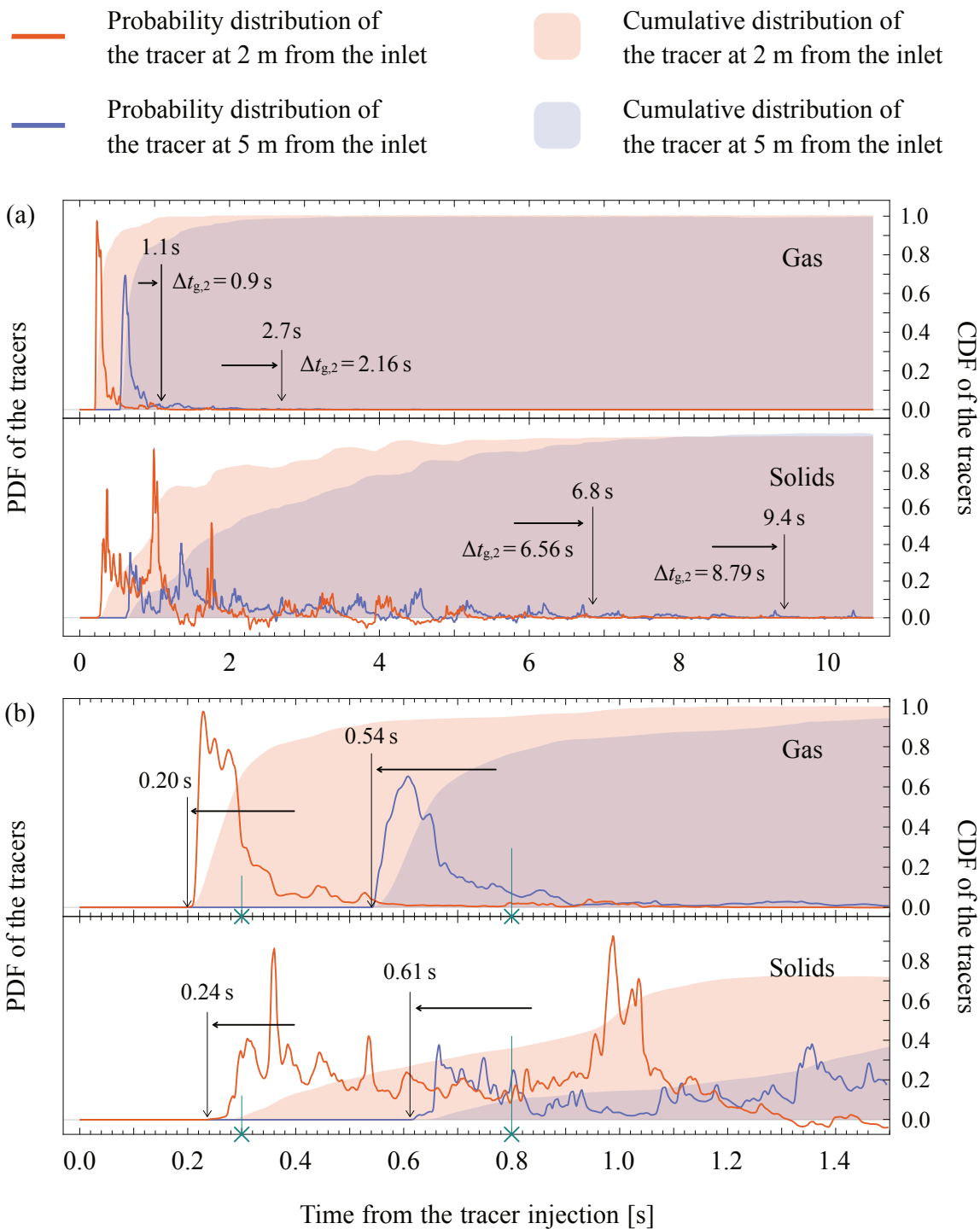


Figure 4.8: Probability and cumulative distribution functions of gas and solids tracer concentrations in the riser

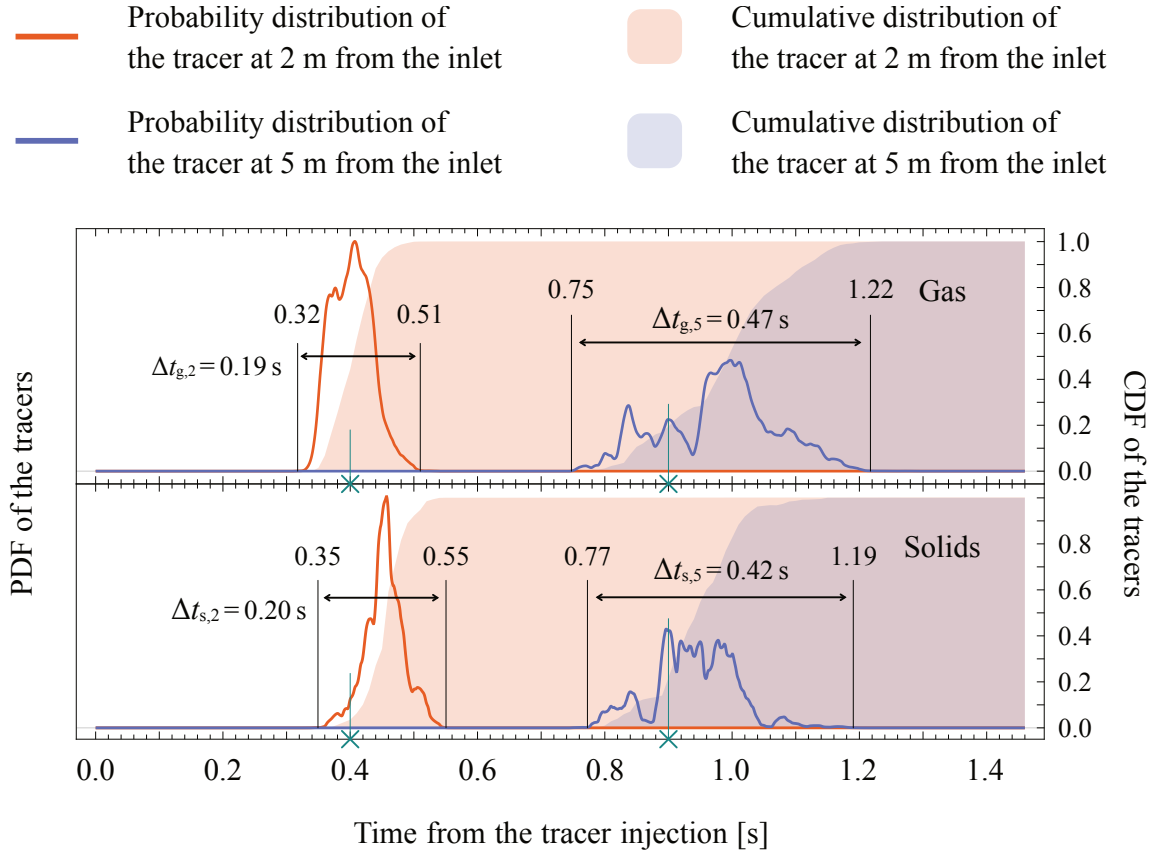


Figure 4.9: Probability and cumulative distribution functions of gas and solids tracer concentrations in the downer

$$\bar{\varepsilon}_g(t, h) = 1 - \bar{\varepsilon}_s(t, h), \quad (4.33)$$

$$\bar{v}_g(t, h) = \frac{1}{d} \frac{1}{\bar{\varepsilon}_g(t, h)} \int_0^d (\varepsilon_g(t, x, h) v_g(t, x, h)) dx, \quad (4.34)$$

$$\bar{v}_s(t, h) = \frac{1}{d} \frac{1}{\bar{\varepsilon}_s(t, h)} \int_0^d (\varepsilon_s(t, x, h) v_s(t, x, h)) dx, \quad (4.35)$$

and h is the height of observation lines. Since the tracers may flow backward to cross the observation lines again after they pass through the lines, the volume flow rate is considered during the calculation. Due to the possibility of tracers flowing backward across the observation lines after they have passed through, the volume flow rate is taken into account during the calculation. The cumulative distribution function (CDF) are

calculated by

$$\sum Y_g^{tc}(t, h) = \frac{\int_0^t \bar{Y}_g^{tc}(\tau, h) d\tau}{\int_0^\infty \bar{Y}_g^{tc}(\tau, h) d\tau}, \quad (4.36)$$

$$\sum Y_s^{tc}(t, h) = \frac{\int_0^t \bar{Y}_s^{tc}(\tau, h) d\tau}{\int_0^\infty \bar{Y}_s^{tc}(\tau, h) d\tau}. \quad (4.37)$$

The figure also provides information on when the tracers reach and leave the observation lines. Additionally, it displays the durations for which the tracers pass through the observation lines.

Table 4.5 summarizes the time points from Figure 4.8 and 4.9 when the tracers arrive at and depart from the observation lines, as well as the duration of their passage through the observation lines.

Table 4.5: Summary of time points and durations [s] of tracers behaviour

Phase	Reactor	$h = 2$ m			$h = 5$ m		
		Arrival	Departure	Duration	Arrival	Departure	Duration
Gas	Riser	0.20	1.10	0.90	0.54	2.70	2.16
	Downer	0.32	0.51	0.19	0.75	1.22	0.47
Solids	Riser	0.24	6.80	6.56	0.61	9.40	8.79
	Downer	0.35	0.55	0.20	0.77	1.19	0.42

Figure 4.10 shows the contours of the concentrations of the gas (orange) and solids (pink) tracers in the riser and downer from the inlet to 5 m. The results at $t = 0.35$ s and $t = 0.8$ s for the riser and $t = 0.4$ s and $t = 0.9$ s for the downer are shown in the figure. The first time point is when the tracers reach the first observation line ($h = 2$ m), and the second time point is when the tracers reach the second observation line ($h = 5$ m). The detailed time points for the riser and downer are marked by green crosses in Figure 4.8 (b) and 4.9.

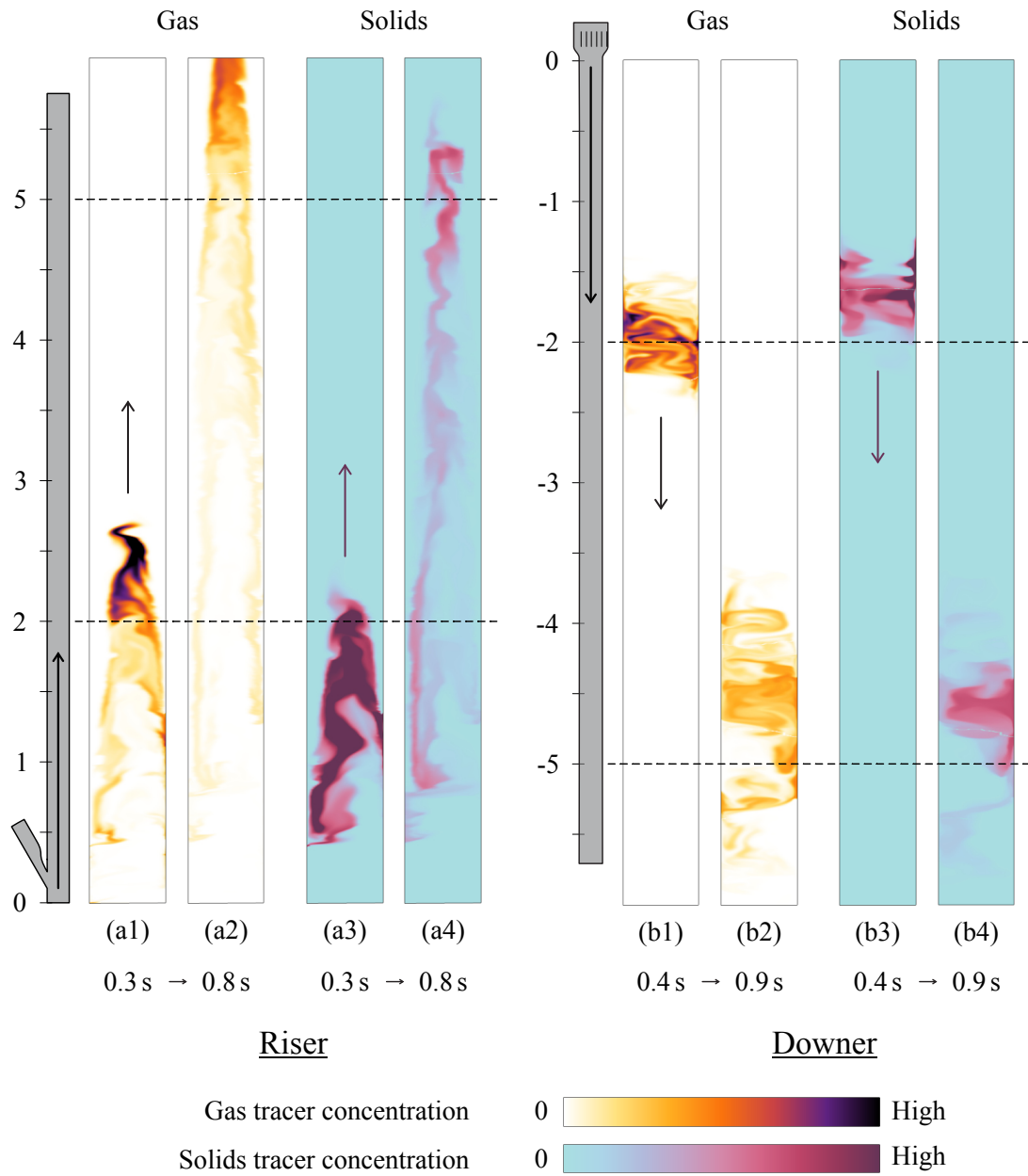


Figure 4.10: Contours of the gas and solids tracer in the (a) riser and (b) downer

RTD of the downer The results for the downer reactor's RTD are quite clear, as shown in Figure 4.9. The gas tracer, along with the gas phase, reaches the observation line at 2 m at around 0.32 s and takes approximately 0.19 s for the tracer to completely pass the first observation line. The average residence time of the gas tracer in the range of 0 to 2 m is approximately 0.4 s. For the solids tracer, it starts passing the first observation line at 0.25 s and takes about 0.20 s to pass through entirely. The average residence time of the solids tracer within the first 2 m is greater than 0.4 s. As for the gas tracer passing through the second observation line located at 5 m, it takes about 0.47 s, with an average residence time within the first 5 m being 1 s. However, the solids tracer passes the second observation line in 0.42 s, and its average residence time is less than 0.4 s.

Based on the results above, firstly, the average residence time of the gas tracer at the two observation lines aligns with the times predicted by the U_g . This result indicates that the influence of gravity, frictional forces from the walls, and drag forces from the particles on gas flow is minimal. In contrast, the solids tracer lingers longer before the first observation line compared to the gas tracer and spends less time before the second observation line. This is a result of the combined effect of gravity and drag force acting on the particles. When particles first enter the downer, their velocity is slow, and gravity, along with the drag force, accelerates them. As a result, the average velocity of the particles in the 0 to 2 m range is less than U_g , causing them to arrive at the first observation line later than the gas tracer. When the particles reach the height of 1 m, their velocity surpasses the average gas velocity. Then, gravity continues to accelerate the particles, while drag forces slow down this acceleration, eventually reaching a state of force equilibrium. During this process, the particles continue to move downward, and their average velocity exceeds U_g , causing them to overtake the gas tracer, resulting in earlier passage through the second observation line.

Secondly, both gas and solids tracers take longer to pass through the second observation line compared to the first observation line, roughly about 2 to 2.5 times longer. However, their main peaks in the RTD at the second observation line are still quite distinct. In other words, the majority of tracers, approximately 78 % for the gas tracer and 84 % for the solids tracer, pass through the observation line within a relatively short time. The tracers that pass through earlier and later can be attributed to the diffusion of the gas tracer and the non-uniform radial velocity distribution of the particles.

Thirdly, the moments when gas and solids tracers reach and leave the observation lines are very close to each other. The close moments indicate that during their downward movement, gas and particles remain synchronized, which is consistent with the analysis of the slip velocity distributions presented in Section 4.4.2.

RTD of the riser The results of the RTD in the riser are much more complex, as shown in Figure 4.8. Gas tracers reach the first observation line ($h = 2$ m) at 0.2 s, which is consistent with their behaviour in the downer. However, before 0.4 s, the 83 % of gas tracers have already passed through the line, indicating that the tracers flow faster than the average gas flow. The remaining 17 % of tracers take until 1.1 s to fully pass through the first observation line, with a total duration of 0.9 s. This duration is significantly longer than the 0.19 s observed in the downer. A similar situation occurs when tracers pass the second observation line ($h = 5$ m). Gas tracers reach this line at 0.54 s, which is 0.21 s earlier than in the downer. More than 85 % of the tracers have traversed the line before 1 s. However, it takes until 2.7 s for all tracers to have passed through the line, with a total duration of 2.16 s. This duration is 4.6 times longer than their residence time in the downer.

Figure 4.10 provides an explanation for these phenomena. The distribution of gas tracers in the riser forms an arrowhead shape: the central portion rapidly flows upward,

while tracers near the wall on both sides trail behind, as illustrated in Figure 4.10 (a1). As the gas flow continues to move upward, the tracers in the central region ascend at a very fast pace. However, the tracers in the wall region move upward slowly, even coming to a standstill or flowing downward, causing their “tails” to grow longer, as shown in Figure 4.10 (a2). Consequently, the central part of the gas flow carries the majority of gas tracers, allowing them to pass through the observation lines earlier than the overall gas flow, while the remaining tracers are concentrated near the wall region, moving at a slower pace and struggling to reach the observation lines.

In the downer, such a gas tracer distribution does not exist. Gas tracers in the downer are distributed relatively evenly in the radial direction, and they mostly move downward together. From the time-averaged results in Figure 4.5, the velocity difference between the centre and wall regions in the riser can be as high as 13 m/s, while in the downer, it does not exceed 2 m/s. This difference is a direct reason for the distinct RTD of the gas tracer between the riser and downer.

Regarding the solids tracers in the riser, the first tracer reached the initial observation line at 0.24 s, as shown in Figure 4.8. By 1.1 s, the PDF curve exhibited two prominent peaks, with a reduced number of tracers passing through the line between these two peaks. Following these peaks, approximately 70 % of the solid tracers traverse the line. At 1.3 s, some tracers began to backtrack to their positions before the first observation line, creating a reflux. At 1.7 s, a substantial number of tracers once again flowed past the line. In the subsequent time intervals, peaks and troughs alternated on the PDF curve of the solid tracers. The peak duration is roughly between 0.2 s and 0.25 s, while the troughs lasted approximately 0.5 s to 0.75 s. Overall, there are significantly more tracers passing upward across the line than tracers flowing downward in reflux. In this alternating pattern, by 6.8 s, 99 % of the solid tracers had passed through the first observation line, taking a total

of 6.56 s. This duration is 7.3 times longer than the time it took for gas tracers to cross the first observation line in the riser and 16.4 times longer than the time it took for solids tracers to cross in the downer. The situation in which the solids tracer passes through the second observation line is very similar to when the tracer passes through the first one, with the only difference being that the tracer struggles more when moving upward. At 1.6 s, the first two higher peaks end, but only about 40 % of the solids tracer traverses the line. Subsequently, there is also a phenomenon of tracer backflow and alternating peaks and valleys, although the boundaries between the peaks and valleys are not clear. Based on a few less distinct peaks, their duration is also approximately between 0.2 s and 0.25 s. Finally, at 9.4 s, 99 % of the solids tracer passes through the second observation line, taking a total of 8.79 s. This duration is 4 times longer than the time it takes for the gas tracer to cross the second line in the riser and 21 times longer than the time it takes for the solids tracer to cross the second line in the downer.

In Figure 4.10 (a3) and (a4), it is evident that in the riser, the distribution of the solids tracer are similar to those of the gas tracer in Figure 4.10 (a1) and (a2): both display arrow-shaped distributions, and they both form tails near the wall. A notable difference lies in the central region where a limited number of solids tracers accompany the primary particle flow, and a significant amount of solids tracer is retained in the tails. This is attributed to the higher density of particles and are more affected by gravity, causing them prone to stagnate or move downward in regions where the upward gas flow velocity is lower.

Mechanisms for the flow structures in the riser and downer Once the flow in the riser reaches a steady state, the particle distribution exhibits a core-annulus structure. Solids holdup in the central region is low, while in the wall region, solids holdup is high. The downward movement of particles near the wall drives the gas to flow downward in

this region. However, to maintain a constant gas volume flow rate, the gas in the central region has a greater upward velocity. Due to this interaction between gas and particles, the velocity profile of the gas flow assumes a parabolic shape in the radial direction. This flow field results in two distinct features in the distribution of the gas tracer: arrowheads and tails. Solids in such a gas flow field exhibit more complex flow behaviour.

After particles enter the riser from the returning pipe, they are evenly distributed in the radial direction. Due to the higher gas velocity in the central region and the lack of influence from the wall, particles in this region are lifted by the gas flow and move upward. However, this group of particles is not a cohesive entity, and due to collisions, some particles start moving laterally and separate from the particle stream in the central region at point A in Figure 4.11. After separation, the particles originally in the central

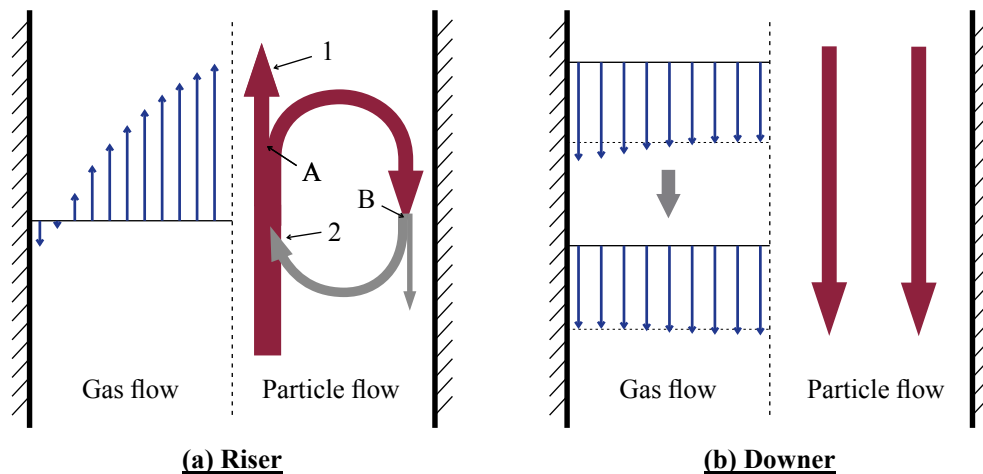


Figure 4.11: Particle flow path in the (a) riser and (b) downer

region continue to move upward at high speed, and these upward-moving particles pass through the observation lines and create the first peak in the PDF curve in Figure 4.8. The particles that separated at point A start moving toward the wall. As they get closer to the wall, their velocity decreases due to the radial gradient in gas velocity, leading to the formation of tails. Due to collisions between particles and with the wall, some

particles move away from the wall and move back toward the central region at point B in Figure 4.11. These particles are re-accelerated by the fast gas flow in the central region and move upward again. These particles that return to the central region and pass through the observation lines create the second peak in the PDF curve. This results in two adjacent peaks in the PDF curve for particle flows 1 and 2, with a trough between them. In cases where solids tracer is predominantly near the wall, the PDF of the solids tracer at the trough could be less than 0, indicating the reflux of the solids tracer. Based on the above mechanism, internal particle circulations occur in the riser, leading the particles move from the centre to the wall and back to the centre.

It's worth to note that the flow field with high velocity in the centre and low velocity near the wall exists throughout the riser. Therefore, the quantity of the internal particle circulations are not fixed and can appear at any height in the riser. Due to the interaction of adjacent internal circulations and the high chaos of gas-solids interactions, at one moment, particles may be moving toward the wall, and in the next moment, particles at the same height may be moving from the wall to the centre. In addition, in the simulation, the solids tracer introduces the riser simultaneously, but the particles continuously enter the riser without interruption. As a result, the particle flow in the riser does not exhibit a up-and-down flow behaviour, like a pulsation. The up-and-down flow behaviour appears in the PDF result because the particles entered the riser at the same time. This result simply demonstrates that there is a widespread presence of the internal particle circulations in the riser, leading to significant axial mixing. This mixing allows particles entering the riser with a time difference of 10 s to meet within the reactor. And 10 s is sufficient for particles in the central region to move upward nearly 100 m in the riser. These internal circulating particles also entrain the surrounding gas, and promotes a higher degree of mixing in the axial direction for reactants that have not yet participated in the reaction. Consequently, it largely affects the distribution of reactants in the riser. Therefore, relying solely on

reactant concentration for analyzing the progress and behaviour of reactions within the riser may provide a one-sided perspective, and the conclusions drawn from such analysis may be subject to dispute.

Regarding the downer, the gas velocity is evenly distributed in the radial direction, and there is no change in velocity direction along the radial direction. Furthermore, there is no evidence to indicate the presence of any backflow of particles or internal particle circulation in the downer. As a result, when compared to the riser, the gas mixing and solids mixing in the axial direction is not significant and can even be considered extremely weak. These factors contribute to distinct differences in the reactant concentration profile between the downer and the riser as shown in Figure 4.3 (c) and Figure 4.4 (c).

4.5 Conclusion

Due to the flow direction of gas and solids in a fluidized bed reactor, which may be either aligned with or different from the direction of gravity, distinct hydrodynamic characteristics and reaction behaviours were observed in the CFB riser and downer. In the riser, particles overcome gravity to move upwards, resulting in forming upright and elongated clusters and clear interfaces between the gas and solids phases. The flow field in the riser exhibits a core-annulus structure, which decreases the efficiency of the gas-solids contact. However, under the same operating conditions, the riser is better at retaining more particles in the reactor. In the downer, particles move along the direction of gravity, and particle aggregates are freer and less compact. The profiles of solids holdup, particle velocity, and ozone concentration in the downer are more uniform in both the axial and radial directions. Consequently, the downer exhibits higher gas-solids contact efficiency and a more evenly distributed reaction areas.

In the highly non-uniform velocity field of the riser, internal particle circulation occurs, resulting in strong axial mixing. This back mixing significantly extends the particle residence time, almost tenfold longer than the average residence time. As a result, the variation in the axial profile of ozone concentration in the flow developed region of the riser is minimal. In contrast, particles in the downer always move together with the gas flow, leading to a simpler flow behaviour and the absence of noticeable backflow.

A comparative analysis of the RTD results in the riser and downer reveals that backflow has a significant impact on the reaction behaviour and reactant distribution in the riser. In future research, it is essential to quantitatively assess the specific effects of backflow on fluidized bed reactors.

References

- ANSYS, Inc. (2022). Ansys Fluent, Release 2022R1. ANSYS, Inc.
- Bird, R. B., Stewart, W. E., Lightfoot, E. N., & Klingenberg, D. J. (2015). *Introductory transport phenomena*. Wiley Global Education.
- Ding, J., & Gidaspow, D. (1990). A bubbling fluidization model using kinetic theory of granular flow. *AIChE journal*, 36(4), 523–538.
- Ergun, S. (1952). Fluid flow through packed columns. *Chemical engineering progress*, 48(2), 89.
- Gidaspow, D. (1994). *Multiphase flow and fluidization: Continuum and kinetic theory descriptions*. Academic Press.
- Gidaspow, D., Bezburuah, R., & Ding, J. (1991). Hydrodynamics of circulating fluidized beds: Kinetic theory approach. *Proceedings of the 7th International Conference on Fluidization, Gold Coast, Australia, 3-8 May 1992*.
- Huilin, L., & Gidaspow, D. (2003). Hydrodynamics of binary fluidization in a riser: Cfd simulation using two granular temperatures. *Chemical engineering science*, 58(16), 3777–3792.
- Johnston, P. M., Zhu, J.-X., de Lasa, H. I., & Zhang, H. (1999). Effect of distributor designs on the flow development in downer reactor. *AIChE journal*, 45(7), 1587–1592.
- Lun, C. K. K., Savage, S. B., Jeffrey, D. J., & Chepurniy, N. (1984). Kinetic theories for granular flow: Inelastic particles in couette flow and slightly inelastic particles in a general flowfield. *Journal of fluid mechanics*, 140, 223–256.
- Peng, B., Zhu, J., & Zhang, C. (2010). Numerical study on the effect of the air jets at the inlet distributor in the gas- solids circulating fluidized-bed risers. *Industrial & Engineering Chemistry Research*, 49(11), 5310–5322.
- Schaeffer, D. G. (1987). Instability in the evolution equations describing incompressible granular flow. *Journal of differential equations*, 66(1), 19–50.
- Sinclair, J. L., & Jackson, R. (1989). Gas-particle flow in a vertical pipe with particle-particle interactions. *AIChE Journal*, 35, 1473–1486. <https://doi.org/10.1002/aic.690350908>
- Sun, Z. (2019). *Numerical studies on hydrodynamics in various circulating fluidization systems* [Doctoral dissertation, The University of Western Ontario]. <https://ir.lib.uwo.ca/etd/6423/>

- Sun, Z., & Zhu, J. (2019). A consolidated flow regime map of upward gas fluidization. *AIChE Journal*, 65(9), e16672.
- Wang, C. (2013). *High density gas-solids circulating fluidized bed riser and downer reactors* [Doctoral dissertation, The University of Western Ontario]. <https://ir.lib.uwo.ca/etd/1572/>
- Wang, C., Barghi, S., & Zhu, J. (2014a). Hydrodynamics and reactor performance evaluation of a high flux gas-solids circulating fluidized bed downer: Experimental study. *AIChE Journal*, 60(10), 3412–3423.
- Wang, C., Li, C., & Zhu, J. (2015a). Axial solids flow structure in a high density gas–solids circulating fluidized bed downer. *Powder Technology*, 272, 153–164.
- Wang, C., Li, C., Zhu, J., Wang, C., Barghi, S., & Zhu, J. (2015b). A comparison of flow development in high density gas-solids circulating fluidized bed downer and riser reactors. *AIChE Journal*, 61(4), 1172–1183.
- Wang, C., Wang, G., Li, C., Barghi, S., & Zhu, J. (2014b). Catalytic ozone decomposition in a high density circulating fluidized bed riser. *Industrial & Engineering Chemistry Research*, 53(16), 6613–6623.
- Wang, C., Zhu, J., & Barghi, S. (2015c). Performance evaluation of high density riser and downer: Experimental study using ozone decomposition. *Chemical Engineering Journal*, 262, 478–489.
- Wang, C., Zhu, J., Barghi, S., & Li, C. (2014c). Axial and radial development of solids holdup in a high flux/density gas–solids circulating fluidized bed. *Chemical Engineering Science*, 108, 233–243.
- Wang, C., Zhu, J., Li, C., & Barghi, S. (2014d). Detailed measurements of particle velocity and solids flux in a high density circulating fluidized bed riser. *Chemical Engineering Science*, 114, 9–20.
- Wen & Yu. (1966). Mechanics of fluidization. *Fluid Particle Technology, Chem. Eng. Progress. Symposium Series*, 62, 100–111.
- Zehner, P., & Schlünder, E. (1970). Wärmeleitfähigkeit von schüttungen bei mäßigen temperaturen. *Chemie Ingenieur Technik*, 42(14), 933–941.

Chapter 5

A machine-learning aided filtered reactive transport model for a wide-range of flow field conditions in gas-solids fluidization systems

5.1 Introduction

The current chapter aims to develop a filtered correction model to modify the reaction rate in the pseudo-homogeneous reactive transport model developed in Chapter 3. A filtered reactive transport model will be obtained by introduced the filtered correction model to the pseudo-homogeneous reactive transport model. Initially, a series of gas-solids fluidization simulations will be conducted in a periodic domain using a high-resolution mesh to collect raw data. Subsequently, a dataset comprising flow features, reaction features, and reaction correction coefficients for the reaction will be generated through a filtration algorithm. Subsequently, a neural network model will be developed and trained to establish a relationship between the flow and reaction field features and the reaction correction coefficients.

The main content of this chapter consists of three parts. Section 5.2 introduces the two-fluid model and Section 5.3 provides simulation details for the cases involving the high-resolution periodic domain. The development process of the filtered model for the

ozone decomposition reaction is presented in Section 5.4. The results are analyzed in Section 5.5.

5.2 Numerical models

5.2.1 Two-fluid model

The Eulerian-Eulerian two-fluid model coupling with the kinetic theory for granular flow (KTGF) is used in this study to simulate the gas-solids fluidization system.

Governing equations The mass conservation equations of gas and solids phases are given as:

$$\partial_t (\varepsilon_g \rho_g) + \nabla \cdot (\varepsilon_g \rho_g \vec{u}_g) = 0, \quad (5.1)$$

$$\partial_t (\varepsilon_s \rho_s) + \nabla \cdot (\varepsilon_s \rho_s \vec{u}_s) = 0, \quad (5.2)$$

$$\varepsilon_g + \varepsilon_s = 1, \quad (5.3)$$

where ε is the volume fraction, ρ is the density, and \vec{u} is the velocity of a certain phase.

The momentum conservation equations of gas and solids phases are given as:

$$\frac{\partial}{\partial t} (\varepsilon_g \rho_g \vec{u}_g) + \nabla \cdot (\varepsilon_g \rho_g \vec{u}_g \otimes \vec{u}_g) = -\varepsilon_g \nabla P + \bar{\tau}_g + \varepsilon_g \rho_g \vec{g} + K_{sg} (\vec{u}_s - \vec{u}_g), \quad (5.4)$$

$$\bar{\tau}_g = \varepsilon_g \mu_g \left(\nabla \vec{u}_g + \nabla \vec{u}_g^T \right) + \varepsilon_g \left(\lambda_g - \frac{2}{3} \mu_g \right) \nabla \cdot \vec{u}_g \bar{\mathbf{I}},$$

$$\frac{\partial}{\partial t} (\varepsilon_s \rho_s \vec{u}_s) + \nabla \cdot (\varepsilon_s \rho_s \vec{u}_s \otimes \vec{u}_s) = -\varepsilon_s \nabla P + \bar{\bar{\tau}}_s + \varepsilon_s \rho_s \vec{g} + K_{sg} (\vec{u}_g - \vec{u}_s), \quad (5.5)$$

$$\bar{\bar{\tau}}_s = \varepsilon_s \mu_s \left(\nabla \vec{u}_s + \nabla \vec{u}_s^T \right) + \varepsilon_s \left(\lambda_s - \frac{2}{3} \mu_s \right) \nabla \cdot \vec{u}_s \bar{\bar{I}},$$

where $\bar{\bar{\tau}}$ is the stress-strain tensor, μ and λ are the shear and bulk viscosity, $\bar{\bar{I}}$ is the unit tensor. K_{sg} is the interphase momentum exchange coefficient between the gas phase and solids phase. As for the solids phase, the solids pressure, p_s , solids shear viscosity, μ_s , and solids bulk viscosity, λ_s , are related to the granular temperature, which is obtained from the kinetic theory of granular flow (Gidaspow, 1994).

Kinetic theory of granular flow The granular temperature of the particles, Θ_s , is related to the kinetic energy of the random motion of the particles (Sinclair & Jackson, 1989) and calculated by

$$\Theta_s = \frac{1}{3} v'_{s\tau} v'_{s\tau}, \quad (5.6)$$

where $v'_{s\tau}$ is the fluctuating solids velocity, which is related to the collisions among particles. The equation for the granular temperature derived from the kinetic theory (Gidaspow, 1994) is shown as

$$\begin{aligned} \frac{3}{2} \left[\frac{\partial}{\partial t} (\varepsilon_s \rho_s \Theta_s) + \nabla \cdot (\varepsilon_s \rho_s \vec{u}_s \Theta_s) \right] = & \left(-p_s \bar{\bar{I}} + \bar{\bar{\tau}}_s \right) : \nabla \vec{v}_s + \\ & + \nabla \cdot (k_{\Theta_s} \nabla \Theta_s) - \gamma_{\Theta_s} + \phi_{gs}, \end{aligned} \quad (5.7)$$

where $\left(-p_s \bar{\bar{I}} + \bar{\bar{\tau}}_s \right) : \nabla \vec{v}_s$ is the energy generation by the solids stress tensor, $(k_{\Theta_s} \nabla \Theta_s)$ is the diffusion energy, (γ_{Θ_s}) is the collisional dissipation of energy, and (ϕ_{gs}) is the energy exchange between the gas and solids phases. The collisional dissipation of energy is given by Lun et al. (1984),

$$\gamma_{\Theta_s} = \frac{12 (1 - e_{ss}^2) g_{0,ss}}{d_p \sqrt{\pi}} \rho_s \varepsilon_s \Theta_s^{1.5}, \quad (5.8)$$

where the e_{ss} is the particle-particle restitution coefficient and $g_{0,ss}$ is the radial distribution function of particles. The diffusion coefficient for granular energy, k_{Θ_s} , is given by Gidaspow (1994):

$$k_{\Theta_s} = \frac{150 \rho_s d_p \sqrt{\Theta_s \pi}}{384 (1 + e_{ss}) g_{0,ss}} \left(1 + \frac{6}{5} \varepsilon_s g_{0,ss} (1 + e_{ss}) \right)^2 + 2 \rho_s \varepsilon_s^2 d_p (1 + e_{ss}) g_{0,ss} \sqrt{\Theta_s / \pi}. \quad (5.9)$$

The solids pressure in the solids-phase momentum equation composes of a kinetic term and a particle collision term:

$$p_s = \varepsilon_s \rho_s \Theta_s + 2 \rho_s (1 + e_{ss}) \varepsilon_s^2 g_{0,ss} \Theta_s, \quad (5.10)$$

where e_{ss} is the restitution coefficient for particle collisions and $g_{0,ss}$ is the radial distribution function.

The solids shear stresses in the solids-phase momentum equation are related to the shear and bulk viscosities. The bulk viscosity (Lun et al., 1984) is calculated by:

$$\lambda_s = \frac{4}{3} \varepsilon_s^2 \rho_s d_p g_{0,ss} (1 + e_{ss}) \left(\frac{\Theta_s}{\pi} \right)^{0.5}. \quad (5.11)$$

The shear viscosity contains collisional, kinetic (Gidaspow, 1994), and fractional viscosity (Schaeffer, 1987) are calculated by:

$$\mu_{s,col} = \frac{4}{5} \varepsilon_s \rho_s d_p g_{0,ss} (1 + e_{ss}) (\Theta_s / \pi)^{0.5}, \quad (5.12)$$

$$\mu_{s,kin} = \frac{10 \rho_s d_p \sqrt{\Theta_s \pi}}{96 \varepsilon_s (1 + e_{ss}) g_{0,ss}} \left(1 + \frac{4}{5} g_{0,ss} \varepsilon_s (1 + e_{ss}) \right)^2, \quad (5.13)$$

$$\mu_{s,fr} = \frac{p_{fr} \sin \phi}{2\sqrt{I_{2D}}}. \quad (5.14)$$

Gidaspow drag model Combining the Wen and Yu model (Wen & Yu, 1966) and the Ergun equation (Ergun, 1952) results in the Gidaspow drag model (Gidaspow et al., 1991).

$$K_{sg} = \begin{cases} \frac{3}{4} C_D \frac{\varepsilon_s \varepsilon_g \rho_g |\vec{v}_s - \vec{v}_g|}{d_p} \varepsilon_g^{-2.65}, & \varepsilon_g > 0.8 \\ 150 \frac{\varepsilon_s^2 \mu_g}{\varepsilon_g d_p^2} + 1.75 \frac{\rho_g \varepsilon_s |\vec{v}_s - \vec{v}_g|}{d_p}, & \varepsilon_g \leq 0.8 \end{cases} \quad (5.15)$$

where

$$C_D = \frac{24}{\varepsilon_g Re_s} \left(1 + 0.15 (\varepsilon_g Re_s)^{0.687} \right). \quad (5.16)$$

5.2.2 Reactive transport model for ozone the decomposition reaction

The pseudo-homogeneous reactive transport equation for the ozone decomposition reaction that developed in Chapter 3 is used in this study, which is expressed as:

$$\frac{\partial}{\partial t} (\varepsilon_g \rho_g Y_g^{O_3}) + \nabla \cdot (\varepsilon_g \rho_g \vec{u}_g Y_g^{O_3} - \varepsilon_g \Gamma_g^{O_3} \nabla Y_g^{O_3}) = -k_r \rho_g \varepsilon_s Y_g^{O_3}. \quad (5.17)$$

where $Y_g^{O_3}$ is the mass fraction of ozone in the gas phase.

$$\Gamma_g^{O_3} = \rho_g \mathcal{D}_{O_3,m} \quad (5.18)$$

is the diffusivity of ozone in the air. $\mathcal{D}_{O_3,m}$ is the effective mass diffusion coefficient of ozone in the air, which is given by Zehner and Schlünder (1970):

$$\mathcal{D}_{O_3,m} = \frac{\mathcal{D}_{O_3-air} (1 - \varepsilon_s^{1/2})}{\varepsilon_g}, \quad (5.19)$$

where $\mathcal{D}_{\text{O}_3\text{-air}}$ represents the mass diffusion coefficient of ozone in the air. The apparent reaction constant, k_r , is based on the volume of catalysts and measured by Wang (2013). The parameters used in the reactive transport model are listed in Table 5.1.

Table 5.1: Parameters used in the simulations using a periodic domain

Physical parameters		
Gas		Air
Inlet ozone mass fraction	1.6653×10^{-4}	
Diffusion coefficient of ozone	1.48535×10^{-5}	m^2/s
Particle		FCC
Particle density	1780	kg/m^3
Particle diameter	70	μm
Friction packing limit	0.54	
Packing limit	0.56	
Particle-particle restitution coefficient	0.9	
Apparent reaction constant	49.2	s^{-1}
Gravitational acceleration	-9.81	m/s^2
Mesh information		
Domain size	48×500	mm
Cell length	0.21	mm
Cell number	431,073	
Operating conditions		
Gas velocity profile	1, 2, 5, 8	m/s
Pre-packed solids holdup	0.05, 0.1, 0.15, 0.25	

5.3 CFD setups for high-resolution simulations

Domain and mesh The periodic domain has a height of 500 mm and a width of 48 mm, as shown in Figure 5.1 (a). The mesh is generated by ANSYS ICEM (ANSYS, Inc., 2021) and is depicted in Figure 5.1 (b). It consists of uniform square structured grids with a cell size of $3 d_p$ (0.21 mm), which can capture the meso-scale flow structures of gas-solids fluidization systems (Fullmer & Hrenya, 2016; Wang et al., 2009).

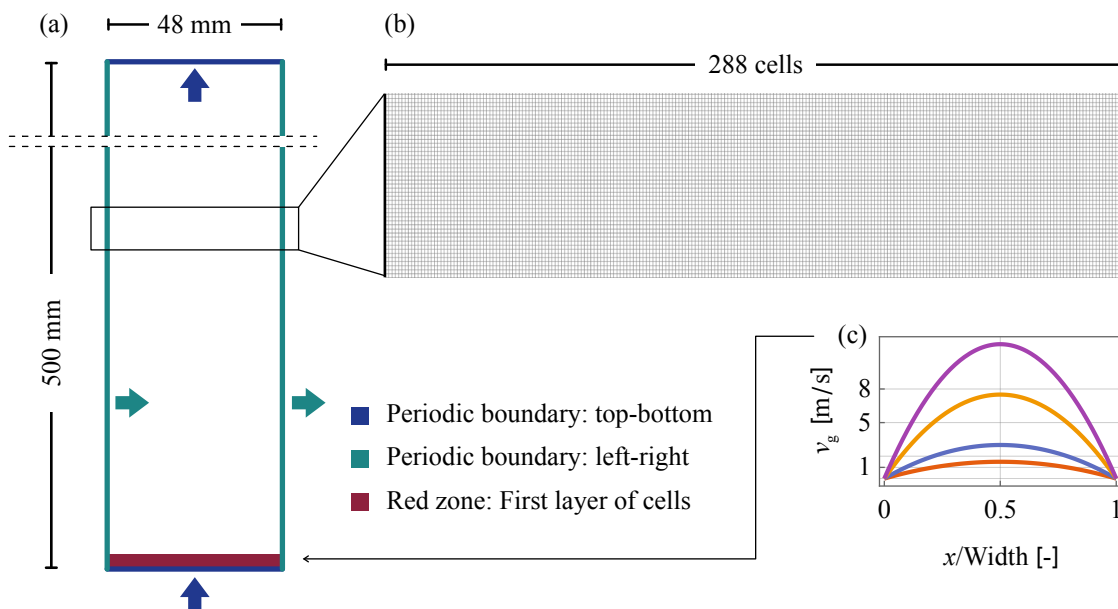


Figure 5.1: Periodic domain configuration

Conditions of boundary, zone, and operating The rectangular domain is bounded by four sides, which are set as two pairs of translational periodic boundaries: top-bottom and left-right. The first layer of cells near the bottom is separated as an independent cell zone domain (red zone in Figure 5.1 (a)) to allow for the establishment of different superficial gas velocities. To reproduce the flow fields with high gas velocity and high slip velocity observed in the experimental data of the CFB riser reactor, fixed gas velocity profiles are applied to the red zone. To encompass a wide range of flow fields, four parabolic profiles with mean values of 1, 2, 5, and 8 m/s are chosen, as shown in Figure 5.1 (c). Regarding the solids phase, the domains are pre-packed with particles at different solids holdups (0.05, 0.1, 0.15, and 0.25) to represent various particle amounts in local flow fields of the CFB riser reactor. Therefore, these high-resolution periodic cases can be used to model a series of flow fields of gas-solids fluidization systems, capable of representing any local flow field within the CFB riser reactor.

Models and solvers ANSYS Fluent (ANSYS, Inc., 2022) is used to simulate the high-resolution periodic cases. The information of the CFD model are summarized in Table 5.2.

Table 5.2: CFD model for simulations in a periodic domain

Software & Solver	
Software	ANSYS Fluent 2022R1
Solver	Two-dimensional, transient
Models	
Multiphase model	Eulerian-Eulerian
Granular temperature model	Ding and Gidaspow (1990)
Granular viscosity	Gidaspow (1994)
Granular bulk viscosity	Lun et al. (1984)
Solids pressure	Lun et al. (1984)
Granular conductivity	Gidaspow (1994)
Frictional viscosity	Schaeffer (1987)
Frictional pressure	KTGF
Radial distribution	Lun et al. (1984)
Drag coefficient	Huilin and Gidaspow (2003)
Viscous model	Laminar
Solvers	
Scheme	Phase coupled SIMPLE
Gradient discretization	Least squares cell based
Pressure discretization	PRESTO!
Momentum discretization	Second order upwind
Volume fraction discretization	Second order upwind
Granular temperature discretization	Second order upwind
UDS discretization	Second order upwind
Residual	5×10^{-5}
Time step [s]	2×10^{-5}

5.4 Development of the filtered correction model

5.4.1 Data collection

The raw dataset is generated from the simulation results under various superficial gas velocities and solids holdups. Taking the data collection process of the case with an initial

solids holdup of 0.05 as an example, the superficial gas velocity is initially set to the lowest value of 1 m/s. The flow experiences different stages from the developing stage to the fully developed stage. The developing stage begins from the start of particle acceleration and ends when the particles in the system stop accelerating. During this process, the slip velocity undergoes a rapid increase to a maximum value and then decreases to a steady state. As the gas-solids flow reaches a fully developed state, the superficial gas velocity is increased to the next stage, which is 2 m/s. This process is repeated until the superficial gas velocity reaches the highest value of 8 m/s. Figure 5.2 shows the time series in the mean gas, solids, and slip velocities of the periodic domain of the above-mentioned processes.

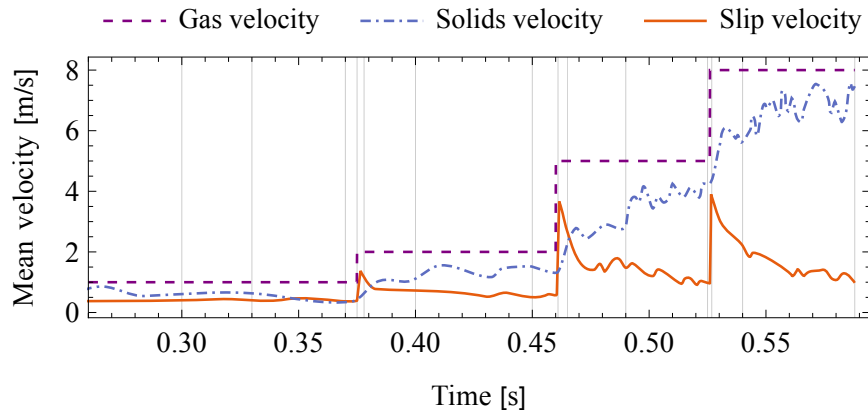


Figure 5.2: Time series of the mean gas, solids, and slip velocity in the periodic domain ($\epsilon_{s,0} = 0.05$)

The light grey vertical lines in the figure represent the time points at which the hydrodynamic and reaction data are collected. The recorded data includes spatial coordinates, solids holdups, gas velocities, particle velocities, slip velocity, ozone concentrations. A total of 44 cases of flow field and reaction data are collected.

5.4.2 Filtration process

This study employs the same filtering method used by Holloway and Sundaresan (2012), Zhu et al. (2019), and Huang et al. (2021). Following is a description of the filtering calculation formulas for flow field variables. Figure 5.3 provides a graphical explanation for the filtration procedure.

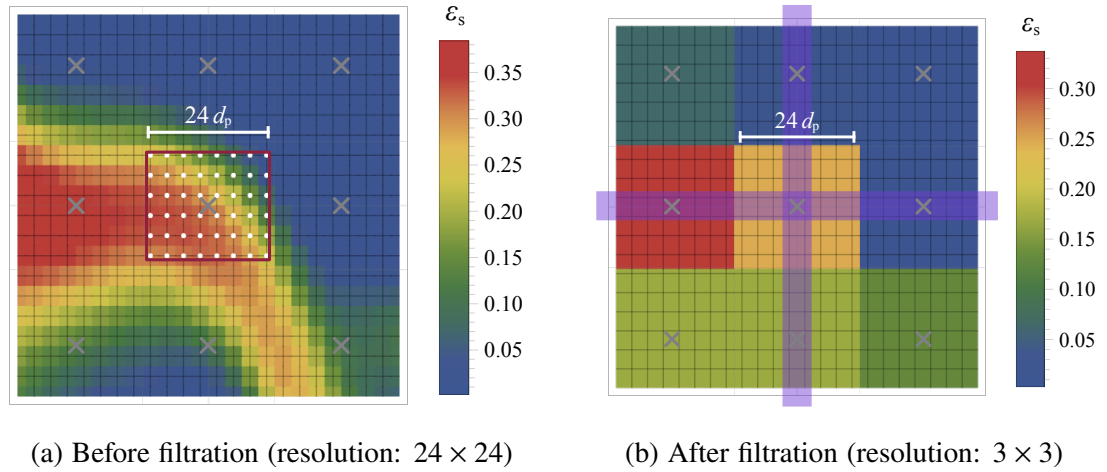


Figure 5.3: Example of the filtration process for solids holdups

The filtered solids holdup, $\bar{\varepsilon}_s$, is defined as

$$\bar{\varepsilon}_s(\vec{x}, t) = \int_V \varepsilon_s(\vec{y}, t) G(\vec{x}, \vec{y}) d\vec{y} \quad (5.20)$$

where \vec{x} represents spatial coordinates of the center of the filter box and \vec{y} represents the cell coordinates in the fine mesh computational domain. The function G donates the filtering weight:

$$G(\vec{x}, \vec{y}) = \begin{cases} \frac{V(\vec{y})}{V_{\text{filter}}(\vec{x})}, & |\vec{x} - \vec{y}| \leq \frac{\Delta_{\text{filter}}}{2} \\ 0, & \text{otherwise} \end{cases} \quad (5.21)$$

where V_{filter} and Δ_{filter} are the volume and length of the filter box, respectively. The $V(\vec{y})$

is the volume of the cell at position \vec{y} .

Figure 5.3 depicts an example of the filtration process for solids holdups. Figure (a) shows a portion of the solids holdup contour obtained from numerical results of a high-resolution case (cell size: $3 d_p$). White dots and grey crosses represent the central positions of the cells (\vec{y}) and the filter boxes (\vec{x}), respectively. The red lines bound the filter box, whose size is $24 d_p$. The symbol $\bar{\varepsilon}_s$ represents the spatial mean of the solids holdups in the cells marked by the white dots, and the filtered solids holdup is represented as the yellow square in the centre of Figure (b). By moving the filter box throughout the entire domain, a field of filtered solids holdups can be obtained.

The filtered ozone mass fraction, $\tilde{Y}_g^{O_3}$, is defined as:

$$\tilde{Y}_g^{O_3}(\vec{x}, t) = \frac{1}{\bar{\varepsilon}_g(\vec{x}, t)} \int_V \varepsilon_g(\vec{y}, t) G(\vec{x}, \vec{y}) Y_g^{O_3}(\vec{y}, t) d\vec{y}, \quad (5.22)$$

where the tilde ‘ \sim ’ represents the Favre average, which is a volume-weighted average for the ozone mass fraction. A field of filtered ozone mass fractions can be obtained by the same method as the filtration of the solids holdups.

The filtered mass transport equation of first-order reaction is expressed as (Holloway & Sundaresan, 2012):

$$\frac{\partial}{\partial t} \left(\bar{\varepsilon}_g \rho_g \tilde{Y}_g^{O_3} \right) + \nabla \cdot \left(\overline{\rho_g \varepsilon_g \vec{v}_g Y_g^{O_3}} - \Gamma_g^{O_3} \overline{\varepsilon_g \nabla Y_g^{O_3}} \right) = -k_r \overline{\rho_g \varepsilon_s Y_g^{O_3}}. \quad (5.23)$$

Cloete (2018) found that the diffusion term has little influence on the overall conversion of reactants. Thus, the reaction correction coefficient of the filtered reaction rate, H_r , can be determined by:

$$H_r = \frac{\text{filtered reaction rate}}{\text{homogeneous reaction rate}} = \frac{\overline{\varepsilon_s Y_g^{O_3}}}{\bar{\varepsilon}_s \tilde{Y}_g^{O_3}}. \quad (5.24)$$

The denominator is the reaction rate when all the parameters, such as solids holdup and ozone mass fraction, are evenly distributed in the filter box, as shown in Figure 5.3 (b). The numerator is the mean reaction rate in the same filter box but under the condition that the high-resolution fields of solids holdup and ozone mass fraction are not filtered, as shown in Figure 5.3 (a). Accordingly, this correction coefficient represents the difference in the reaction rate caused by the different resolutions of the distributions of the reactants and particles. Furthermore, this coefficient can be used to correct the reaction rate in gas-solids fluidization simulations using coarse meshes. By moving the filter box throughout the entire computational domain, the reaction correction coefficients corresponding to different flow fields and ozone concentration fields can be obtained.

5.4.3 Selection and calculation of the features

A large number of reaction correction coefficients have been obtained using the filtration algorithm. Different filter boxes correspond to different coefficients and have different characteristics, including filter sizes, flow fields, and ozone concentration fields. To accurately select a coefficient for a cell in the case using a coarse mesh, it is necessary to establish a relationship between the coefficients and these characteristics. Hence, the selection of features to represent characteristics in the filter boxes is essential.

Solids holdups ($\bar{\varepsilon}_s$), slip velocities (\bar{v}_{slip}), ozone mass fractions ($\bar{Y}_g^{\text{O}_3}$), and sizes of filter boxes (Δ_{filter}) are often used features in the filtered models (Huang et al., 2021; Igci et al., 2008; Milioli et al., 2013; Sarkar et al., 2016). Equations (5.20) and (5.22) give the expresses to calculate the filtered solids holdups and filtered ozone mass fractions. The filtered slip velocities can be calculated using the norm of the difference between the

Favre-averaged gas and solids velocities, as given by:

$$\tilde{\mathbf{v}}_s(\mathbf{x}, t) = \frac{1}{\bar{\varepsilon}_s(\mathbf{x}, t)} \int_V \varepsilon_s(\mathbf{y}, t) G(\mathbf{x}, \mathbf{y}) \mathbf{v}_s(\mathbf{y}, t) d\mathbf{y}, \quad (5.25)$$

$$\tilde{\mathbf{v}}_g(\mathbf{x}, t) = \frac{1}{\bar{\varepsilon}_g(\mathbf{x}, t)} \int_V \varepsilon_g(\mathbf{y}, t) G(\mathbf{x}, \mathbf{y}) \mathbf{v}_g(\mathbf{y}, t) d\mathbf{y}, \quad (5.26)$$

$$\bar{v}_{\text{slip}}(\mathbf{x}, t) = \left\| \tilde{\mathbf{v}}_g(\mathbf{x}, t) - \tilde{\mathbf{v}}_s(\mathbf{x}, t) \right\|. \quad (5.27)$$

Due to the complex meso-scale flow structures existing in the CFB riser reactors, differentiating between various conditions in the filter boxes using only three features is difficult. More features are needed. According to Figure 5.3, the flow field information is largely eliminated after the filtration, making it impossible to recreate the characteristics inside a filter box using only the data from within the filter box. To address this limitation, Zhu et al. (2020) introduced two additional features: axial gradients of voidages and axial gradients of gas pressures, resulting in a more accurate regression result. Therefore, including gradient features would likely further improve the regression performance.

Taking Figure 5.3 (b) as an example, along the purple belts in the figure, both the vertical and horizontal gradients of the solids holdup are decreasing. It is evident that the left-bottom corner of the red filter box contains more particles than the right-top corner. The inference results align with the contour of Figure 5.3 (a). Hence, adding more gradient-related features, both vertical and horizontal, can significantly improve the regression performance. In this work, gradients of pressures ($\partial_{\mathbf{x}} \bar{P}$), solids holdups ($\partial_{\mathbf{x}} \bar{\varepsilon}_s$), slip velocities ($\partial_{\mathbf{x}} \bar{v}_{\text{slip}}$), and ozone mass fractions ($\partial_{\mathbf{x}} \bar{Y}_g^{O_3}$) in the all directions are included to have a better regression between the characteristics in the filter boxes and reaction correction coefficients.

The calculation of the gradients is based on the filtered variables. Firstly, the filtered coordinates and all the features mentioned above are computed. Due to the structured grid used for the computational domain, it is easy to determine the variables at the same horizontal and vertical positions. Therefore, interpolation functions at various horizontal and vertical positions can be obtained. The third-order spline interpolation method is used for these calculations. Finally, the gradients of different spatial coordinates can be calculated by taking the derivatives of the interpolation functions.

After the data collection and processing, a dataset is established, containing more than two million pieces of data. All calculations are implemented using Wolfram Engine (Wolfram Research, Inc., 2022), and all source codes have been published on GitHub¹.

5.4.4 Development and regression of the neural network model

The established dataset and the relationship between the reaction correction coefficients and the features can be expressed as:

$$f\left(\bar{\varepsilon}_s, \bar{v}_{\text{slip}}, \bar{Y}_g^{\text{O}_3}, \Delta_{\text{filter}}, \frac{\partial \bar{P}}{\partial \bar{x}}, \frac{\partial \bar{\varepsilon}_s}{\partial \bar{x}}, \frac{\partial \bar{v}_{\text{slip}}}{\partial \bar{x}}, \frac{\partial \bar{Y}_g^{\text{O}_3}}{\partial \bar{x}}\right) = H_r. \quad (5.28)$$

Each data entry has 12 input features and 1 output, and the scale of the dataset is more than two million. This poses a challenge for the application of conventional empirical fitting techniques, such as polynomial regression. Therefore, in this work, a neural network model will be used for the regression.

Figure 5.4 depicts the structure of the neural network model used in this work. The neural network model comprises an input layer, several hidden layers, and an output layer. Prior to entering the hidden layer, the raw data is normalized to balance the impact of

¹GitHub repository website: <https://github.com/DengZhengyuan/CFB-filter-model>

all features during training and to counteract the dominance of certain features based on their scale. This improvement enhances numerical stability and computation accuracy. Next, the normalized features serve as the inputs for the hidden layer. The outputs from each layer serve as inputs for the subsequent layer until reaching the final output layer. The output of the output layer represents the predicted result, which in this case is the reaction correction coefficient. Within the hidden layer, the inputs from the preceding layer undergoes linear combination and weighting by the units before passing through the activation function to the next layer. Each layer is composed of a specific number of units. The number of the units in the input layer is determined by the number of features, while there is only one unit in the output layer. The inclusion of more hidden layers and more units within each hidden layer enables the neural network to model more complex conditions. However, this also escalates the training and computational costs.

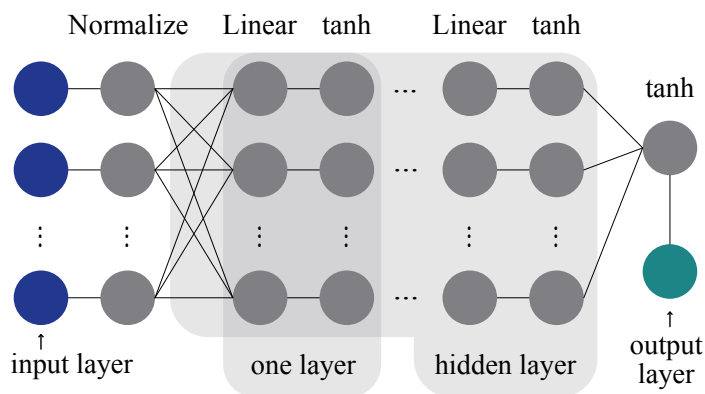


Figure 5.4: Neural network structure

In this study, TensorFlow (version 2.8.2) is used for constructing and training the neural network model (Martín Abadi et al., 2015). The Z-score normalization is utilized to address the situation that the raw data contains few outliers.

$$z = \frac{x - \mu}{\sigma}, \quad (5.29)$$

where x is the raw data, μ is the mean of the raw data, and σ is the standard deviation of the raw data. By the Z-score, each feature distribution has a mean of zero and a standard deviation of one. The hyperbolic tangent,

$$y = \tanh(x), \quad (5.30)$$

is employed as the activation function. The ADAM (ADAPtive Moment estimation) is used as the optimizer (Kingma & Ba, 2014). Four different loss functions, namely mean absolute error (MAE), mean squared error (MSE), mean absolute percentage error (MAPE), and Huber loss, will be tested to identify a better one.

$$L_{\text{MAE}} = \frac{1}{n} \sum_i^n |y_i - \hat{y}_i| \quad (5.31)$$

$$L_{\text{MSE}} = \frac{1}{n} \sum_i^n (y_i - \hat{y}_i)^2 \quad (5.32)$$

$$L_{\text{MAPE}} = \frac{1}{n} \sum_i^n \left| \frac{y_i - \hat{y}_i}{y_i} \right| \quad (5.33)$$

$$L_{\text{Huber}}(\delta) = \frac{1}{n} \sum_i^n \begin{cases} 0.5 (y_i - \hat{y}_i)^2, & \text{for } |y_i - \hat{y}_i| \leq \delta \\ \delta (|y_i - \hat{y}_i| - 0.5 \delta) & \text{otherwise} \end{cases} \quad (5.34)$$

Additionally, various combinations of the number of hidden layers and the number of units within each layer will be attempted and discussed later.

5.4.5 Summary of the development of the reaction correction model

The reaction correction model is a neural network that calculates the reaction correction coefficient based on the flow fields and ozone concentration fields. The coefficient is

obtained through the filtration and used to correct the reaction rate in the gas-solids fluidization simulations using coarse meshes. The development of the model is divided into 4 steps:

1. the simulations of the high-resolution cases using periodic boundary conditions (Section 5.3),
2. the raw data collection from the high-resolution cases (Section 5.4.1),
3. the filtering process and the generation of the dataset (Section 5.4.2 and Section 5.4.3),
4. and the training of the neural network model (Section 5.4.4).

5.5 Results and discussions

5.5.1 Comparison of flow structures at different operating conditions

Figure 5.5 depict contours of the solids holdup (green) and the ozone concentration (orange) in the cases using the high-resolution mesh at four different superficial gas velocities. The plotted domain ranges from 0.15 to 0.35 m longitudinally and the full lateral range (0 to 0.048 m). The results for the four superficial gas velocities in the figure are chosen at the time point when they have reached the fully developed stage. At this stage, the particles have achieved full acceleration, and their slip velocities have reached their minimums (about 0.5 m/s). As a result, these results can accurately depict the variations in the flow and ozone concentration fields at different superficial gas velocities.

As evident from the contours of the solids holdup, the shapes of the clusters change with the superficial gas velocity. In the flow field at a low superficial gas velocity, the clusters are smaller and exhibit more fine structures. Even the clusters with lower solids holdups retain clear demarcations from the surrounding gas bulk phase. These clusters can exist in an vertical or horizontal orientation within the flow field. Under

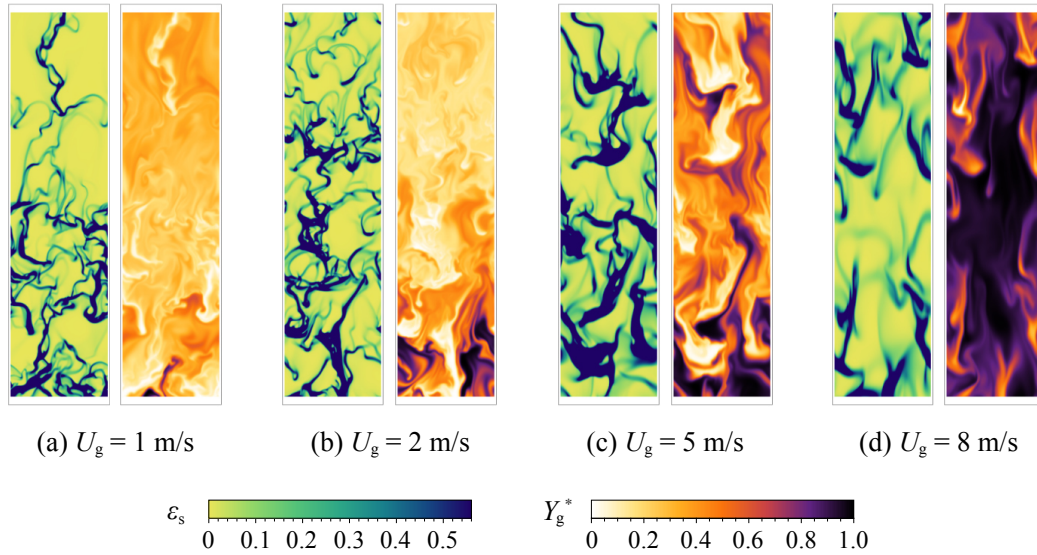


Figure 5.5: Contours of the solids holdup and the ozone concentration in the cases using the high-resolution mesh

lower superficial gas velocities, the aggregation behaviour of the particles depends on the combined influence of particle interactions and the airflow. The upward gas flow does not wield a decisive impact on either the aggregation process or the shape of the clusters. Nevertheless, as the superficial gas velocity increases, the size of individual clusters enlarges, and the occurrence of fine structures of smaller sizes diminishes. The clusters tend to aggregate in an upright manner, while the demarcations between the dilute clusters and the gas bulk phase lose clarity. Under higher superficial gas velocities, the aggregation process and the shape of the clusters are more influenced by the upward gas flow.

Regarding the contours of the ozone concentration, under lower superficial gas velocities, the ozone in the regions where many clusters appear will be completely reacted, leading to a lower average reaction rate within the region. However, under higher superficial gas velocities, even though the ozone concentration in the regions where clusters appear is lower, there will not be a situation where ozone is completely reacted.

Consequently, even if the results of the solids holdup and ozone concentration are selected at the same stage and with the same slip velocity, different superficial gas velocities result in different particle distributions and reaction behaviours. Therefore, collecting flow and ozone concentration field data at different superficial gas velocities is necessary to encompass the various conditions of the CFB riser reactor.

5.5.2 Range checking of the features

Although the neural network model can extrapolate to predict the reaction correction coefficients for the conditions that are not included in the dataset, the model's accuracy is limited by the range of the dataset. Also, it is difficult for researchers to determine whether the predicted results are reliable if the flow and reaction conditions are beyond the range of the dataset. Therefore, it is better to have a wider dataset that encompass more flow and reaction conditions in the CFB riser reactors. Section 5.4.1 and Section 5.4.3 have presented the strategy for generating the dataset, which encompass a wide range of the flow and reaction conditions. In this section, the range checking is carried out by comparing the distributions of the features from the cases using high-resolution mesh and the case of the CFB riser simulation.

Figure 5.6 depicts the distributions of 11 features in the cases of high-resolution simulations and the riser simulation. The features include solids holdup, slip velocity, ozone concentration, and their gradients, along with pressure gradients. The orange and blue bars represent the results from the riser and high-resolution simulations, while the red dotted lines represent the probability of 0.1%. As shown in the figure, the distributions of solids holdup, slip velocity, ozone concentration, gradient of ozone concentration, and gradient of pressure in the high-resolution dataset have a sufficient range to encompass all the flow and reaction conditions in the riser simulation. However, the data of the gradients

of solids holdup and slip velocity encompass the majority of the flow field in the riser, with fewer than 1% of extreme situations not being included in the dataset.

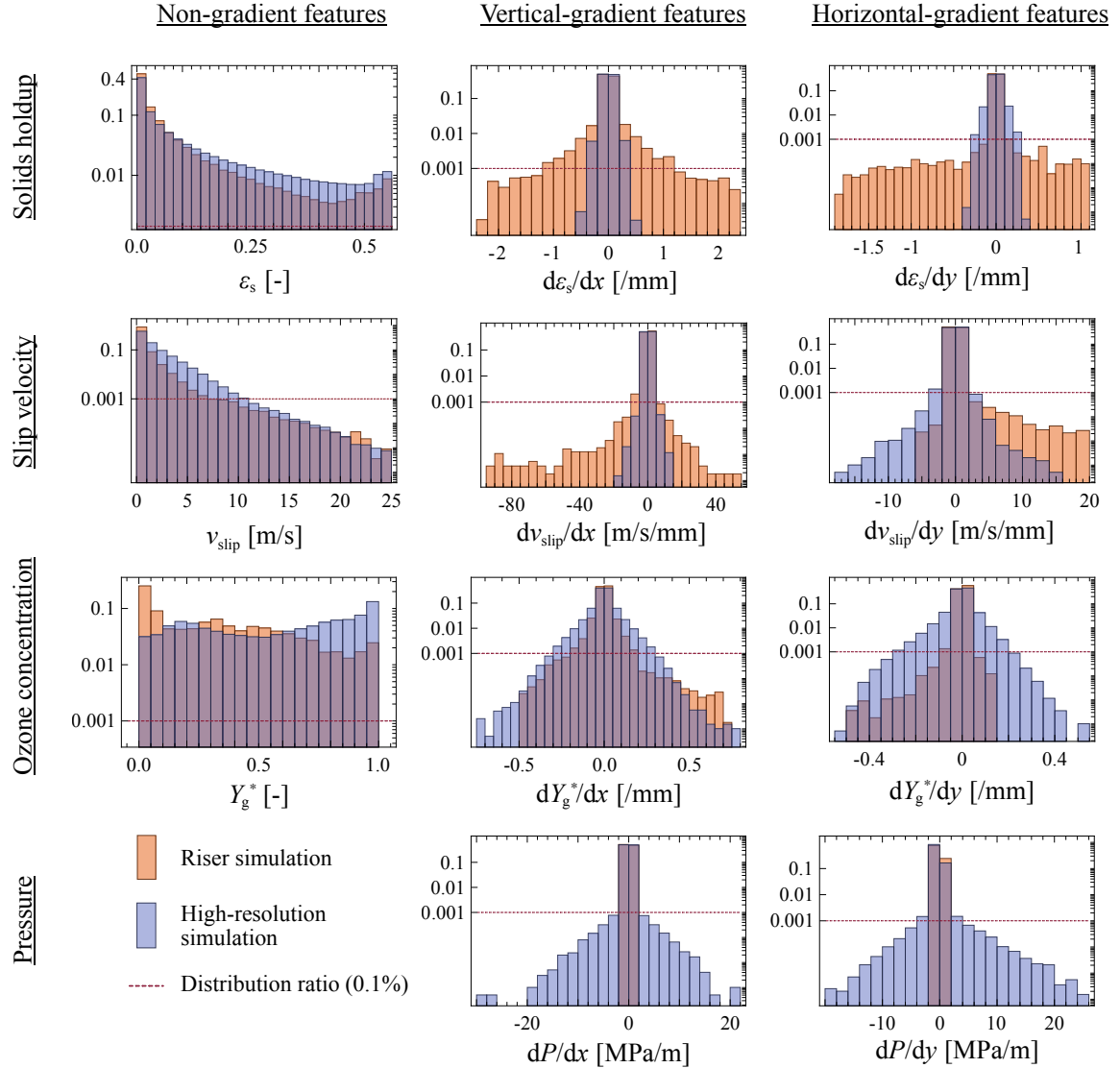


Figure 5.6: Comparison of the probability density distributions of the features in the cases of using the high-resolution mesh (results from this study) and the case of the riser simulation (results from Chapter 3 and 4)

Therefore, the results of the comparison of the probability density distributions of the features reveal that the high-resolution dataset can encompass the majority of conditions present in the flow fields and ozone concentration fields within the riser reactor. Based on

these results, the neural network model developed in this study is likely to have a higher accuracy compared to models developed using smaller datasets. However, there is still a noteworthy issue. The features characterizing the flow fields and ozone concentration fields are not entirely independent in gas-solids fluidization systems. They are collected and recorded simultaneously within a specific spatial range, exhibiting interrelated behaviour. Nevertheless, in the range checking conducted in this section, they are independently compared and discussed. As a result, this check can only indicate that the dataset includes a wide range of features, but it cannot directly prove the comprehensiveness of the dataset concerning all the flow and reaction conditions within the riser.

5.5.3 The structure and loss function of the neural network model

Structures of the neural network In order to ensure that the model is not overly complicated, leading to heightened computational cost, and can effectively capture the complex correlation between the inputs and output, different neural network structures are tested.

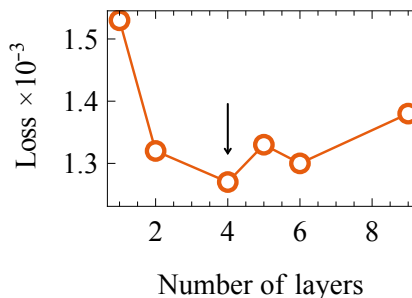


Figure 5.7: Effects of the number of layers of the neural network model on the training loss

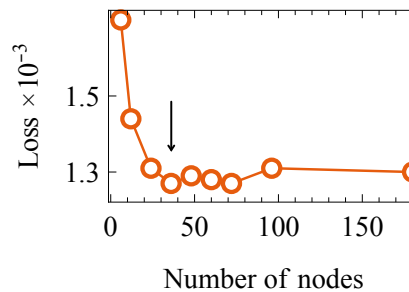


Figure 5.8: Effects of the number of nodes of the neural network model on the training loss

The relationship between the number of hidden layers and the validation loss of the neural network model is shown in Figure 5.7. The tested numbers of hidden layers are 1, 2, 4, 6, and 9, each with 60 nodes in every hidden layer. The utilized loss function in

this test is MAE. Until the number of hidden layers reaches 4 from 1, the validation loss decrease rapidly. Then, the loss fluctuates and has a rising pattern.

Figure 5.8 shows the relationship between the number of nodes in each hidden layer and the validation loss. The number of hidden layers is fixed at 4, while the numbers of nodes tested in each hidden layer are set to 6, 12, 24, 36, 60, 96, and 180. The loss decreases as the number of nodes decreases, until it reaches 36, beyond which the loss stabilizes.

Therefore, the neural network model featuring 4 hidden layers with 36 nodes in each layer strikes the optimal balance between computational cost and regression performance. This configuration is chosen as the neural network model's structure for this study.

Loss functions Four loss functions (Equations (5.31) to (5.34)) are evaluated. Figure 5.9 depicts the comparisons of actual and predicted reaction correction coefficients for the regression results using the different loss functions. As shown in the figure, the regression results obtained through different loss functions are close, with the results distributed symmetrically around the $y = x$ line. More than 90% of the predictions have a relative error of less than 10%, while over 99% of the predictions have a relative error within 20%. The distributions of MAE and MAPE distributions of the actual and predicted reaction correction coefficients for the models using the different loss functions are depicted in Figure 5.10 and Figure 5.11, respectively. From the results, it can be observed that models trained using the MSE and Huber loss functions exhibit a more dispersed error distribution with the central location deviating from 0. In contrast, the performance of models employing the MAE and MAPE loss functions is better. In addition, the MAPE loss function provides a more accurate regression for data with smaller values compared to what MAE achieves. Therefore, the MAPE loss function is used as the neural network model's loss function in this study.

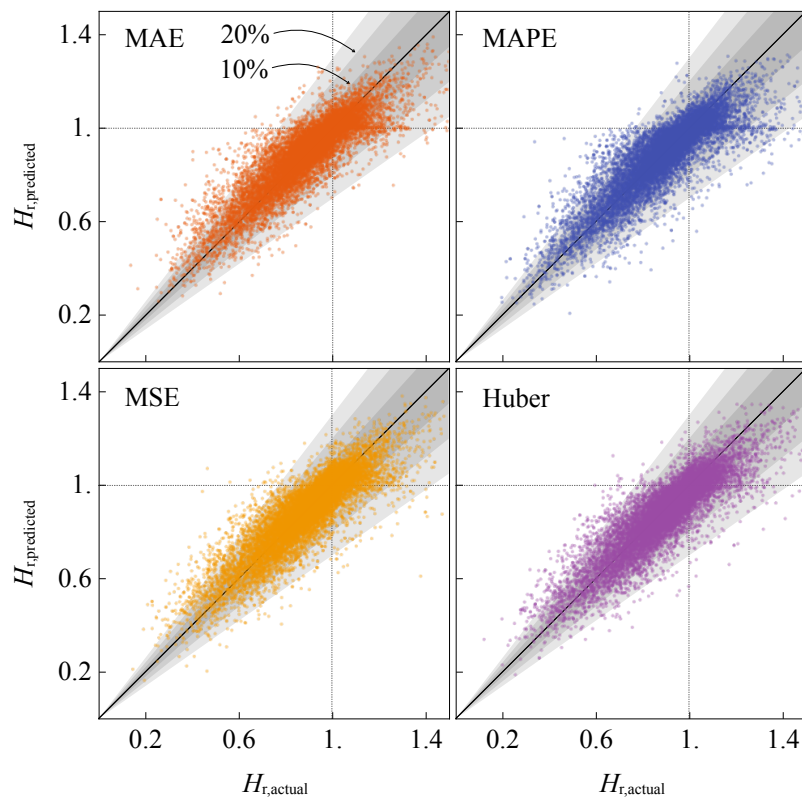


Figure 5.9: Comparison of the actual and predicted reaction correction coefficients for the regression results using the different loss functions

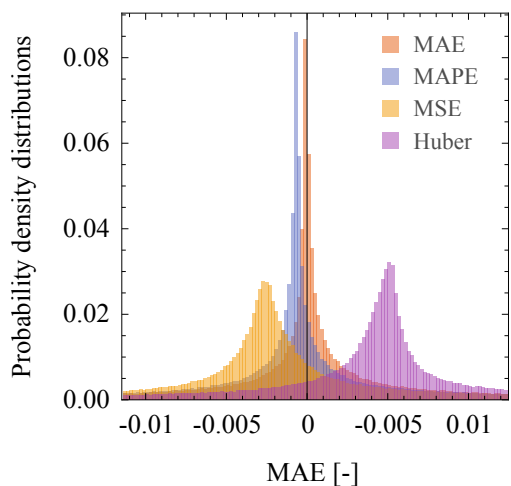


Figure 5.10: Probability density distributions of the MAE

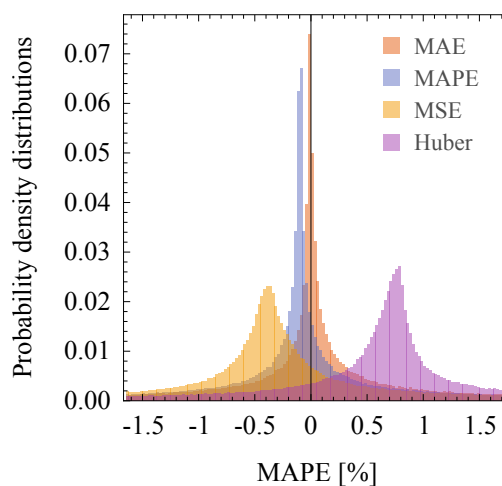


Figure 5.11: Probability density distributions of the MAPE

5.5.4 Analysis of the feature importance

Despite the neural network model is powerful in the regression of complex systems, the trained model resembles a “black box”. The lack of an intuitive understanding of the internal mechanisms for models poses challenges in evaluating how input features affect the outputs. SHAP (SHapley Additive exPlanations) is an explanation for the output of a machine learning model based on game theory (Lundberg & Lee, 2017). It connects optimal credit allocation with local explanations through the utilization of classic Shapley values from game theory and their associated expansions.

Taking the result in Figure 5.12 as an example, the figure depicts each feature’s Shapley value of one specific data entry. The horizontal bars represent the movement and direction of each feature’s contribution. First, a sample group is composed of a randomly selected subset of 100 data entries from the validation dataset. The output of the sample group represents the average of the outputs from the sample group. Then, one data entry from the validation dataset is selected as the target for analysis. Based on the SHAP algorithm, each feature of the target data entry is compared to the sample data entries to derive the Shapley values for each feature (depicted as bars in the figure). The Shapley values for the features can be interpreted as the contributions to the final output compared to the sample’s output, and the cumulative contribution of all features results in the deviation of the final output from the sample group’s output. For example, the solids holdup has the most substantial contribution to the final reaction correction coefficient, amounting to +0.165. This feature positively shifts the final output by 0.165 in relation to the sample’s output. However, the impact of horizontal gradient of ozone concentration essentially offsets the influence of the the solids holdup. With all features taken into consideration, the final output has shifted by -0.2475 relative to the output of the sample group. Accordingly, both the significance and the contribution of each feature

can be quantitatively determined.

Figure 5.13 presents a summary of the Shapley values for 1000 randomly selected data entries from the validation dataset. The output of the sample group is set as 0. The horizontal positions of the points indicate the deviation from the output of the sample group, while the colour of the points represents the magnitude of the features within their respective distributions. The order of the features on the vertical axis, from top to bottom, represents the importance of the contribution. The features labelled with underlines are the non-gradient features; the remaining ones are the gradient features. The variable x denotes the horizontal position, and y denotes the vertical position. The sample space of these 1000 data entries is assumed to have the same distribution as the validation dataset's space. Therefore, the feature importance analysis within this sample space can accurately reflect the statistical characteristics of the features' contributions to the reaction correction coefficients in the developed model.

Influences of the non-gradient features As shown in Figure 5.13, the non-gradient features contribute in the following importance order: filter size, ozone concentration, solids holdup, and slip velocity.

In the flow field of a high-resolution periodic with fixed operating conditions, the meso-scale structures, such as the size and shape of the clusters, remain consistent. During the filtration process, using a larger filter box results in a higher quantity of meso-scale structures contained within the box. Conversely, a smaller filter box contains fewer meso-scale structures. When the filter box is sufficiently small, there may not even be enough space to accommodate a complete meso-scale structure. As a result, a more evenly distributed gas-solids mixture has more opportunities to appear in the smaller filter box. In such situations, the contact efficiency between ozone and catalysts increases, leading to a higher reaction rate. Consequently, the mean reaction rate within a smaller filter box

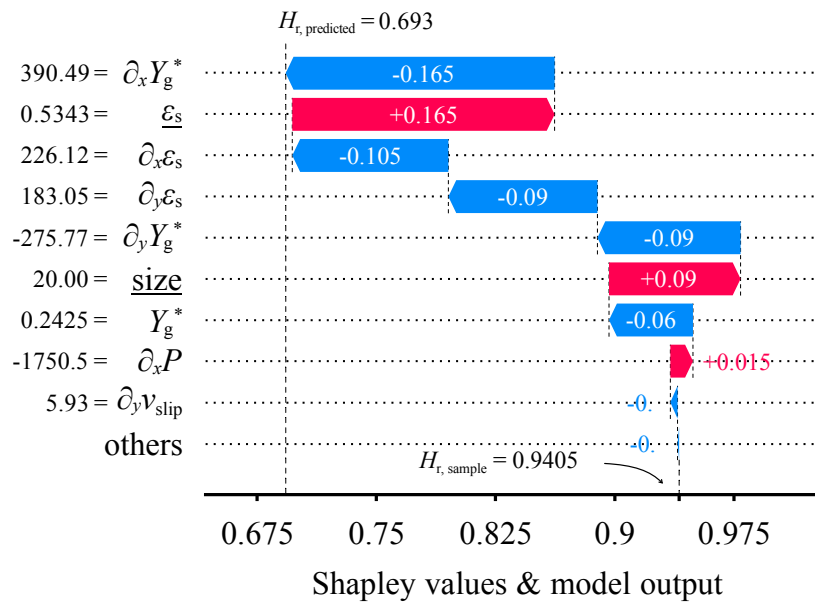


Figure 5.12: Shapley values of one data entry

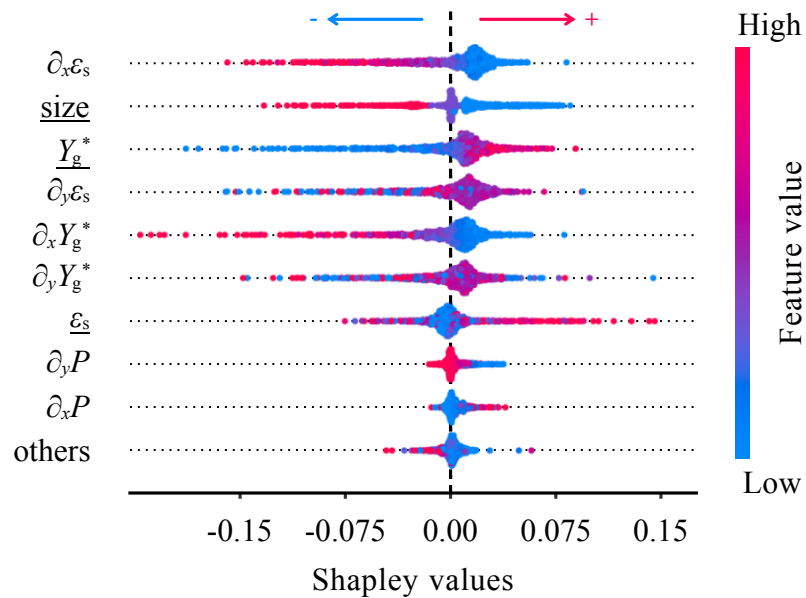


Figure 5.13: Shapley values of 1000 data entries

normally has a larger reaction rate than that in a larger filter box, even though they have the same solids holdup. Therefore, the size of the filter box has negative impacts on the reaction correction coefficient.

As for the features of solids holdup and ozone concentration, more particles and ozone appear in a filter box yields a larger reaction correction coefficient, according to Figure 5.13. Assuming solids holdup and ozone concentration remain constant, let's consider two extreme scenarios. In the first scenario, both particles and ozone are uniformly distributed within the space. Here, the efficiency of contact between reactants and catalysts is at its highest, leading to the maximum reaction rate. In the second scenario, particles and ozone are distributed in different, non-overlapping positions within the space. In this case, reactants and catalysts do not come into contact, resulting in a reaction rate of zero. While these two extreme scenarios are unlikely to occur in the gas-solids fluidizations, if this space, encompassing both gas and solids, is considered as a system, its state tends to lean towards one of these scenarios under different flow conditions. Therefore, the solids holdup and ozone concentration have positive impacts on the reaction correction coefficient.

As for actual flows field existed in the periodic domain. Due to particle aggregation, the space is divided into two regions: a dense region and a dilute region, based on the solids holdup. If the amount of particles or ozone within the system is reduced, the dilute region will occupy more space in the system. In the dense region, catalyst concentration is high, leading to the rapid consumption of ozone. In the dilute region, ozone consumption is slower. Moreover, because particles create resistance against the airflow, the fresh gas flow tends to traverse the dilute region, which results in the dense region not receiving an ozone replenishment. Consequently, when lower amounts of particles and ozone are present in the space, catalyst utilization becomes inefficient, resulting in low contact

efficiency between reactants and catalysts. At this situation, the state of the system is similar to the second scenario. Conversely, if the amount of particles or ozone is increased in the system, the occupation of the dense region will increase. The reactants have more opportunities to contact the catalysts, and the fresh air flow cannot easily escape via the dilute region. The state of the system becomes more similar to the first scenario, leading to higher contact efficiency.

Other non-gradient features have a limited influence on the reaction correction coefficient in this neural network model.

Influences of the gradient features Before exploring the influences of the gradient features, it is important to explain the processing of the gradient features in the step of the generation of the dataset. In the periodic domain, there is no difference in the flow field in the horizontal direction. Also, in the riser, the flow field is symmetric about the central axis of the riser. Therefore, for horizontal gradients, there is no need to indicate the direction with symbols; numerical values alone can represent their characteristics. In the vertical direction, both gas and particles in the flow field are subjected to downward gravitational forces, yet both gas and particles exhibit an overall upward movement. They demonstrate differences in the vertical direction. Hence, the direction of the vertical gradients is necessary. Therefore, the model uses the absolute values of the horizontal gradients as inputs, while retaining the symbols for the vertical gradients.

As a result of the aforementioned processing, a clear monotonic relationship exists between the horizontal gradient features and the reaction correction coefficients. The gradients of solids holdup and ozone concentration in the horizontal direction have significant impacts on the coefficients. Smaller gradients imply a more uniform distribution of particles and ozone in the horizontal direction. This also signifies higher efficiency in the contact between reactants and catalysts. According to Figure 5.13, when the two gradients

are smaller, the correction coefficient becomes larger, which benefits the occurrence of the reaction. Therefore, the horizontal gradients of solids holdup and ozone concentration have negative impacts on the reaction correction coefficient.

Other gradient features in the horizontal direction have a limited influence on the reaction correction coefficient in this neural network model. Furthermore, due to the processing method, the gradient features in the vertical direction are not analyzed in this section.

In summary, SHAP offers a viable approach to explaining complicated neural network models. It demonstrates the influence of the selected features on the reaction correction coefficients in the filter model. Furthermore, it aids in understanding of how the flow fields and ozone concentration fields influence reaction behaviours in the gas-solids fluidized system. Table 5.3 summarized the importance and contribution of the features based on the results of the SHAP analysis. Gradient-related features have the same or even stronger importance for model result prediction compared to non-gradient features. This further illustrates that incorporating gradient-related features during model development improves overall model performance. It also indicates that gradient-related features have a better ability to represent the flow and reaction fields caused by particle clustering.

Table 5.3: Importance and contribution of features

Feature	Gradient	Contribution	Importance
$\partial_{\vec{x}}\varepsilon_s$	√	−	1, 4
$\partial_{\vec{x}}Y_g$	√	−	5, 6
Δ_{filter}	×	−	2
Y_g	×	+	3
ε_s	×	+	7

5.6 Conclusions

The present study using the filtration method to develop a reaction correction model that quantifies the influence of meso-scale gas-solids flow structures on the ozone decomposition reaction in the gas-solids fluidization systems.

The differences in the flow field and ozone concentration field at various superficial gas velocities, along with the comparison of the feature ranges between the numerical results from periodic simulations and the CFB riser simulation, demonstrated the necessity of collecting data across a wider range of operating conditions. This wide-range data collection is essential to encompass a greater variety of flow structures present within the CFB riser. The neural network is employed to correlate the features and reaction correction coefficients obtained through filtration of the data from the high-resolution simulations. During the training process, the structure with 4 layers and 36 nodes in each layer is the most cost-effective.

The SHAP method is used to assess the importance of features. For the non-gradient features, filter size, ozone concentration, and solids holdup had a greater impact. Smaller filter size, higher ozone concentration, or higher solids holdup leading to better contact efficiencies between reactants and catalysts, resulting in reaction rates approaching those of a homogeneous state. For the gradient features, the reaction correction is most significantly influenced by the gradient of solids holdup and ozone concentration. Greater gradients indicated the presence of more heterogeneous flow structures, resulting in reduced gas-solids contact and reaction rate.

In the next step, this model will be applied in a CFB riser simulation to explore its performance in real scenarios.

References

- ANSYS, Inc. (2021). Ansys ICEM, Release 2021R1. ANSYS, Inc.
- ANSYS, Inc. (2022). Ansys Fluent, Release 2022R1. ANSYS, Inc.
- Cloete, J. H. (2018). *Development of anisotropic filtered two fluid model closures* [Doctoral dissertation, Norwegian University of Science and Technology].
- Ding, J., & Gidaspow, D. (1990). A bubbling fluidization model using kinetic theory of granular flow. *AIChE journal*, 36(4), 523–538.
- Ergun, S. (1952). Fluid flow through packed columns. *Chemical engineering progress*, 48(2), 89.
- Fullmer, W. D., & Hrenya, C. M. (2016). Quantitative assessment of fine-grid kinetic-theory-based predictions of mean-slip in unbounded fluidization. *AIChE Journal*, 62(1), 11–17.
- Gidaspow, D. (1994). *Multiphase flow and fluidization: Continuum and kinetic theory descriptions*. Academic Press.
- Gidaspow, D., Bezburuah, R., & Ding, J. (1991). Hydrodynamics of circulating fluidized beds: Kinetic theory approach. *Proceedings of the 7th International Conference on Fluidization, Gold Coast, Australia, 3-8 May 1992*.
- Holloway, W., & Sundaresan, S. (2012). Filtered models for reacting gas–particle flows. *Chemical engineering science*, 82, 132–143.
- Huang, Z., Wang, L., & Zhou, Q. (2021). Development of a filtered reaction rate model for reactive gas–solid flows based on fine-grid simulations. *AIChE Journal*, 67(5), e17185.
- Huilin, L., & Gidaspow, D. (2003). Hydrodynamics of binary fluidization in a riser: Cfd simulation using two granular temperatures. *Chemical engineering science*, 58(16), 3777–3792.
- Igci, Y., Andrews IV, A. T., Sundaresan, S., Pannala, S., & O’Brien, T. (2008). Filtered two-fluid models for fluidized gas–particle suspensions. *AIChE Journal*, 54(6), 1431–1448.
- Kingma, D. P., & Ba, J. (2014). Adam: A method for stochastic optimization. *arXiv preprint arXiv:1412.6980*.
- Lun, C. K. K., Savage, S. B., Jeffrey, D. J., & Chepuruiy, N. (1984). Kinetic theories for granular flow: Inelastic particles in couette flow and slightly inelastic particles in a general flowfield. *Journal of fluid mechanics*, 140, 223–256.

- Lundberg, S. M., & Lee, S.-I. (2017). A unified approach to interpreting model predictions. In I. Guyon, U. V. Luxburg, S. Bengio, H. Wallach, R. Fergus, S. Vishwanathan, & R. Garnett (Eds.), *Advances in neural information processing systems 30* (pp. 4765–4774). Curran Associates, Inc. <http://papers.nips.cc/paper/7062-a-unified-approach-to-interpreting-model-predictions.pdf>
- Martín Abadi, Ashish Agarwal, Paul Barham, Eugene Brevdo, Zhifeng Chen, Craig Citro, Greg S. Corrado, Andy Davis, Jeffrey Dean, Matthieu Devin, Sanjay Ghemawat, Ian Goodfellow, Andrew Harp, Geoffrey Irving, Michael Isard, Jia, Y., Rafal Jozefowicz, Lukasz Kaiser, Manjunath Kudlur, . . . Xiaoqiang Zheng. (2015). TensorFlow: Large-scale machine learning on heterogeneous systems [Software available from tensorflow.org]. <https://www.tensorflow.org/>
- Milioli, C. C., Milioli, F. E., Holloway, W., Agrawal, K., & Sundaresan, S. (2013). Filtered two-fluid models of fluidized gas-particle flows: New constitutive relations. *AIChE Journal*, 59(9), 3265–3275.
- Sarkar, A., Milioli, F. E., Ozarkar, S., Li, T., Sun, X., & Sundaresan, S. (2016). Filtered sub-grid constitutive models for fluidized gas-particle flows constructed from 3-d simulations. *Chemical Engineering Science*, 152, 443–456.
- Schaeffer, D. G. (1987). Instability in the evolution equations describing incompressible granular flow. *Journal of differential equations*, 66(1), 19–50.
- Sinclair, J. L., & Jackson, R. (1989). Gas-particle flow in a vertical pipe with particle-particle interactions. *AIChE Journal*, 35, 1473–1486. <https://doi.org/10.1002/aic.690350908>
- Wang, C. (2013). *High density gas-solids circulating fluidized bed riser and downer reactors* [Doctoral dissertation, The University of Western Ontario]. <https://ir.lib.uwo.ca/etd/1572/>
- Wang, J., van der Hoef, M. A., & Kuipers, J. (2009). Why the two-fluid model fails to predict the bed expansion characteristics of geldart a particles in gas-fluidized beds: A tentative answer. *Chemical Engineering Science*, 64(3), 622–625.
- Wen & Yu. (1966). Mechanics of fluidization. *Fluid Particle Technology, Chem. Eng. Progress. Symposium Series*, 62, 100–111.
- Wolfram Research, Inc. (2022). Wolfram Engine, Version 13.2. *Wolfram Research, Inc., Champaign, IL, 2022*. <https://www.wolfram.com/engine/>
- Zehner, P., & Schlünder, E. (1970). Wärmeleitfähigkeit von schüttungen bei mäßigen temperaturen. *Chemie Ingenieur Technik*, 42(14), 933–941.

Zhu, L.-T., Liu, Y.-X., & Luo, Z.-H. (2019). An enhanced correlation for gas-particle heat and mass transfer in packed and fluidized bed reactors. *Chemical Engineering Journal*, 374, 531–544.

Zhu, L.-T., Tang, J.-X., & Luo, Z.-H. (2020). Machine learning to assist filtered two-fluid model development for dense gas–particle flows. *AIChE Journal*, 66(6), e16973.

Chapter 6

Investigating the impact of particle clustering phenomenon on reaction behaviours in a CFB riser reactor

6.1 Introduction

In Chapter 3, a pseudo-homogeneous reactive transport model (PHRTM) was developed to describe the ozone decomposition reaction in the gas-solids fluidization system for CFD simulations. However, the results exhibited deviations from the experimental results. In Chapter 5, a filtered correction model was developed to modify the reaction term in the pseudo-homogeneous reactive transport model. This model incorporates the influence of meso-scale flow structures in gas-solids fluidizations, thereby adjusting the reaction rate of ozone decomposition for improved accuracy. Therefore, in this chapter, the filtered reactive transport model (FRTM) will be used for simulations of the CFB riser reactor. The numerical results from both the pseudo-homogeneous model and the filtered model will be compared with the experimental results. Additionally, the differences of the two numerical results arising from the filtered model will be analyzed.

6.2 Numerical models

6.2.1 Two-fluid model

The Eulerian-Eulerian two-fluid model coupling with the kinetic theory for granular flow (KTGF) is used in this study to simulate the gas-solids fluidization system.

Governing equations The mass conservation equations of gas and solids phases are given as:

$$\partial_t (\varepsilon_g \rho_g) + \nabla \cdot (\varepsilon_g \rho_g \vec{u}_g) = 0, \quad (6.1)$$

$$\partial_t (\varepsilon_s \rho_s) + \nabla \cdot (\varepsilon_s \rho_s \vec{u}_s) = 0, \quad (6.2)$$

$$\varepsilon_g + \varepsilon_s = 1, \quad (6.3)$$

where ε is the volume fraction, ρ is the density, and \vec{u} is the velocity of certain phase.

The momentum conservation equations of gas and solids phases are given as:

$$\frac{\partial}{\partial t} (\varepsilon_g \rho_g \vec{u}_g) + \nabla \cdot (\varepsilon_g \rho_g \vec{u}_g \otimes \vec{u}_g) = -\varepsilon_g \nabla P + \bar{\bar{\tau}}_g + \varepsilon_g \rho_g \vec{g} + K_{sg} (\vec{u}_s - \vec{u}_g), \quad (6.4)$$

$$\bar{\bar{\tau}}_g = \varepsilon_g \mu_g \left(\nabla \vec{u}_g + \nabla \vec{u}_g^T \right) + \varepsilon_g \left(\lambda_g - \frac{2}{3} \mu_g \right) \nabla \cdot \vec{u}_g \bar{\bar{I}},$$

$$\frac{\partial}{\partial t} (\varepsilon_s \rho_s \vec{u}_s) + \nabla \cdot (\varepsilon_s \rho_s \vec{u}_s \otimes \vec{u}_s) = -\varepsilon_s \nabla P + \bar{\bar{\tau}}_s + \varepsilon_s \rho_s \vec{g} + K_{sg} (\vec{u}_g - \vec{u}_s), \quad (6.5)$$

$$\bar{\bar{\tau}}_s = \varepsilon_s \mu_s \left(\nabla \vec{u}_s + \nabla \vec{u}_s^T \right) + \varepsilon_s \left(\lambda_s - \frac{2}{3} \mu_s \right) \nabla \cdot \vec{u}_s \bar{\bar{I}},$$

where $\bar{\bar{\tau}}$ is the stress-strain tensor, μ and λ are the shear and bulk viscosity, $\bar{\bar{I}}$ is the unit

tensor. K_{sg} is the interphase momentum exchange coefficient between the gas phase and solids phase. As for the solids phase, the solids pressure, p_s , solids shear viscosity, μ_s , and solids bulk viscosity, λ_s , are related to the granular temperature, which is obtained from the kinetic theory of granular flow (Gidaspow, 1994).

Kinetic theory of granular flow The granular temperature of the particles, Θ_s , is related to the kinetic energy of the random motion of the particles (Sinclair & Jackson, 1989) and calculated by

$$\Theta_s = \frac{1}{3} v'_{s\tau} v'_{s\tau}, \quad (6.6)$$

where $v'_{s\tau}$ is the fluctuating solids velocity, which related to the collisions among particles. The equation for the granular temperature derived from the kinetic theory (Gidaspow, 1994) is shown as

$$\begin{aligned} \frac{3}{2} \left[\frac{\partial}{\partial t} (\varepsilon_s \rho_s \Theta_s) + \nabla \cdot (\varepsilon_s \rho_s \vec{u}_s \Theta_s) \right] = & \left(-p_s \bar{\bar{\mathbf{I}}} + \bar{\bar{\boldsymbol{\tau}}}_s \right) : \nabla \vec{v}_s + \\ & + \nabla \cdot (k_{\Theta_s} \nabla \Theta_s) - \gamma_{\Theta_s} + \phi_{gs}, \end{aligned} \quad (6.7)$$

where $\left(-p_s \bar{\bar{\mathbf{I}}} + \bar{\bar{\boldsymbol{\tau}}}_s \right) : \nabla \vec{v}_s$ is the energy generation by the solids stress tensor, $(k_{\Theta_s} \nabla \Theta_s)$ is the diffusion energy, (γ_{Θ_s}) is the collisional dissipation of energy, and (ϕ_{gs}) is the energy exchange between the gas and solids phases. The collisional dissipation of energy is given by Lun et al. (1984), which can be expressed as

$$\gamma_{\Theta_s} = \frac{12(1 - e_{ss}^2) g_{0,ss}}{d_p \sqrt{\pi}} \rho_s \varepsilon_s \Theta_s^{1.5}, \quad (6.8)$$

where the e_{ss} is the particle-particle restitution coefficient and $g_{0,ss}$ is the radial distribution function of particles. The diffusion coefficient for granular energy, k_{Θ_s} , is given by

Gidaspow (1994):

$$\begin{aligned}
 k_{\Theta_s} = & \frac{150 \rho_s d_p \sqrt{\Theta_s \pi}}{384 (1 + e_{ss}) g_{0,ss}} \left(1 + \frac{6}{5} \varepsilon_{ss} g_{0,ss} (1 + e_{ss}) \right)^2 + \\
 & + 2 \rho_s \varepsilon_s^2 d_p (1 + e_{ss}) g_{0,ss} \sqrt{\Theta_s / \pi}.
 \end{aligned} \tag{6.9}$$

The solids pressure in the solids-phase momentum equation composes of a kinetic term and a particle collision term:

$$p_s = \varepsilon_s \rho_s \Theta_s + 2 \rho_s (1 + e_{ss}) \varepsilon_s^2 g_{0,ss} \Theta_s, \tag{6.10}$$

where e_{ss} is the restitution coefficient for particle collisions and $g_{0,ss}$ is the radial distribution function.

The solids shear stresses in the solids-phase momentum equation are related to the shear and bulk viscosities. The bulk viscosity (Lun et al., 1984) is calculated by:

$$\lambda_s = \frac{4}{3} \varepsilon_s^2 \rho_s d_p g_{0,ss} (1 + e_{ss}) \left(\frac{\Theta_s}{\pi} \right)^{0.5}. \tag{6.11}$$

The shear viscosity contains collisional, kinetic (Gidaspow, 1994), and fractional viscosity (Schaeffer, 1987) are calculated by:

$$\mu_{s,col} = \frac{4}{5} \varepsilon_s \rho_s d_p g_{0,ss} (1 + e_{ss}) (\Theta_s / \pi)^{0.5}, \tag{6.12}$$

$$\mu_{s,kin} = \frac{10 \rho_s d_p \sqrt{\Theta_s \pi}}{96 \varepsilon_s (1 + e_{ss}) g_{0,ss}} \left(1 + \frac{4}{5} g_{0,ss} \varepsilon_s (1 + e_{ss}) \right)^2, \tag{6.13}$$

$$\mu_{s,fr} = \frac{p_{fr} \sin \phi}{2\sqrt{I_{2D}}}. \tag{6.14}$$

Gidaspow drag model Combining the Wen and Yu model (Wen & Yu, 1966) and the Ergun equation (Ergun, 1952) results in the Gidaspow drag model (Gidaspow et al., 1991).

$$K_{sg} = \begin{cases} \frac{3}{4} C_D \frac{\varepsilon_s \varepsilon_g \rho_g |\vec{v}_s - \vec{v}_g|}{d_p} \varepsilon_g^{-2.65}, & \varepsilon_g > 0.8 \\ 150 \frac{\varepsilon_s^2 \mu_g}{\varepsilon_g d_p^2} + 1.75 \frac{\rho_g \varepsilon_s |\vec{v}_s - \vec{v}_g|}{d_p}, & \varepsilon_g \leq 0.8 \end{cases} \quad (6.15)$$

where

$$C_D = \frac{24}{\varepsilon_g Re_s} \left(1 + 0.15 (\varepsilon_g Re_s)^{0.687} \right). \quad (6.16)$$

6.2.2 Reactive transport model for the ozone decomposition reaction

The pseudo-homogeneous reactive transport model (PHRTM) for the ozone decomposition that developed in Chapter 3 is used in this simulation, which is described as:

$$\frac{\partial}{\partial t} (\varepsilon_g \rho_g Y_g^{O_3}) + \nabla \cdot (\varepsilon_g \rho_g \vec{u}_g Y_g^{O_3} - \varepsilon_g \Gamma_g^{O_3} \nabla Y_g^{O_3}) = -k_r \rho_g \varepsilon_s Y_g^{O_3}. \quad (6.17)$$

where $Y_g^{O_3}$ is the mass fraction of ozone in the gas phase.

$$\Gamma_g^{O_3} = \rho_g \mathcal{D}_{O_3,m} \quad (6.18)$$

is the diffusivity of ozone in the air. $\mathcal{D}_{O_3,m}$ is the effective mass diffusion coefficient of ozone in the air (Zehner & Schlünder, 1970),

$$\mathcal{D}_{O_3,m} = \mathcal{D}_{O_3-air} \frac{1 - \varepsilon_s^{1/2}}{\varepsilon_g}, \quad (6.19)$$

where \mathcal{D}_{O_3-air} represents the mass diffusion coefficient of ozone in air. The apparent reaction constant, k_r , is based on the volume of catalysts and measured by Wang (2013).

The above parameters are listed in Table 6.1.

Table 6.1: Parameters used for the CFB riser simulation

Physical parameters		
Gas	Air	
Inlet ozone mass fraction	1.6653×10^{-4}	
Diffusion coefficient of ozone	1.48535×10^{-5}	m^2/s
Particle	FCC	
Particle density	1780	kg/m^3
Particle diameter	70	μm
Friction packing limit	0.54	
Packing limit	0.56	
Particle-particle restitution coefficient	0.9	
Apparent reaction constant	49.2	s^{-1}
Gravitational acceleration	-9.81	m/s^2
Mesh information		
Domain size	$76.2 \times 10,200$	mm
Max cell length	1.89	mm
Cell number	271,884	
Operating conditions		
Gas velocity profile	5	m/s
Solids circulation rate	300	$\text{kg}/\text{m}^2/\text{s}$
Pre-patched solids holdup	0.205	
Wall boundary conditions		
Gas	no-slip	
Solids		
Specularity coefficient	0.01	
Particle-wall restitution coefficient	0.9	

The filtered reactive transport model (FRTM) for the ozone decomposition, which incorporates the filtered correction model and PHRTM, is expressed as following:

$$\frac{\partial}{\partial t} \left(\varepsilon_g \rho_g Y_g^{\text{O}_3} \right) + \nabla \cdot \left(\varepsilon_g \rho_g \vec{u}_g Y_g^{\text{O}_3} - \varepsilon_g \Gamma_g^{\text{O}_3} \nabla Y_g^{\text{O}_3} \right) = -H_r k_r \rho_g \varepsilon_s Y_g^{\text{O}_3}, \quad (6.20)$$

where H_r is the reaction correction coefficient, which is calculated by the filtered correction

model:

$$H_r = f \left(\bar{\varepsilon}_s, \bar{v}_{\text{slip}}, \bar{Y}_g^{\text{O}_3}, \Delta_{\text{filter}}, \frac{\partial \bar{P}}{\partial \bar{x}}, \frac{\partial \bar{\varepsilon}_s}{\partial \bar{x}}, \frac{\partial \bar{v}_{\text{slip}}}{\partial \bar{x}}, \frac{\partial \bar{Y}_g^{\text{O}_3}}{\partial \bar{x}} \right). \quad (6.21)$$

6.3 CFB riser simulation

6.3.1 Configuration of the CFB riser system

The CFB system depicted in Figure 6.1 (a) is used by Wang et al. (2014) to carry out the study on the ozone decomposition reaction. It contains a riser, a downer/downcomer, a returning pipe, separations, and other accessories. The riser is a vertical column with a height of 10.2 m and a diameter of 7.62 cm. In the CFB system, gas enters the riser from the bottom of the riser through a gas distributor with an 18 % opening region ratio (γ_g). Particles are introduced into the riser through the return pipe (5 cm i.d.) at the bottom of the riser. The gas conveys the particles upward along the riser. These particles are trapped at the top of the riser by the cyclones, stored in the storage tank, and then returned to the bottom of the riser through the returning pipe.

6.3.2 Computational domain, mesh, and solver

The computational domain for CFB riser simulations is depicted in Figure 6.1 (b). The downcomer, storage tank and cyclones are not included in the simulation. The exit elbow at the top of the riser and the return pipe are maintained. At the junction of the riser column and the return pipe, plates are installed to prevent the high-speed gas in the riser from flowing into the return pipe (Wang et al., 2014).

An unstructured quadrilateral mesh is used, with a maximum cell size of $27 d_p$ and a total of 271,844 cells. Near the wall, a five-layer mesh is utilized, with the first layer

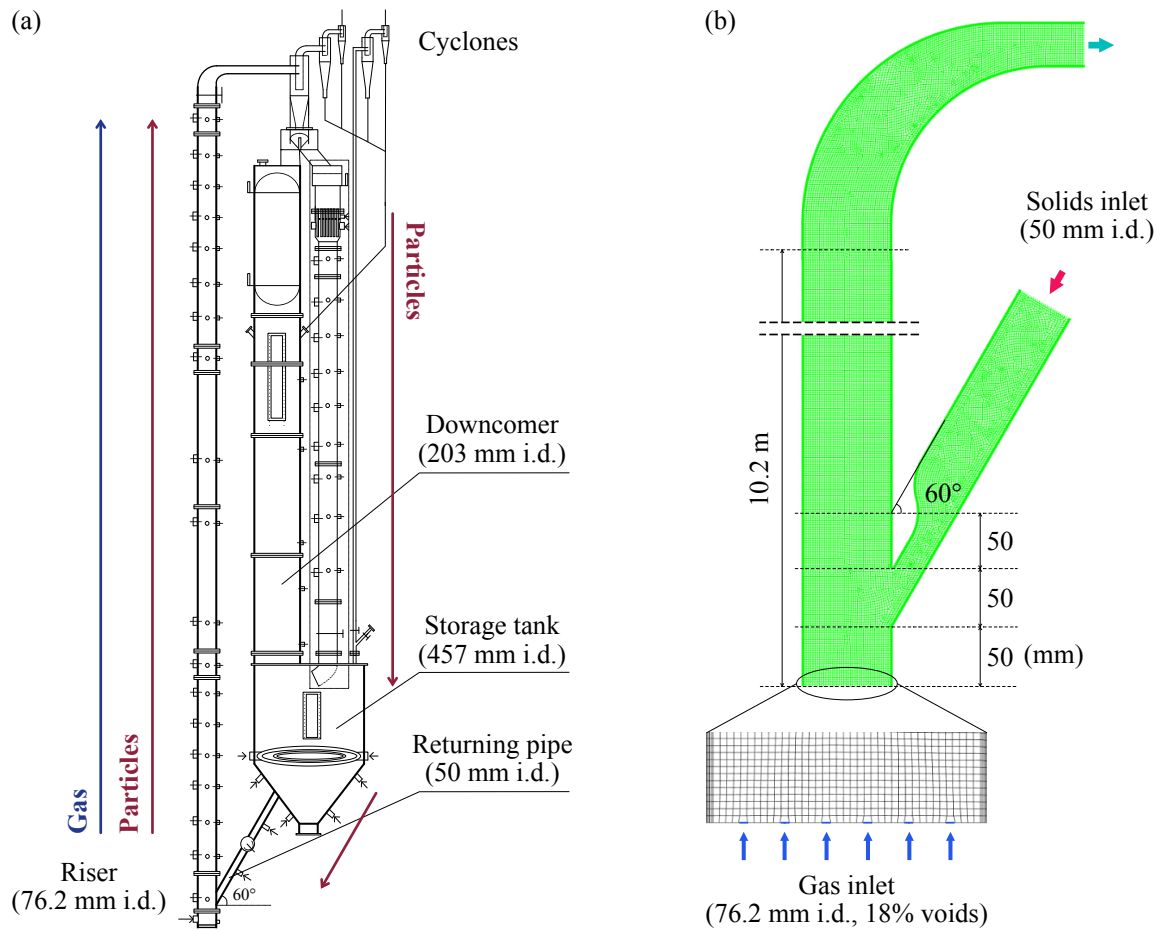


Figure 6.1: Schematic and mesh of the circulating fluidized bed system

having a thickness of $3 d_p$. According to the grid independence test conducted by Sun et al. (2022), a comparison with a finer mesh (total cell number of around 480,000) revealed deviations in key hydrodynamic characteristics of less than 2%. The simulation of this CFB riser reactor is performed using ANSYS Fluent (ANSYS, Inc., 2022). Additional information about the model and solver can be found in Table 6.2.

6.3.3 Boundary conditions and operating conditions

In this study, two simulation methods are used to simulate the CFB riser system.

Table 6.2: Information on CFD model for the CFB riser simulation

Software & Solver	
Software	ANSYS fluent 2022R1
Solver	Two-dimensional, transient
Models	
Multiphase model	Eulerian-Eulerian
Granular temperature model	Ding and Gidaspow (1990)
Granular viscosity & Granular conductivity	Gidaspow (1994)
Granular bulk viscosity & Solids pressure	Lun et al. (1984)
Frictional viscosity	Schaeffer (1987)
Frictional pressure	KTGF
Radial distribution	Lun et al. (1984)
Drag coefficient	Huilin and Gidaspow (2003)
Viscous model	Laminar
Solvers	
Scheme	Phase coupled SIMPLE
Gradient discretization	Least squares cell based
Pressure discretization	PRESTO!
Momentum discretization	Second order upwind
Volume fraction discretization	Second order upwind
Granular temperature discretization	Second order upwind
Turbulent kinetic energy	Second order upwind
Specific dissipation rate	Second order upwind
UDS discretization	Second order upwind
Residual	5×10^{-5}
Time step [s]	5×10^{-5}

Method 1 The first method (referred to as Method 1) is an approach to strictly implementing experimental operating conditions. The velocity profiles based on the superficial gas velocity (U_g) and the solids circulation rate (G_s) are used as the inlet conditions for simulations of CFB riser. As shown in Figure 6.1 (b), the gas inlet boundary condition is defined as a jet velocity profile to consider the effects of the gas distributor in the riser

(Peng et al., 2010). Each jet have the same gas velocity, which is given by

$$v_g = \frac{U_g}{\gamma_g}, \quad (6.22)$$

where U_g donates the superficial gas velocity and $\gamma_g = 0.18$ is the opening region ratio of the gas distributor. Solids enter the riser via the returning pipe on the lower-right side of the computational domain. The value of inlet solids velocity is derived from the following equation:

$$v_s = \frac{G_s A_r}{\rho_p \varepsilon_{s,0} A_p}, \quad (6.23)$$

where G_s is the solids circulation rate, $\varepsilon_{s,0} = 0.5$ is the inlet solids holdup, A_r and A_p are the cross-sectional region of the riser and the returning pipe, respectively. The outlet on the upper left side of the computational domain is set as the outflow.

Method 2 The objective of the second method (referred to as Method 2) is to simulate the circulation operation in the riser reactor. It uses the same gas inlet boundary conditions as Method 1. However, the solids flux at the solids inlet is set to be equal to the solids flux at the riser outlet. Consequently, the solids velocity at the solids inlet is defined as follow equation:

$$v_{s,inlet}(t) = \frac{\dot{V}_{s,outlet}(t)}{A_p}, \quad (6.24)$$

where $\dot{V}_{s,outlet}(t)$ is the volume flow rate of the solids at the outlet. As this flow rate varies over time, the inlet velocity of solids also changes accordingly. Since no external source introduces particles into the computational domain, the particles are initially packed within the riser. The pre-packed particles have an averaged solids holdup of 0.105 for the case of $U_g = 5$ m/s and $G_s = 300$ kg/m²/s according to Wang (2013).

Therefore, simulations for four cases are conducted in the study, as shown in Table 6.3. Other parameters used in the simulation is listed in Table 6.1.

Table 6.3: CFB riser case information

Case	Model	Equation	Method
Case 1	PHRTM	(6.17)	1
Case 2	FRTM	(6.20)	1
Case 3	PHRTM	(6.17)	2
Case 4	FRTM	(6.20)	2

6.4 Results and discussions

6.4.1 Time-averaged flow fields and reaction fields

Figures 6.2 (a), (b), and (c) show the cross-sectional averaged profiles of solids holdup, solids flux, and ozone concentration along the axial direction of the CFB riser reactor. The red open-markers represents experimental data by Wang et al. (2014), and the solid lines represent the numerical results of Case 1 and Case 2. Figures 6.2 (d) and (e) show the deviations in solids holdup and ozone concentration between the numerical results and experimental data. Figure 6.3 shows the comparisons for Case 3 and Case 4. The numerical results of the cross-sectional profiles are calculated by following equations:

$$\bar{\varepsilon}_{s,h}(h) = \frac{1}{t_1 - t_0} \int_{t_0}^{t_1} \left(\frac{1}{d_{rs}} \int_0^{d_{rs}} \varepsilon_s(t, x, h) dx \right) dt, \quad (6.25)$$

$$\bar{F}_{s,h}(h) = \frac{\rho_s}{t_1 - t_0} \int_{t_0}^{t_1} \left(\frac{1}{d_{rs}} \int_0^{d_{rs}} (\varepsilon_s(t, x, h) v_s(t, x, h)) dx \right) dt, \quad (6.26)$$

$$\bar{Y}_{g,h}^*(h) = \frac{1}{t_1 - t_0} \int_{t_0}^{t_1} \left(\frac{1}{d_{rs}} \frac{1}{\bar{\varepsilon}_{g,h_i}(t, h)} \int_0^{d_{rs}} (\varepsilon_g(t, x, h) Y_g^*(t, x, h)) dx \right) dt, \quad (6.27)$$

where d_{rs} is the diameter/width of the riser, x is the radial/horizontal direction positions, and h is the axial/vertical direction positions. The ozone concentration used in

Equation (6.27) is reduced by the inlet ozone concentration:

$$Y_g^* = \frac{Y_g}{Y_{g,0}}, \quad (6.28)$$

where the $Y_{g,0}$ is the ozone concentration at the inlet.

Figure 6.4 illustrates radial profiles of time-averaged solids holdup, particle velocity, and ozone concentration, at two axial locations, representing the flow developing region ($h = 0.57$ m) and flow developed region ($h = 4.78$ m). Similarly, Figure 6.5 shows axial profiles of the same parameters for the flow and reaction fields at two radial locations, representing the central ($x/R = 0$) and wall ($x/R = 0.95$) regions.

Flow fields and reaction fields in the cases using Method 1 When Method 1 is used, the simulation results show that in the bottom region of the riser (0 to 2 m), the particle quantity is approximately 50% less than to the experimental results. In the region of 2 to 10 m, there is a good agreement between numerical and experimental results, as shown in Figure 6.2 (a). In the radial direction, in the bottom region, the solids holdup from the numerical results is lower near the wall compared to the experimental results, as shown in Figure 6.4 (b). In the flow developed region, the numerical results are in good agreement with the experimental results, as shown in Figure 6.4 (a). Throughout the entire reactor, the numerical results exhibit a noticeable core-annulus structure, characterized by high solids holdup in the annulus region and low solids holdup in the core region. In the axial direction, the solids holdup profile in the central region is in good agreement with the experimental data, as shown in Figure 6.5 (a). However, in the wall region, the profile of simulation results remains constant at 0.2, which is different from the experiment where it varies from 0.4 to 0.1, as shown in Figure 6.5 (b).

Regarding the solids velocity and flux, due to the solids inlet boundary condition

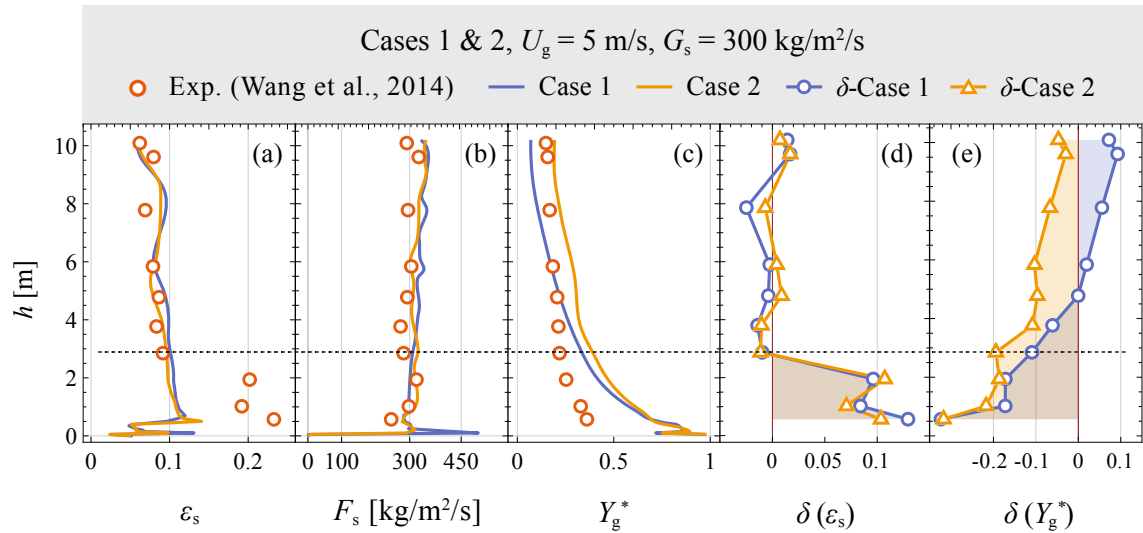


Figure 6.2: Comparison of numerical results and experimental data for cross-sectionally averaged time-averaged profiles along the axial direction for Case 1 (PHRTM) and Case 2 (FRTM)

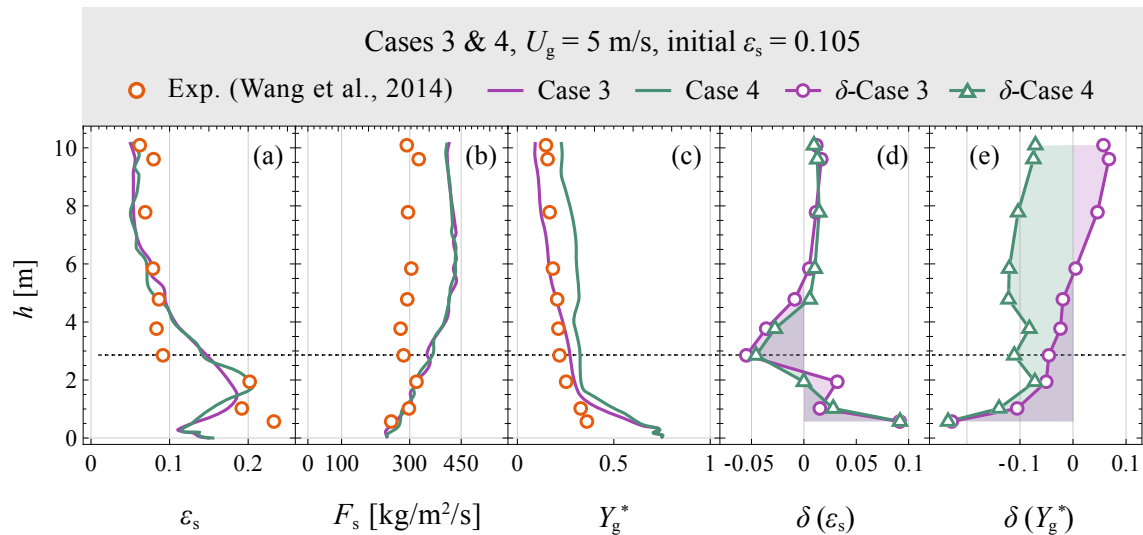


Figure 6.3: Comparison of numerical results and experimental data for cross-sectionally averaged time-averaged profiles along the axial direction for Case 3 (PHRTM) and Case 4 (FRTM)

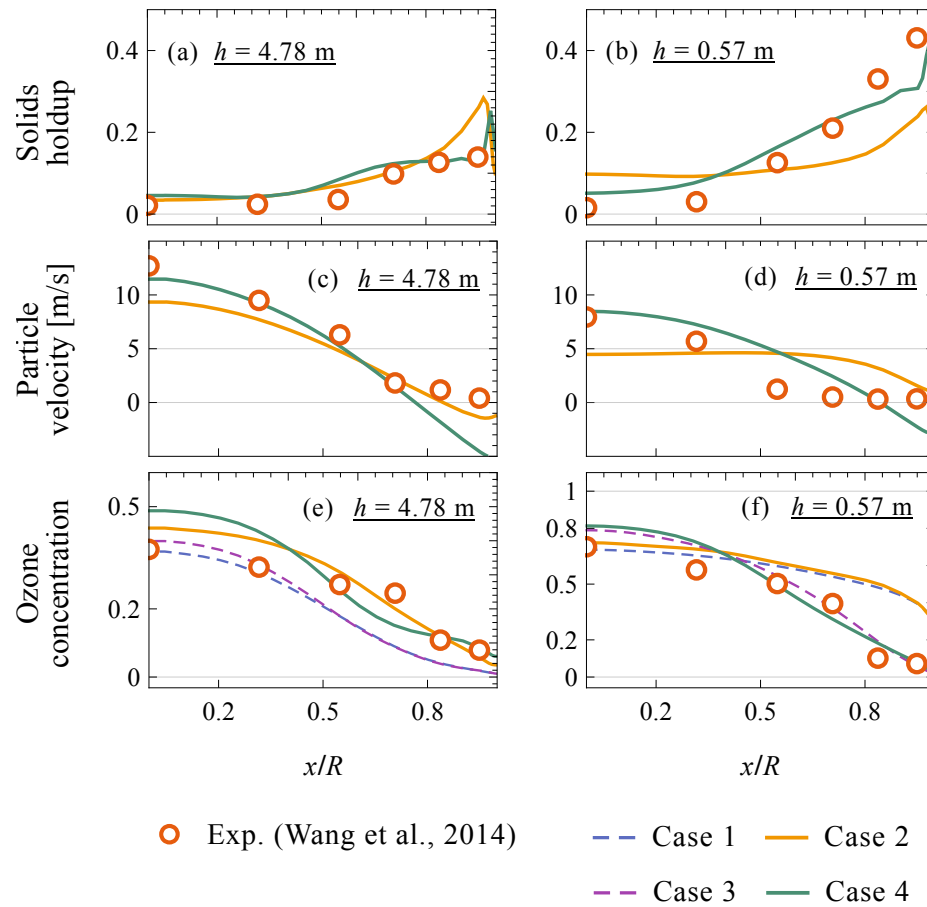


Figure 6.4: Comparison of the time-averaged radial profiles at flow developing and developed regions between numerical results and experimental data

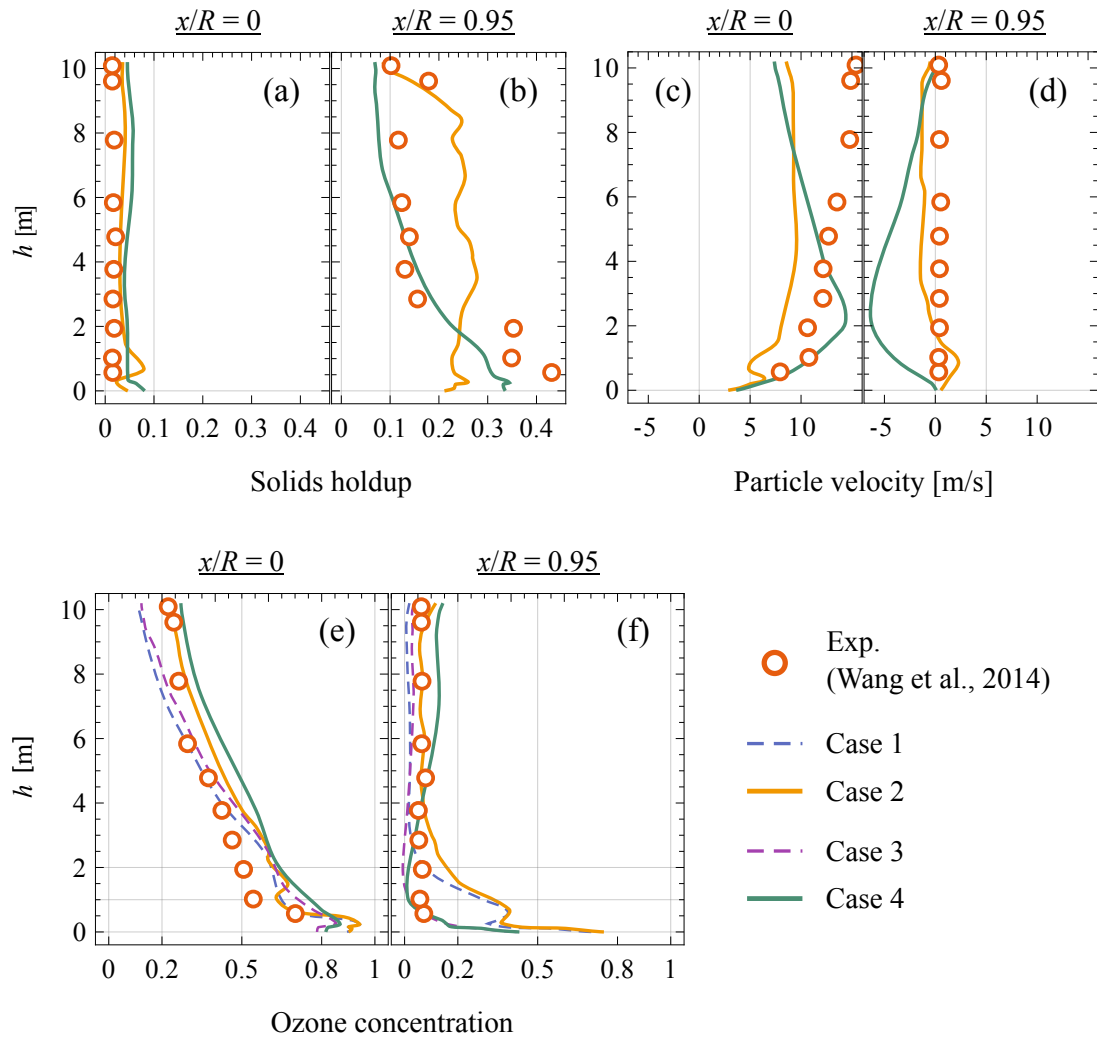


Figure 6.5: Comparison of the time-averaged axial profiles at central and wall regions between numerical results and experimental data

of Method 1 being set based on the G_s , the solids flux is in complete accordance with the experimental data in Figure 6.2 (b). Radially, within the bottom region, the particle velocity profile remains relatively constant at the center of the riser, equal to the superficial gas velocity, and gradually decreases to zero near the wall, as shown in Figure 6.4 (d). In the flow developed region, the velocity profile assumes a parabolic shape. The velocity is slightly below 0 in the wall region and reaches up to 12 m/s in the central region. Axially, the profiles of particle velocity in the numerical results have the same shape as the experimental results, as shown in Figure 6.5 (c). However, in the central region of the riser, the velocity is approximately 5 m/s lower than that in the experimental data.

In terms of the ozone concentration, distinct differences appear in the ozone concentration profiles between the cases using the PHRTM and FRTM. In the inlet region (0 to 1 m), the filtered model does not bring significant differences to the ozone concentration profiles. In this region, in contrast to the experimental results, the ozone concentration is higher in the wall region because fewer particles appear in this region, as shown in Figure 6.4 (f). In the region of 1 to 2 m, the ozone reaction in Case 2, which uses the filtered model, is lower compared to Case 1 by approximately $0.05 Y_{g,0}$, as shown in Figure 6.2 (c) and (e). Figure 6.5 indicates that this difference primarily originates from the difference of ozone concentration in the wall region. In the region from 2 to 10 m, the differences in ozone concentration between Cases 1 and 2 gradually increase to $0.1 Y_{g,0}$ and remain almost constant along the axial direction, as shown in Figure 6.2 (e). At the outlet of the riser, there are $0.19 Y_{g,0}$ remains in the gas phase in Case 1, whereas only $0.07 Y_{g,0}$ remains in Case 2. Compared to the remaining $0.15 Y_{g,0}$ of ozone in the experimental results, the introduction of the filtered correction model has improved on the PHRTM. From Figure 6.4, the radial distribution trend of the ozone concentration in Case 1 and Case 2 is essentially the same, but the profile of Case 2 is lower and corresponds more closely to the experimental results. From the axial profiles, the reaction rate in the central region

of the riser in Case 2 gradually slows down. In the wall region, the ozone concentration remains a constant, unlike in Case 1 whose ozone is fully reacted. These phenomena align more closely with the experimental results.

In short, when using Method 1, good agreement is observed between the hydrodynamic characteristics in the numerical results and the experimental results for the region above 2 m in the riser. When using the PHRTM, the reaction is too fast, whereas the FRTM decreases the reaction rate, resulting in an ozone concentration profile that better matches the experimental results. Therefore, the introduction of the reaction correction coefficient in the PHRTM has provided a good correction to the reaction behaviour in the CFB riser reactor.

Flow fields and reaction fields in the cases using Method 2 When using Method 2 for simulation, the total quantity of particles in the riser is initially established based on experimental results and remains constant throughout the simulation. Under the combined influence of airflow and gravity, particles within the riser assume a new distribution from the initial uniform distribution. According to Figure 6.3 (a), the time-averaged cross-sectional solids holdup has an S-shaped distribution along the axial direction of the riser and exhibits a typical core-annulus structure in the radial direction, as shown in Figure 6.4 (a) and (b). This distribution demonstrates an excellent agreement in the axial, radial, and cross-sectional profiles when compared with the experimental results.

Nonetheless, notable differences arise between the numerical results and experimental data for particle velocity profiles and solids flux within the riser. Figure 6.3 (b) shows the solids flux from the numerical results exceeds the G_s by approximately 50 %. Figure 6.5 (d) show that particles exhibit rapid downward flow near the wall, reaching a maximum velocity of 5 m/s at a height between 2 to 3 m. To maintain a consistent solids flux in the riser, the particles move upward at the centre of the riser with a velocity of up to 15 m/s

at this particular height. Then, along the axial direction of the riser, both upward and downward particle velocities decrease. These particle velocity profiles deviate from the numerical results of cases using Method 1 as well as the experimental data, consequently giving rise to distinctive ozone concentration profiles.

In the bottom region (0 to 1 m), according to Figure 6.3 (c), the ozone concentration profiles of Cases 3 and 4 are almost the same. Compared to Cases 1 and 2, more ozone is reacted in Cases 3 and 4 due to the presence of more particles in the bottom region. Therefore, the ozone concentration profiles of Cases 3 and 4 exhibit better agreements with the experimental results than those of Case 1 and 2. The profiles in the radial direction at the bottom region also matches well, as shown in Figure 6.4 (f). On the other hand, in the region from 2 to 10 m in the riser, the influence of the filtered reactive transport model results in less ozone being reacted in Case 4. As shown in Figure 6.5 (e), in the central region of the riser, results of Case 3 exhibits a higher reaction rate and more ozone is reacted compared to both the results of Case 4 and the experimental data. The trend of the ozone concentration profile of Case 4 agrees well with the experimental results, although the values are higher. In the wall region, as shown in Figure 6.5 (f), the ozone concentration profile in Case 4 slightly increases with height. This phenomenon can be attributed to multiple factors at play. Firstly, at the bottom of the wall region, significant amount of particles blockages there, which leads to an increase in gas flow velocity in the central region. This fast gas flow carries a substantial amount of unreacted ozone into the region above 2 m. Conversely, in the wall region above 2 m, particle blockage is no longer present, resulting in a decrease in gas flow velocity and allowing ozone to flow and diffuse into the wall region. Additionally, the influence of the filtered reactive transport model reduces the reaction rate within the wall region. All these factors collectively contribute to the observed phenomenon of higher ozone concentration in the annulus region above 2 m compared to below 2 m.

In short, by using Method 2, the distribution of solids and ozone in the riser is in good agreement with the experimental data, except for the particle velocity and solids flux. The correction made by the FRTM reduces the reaction rate and leads to the ozone concentration profiles in the core region agree well with the experimental data. However, there is an excessive reduction of the reaction rate in the wall region. Ultimately, after correction by the FRTM, the ozone concentration at the outlet is $0.22 Y_{g,0}$, compared to the value of $0.09 Y_{g,0}$ from the case with the PHRTM. In comparison to the remaining $0.15 Y_{g,0}$ of ozone in the experimental results, the introduction of the FRTM in the cases using Method 2 has slightly over-reduced the reaction rate in the riser.

In summary of this section, under different methods, the filtered reactive transport model has consistently corrected the reaction rate in the gas-solids CFB riser reactor, resulting in an overall reduction in the reaction rate. The model has a limited impact on the bottom region but exerts a significant influence between 2 to 10 m in the riser. In the core region, the model has improved the consistency of the ozone concentration profile with the experimental results.

6.4.2 Effects of the reaction correction coefficients in the riser

Figure 6.6 shows the cross-sectional profiles of the reaction rate and reaction correction coefficient along the axial direction of the riser. The numerical results of the cross-sectional profiles for reaction rates and reaction correction coefficient are calculated by following equations:

$$\bar{r}_h(h) = \frac{1}{t_1 - t_0} \int_{t_0}^{t_1} \left(\frac{1}{d_{rs}} \int_0^{d_{rs}} \left(H_r k_r \rho_g \varepsilon_s Y_g^{O_3} \right) dx \right) dt, \quad (6.29)$$

$$\bar{H}_{r,h}(h) = \frac{1}{t_1 - t_0} \int_{t_0}^{t_1} \left(\frac{1}{d_{rs}} \int_0^{d_{rs}} H_r(t, x, h) dx \right) dt. \quad (6.30)$$

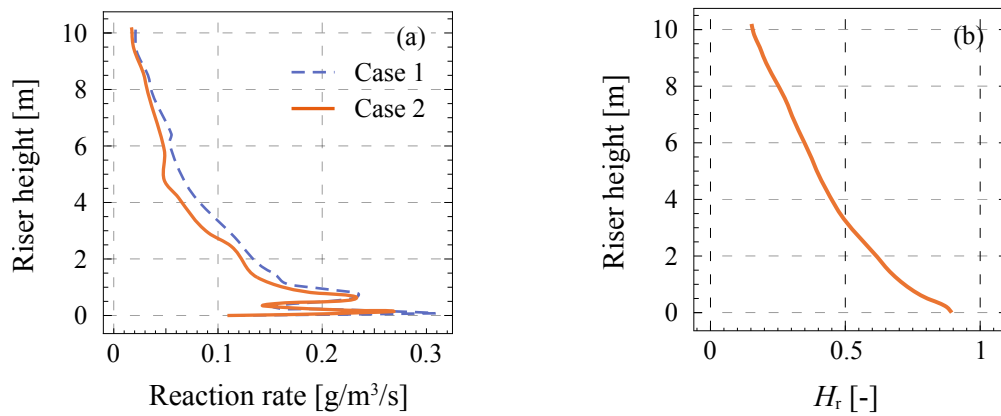


Figure 6.6: Comparison of reaction rates in the cases using the PHRTM and FRTM: (a) time-averaged cross-sectional profiles of the reaction rate and (b) reaction correction coefficient along the axial direction of the riser

Figure 6.7 (a) shows the amount of ozone reacted in 1 s within different longitudinal intervals. The entire riser is divided into five intervals, with each section having a height of 2 m. Figure 6.7 (b) illustrates the distribution of the reaction correction coefficient for each interval.

Figure 6.8 displays the time-averaged results of the reaction correction coefficient in the riser of Case 2, consisting of three plots: the (a) contour of the riser, (b) axial profiles, and (c) radial profiles. Figure 6.8 (b) depicts the axial profiles at three radial positions from the center to the wall of the riser. Figure 6.8 (c) illustrates the radial profiles at three axial positions from the bottom to the top of the riser.

Figure 6.9 reveals the instantaneous flow fields and reaction fields of Case 2 at the (a) top and (b) bottom of the riser. The contours depict two sections of the riser: the region from 0.3 to 0.8 m and the region from 9.5 to 10.0 m. The variables of the fields include (1) solids holdup, (2) ozone concentration, (3) reaction correction coefficient, and three

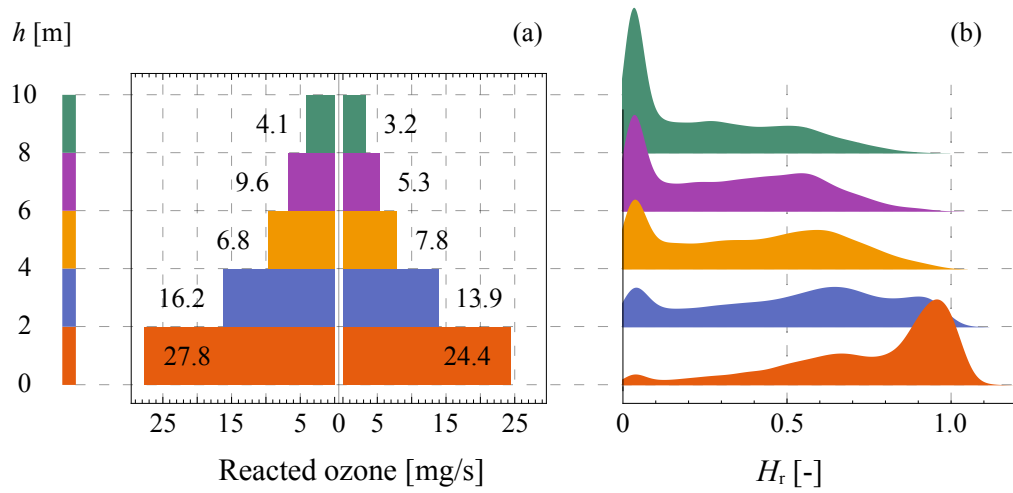


Figure 6.7: Comparison of reaction rate in the simulations using the PHRTM and FRTM: (a) the amount of ozone reacted in different height sections of the riser in 1 s and (b) the distributions of the reaction correction coefficient in each height section for Case 2

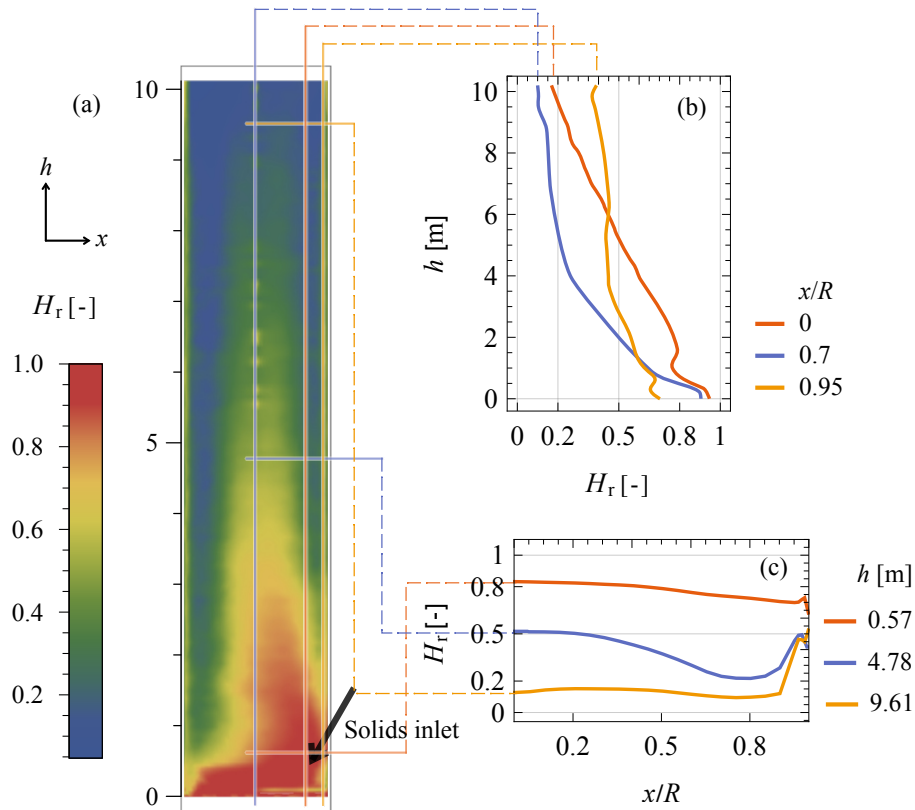


Figure 6.8: Time-averaged results of the reaction correction coefficient of Case 2: (a) contour of the whole computational domain, (b) axial profiles at different radial locations, and (c) radial profiles at different axial locations

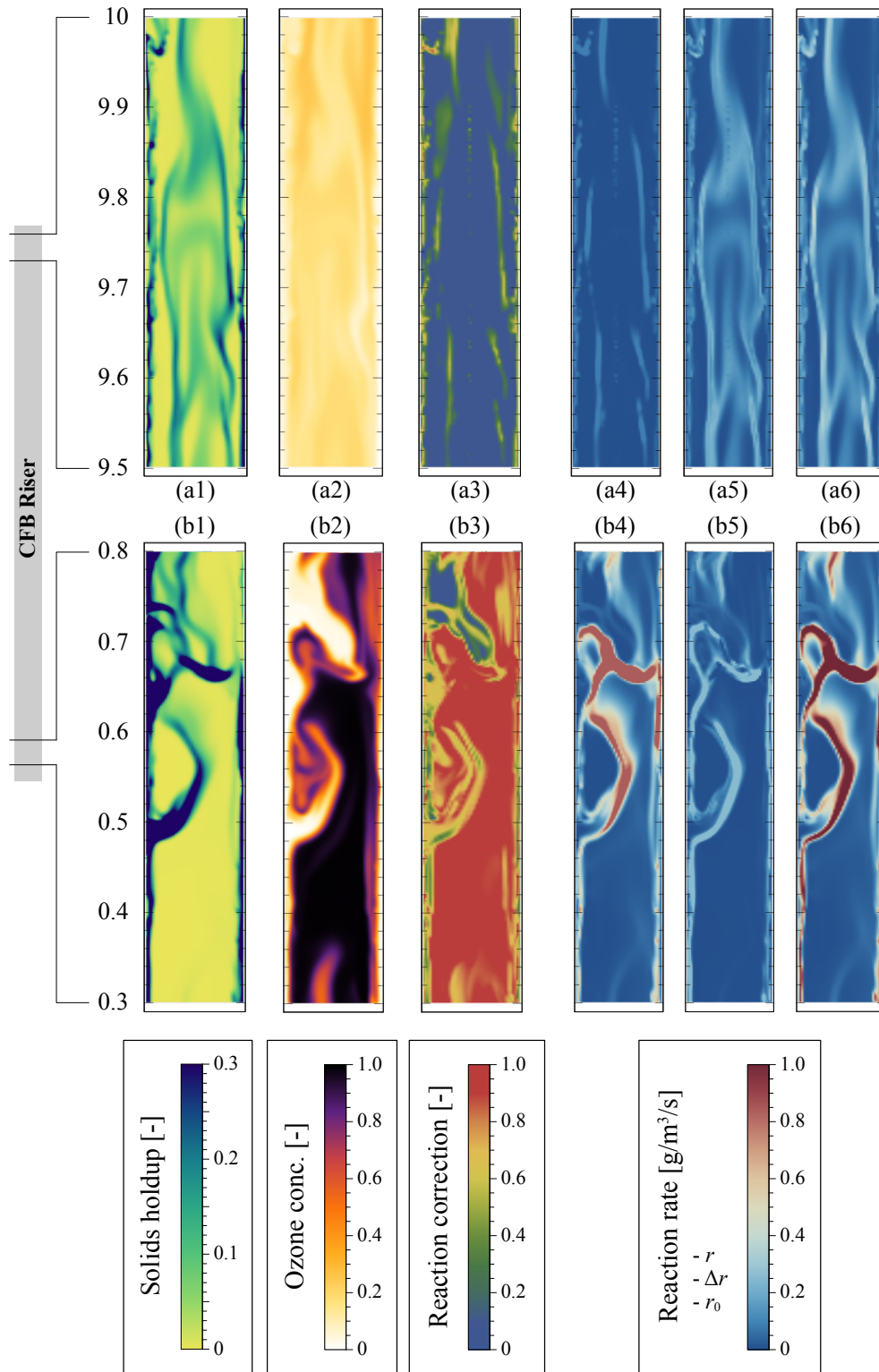


Figure 6.9: Instantaneous flow fields and reaction fields of Case 2

reaction rates. The three reaction rates are:

$$r = r_0 H_r = H_r k_r \rho_g \varepsilon_s Y_g^{O_3}, \quad (6.31)$$

$$\Delta r = r - r_0 = r - \frac{r}{H_r}, \quad (6.32)$$

$$r_0 = \frac{r}{H_r} = k_r \rho_g \varepsilon_s Y_g^{O_3}, \quad (6.33)$$

where r_0 is (6) the reaction rate of the PHRTM, (4) r is the reaction rate of the FRTM, and (5) Δr is the difference between the two reaction rates.

Flow developing region (bottom region) Section 6.4.1 mentioned that the ozone concentration profiles in the bottom region does not change significantly between Case 1 (PHRTM) and Case 2 (FRTM). As shown in Figure 6.6 (a), the fluctuation in the reaction rate is significant in the bottom region. However, when compared to the case using the PHRTM, the FRTM does not bring a noticeable change in the reaction rate. In the bottom region, the overall correction coefficients decrease from 0.9 to 0.7 along the riser from 0 to 1 m, as shown in Figure 6.6 (b). In the radial direction, as shown in Figure 6.8 (c), the correction coefficients are relatively uniform, with values of approximately 0.8. In Figure 6.7 (b), the orange distribution represents the correction coefficient distribution in the 0 to 2 m region. Most H_r in this region are around 0.95, with some ranging from 0.5 to 0.8. These results regarding reaction rates and H_r can account for the results in the previous section, indicating that the impact of FRTM on the ozone concentration profile in the bottom region is not significant. However, as depicted in Figure 6.7 (a), only 24.4 mg of ozone reacts within the 0 to 2 m region in 1 second when using the FRTM, which is 3.4 mg less than when using the PHRTM.

Figure 6.9 (b) displays the instantaneous results in the bottom region of the riser.

Within the core region of the riser, large and dense clusters have emerged, occupying regions with an ozone concentration close to 0. In contrast, outside these clusters, ozone concentrations are near $Y_{g,0}$. The regions with higher reaction rates are primarily located at the edges of these clusters. The FRTM provides reaction correction coefficients close to 0 in regions with very low ozone concentrations and close to 1.0 in regions with high ozone concentrations. However, in both types of regions, the reaction rates are too low to impact the overall reaction rate and the ozone concentration in the bottom region. As shown in Figure 6.9 (b5), the FRTM significantly corrects reactions in the regions near the edges of clusters and close to the wall. After the corrections, the reaction zones in the bottom region do not decrease, but the overall reaction rate decreases.

Therefore, the majority of H_r in the distribution near 0.95 is more concentrated in the region where the reaction rates are low. In the regions at the edges of the clusters, where the reaction rates are high, there is a reduction in reaction rates under the influence of the FRTM. This results in a decrease in the amount of ozone reacted, as observed in Figure 6.7 (a). However, the overall profiles of the reaction rate and ozone concentration at the bottom do not exhibit a significant decrease when compared to Case 1. These results contradict the analysis presented above.

Flow developed region Under the influence of the FRTM, distinct differences appear in ozone concentration profiles between Case 1 and 2, as depicted in Figure 6.2 (c), 6.4 (e), 6.5 (e) and 6.5 (f). Firstly, there is a notable decreasing in the overall H_r from 0.65 to 0.15 within the 2 to 10 m range, leading to a lower reaction rate in Case 2 compared to Case 1, as illustrated in Figure 6.6. Secondly, during the particle flow's development process, changes occur in the radial distributions as follows: In the core region, H_r decreases linearly from 1 to 0.2 with increasing height; in the region of $x/R = 0.7$, H_r sharply drops to 0.2 within the 0 to 4 m range, followed by a slowly decline in the rest of the riser. The

wall region follows a similar trend to the region of $x/R = 0.7$ but maintains a higher H_r value of 0.5 at the end.

These characteristics of H_r distribution in the developed region result in distinct reaction behaviour compared to the bottom region. In the developed region, the distributions of solids holdup and ozone concentration are more uniform, as shown in Figure 6.9 (a1) and (a2), providing reactants with increased opportunities to interact with catalysts. However, Figure 6.9 (a3) reveals that the FRTM yields low H_r values (less than 0.1) in most regions of the developed region, except for the wall and dense streamer regions. Consequently, a significant reduction in the reaction rate within the core region is observed when comparing the results of Figure 6.9 (a4) and (a6). Unlike the FRTM's influence in the bottom region, not only do local reaction rates decrease, but the region where reactions occur also contracts. Hence, in each section above 2 m of the riser, there is a more substantial decrease in reacted ozone under the FRTM's influence. The distribution of H_r in each section in the region of 2 to 10 m of the riser indicates a prevalence of H_r values in the range of 0 to 0.1, effectively diminishing the overall reaction rate in this region.

In this section, by examining the effective reduction of the reaction rate within the reactor, the differing effects of the FRTM on the bottom region and the developed region are discovered. In the bottom region, the FRTM primarily decreases the reaction rate of regions with high reaction rates. However, in the developed region, it not only decreases the local reaction rate but also diminishes the region where reactions take place. This partially explains the phenomenon observed in the ozone concentration profiles, where there is minimal difference in the bottom region but a more significant difference in the developed region.

6.5 Conclusions

The machine learning-aided FRTM has been successfully integrated with gas-solids CFB riser simulations. Two simulation methods were used for simulations of the riser reactor to explore the performance of the FRTM. The introduction of the FRTM led to an overall reduction in the reaction rate and an improved agreement between experimental data and numerical results. In the bottom region, ozone concentration profiles are similar in both cases, whether or not the FRTM is used. In this region, the model primarily decreased the reaction rate in regions with very high reaction rates. However, in the developed region, more ozone remains in the reactor along the axial direction of the riser when the filtered model is utilized. In this region, the model reduced the region where reactions occurred in the core region of the riser.

References

- ANSYS, Inc. (2022). Ansys Fluent, Release 2022R1. ANSYS, Inc.
- Ding, J., & Gidaspow, D. (1990). A bubbling fluidization model using kinetic theory of granular flow. *AIChE journal*, 36(4), 523–538.
- Ergun, S. (1952). Fluid flow through packed columns. *Chemical engineering progress*, 48(2), 89.
- Gidaspow, D. (1994). *Multiphase flow and fluidization: Continuum and kinetic theory descriptions*. Academic Press.
- Gidaspow, D., Bezburuah, R., & Ding, J. (1991). Hydrodynamics of circulating fluidized beds: Kinetic theory approach. *Proceedings of the 7th International Conference on Fluidization, Gold Coast, Australia, 3-8 May 1992*.
- Huilin, L., & Gidaspow, D. (2003). Hydrodynamics of binary fluidization in a riser: Cfd simulation using two granular temperatures. *Chemical engineering science*, 58(16), 3777–3792.
- Lun, C. K. K., Savage, S. B., Jeffrey, D. J., & Chepuruiy, N. (1984). Kinetic theories for granular flow: Inelastic particles in couette flow and slightly inelastic particles in a general flowfield. *Journal of fluid mechanics*, 140, 223–256.
- Peng, B., Zhu, J., & Zhang, C. (2010). Numerical study on the effect of the air jets at the inlet distributor in the gas- solids circulating fluidized-bed risers. *Industrial & Engineering Chemistry Research*, 49(11), 5310–5322.
- Schaeffer, D. G. (1987). Instability in the evolution equations describing incompressible granular flow. *Journal of differential equations*, 66(1), 19–50.
- Sinclair, J. L., & Jackson, R. (1989). Gas-particle flow in a vertical pipe with particle-particle interactions. *AIChE Journal*, 35, 1473–1486. <https://doi.org/10.1002/aic.690350908>
- Sun, Z., Zhang, C., & Zhu, J. (2022). Numerical investigations on gas–solid flow in circulating fluidized bed risers using a new cluster-based drag model. *Particuology*, 63, 9–23.
- Wang, C. (2013). *High density gas-solids circulating fluidized bed riser and downer reactors* [Doctoral dissertation, The University of Western Ontario]. <https://ir.lib.uwo.ca/etd/1572/>
- Wang, C., Wang, G., Li, C., Barghi, S., & Zhu, J. (2014). Catalytic ozone decomposition in a high density circulating fluidized bed riser. *Industrial & Engineering Chemistry Research*, 53(16), 6613–6623.

CHAPTER 6. INVESTIGATING THE IMPACT OF PARTICLE ...

- Wen & Yu. (1966). Mechanics of fluidization. *Fluid Particle Technology, Chem. Eng. Progress. Symposium Series*, 62, 100–111.
- Zehner, P., & Schlünder, E. (1970). Wärmeleitfähigkeit von schüttungen bei mäßigen temperaturen. *Chemie Ingenieur Technik*, 42(14), 933–941.

Chapter 7

Conclusions and Recommendations

7.1 Thesis summary and conclusions

This thesis work comprehensively investigates reaction behaviours of the catalytic ozone decomposition reaction in a gas-solids CFB reactor using numerical methods. The hydrodynamic characteristics within CFB predominantly influence the reaction behaviours.

Figure 7.1 depicts a schematic of the simplified steps of the ozone decomposition reaction occurring in a gas-solids fluidization system. The journey of ozone from the air

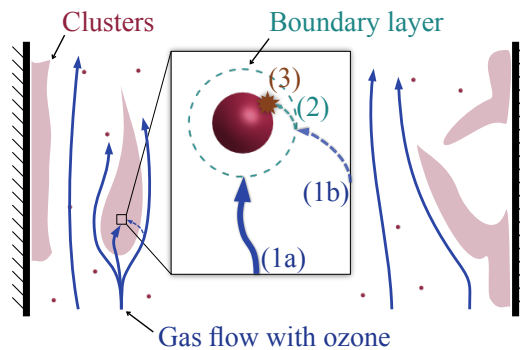


Figure 7.1: Steps of the ozone decomposition reaction occurring in a gas-solids fluidization system

stream to the catalyst particles, and its subsequent reaction process, emphasizes that the reaction is affected by many factors, which include the hydrodynamic characteristics, mass transfer, and reaction kinetics. The hydrodynamic characteristics of a CFB reactor are

CHAPTER 7. CONCLUSIONS AND RECOMMENDATIONS

influenced by factors such as the direction of particle flow, inlet structure, and operating conditions. The key characteristic of the flow is the heterogeneous gas-solids distribution, which arises from two main causes: macro-segregation due to the core-annulus structure and micro-segregation resulting from particle clustering. This heterogeneity makes the reaction behaviours in the CFB reactor complex and difficult to predict. This study methodically explores the effects of the hydrodynamic characteristics on the ozone decomposition reaction behaviours in a CFB reactor, highlighting their collective impact on the reaction process.

Initially, a pseudo-homogeneous reactive transport model for the ozone decomposition reaction was developed based on experimental data. The validation of this model in a micro fixed-bed reactor demonstrates its robustness and applicability in describing ozone behaviours in a gas-solids fluidization system.

Building on this foundation, the study then explores the effects of turbulence models, specularly coefficients, and simulation methods on hydrodynamic characteristics and reaction behaviours within a 10.2-meter CFB riser reactor. Employing the $k-\epsilon$ turbulence model, as opposed to a laminar model, results in more uniform flow and reaction fields. This model also reduces gas-solids segregation within the riser reactor, thereby enhancing contact efficiency. However, it is noted that the $k-\epsilon$ turbulence model has a tendency to overestimate the intensity of turbulence, leading to flow structures that significantly deviate from experimental observations. Adopting a smaller specularly coefficient increases the tendency of particles near the wall to flow downwards, causing a denser bottom region and a more dilute upper region in the riser. The extra particles accumulating at the bottom thickens the annulus region, allowing more ozone reactions in the bottom region, but also reduces contact efficiency there.

The comparative analysis of riser and downer reactors under various operating con-

CHAPTER 7. CONCLUSIONS AND RECOMMENDATIONS

ditions unveils the profound impact of gravitational orientation on hydrodynamic characteristics and reaction behaviours of the CFB reactors. Within the riser, clusters are upright and elongated, with a clear phase interface between the gas and solids. The radial distributions of solids holdup, particle velocity, and ozone concentration in the riser all exhibit significant gradients. Conversely, in the downer, particle aggregates are freer and less compact. The distributions of the reactants and catalysts are more uniform, along with more stable and synchronized gas-solid flows, leading to higher efficiency of gas-solids contact and reaction compared to the riser. Undoubtedly, the downer is a more superior reactor. However, under the same operating conditions, the lower particle holdup in the downer remains a significant drawback that cannot be overlooked.

Tracking the flow of gas and solids in the riser and downer revealed distinctly different flow structures in these two reactors. The analysis of RTD results and instantaneous contours indicated that the downer exhibits characteristics similar to a PFR, whereas the riser displays strong backmixing in the axial direction. Consequently, an internal particle circulation mechanism was proposed to account for the observed backmixing in the riser. In addition, the exponential shape of the axial profile of ozone concentration in the riser can be attributed not only to high solids holdup and high reactant concentration at the bottom, as well as the intense interaction and mixing of reactants and catalysts, but also to the substantial axial backmixing, which leads to enhanced ozone mixing.

To further explore the impact of meso-scale flow structures on reaction behaviours, a sub-grid reactive transport model was developed using the filtering method and artificial neural network model (ANN). Expanding the dataset with a wider range of filtered data and incorporating more gradient features allowed the model to adapt to a greater variety of flow structures within CFB riser reactors and more accurately determine the appropriate reaction correction coefficient. ANN became indispensable for regression tasks with

such large data volumes and complex relationships. The feature importance analysis using the SHAP method revealed that the reaction correction coefficient is significantly influenced by factors like filter size, ozone concentration, solids holdup, and the gradients of solids holdup and ozone concentration, demonstrating clear monotonic relationships between these features and the coefficient. Different distributions of H_r in the regions of developing and developed flow highlighted the varying roles meso-scale structures play in reaction behaviours. In the developing flow region, rapid changes in meso-scale structures do not lead to noticeable micro-segregation of the two phases, so the reaction rate remains unaffected. However, in the developed flow region, the stability of meso-scale structures results in segregation of reactants and catalysts, subsequently decreasing the reaction rate.

7.2 Limitations and recommendations

This work has studied the impact of many factors on hydrodynamic characteristics, as well as the subsequent discussion on the influence of these characteristics on reaction behaviors. However, the reaction behaviors in a CFB reactor remain a complex issue affected by multiple factors, and the research in this thesis is far from sufficient to understand it. The following points outline some of the shortcomings of this work and perspectives for future research in this field.

The necessity of three-dimensional simulations Due to limitations in computational resources, all the modelling work in this thesis is conducted in two dimensions, which is an obviously shortcoming. Although in many scenarios, two-dimensional simulations can substitute for three-dimensional simulations, two-dimensional cases can never perfectly replicate real three-dimensional environments. For example, differences in cross-sectional averaged profiles caused by cylindrical and square columns, as well as potential changes in internal solids circulation, can lead to variances in quantitative analysis of the reaction.

CHAPTER 7. CONCLUSIONS AND RECOMMENDATIONS

Therefore, when conditions permit, the use of three-dimensional simulation is undoubtedly preferable.

Currently, the introduction of sub-grid models for TFM has made three-dimensional simulation of industrial-scale CFB reactors possible, and a considerable number of articles have reported on such work. However, when applying sub-grid models to TFM, there are two issues that cannot be overlooked:

1. In CFB riser reactors, features such as solids holdup, particle velocity, and ozone concentration exhibit significant gradients in their radial distribution, particularly near the walls where changes are especially drastic. Therefore, a sufficient number of grids is needed for discretization in the radial direction. According to findings in this study, 40 grids are necessary in two-dimensional cases. When there are 60 or even 80 grids in the radial direction, radial profiles show further improvement. Reducing the number of grids in the radial direction leads to flattened radial profiles due to the inability to give larger gradients.

Sub-grid models are typically applicable to mesh sizes ranging from a few tens to a couple of hundred d_p , but in some cases, this may conflict with the number of grids needed in the radial direction. For the CFB riser reactor studied in this work, with a diameter of 0.0762 m, if the filter size is set at 50, only 22 grids can be placed in the radial direction, and if the filter size is 25, then 44 grids can be placed. However, considering the height of 10.2 m for this CFB riser reactor, about 6000 grids are needed in the axial direction. If it's a two-dimensional case, a total of 250,000 grids is acceptable, but in a three-dimensional case, it would require close to 10 million grids, which is unfeasible. Even with an effective sub-grid model, due to the limitations on the number of grids in the radial direction, it cannot effectively reduce computational costs. Using grids with a larger aspect ratio and developing

CHAPTER 7. CONCLUSIONS AND RECOMMENDATIONS

corresponding sub-grid models is a possible solution. Fortunately, most industrial fluidized bed reactors do not have such extreme aspect ratios, but this potential limitation of sub-grid models does exist.

2. Another issue is that if one intends to develop sub-grid models for mass transfer, heat transfer, and reaction, it is necessary to conduct the development in the same systems and scenarios as those used for developing hydrodynamic sub-grid models. It may be risky and unreasonable to develop models for reactions and others directly based on a hydrodynamic sub-grid model developed by others.

Therefore, in future research, focusing more efforts on DEM may be reasonable, especially in studying particle interactions and reactions, where DEM has greater advantages. Notably, some studies have successfully deployed DEM on GPUs, which has significantly reduced computational costs (Lu, 2022; Musser et al., 2022). This makes it feasible to use DEM for simulating industrial-scale fluidized bed reactors in the future.

More complicated chemical reactions in CFB reactors should be studied It's worth noting that due to the simplicity of ozone decomposition, the reaction does not cause temperature and gas volume changes when occurring in the reactor. Additionally, when this reaction occurs on FCC catalysts, it is controlled by the reaction rate rather than by mass transfer. Therefore, the impact of external mass transfer is not considered in the modelling process. However, for industrial reactions, such as FCC, temperature and volume change during the reaction process, especially the significant increase in volume, greatly affects the motion, distribution, and clustering behavior of particles. These effects cannot be reflected in cold state experiments, ozone decomposition experiments, or current simulations.

Turbulence models and drag models in fluidization systems Although, after comparing with experimental results, this thesis prefers to use the laminar flow model for the gas phase, using this model in gas-solids fast fluidization simulations is not reasonable. However, using classic turbulence models like $k-\epsilon$ model or $k-\omega$ model in multiphase simulations is also unreasonable. Reported experiments have also shown that the presence of particles significantly weakens the turbulence intensity of the gas fluid. Therefore, it is necessary to specifically develop turbulence models for multiphase systems.

Regarding drag models, the field is still commonly using experiment-based models, such as Wen-Yu model. These models are cleverly constructed and can give good results in many cases. However, most of these models are based on experimental results from liquid-solids fluidization systems and seem inadequate for modern research that demands increasingly higher precision.

Currently, DNS and LBM have shown great capability in developing new turbulence models and drag models, but they are still in the early stages of development and require more researchers to invest more effort in their advancement.

Effects of factors on the CFB reactor performance should be considered comprehensively Studying the performance of a reactor by numerical methods should be a comprehensive consideration of the reactor. Due to the significant impact of heterogeneous meso-scale flow structures on various aspects of fluidized bed reactors, which also represent a focus and difficulty in fluidized bed research, researchers often invest considerable effort into studying meso-scale structures and their effects, attributing many phenomena in reactors to them. However, there are other influencing factors that also play a significant role, and these factors, along with meso-scale structures, affect the overall performance of the reactor.

CHAPTER 7. CONCLUSIONS AND RECOMMENDATIONS

When researchers conduct experiments, all the factors mentioned above that can affect reactor performance are at play, contributing to the final data results. However, in current modelling work, researchers often simplify and omit some of the factors, either necessarily or unnecessarily. For example, omitting almost all inlet structures, omitting the other half of the equipment in CFB that is not the target of the study, simplifying particle size distribution to mean diameter, etc. Some simplifications and omissions are due to limitations of computational cost, while others are avoidable. As a result, some modelling works, having neglected certain factors, may overemphasize the impact of the factors they have considered, especially when comparing and validating their models with experimental results. However, it is also highly likely that the factors ignored in simulations have caused discrepancies between numerical results and experimental data, especially when simulating large-scale equipment.

In summary, modelling a CFB reactor should involve a more comprehensive consideration of all factors that affect reactor performance. This entails considering as many of these factors as possible into the simulations. For factors that cannot be integrated due to certain limitations, their impact should be acknowledged and considered in the subsequent analysis or discussion. Consequently, this approach places higher demands on modellers: modelling work should not be seen as separate from experimental work. Researchers need to be sufficiently familiar with the structure and operation of reactors, rather than relying solely on descriptions from academic papers.

References

- Lu, L. (2022). GPU accelerated MFiX-DEM simulations of granular and multiphase flows. *Particuology*, 62, 14–24.
- Musser, J., Almgren, A. S., Fullmer, W. D., Antepara, O., Bell, J. B., Blaschke, J., Gott, K., Myers, A., Porcu, R., Rangarajan, D., et al. (2022). MFiX-Exa: A path toward exascale CFD-DEM simulations. *The International Journal of High Performance Computing Applications*, 36(1), 40–58.

Appendix A

Codes used in the thesis

All the codes related to the works in this thesis have been published on Github:

<https://github.com/DengZhengyuan/Codes-of-my-thesis>

This code repository compresses three folders and is organized in the following structure:

1. Folder, “Reaction model & tracer process”, contains the codes for the pseudo-homogeneous reactive transport model for the ozone decomposition reaction used in Chapters 3 to 6 and the tracer process in Chapter 4.
 - (a) “homogeneous_reaction_model.c” is a user-defined function (UDF) code for ANSYS Fluent, written in C Language. The code supports a source term and a diffusion term for a user-defined scalar (UDS) equation, which is used for the catalytic ozone decomposition reaction in CFB reactors. The UDS applies solely to the gas phase and describes the changes in ozone mass fraction within the computational domain. The UDS occupied the first scalar position (UDS-0) in the scalar transport equation panel of ANSYS Fluent. The code utilized three user-defined memory (UDM) positions (UDM-0 to UDM-2) for recording slip velocity, reaction rate, and reduced ozone concentration, respectively.
 - (b) “export_data_of_tracers.c” is a UDF code for ANSYS Fluent, written

APPENDIX A. CODES USED IN THE THESIS

in C Language. The code records data at 2 m, 5 m, and 10 m in the riser and writes them to the file “`tracer_out.csv`”. Each data entry includes: current time (t), x -coordinate (x), y -coordinate (y), solids holdup (ϵ_s), gas velocity (v_g), solids velocity (v_s), gas tracer concentration (Y_g^{tr}), and solids tracer concentration (Y_s^{tr}). The code runs once after every 10 time steps at the end of the current time step iteration. It can also be used in downer cases.

- (c) “`calculate_time_series_of_tracer.wl`” is written in Wolfram Language. The code reads the data file “`tracer_out.csv`” outputted by the last code and spatially averages the tracer concentration of gas and solids at the same height for each time point. This process yields the average tracer concentration at each height for each time point. In calculating the spatial average, the local volume flow rate of the gas and solids phases is considered. Finally, the code will output a data file named “`data-tc.csv`”, each entry of which comprises a time point, gas tracer concentration at different heights, and solids tracer concentration at different heights. The time series data of tracer concentrations at different heights can be further processed or plotted.
- (d) “`other_UDF_codes.c`” is a UDF code for ANSYS Fluent, written in C Language. The code includes three models: (I) implements an external mass transfer model that developed by Scala (2013). (II) implements the Gidaspow drag model, which is used to conveniently introduce a sub-grid drag model or to make other modifications. (III) monitors the mass flow rate of the solids phase at the outlet and set the mass flow rate of the solids phase at the inlet to the same value.

2. Folder, “`Filtered model`”, contains the codes for the filtration process in Chapter 5. The order of code usage is shown in Figure A.1.

- (a) “`cal_filter_2D.wl`” is written in Wolfram Language. The code is used to

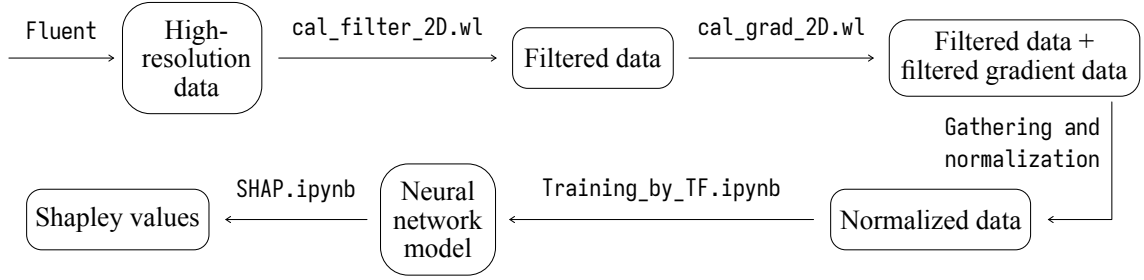


Figure A.1: Order of code usage in the filtering process

filter data that exported from Fluent. The data files should be stored in the folder “data” in the same directory. Each file containing data for the entire periodic domain and corresponds to one initial solids holdup and one time point. The data collection process is described in Section 5.4.1. Each entry of data includes: node number, x , y , $Y_g^{O_3}$, P , $v_{g,x}$, $v_{g,y}$, $v_{s,x}$, $v_{s,y}$, and ε_s . In the code, the variable “range” should be given and represents the size of the filter box, which is a multiple of d_p . The filtered data will be saved in the folder “table” in the same directory. Each piece of data in every file, in order, includes 17 variables: Δ_{filter} , x , y , ε_s , P , $v_{g,x}$, $v_{s,x}$, $v_{g,y}$, $v_{s,y}$, $v_{\text{slip},y}$, v_{slip} , $Y_g^{O_3}$, external mass transfer coefficient (k_m), drag coefficient in the y -direction (β_y), drag force correction coefficient (H_d), reaction correction coefficient (H_r), and external mass transfer correction coefficient (H_m). All the exported variables, include the coordinates, are filtered data.

- (b) “cal_filter_3D.wl” is written in Wolfram Language. It can do the filtering process for data obtained from three-dimensional periodic simulations. The inputs and outputs are the same as those for the code “cal_filter_2D.wl”, with the addition of the z -coordinate and related variables.
- (c) “cal_grad_2D.wl” is written in Wolfram Language. This codes calculates the gradients and generates table contain the gradients and other pa-

APPENDIX A. CODES USED IN THE THESIS

parameter in the raw dataset. The input data are generated from the code “cal_filter_2D.wl”. The parameter “precision” is the only parameter need to be set. It specifies the precision for processing filtered coordinates, ensuring that all filtered data are positioned on a structured mesh. The exported data files will be stored in the folder “tableGrad” in the same directory. Each data entry in each data file contains 27 variables, including gradients of solids holdup in x - and y -direction ($\partial\varepsilon_s/\partial x$, $\partial\varepsilon_s/\partial y$), gradients of pressure in x - and y -direction ($\partial P/\partial x$, $\partial P/\partial y$), gradients of y -direction slip velocity in x - and y -direction ($\partial v_{\text{slip},y}/\partial x$, $\partial v_{\text{slip},y}/\partial y$), gradients of slip velocity in x - and y -direction ($\partial v_{\text{slip}}/\partial x$, $\partial v_{\text{slip}}/\partial y$), and gradients of reduced ozone concentration in x - and y -direction ($\partial Y_g^{\text{O}_3}/\partial x$, $\partial Y_g^{\text{O}_3}/\partial y$), as well as the 17 input variables. These data are prepared for training the neural network.

(d) “Training_by_TF.ipynb” is written in Python. The code adopts TensorFlow to build an ANN and uses the data output by “cal_filter_2D.wl” for training. Data needs to be reordered and normalized before input. For two-dimensional reaction data, each data entry is sequenced as follows: Δ_{filter} , ε_s , $\partial\varepsilon_s/\partial x$, $\partial\varepsilon_s/\partial y$, $\partial p/\partial x$, $\partial p/\partial y$, v_{slip} , $\partial v_{\text{slip}}/\partial x$, $\partial v_{\text{slip}}/\partial y$, $Y_g^{\text{O}_3}$, $\partial Y_g^{\text{O}_3}/\partial x$, $\partial Y_g^{\text{O}_3}/\partial y$, H_r . The code also supports the training of two-dimensional drag force data and three-dimensional data.

(e) “SHAP.ipynb” is written in Python. The code uses the package “shap” to calculate the Shapley values of the trained ANN model. It requires the trained model and the training or validation data as inputs.

3. Folder, “Others”, contains the other codes that are related to the works in this thesis.

(a) “exp.wl” is written in Wolfram Language. It support a package “exp” for Wolfram programs to calculate cross-sectional averaged values of solids holdup,

APPENDIX A. CODES USED IN THE THESIS

particle velocity, and ozone concentration from the experimental data.

- (b) “set_position-L.jou” is a journal file for ANSYS Fluent and is written in Scheme Language. The code sets monitor lines for the CFB riser according to Li (2010)’s experiments.
- (c) “set_position-W.jou” is a journal file for ANSYS Fluent and is written in Scheme Language. The code sets monitor lines for the CFB riser according to Wang (2013)’s experiments.
- (d) “set_position-D-W.jou” is a journal file for ANSYS Fluent and is written in Scheme Language. The code sets monitor lines for the CFB downer according to Wang (2013)’s experiments.
- (e) “export_data_for_downer.py” is written in Python. The code uses package “pyfluent” to read the data files at different time points that exported by Fluent. Then, find the variables at the monitor lines that set by the journal files listed above. Finally, the code will output three data files for each time point, which include axial data, radial data, and overall data respectively. Each entry of each data file comprises x , y , v_{slip} , reaction rate (r), $Y_{\text{g}}^{\text{O}_3}$, $v_{\text{g},y}$, $v_{\text{s},y}$, and ε_{s} . The case and data files of CFB riser reactors can also be processed by this code with some modifications.
- (f) “intDowner.wl” is written in Wolfram Language. It support a package “intDowner” for Wolfram programs to calculate cross-sectional averaged values of solids holdup, particle velocity, and ozone concentration from the numerical results. The numerical results are generated by the last code. At the end of the code, an example is given to show how to use these functions to calculate the time-averaged profiles along the axial direction of the cross-sectional averaged numerical results, as shown in Figure 4.4. The calculation expresses as Equations (4.26), (4.27), and (4.28) in Section 4.4.1. The results of CFB

APPENDIX A. CODES USED IN THE THESIS

riser reactors can also be processed by this code with some modifications.

References

- Li, D. (2010). *Investigation of circulating fluidized bed riser and downer reactor performance for catalytic ozone decomposition* [Doctoral dissertation, The University of Western Ontario].
- Scala, F. (2013). Particle-fluid mass transfer in multiparticle systems at low reynolds numbers. *Chemical Engineering Science*, 91, 90–101.
- Wang, C. (2013). *High density gas-solids circulating fluidized bed riser and downer reactors* [Doctoral dissertation, The University of Western Ontario]. <https://ir.lib.uwo.ca/etd/1572/>

Curriculum Vitae

Name: Zhengyuan Deng

Post-Secondary Education and Degrees: Department of Chemical & Biochemical Engineering
The University of Western Ontario
London, Ontario, Canada
2018 - present Ph. D. candidate

School of Chemical Engineering and Pharmacy
Wuhan Institute of Technology
Wuhan, Hubei, China
2012 - 2016 B. Eng.

Honours and Awards: Second Class Prize, 2016
Hubei Province College Student Chemical Academic Innovation Colloquium

National Scholarship, 2015
Ministry of Education of the People's Republic of China

President Scholarship, 2014
Wuhan Institute of Technology, Wuhan, Hubei, China

Related Experience: Research and Teaching Assistant, 2019 - 2023
The University of Western Ontario, London, Ontario

Visiting Student, 2021
Shanghai Jiao Tong University, Shanghai, China

Research Assistant, 2016 - 2017
Wuhan Institute of Technology, Wuhan, Hubei, China

Publications:

- Cui, R., Sun, Z., Deng, Z., & Zhu, J. (2023). A numerical study of fluidization characteristics in transition from aggregative to particulate flow. *Powder Technology*, 119108.
- Deng, Z., Xia, Y., Long, B., & Ding, Y. (2017). Volumetric properties of diisopropyl ether with acetone at temperatures from 283.15 K to 323.15 K: An experimental and theoretical study. *Journal of Molecular Liquids*, 243, 257–264.
- Liu, W., Deng, Z., Zhang, Y., Zhu, X., Huang, J., Zhang, H., & Zhu, J. (2024). Decoding powder flowability: Machine learning pioneers the analysis of particle-size distribution effects. *Powder Technology*, 435, 119407.
- Long, B., Xia, Y., Deng, Z., & Ding, Y. (2017). Understanding the enhanced solubility of 1, 3-benzenedicarboxylic acid in polar binary solvents of (acetone+water) at various temperatures. *The Journal of Chemical Thermodynamics*, 105, 105–111.